Title
Investigating Valley States and their Interactions in Silicon/Silicon-Germanium Quantum Dots

Author
Penthorn, Nicholas

Publication Date
2020

Peer reviewed|Thesis/dissertation

UNIVERSITY OF CALIFORNIA
Los Angeles

Investigating Valley States and their Interactions in Silicon/Silicon-Germanium Quantum Dots

A dissertation submitted in partial satisfaction
of the requirements for the degree
Doctor of Philosophy in Physics

by

Nicholas Evan Penthorn

2020

ABSTRACT OF THE DISSERTATION

Investigating Valley States and their Interactions in Silicon/Silicon-Germanium Quantum Dots

by

Nicholas Evan Penthorn
Doctor of Philosophy in Physics
University of California, Los Angeles, 2020
Professor HongWen Jiang, Chair

Quantum computing in nanoscale silicon heterostructures has received much attention, both from the scientific community and private industry, largely due to compatibility with highly-developed silicon-based device fabrication and design present in essentially all aspects of modern life. Breakthroughs in quantum control and coupled qubit systems in silicon in the last five years have accelerated scientific research in this area, with gate-defined quantum dots at the forefront of this effort.

As techniques for quantum control become more sophisticated, subtle details of the silicon band structure are now of vital importance for the ultimate success of silicon quantum computing. Chief among these band features are the valley states, regions of the conduction band that form the ground state and a nearly degenerate excited state in quantum dot heterostructures. These valley states and their effects on electron dynamics can lead to quantum information loss and qubit decoherence, and so detailed characterization of the valleys is of great importance.

In this work, I first describe a spectroscopic technique utilizing fast voltage pulses on one

or two gates in a double quantum dot device to precisely measure the relevant valley state energies in both quantum dots as well as the coupling between valley states and electron orbital states. With this information, the valley states are leveraged to form a novel qubit basis with innate protection against decoherence from charge noise. Sub-nanosecond operations on this "valley qubit" are used to demonstrate complete quantum control. Finally, using real-time read-out of energy-selective tunneling in a single quantum dot, pure valley state coherence in the form of intervalley relaxation is directly probed. This relaxation is subsequently linked to spin-valley electron dynamics and the observance of a valley-dependent tunneling process is discussed theoretically using tight-binding formalism.

The dissertation of Nicholas Evan Penthorn is approved.

Kang Lung Wang

Karoly Holczer

Stuart Brown

HongWen Jiang, Committee Chair

University of California, Los Angeles

2020

To Wendy, the greatest collaborator I could hope for.

TABLE OF CONTENTS

LIST OF FIGURES

LIST OF TABLES

ACKNOWLEDGMENTS

It is overwhelming to consider the help and support I've received over the years that led to this undertaking. First and foremost, I couldn't have asked for a better advisor than HongWen Jiang. His passion for the research and genuine interest in my success as a graduate student are the reasons this document exists. I've deeply enjoyed our conversations, both casual and professional, and even his off-hand suggestions led to some of the biggest leaps in progress. I will always strive to follow his example in whatever comes next.

I'm grateful to Todd Averett for giving me my first real opportunity for scientific research as an undergraduate in Virginia. Beyond his skills as a teacher and as an experimentalist, I will forever appreciate his excellent taste in music.

I would like to thank Seth Putterman and the Julian Schwinger Foundation for their support, allowing me to do interesting research in both quantum dots and magnetic tunnel junctions — at times simultaneously. I'm grateful to Seth in particular for some thought-provoking discussions on quantum mechanics and the effects of measurement on quantum systems. I also extend my gratitude to our collaborator Lisa Edge at HRL Laboratories, whose expertise in silicon wafer growth facilitated our best experimental results.

Fellow graduate students Nayana Rajapakse and John Dean Rooney have my thanks for their friendship and advice during the years our research overlapped. Whether it was sharing a curtained-off desk space with Nayana away from the clatter of helium compressors or exploring Annapolis at a conference with John, my graduate experience was greatly enriched by their companionship. Similarly, I would like to thank Niels Thompson for his willingness to help with various projects around the lab, especially when I inadvertently break something.

It would be criminal of me to neglect mentioning my lab predecessors Blake Freeman and Joshua Schoenfield. Without their systematic and often selfless progress in perfecting our double quantum dot design in Si/SiGe and developing experimental techniques, none of the

results described here would have been remotely possible. Whenever I ran into problems or had physics questions as a new member of the lab, I could always turn to Blake and Joshua, who would address my every issue without a hint of impatience. Since I now know of the mad scramble to complete everything before graduation rears its ugly head, I can't have made life easy for them in their final years as graduate students. Despite that, Blake and Joshua set a tone of camaraderie and real intellectual curiosity that I felt throughout my graduate studies, even after they moved on to bigger things.

A lab operating in a vacuum could not operate for long. The amazing facilities management team has done so much to keep our lab running smoothly with no disasters. Craig Reeves, Jules Berger, and Cameron Irvin have consistently gone out of their way to fix any problems we have, no matter how small. Ernie Najar made sure that my various lab orders orbiting Los Angeles got to me, but also made time for some great conversations. Harry Lockhart and the machine shop staff have my gratitude for dealing with my amateur drafting skills. I would also like to thank our EH&S lab safety officer Manu Manamohan for ensuring that we didn't blow ourselves up, despite our best efforts.

This dissertation was the product of six years of graduate work, and I am the product of twenty-nine years of care and support from my family. By the transitive property, this work can really be attributed to Mom, Dad, and Meredith. I may be the only physicist in the family, but the emphasis on critical thinking and creativity they instilled in me from a young age is what drove me along this path.

To my wife and fellow scientist Wendy Herbst, who trekked across the country with me to pursue her own doctorate at UCLA: you made this whole thing worthwhile.

VITA

2011-2012	Undergraduate researcher in Prof. Mumtaz Qazilbash's lab, College of William and Mary.
2012-2014	Undergraduate researcher in Prof. Todd Averett's lab, College of William and Mary. Senior Honor's thesis: *"Precision Polarimetry of Polarized* ^{3}*He".*
2014	B.S. in Physics, College of William and Mary, Virginia.
2014-2015	Teaching Assistant, Department of Physics & Astronomy, University of California, Los Angeles.
2014-2020	Graduate Student Researcher, University of California, Los Angeles.
2014-2018	Graduate Fellowship, University of California, Los Angeles.
2016	M. S. in Physics, University of California, Los Angeles.
2018-2020	Julian Schwinger Foundation Graduate Fellowship.

PUBLICATIONS

N. E. Penthorn, J. S. Schoenfield, L. F. Edge and H. W. Jiang, "Direct measurement of electron intervalley relaxation in a Si/SiGe quantum dot," *arXiv:2007.08680 [cond-mat.mes-hall]* (2020), under review for Physical Review Applied.

N. E. Penthorn, J. S. Schoenfield, J. D. Rooney, L. F. Edge and H. W. Jiang, "Two-axis control of a fast valley qubit in silicon," *npj Quantum Information* **5**, 94 (2019).

N. E. Penthorn, J. S. Schoenfield, J. D. Rooney and H. W. Jiang, "Reduction of charge impurities in a silicon metal-oxide-semiconductor quantum dot qubit device patterned with nano-imprint lithography," *Nanotechnology* **30**, 46 (2019).

N. E. Penthorn, X. Hao, Z. Wang, Y. Huai and H. Jiang, "Experimental observation of single skyrmion signatures in a magnetic tunnel junction," *Physical Review Letters* **122**, 257201 (2019).

CHAPTER 1

Introduction

1.1 Developments in quantum computing

The concept of quantum computing is almost as old as the modern computer. The explosion of research in the nascent field of solid-state physics after World War II led to new understanding of many-body quantum physics, as well as to the development of the transistor in 1947 [202]. With this convergence of a groundbreaking technology and a growing field of study, the idea of a computer that manipulates and measures coherent quantum states follows a natural progression. A conceptual work from 1980 gave a quantum mechanical treatment to computer processes [Ben80] and shortly thereafter the idea of a "universal quantum computer" was discussed by Richard Feynman for the purposes of simulating quantum systems [Fey82]. The power of such a computer would come from the ability of each quantum bit, or "qubit", to couple to other qubits via quantum entanglement. The state of a quantum computer during operations would be a complex, coherent quantum state that collapses to a single outcome across all qubits upon measurement of any single qubit. Entanglement is ultimately the motivation for pursuing quantum computation, as it leads to unique applications tailored to solve problems that are functionally impossible for normal computers, some of which are enumerated below.

As is often the case, it took many more years before experimental efforts were capable of exploring some of the possibilities that were proposed theoretically. It wasn't until the late 1990s that the first physical implementation of a qubit was realized in superconducting

Josephson junctions [MSS01]. Even then, the prospect of a quantum computer with an entire chip of individually addressable qubits seemed far off.

Interest in quantum computing was stimulated by the 2011 development of a 128-qubit quantum annealer by D-Wave Systems [JAG11]. Although its capabilities were limited to a specialized procedure for finding global energy minima, it demonstrated that a scalable quantum system was possible with modern fabrication techniques. Within the last five years, boosted by a healthy amount of international competition [Str][MRT19], the field of quantum computing research has blossomed into a global innovation effort. Google, IBM and Microsoft are developing their own quantum computers [Cas17], and Intel is fabricating silicon-based qubits in partnership with QuTech at Delft University in the Netherlands [LPF18]. Now, even the terms "quantum computing" and "qubit" have made their way into the public lexicon.

1.1.1 Quantum simulation

Many-body quantum systems are hard to isolate in a laboratory setting, which makes it difficult to experimentally probe various condensed matter phenomena. Instead, researchers would like to perform computational simulations of many-body systems under the constraints of some theoretical model. Unfortunately, a large class of physical systems involves interactions between every particle, which for a system of N particles with two available states each involves a Hilbert space of size 2^N. With $N \approx 40$, modern supercomputers are incapable of finding a solution within any reasonable time frame. This category of classically intractable problems includes fundamental phenomena like ferromagnetism and Mott insulators.

With a quantum simulation, each particle in the system of interest can be mapped to one or more qubits. Then the qubits are coupled in a manner that suits the model under study and the quantum system is allowed to evolve naturally. Using ≈ 100 beryllium ions in a Penning trap, researchers were able to simulate ferromagnetism in the 2-D Ising model [BSK12].

1.1.2 Quantum cryptography

Of particular interest to government funding sources is the prospect of encrypting information in such a way that is impossible to decrypt by an eavesdropper, or at least so that any tampering with the information is immediately known. An important concept in quantum encryption is *quantum key distribution*, where some encryption key in the form of a qubit string is shared between parties. The key gives the receiver information on how to decrypt the data. Just this year (2020), researchers in China were able to send entangled photons via satellite over a distance of 1,120 km to transmit a quantum key [YLL20].

Beyond facilitating unbeatable data encryption, a quantum computer would also be able to break any public-key encryption scheme, all of which rely on the fact that normal computers struggle with prime-factoring large numbers. Using Shor's algorithm for integer factorization [Sho94], a quantum computer can find the factors of integer N with approximate time complexity $O(\log^2 N)$. Any classical computer would require at best $\approx O[\exp(2\log^{1/3} N)]$.

1.2 Quantum computing in the abstract

1.2.1 The qubit

In its most general form, a qubit can be any quantum system that has two well-defined, independent energy states. Practically speaking, it must also be possible to probe the two-state system with a measurement that returns one level or the other, in such a way that the states can represent Boolean variables 0 and 1. Ignoring the stipulation that the system is quantum, this definition can be applied to a "classical" bit as well. A solid-state transistor is in the "1" state when it is in the conduction phase due to a gate voltage, and it is in the "0" state when it is in its insulating phase. The major difference is that prior to measurement, a qubit will be in a quantum superposition of its logical basis states, so that the qubit state can be written as

$$|\psi\rangle = c_0 |0\rangle + c_1 |1\rangle , \tag{1.1}$$

where complex state coefficients c_0 and c_1 give the relative weights of the basis states and are typically normalized so that $|c_0|^2 + |c_1|^2 = 1$. Using the language of quantum mechanics, measuring the qubit state amounts to performing a *projective measurement*, wherein the qubit wavefunction collapses and the probability of measuring, for example, the qubit to be in state $|1\rangle$ is just $|\langle 1|\psi\rangle|^2 = |c_1|^2$. Once a projective measurement is made, the qubit is no longer in a coherent state and the system must be re-initialized into a known quantum configuration (for instance, allowing the qubit to relax into the ground state) before further qubit operations.

1.2.2 The Bloch sphere

It is useful to express the basis state coefficients in (1.1) with real-valued parameters that automatically satisfy the normalization condition. One way to do this is to start with the state $|0\rangle$ and apply unitary operations to rotate the state by polar angle θ and azimuthal angle ϕ:

$$|\psi\rangle = \exp(-i\sigma_z\phi)\exp(-i\sigma_y\theta) |0\rangle \tag{1.2}$$

$$= \cos(\theta/2) |0\rangle + e^{i\phi}\sin(\theta/2) |1\rangle . \tag{1.3}$$

In (1.2), σ_y and σ_z are Pauli matrices. From (1.3) it is clear that the sum of absolute squares of these coefficients must be equal to 1, and any (normalized) linear combination of $|0\rangle$ and $|1\rangle$ can be generated with $\theta \in \{0, \pi\}$ and $\phi \in \{0, 2\pi\}$. The form (1.3), and the manner in which it was obtained, is highly suggestive of a unit vector in spherical coordinates. If we treat the qubit state as such a vector, then each possible superposition of $|0\rangle$ and $|1\rangle$

is represented as a unique point on the surface of a unit sphere (Figure 1.1a). Using the coordinate system suggested by the choice of angle notation, we can determine the qubit state representation for a vector pointing along the Cartesian x-axis by setting $\theta = \pi/2$ and $\phi = 0$:

$$|x\rangle = \frac{1}{\sqrt{2}}(|0\rangle + |1\rangle). \tag{1.4}$$

Similarly we can find the states that point along the y and z axes:

$$|y\rangle = \frac{1}{\sqrt{(2)}}(|0\rangle + i\,|1\rangle), \tag{1.5}$$

$$|z\rangle = |0\rangle\,. \tag{1.6}$$

The unit sphere mentioned above, oriented so that the logical $|0\rangle$ state points in the $+z$ direction and the logical $|1\rangle$ points in the $-z$ direction, is known as the *Bloch sphere* and is a useful tool for describing qubits and their operations. In fact, any coherent qubit operation can be represented as a two independent rotations about orthogonal axes, mapping one point on the Bloch sphere surface to another. A simple example of this can be found in the original construction of the Bloch vector (1.2), where we have started with the qubit in $|0\rangle$ and applied a y rotation followed by a z rotation.

1.2.3 Single qubit operations

As demonstrated above, full quantum control of a qubit can only be achieved if rotations can be performed about no less than two orthogonal axes. Without yet going into detail about real-world qubit implementations, there are two fundamental quantum two-state processes that are widely used to accomplish two-axis control: Larmor precession and Rabi oscillations.

Consider a two-level system with energy difference ϵ between levels. Switching now to matrix notation, the simple diagonal Hamiltonian of this system can be written as

$$H = \begin{pmatrix} 0 & 0 \\ 0 & \epsilon \end{pmatrix}, \tag{1.7}$$

where we can choose the ground state energy to be zero for simplicity without affecting the physics. If we apply this Hamiltonian to one of its eigenstates and calculate the time evolution of the system with the Schrödinger equation, we find the trivial solution that the wavefunction is constant in time and no dynamics are obtained. However, if we apply the Hamiltonian to a quantum state that is *not* an eigenstate, for instance $|\psi\rangle = c_0 |0\rangle + c_1 |1\rangle$ $(c_0, c_1 \neq 1)$, we find that

$$|\psi(t)\rangle = c_0 |0\rangle + c_1 \exp(-i\epsilon t/\hbar) |1\rangle \tag{1.8}$$

and if we assume both coefficients are real (i.e. the Bloch vector lies somewhere on the $x - z$ plane), the probability of measuring the qubit Bloch vector to be along x is

$$|\langle \hat{x} | \psi(t) \rangle|^2 = \frac{1}{2} \left[1 + 2 c_0 c_1 \cos\left(\frac{\epsilon t}{\hbar} \right) \right]. \tag{1.9}$$

In other words, the qubit vector undergoes Larmor precession about the z axis of the Bloch sphere with angular frequency $\omega = \epsilon/\hbar$ (in the original Hamiltonian basis), providing one of the required qubit rotation axes. When the qubit starts near a pole of the Bloch sphere by setting either c_0 or c_1 to be very small, the precession is very weak. When the state coefficients are equal (the qubit vector lies on the Bloch sphere equator), the precession is maximized. Of course, Larmor precession can't be directly measured with a projective measurement of an observable quantity since the evolving parameter is the phase ϕ between eigenstates and the z projection of the qubit state is independent of ϕ. However,

the accumulated phase can be mapped to the z axis by way of a second, orthogonal rotation; for instance a $\pi/2$ rotation about the x axis.

The second axis of rotation can be achieved utilizing Rabi oscillations (Figure 1.1b). For this, consider the application of some oscillating potential along the x axis of the form $H_1 = V_0\cos(\omega t)\sigma_x$, where σ_x is the x Pauli matrix. The full Hamiltonian for the system including the original Hamiltonian (1.7) is now

$$H = \begin{pmatrix} 0 & V_0\cos(\omega t) \\ V_0\cos(\omega t) & \epsilon \end{pmatrix}. \tag{1.10}$$

The time evolution of this system is described by two coupled first-order differential equations with no known analytic solution. However, a well-known approximate solution can be found by transforming the qubit state to a reference frame that rotates with the oscillating potential:

$$|\psi\rangle = c_0\,|0\rangle + c_1\,|1\rangle \rightarrow c_0\,|0\rangle + c_1 e^{-i\omega t}\,|1\rangle\,. \tag{1.11}$$

The transformed differential equations in the rotating frame contain some terms of order $\exp(2i\omega t)$. With the *rotating wave approximation*, these terms oscillating at twice the drive frequency can be neglected and the probability of measuring the qubit to be in the excited state is given by

$$|\tilde{c_1}(t)|^2 = \frac{V_0^2}{V_0^2 + (\hbar\omega - \epsilon)^2}\sin^2\left(\frac{\sqrt{V_0^2 + (\hbar\omega - \epsilon)^2}}{2\hbar}t\right), \tag{1.12}$$

where $\tilde{c_1}(t)$ is the state coefficient in the rotating frame given by the mapping (1.11). Equation (1.12) describes rotations of the qubit state about some axis in the $x-y$ plane on the Bloch sphere. The efficiency of oscillations is maximized when the Rabi drive frequency ω matches the two-level energy splitting, and the frequency of oscillations at resonance is

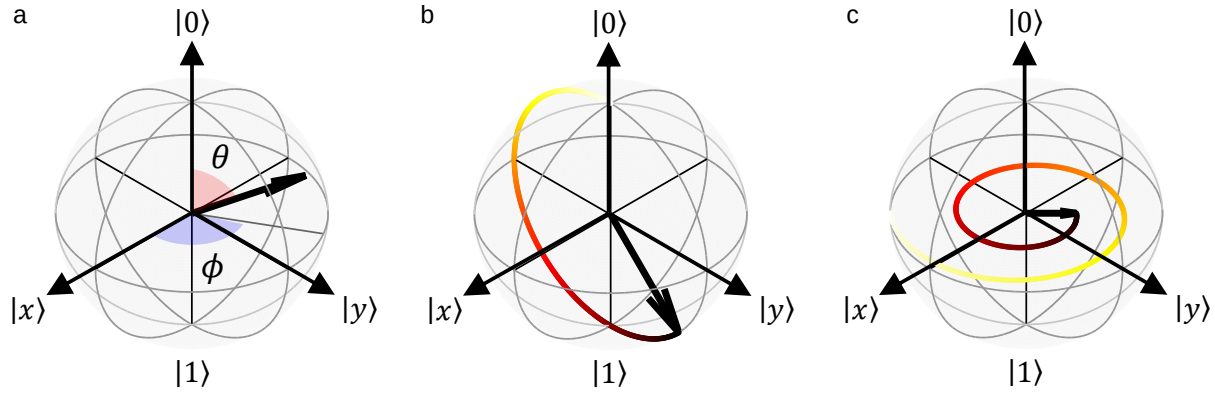

Figure 1.1: The Bloch sphere representation of the qubit state. (A) General state vector 1.3 lies on the surface of the Bloch sphere and is described by spherical coordinates θ and ϕ. (B) Rabi oscillations (x rotations) in the rotating frame. (C) Larmor precession (z rotations) in the presence of dephasing.

proportional to the drive strength V_0. It is important to note that Rabi oscillations can only be considered as simple x or y rotations in the rotating frame. In the lab frame, the qubit vector is actually spiralling from one qubit basis state to the other.

Armed with two rotation-inducing processes, a general qubit operation would be composed of, for example, a short burst of oscillating Rabi drive at the natural qubit frequency followed by a pause to allow Larmor precession.

1.2.4 Multi-qubit states and entanglement

As discussed previously, the true power of quantum computers comes from entanglement between two or more qubits. A multi-qubit state before entanglement can be written as a tensor product of single-qubit states, for example

$$|011\rangle \equiv |0\rangle_1 \otimes |1\rangle_2 \otimes |1\rangle_3 \,. \tag{1.13}$$

By contrast, any quantum state that *cannot* be written as a tensor product of single-qubit states is an entangled state. When two qubits are maximally entangled, any measurement on

both qubits in the same basis will always yield the same result. One simple way to produce an entangled state (although not necessarily maximally entangled) is to apply the two-qubit gate known as a conditional NOT, or "CNOT". The CNOT gate performs an x rotation of angle π on a target qubit, transforming $|0\rangle \rightarrow |1\rangle$ and $|1\rangle \rightarrow |0\rangle$, if and only if the control qubit is in state $|1\rangle$. Generally, if the control qubit is in state $|\psi_a\rangle = a_0 |0\rangle + a_1 |1\rangle$ and the target qubit is in state $|\psi_b\rangle = b_0 |0\rangle + b_1 |1\rangle$, then the result of a CNOT gate would be

$$\text{CNOT}(|\psi_a\rangle, |\psi_b\rangle) = a_0(b_0 |00\rangle + b_1 |01\rangle) + a_1(b_0 |11\rangle + b_1 |10\rangle). \tag{1.14}$$

The only case in which state (1.14) produces no entanglement is when the target qubit is already in state $|\pm x\rangle = 1/\sqrt{2}(|0\rangle \pm |1\rangle)$, which is unaffected by x rotations. It is also straightforward to confirm that when the target qubit starts in the $y-z$ plane, then a CNOT generates maximum entanglement. Since the CNOT requires only a single control axis on one qubit, it is a popular method of experimentally implementing two-qubit entanglement and is a benchmark process for demonstrating a fully realized multi-qubit device.

Although the topic of qubit entanglement and various gate strategies for implementing quantum algorithms is vital in developing physical quantum computers, the focus of this dissertation is single-qubit processes and characterization. As such, it is sufficient to provide a useful reference [AMM14] should the reader be interested in higher-level concepts.

1.2.5 Decoherence

With any physical qubit implementation, there is always the possibility of unwanted coupling of the qubit to the environment. By *environment*, I am referring to perturbations to the qubit in the form of noise or nearby extraneous energy levels. A qubit state that couples to the environment can no longer be considered as a pure state, since the nominally isolated two-state system now interacts in unknown ways with a much larger, multi-state system. Instead, the qubit is in a *mixed state*, or a statistical ensemble of pure states. All possible

mixed states can be represented as points within the Bloch sphere, just as all pure states exist on the Bloch sphere surface. While we can't exactly know the precise quantum mechanical details of the environment, we can measure the effects of environmental coupling on the qubit that manifest as decoherence. Qubit decoherence comes in two flavors, relaxation and dephasing, which in turn lead to errors in $x-y$ rotations and z (phase) rotations, respectively. Relaxation causes the qubit in its excited state $|1\rangle$ to decay to the ground state $|0\rangle$, while dephasing acts as a damping force that on average causes the qubit vector to spiral inward during precession, as in Figure 1.1c (in reality dephasing causes the qubit vector to "blur" so that instead of single spherical angles θ and ϕ to describe the state, there is a distribution of angles centered on θ and ϕ). Often, relaxation and dephasing are characterized in real systems by their characteristic time scales T_1 and T_2. These quantities are explored further in Chapters 5 and 7. In modern research efforts, decoherence is one of the greatest hurdles in achieving a full quantum computer and a simple figure of merit for a physical qubit is the coherence time over the operation time; in other words, how many single-qubit operations are possible before the system loses coherence.

With the introduction of decoherence processes, it is no longer sufficient to describe a general qubit state in the state vector representation. A more useful representation is the *density matrix*:

$$\rho = \sum_j p_j \left|j\right\rangle \left\langle j\right|, \tag{1.15}$$

where states $|j\rangle$ span the Hilbert space relevant to the qubit that may include other energy levels accessible to the physical qubit, and p_j is the corresponding weight of state $|j\rangle$ such that $\sum p_j = 1$. A projective measurement of some observable O can be expressed as $\mathrm{tr}(\rho O)$. The time evolution of a mixed state under a Hamiltonian H is then given by the von Neumann equation:

$$\frac{\partial \rho}{\partial t} = -\frac{i}{\hbar}[H, \rho]. \tag{1.16}$$

This describes unitary evolution, equivalent to the Schrödinger equation. To include decoherence, a generalized master equation known as the Lindblad equation is used (see Chapter 5).

1.3 Semiconductor quantum computing

Certain qubit implementations in physical systems have found success in particular areas. For instance, superconducting qubits and qubits encoded in photon polarization have been used in proof-of-principle implementations of Shor's algorithm, and trapped ions have proven well-suited to certain quantum simulations. Despite these milestones, a great deal of research has pursued qubit implementations in semiconducting structures. The prospect of utilizing the same well-established fabrication processes that have been so finely developed for the most famous semiconductor — silicon — has proven to be a strong motivation both for university and private research. Following a theoretical proposal for qubits as single electron spins in semiconductor quantum dots in 1998 [LD98], early progress in this sub-field was limited to quantum dots in GaAs/AlGaAs heterostructures [HKP07]. Since 2010, interest has shifted to silicon-based devices. Apart from the appealing properties of a very low hyperfine interaction strength and minimal spin-orbit coupling, qubits in silicon would be fully compatible with the impressive technological framework responsible for virtually all computer hardware used today.

1.3.1 Gate-defined quantum dots in silicon

Quantum dots in silicon are a leading device architecture for semiconductor quantum computing owing to a relatively simple fabrication procedure and the flexibility in design. Al-

though quantum dots are certainly not the only semiconductor device architecture being pursued, they comprise the majority of relevant literature. For a discussion on various semiconductor device schemes, see [ZDM13] and [CSD20].

There are two ways of describing quantum dots that offer their own insights. For the more engineering-oriented reader, a quantum dot is a field-effect transistor (FET) where the gate-controlled conduction path is isolated from its source and drain terminals by tunneling barriers. The quantum dot is a conducting island of two-dimensional electron gas (2DEG) formed by a positive bias on the gate electrode, and electrons from the adjacent source and drain charge reservoirs can tunnel into the dot at some rate determined by the tunnel barrier heights. The charge occupation of the quantum dot can be probed with the application of a source-drain bias voltage across the dot, and the resulting current is sensitive to the number of confined electrons.

In the context of atomic physics, a quantum dot can be considered a man-made atom in two dimensions. Confinement in the z direction (out of the plane of the semiconductor wafer), comes from the applied out-of-plane gate voltage and the semiconductor-insulator interface. A two-dimensional (in-plane) confining potential, not substantially different from the Coulomb potential generated from atomic nuclei, is formed by local electric fields from some gate configuration in the vicinity of the quantum dot. Just like atoms in a lattice, electrons in a system of quantum dots have orbital states and some tunable degree of interaction with neighboring sites. Unlike an atomic lattice, the details of the confining potential and the coupling strength between potential wells can be finely tuned over a wide dynamic range, which gives quantum dots a degree of electrical control that surpasses other semiconductor structures. However, with strong electrical control comes equally strong coupling to electronic noise sources that lead to decoherence, like Johnson noise from electronic hardware and $1/f$ noise from charge flucuators embedded in the insulator and at the interface. Additionally, conduction in any semiconductor is determined by the band structure of the material, and every conduction electron in the quantum dot is actually a psuedoparticle

composed of a bare electron and its interactions with atoms in the semiconductor lattice. Band structure effects can have a dramatic impact on elecron dynamics, leading to effects such as the ones described in Chapter 2. A final challenge that deserves mention is the fact that all silicon qubit devices must be operated at cryogenic temperatures, typically $T < 1\text{K}$, in order to prevent thermal population of excited electron states or higher conduction bands.

1.3.2 Quantum dot heterostructures

Although the gate patterns used to form quantum dots generally follow the same basic design rules, there are two distinct material choices for the layers that make up the silicon-based wafer (Figure 1.2). The first type is Si/SiO_2, where the quantum dot forms at the interface of silicon and its native oxide. The wafer is single-crystal silicon with the oxide layer, usually ten nm thick or less, grown with thermal processes [AFD07]. The incredibly abrupt surface potential at the silicon-oxide interface allows for sharp out-of-plane confinement and gates patterned on the wafer are very close to the 2DEG, meaning that deep, stable lateral potentials can be formed. Of course, the main interest in Si/SiO_2 quantum dots is the full compatibility with silicon metal-oxide-semiconductor FET (MOSFET) technology and fabrication processes. From a coherence standpoint, natural silicon has very low intrinsic spin-orbit coupling and minimal magnetic noise from atomic nuclei, assets that are further improved when dealing with isotopically enriched ^{28}Si [ZTT19]. A practical drawback often arises in the form of defects and charge traps at the interface and in the oxide, which generate their own potentials and make it difficult to form intentional, gate-defined quantum dots.

The second common heterostructure is the Si/SiGe quantum dot. In this system, the silicon quantum well is embedded in a SiGe alloy buffer that is weakly insulating [Sch97]. This separates the quantum dot from the surface potential where charge defects can accumulate and makes it much easier for form well-controlled dots [KSW14]. The price for better dot formation is shallower confining potentials, owing to the extended distance of the local gates from the quantum well. Additionally, there are indications that charge noise is slightly

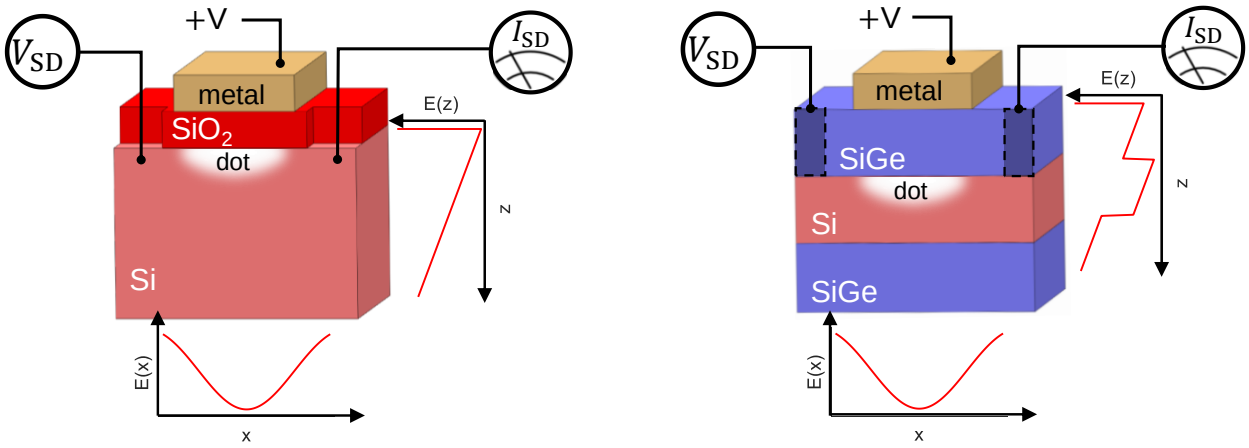

Figure 1.2: Two varieties of quantum dot heterostructures. Left: Si/SiO_2. Right: Si/SiGe. Both structures involve forming a quantum dot with electrostatic potentials from one or more local metallic gates. Potential energy landscapes in the x and z directions $E(x)$ and $E(z)$ for both structures are indicated.

greater in Si/SiGe quantum dots than in Si/SiO_2 [FSJ16].

1.3.3 Qubit encoding schemes

A testament to the freedom of design that quantum dots afford, there are many ways of encoding a qubit; that is, choosing a two-state subspace of the full Hilbert space encapsulating the electron orbitals, spin states, and band occupation. In his seminal work in 2000, theorist David DiVincenzo outlined basic requirements for the physical implementation of quantum computing [DiV00]. Those requirements, which are now known as the *DiVincenzo Criteria*, are now enumerated with bold text taken directly from the paper.

A scalable system with well-characterized qubits. First, any qubit device architecture must be configured so that hundreds or thousands of qubits can exist together with at least nearest-neighbor interactions. A challenge for scalability is the sheer number of wires that must be used to control all of the relevant quantum dot gates. This can be partially resolved with the use of multiplexing, where wires that are never used at the same time

can be shared between qubits. Additionally, every qubit subspace must be composed of two well-defined states with minimal coupling to states outside of the qubit subspace. Related to this and equally important is the capability of one qubit to couple to another, which imposes restrictions on what states can be used as the qubit basis.

The ability to initialize the qubits to a simple fiducial state. This requirement comes from the need for a known, un-entangled qubit state before any operations are performed. A simple initialization scheme is to turn off interactions and allow the qubits to relax to their ground states, i. e. $|\psi\rangle = |000\cdots\rangle$. However, for qubits with excellent coherence times this initialization may be restrictively long, and conversely if the initialization is quick then the qubits probably have poor coherence. One alternative is to first move the qubits into a configuration where the decoherence is maximized, then return them adiabatically to their original subspace after relaxation.

Long relevant coherence times, much longer than the gate operation time. As previously discussed, it must be possible to perform many operations before the qubit loses coherence. In semiconducting systems, the natural coherence times are usually too short for many-qubit operations to be feasible, but there is a way of extending qubit coherence with *quantum error correction*. These correction strategies still require a threshold coherence of $10^4 - 10^5$ times the qubit operation time in order to achieve fault-tolerant quantum computing.

A "universal" set of quantum gates. A given quantum algorithm may involve multi-qubit gates and the qubit control protocols must be equipped to handle this possibility. Fortunately, just as a classical algorithm can be decomposed into single-bit NOT and two-bit NAND gates, a quantum algorithm can be decomposed into a finite set of one- and two-qubit gates. A popular fault-tolerant gate set is the "Clifford+T" set [KMM13], which uses the Hadamard gate $H = (\sigma_x + \sigma_z)/\sqrt{2}$, the Phase gate $P = \sqrt{\sigma_z}$, and the T-gate

$T = |0\rangle\langle 0| + e^{i\pi/4}|1\rangle\langle 1|$ in combination with the two-qubit CNOT gate. The Clifford+T set is fault-tolerant because it includes gate operations needed for controlling ancillary qubits used for quantum error correction protocols.

A qubit-specific measurement capability. Each qubit should be individually addressable with electronic measurements. This can be a real challenge since, in the case of quantum dots, a single electron is tough to measure sensitively. Moreover, with the single quantum dot probe available (a source-drain current through the dot), it is impossible to assign a change in current to a particular electron if there are many quantum dots in series. Qubit-specific measurement can be achieved with charge sensing, a technique that will be described further in Chapter 4.

1.3.4 Charge qubit

With the DiVincenzo Criteria in mind, I will now discuss some well-studied qubit encoding schemes that at least have the potential to satisfy all five requirements. The charge qubit can be formed by a single electron in a double quantum dot potential well (Figure 1.3a). When the two dot energies are very different, the electron can tunnel from the high-energy dot to the low-energy dot. This toggles the qubit state between, for example, $|0\rangle = |L\rangle$ when the electron is in the left dot and $|1\rangle = |R\rangle$ when the electron is in the right dot. When the dot energies are equal, the electron can be found in either dot with equal probability and the qubit state lies on the Bloch sphere equator. Since electric fields are the primary control mechanism, it is very easy to electrically manipulate, measure and couple charge qubits [PYA03]. On the other hand, the charge qubit is highly susceptible to charge noise that limits the coherence time to a few nanoseconds [PPL10].

1.3.5 Spin qubit

Otherwise known as the Loss-DiVincenzo qubit from the original proposal in quantum dots [LD98], the spin states of an electron in the presence of an applied magnetic field form a good qubit basis (Figure 1.3b). Because pure spin states do not directly couple to electric fields, the spin coherence time in quantum dots is unparalleled. For the same reason, spin qubits are very hard to manipulate and read out. In addition to Larmor precession, the second axis of control comes from electron spin resonance (ESR). An oscillating magnetic field, typically the Oersted field from a nearby current-carrying wire, provides the off-diagonal driving Hamiltonian needed to induce Rabi oscillations when the driving frequency matches Zeeman splitting of the spin states: $f_{\mathrm{ESR}} = g\mu_B B/h$ where g is the electron g-factor (nearly equal to 2 when intrinsic spin-orbit coupling is low), μ_B is the Bohr magneton, and h is Planck's constant [HRX14]. An alternate, and possibly more scalable, method of driving Rabi oscillations is by moving the electron in a periodic fashion through a magnetic field gradient. The motion is achieved with oscillating in-plane electric fields from the same gates used to form the quantum dot, and the magnetic field gradient is generated from a thin magnetic layer deposited around the location of the dot. When the frequency of lateral motion is equal to the ESR frequency, electric dipole spin resonance (EDSR) is induced [YTO18]. The spin state can be measured either with Pauli spin blockade in a double-dot transport measurement [HVv04], or with single-dot energy-selective tunneling [EHW04b].

1.3.6 Singlet-triplet qubit

These are usually implemented in a double quantum dot system with two electrons (Figure 1.3c). When both electrons are in one dot, the system is in state $|0\rangle = |S\rangle$, the spin singlet. As the dot energies are changed to move one electron to the empty dot, the spins are decoupled and evolve independently. If some form of spin-orbit coupling is present, such as a difference in magnetic field strength seen by the two dots, then the spins will precess

at different rates. Then, when brought back together, it now becomes possible for the zero-net-spin triplet state to form, $|1\rangle = |T_0\rangle$ [DSH13]. The qubit state can be measured with Pauli spin blockade, either with a transport measurement or with charge sensing. Since the total spin of the two-electron system is zero at all times, the singlet-triplet qubit is immune to magnetic noise. However, since the quantum dot energies are electrically tuned this qubit is still susceptible to charge noise, leading to a dephasing time at best of 10 µs [JJH18].

1.3.7 Charge-spin hybrid qubit

With three electrons in a double quantum dot, it is possible to form a qubit basis that has protection against charge noise in one double-dot tuning limit and fast operation times and charge read-out in the other limit [KSS14]. Exploiting a process where the third electron can tunnel between the dots and facilitate a singlet-triplet transition, the hybrid qubit has one axis of control from Larmor precession between the $|S\rangle$ and $|T_0\rangle$ states and a second axis from Larmor precession in the orthogonal charge basis between $|L\rangle$ and $|R\rangle$. Although both operations are z rotations on the Bloch sphere in their respective bases, when the basis is fixed to be $|S\rangle - |T_0\rangle$ the charge precession resembles x rotation (although it occurs outside of the singlet-triplet subspace and therefore the Bloch vector moves through the origin). This qubit encoding has the benefit of fast manipulation times like the charge qubit, as well as a factor of two improvement in the dephasing time during singlet-triplet operations (Figure 1.3d).

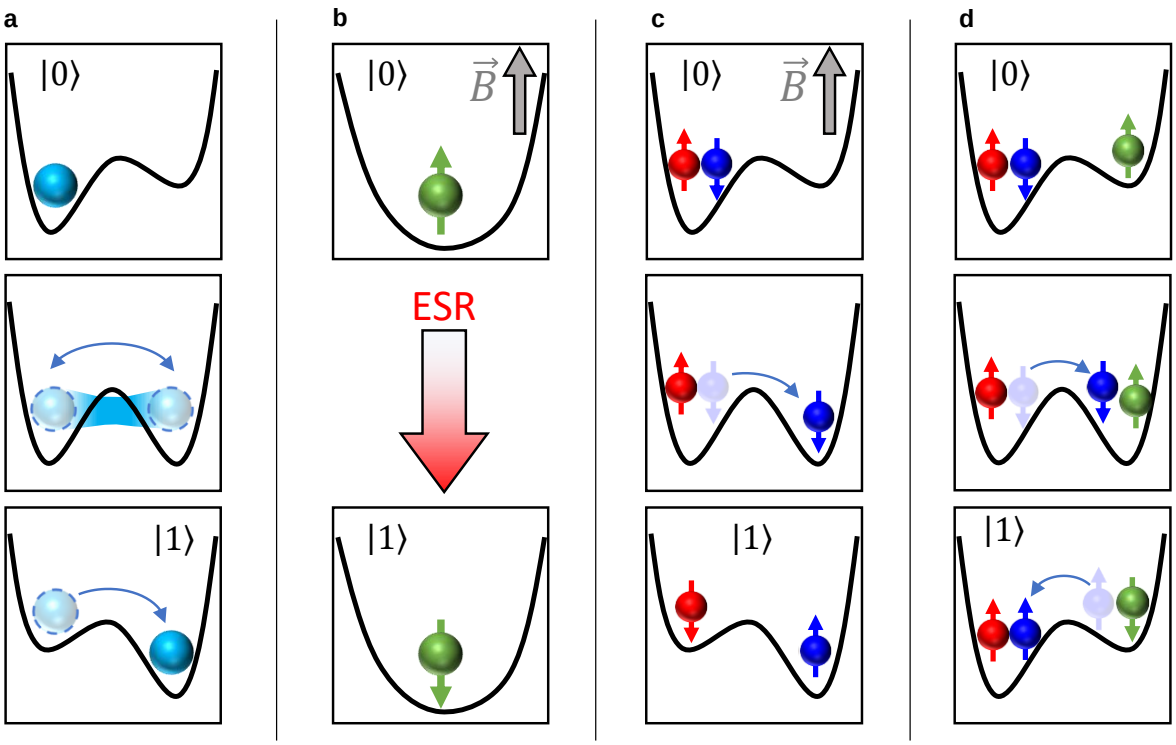

Figure 1.3: Common examples of qubit encodings in quantum dots with simplified operation steps. (A) The charge qubit in a double quantum dot is controlled by modifying the relative dot energies. (B) A single spin in a magnetic field can be manipulated with ESR. (C) The singlet-triplet qubit relies on separation and individual precession of two electron spins. (D) The hybrid qubit utilizes a singlet or triplet state, with a third electron as an exchange mediator in a double-dot system.

CHAPTER 2

Valley states in silicon

2.1 Silicon band structure

When discussing physical qubit implementations, it would be nice to describe a given qubit device as a controlled potential well, into which we can deposit individual charges to form a qubit in the basis we desire. The only energy levels seen by the qubit in this situation would be the levels that form the qubit basis states, well-separated from higher orbital levels. In semiconductor quantum computing, and silicon in particular, we can no longer rely on such a simple model. The energies of electrons in the semiconductor lattice form bands determined by the crystal structure in addition to any intentional levels arising from the device confinement potential.

2.1.1 The silicon lattice

The silicon crystal is described by the diamond lattice [AM76]. The lattice is composed of two inter-penetrating face-centered cubic (fcc) structures, meaning that there is one pair of silicon atoms at the eight points of a cube of side $a = 0.543$ nm and four additional pairs centered in the six cube faces. The silicon atoms in each pair are themselves separated by a distance of $a/4$ (Figure 2.1a). Periodicity of the lattice requires electron wavefunctions to be periodic themselves according to Bloch's theorem:

$$\psi(\mathbf{r}) = e^{i\mathbf{k}\cdot\mathbf{r}}u(\mathbf{r}), \tag{2.1}$$

where $u(\mathbf{r})$ is some periodic function that depends on the crystal lattice in real space and independently satisfies Schrödinger's equation [AM76]. In the nearly free electron model, we assume that electrons are weakly affected by the lattice potential and the wavefunctions resemble the free-space solutions, i. e. plane waves, to zeroth order so that $\psi(\mathbf{r}) \approx e^{i\mathbf{k}\cdot\mathbf{r}}$. The associated free-space energies are simply given by parabolas in k space:

$$E(\mathbf{k}) = \frac{\hbar^2 k^2}{2m}, \tag{2.2}$$

where for now the value of electron mass m is left intentionally vague, since corrections to the free-space solution can alter the effective mass substantially. It turns out that for conductors the parabolic bands obtained in the free electron solution (2.2) are a good approximation within a single reciprocal lattice period (the first Brillouin zone), with modifications from lattice interactions contributing near the Brillouin zone boundary.

2.1.2 Band structure with pseudopotentials

The goal is now to calculate the conduction bands in silicon to find energy minima, which will give the true electron ground state. This can be done perturbatively, keeping in mind the possibility of degenerate states, with the pseudopotential formalism [Phi58]. The periodic part of the wavefunction $u(\mathbf{r})$ and the periodic potential are both Fourier expanded in reciprocal space. The Schrödinger equation at reciprocal lattice vector $\mathbf{G}_l$ then reads

$$\frac{\hbar^2}{2m_0}|\mathbf{k}+\mathbf{G}_l|^2 A_{\mathbf{G}_l} + \sum_n V_{\mathbf{G}_{l-n}} A_{\mathbf{G}_n} = E(\mathbf{k}) A_{\mathbf{G}_l} \tag{2.3}$$

where $A_{\mathbf{G}_l}$ and $V_{\mathbf{G}_l}$ are the Fourier coefficients of $u(\mathbf{r})$ and potential $V(\mathbf{r})$, respectively. Since the lattice potential is explicitly included, the mass term m_0 is just the free electron mass.

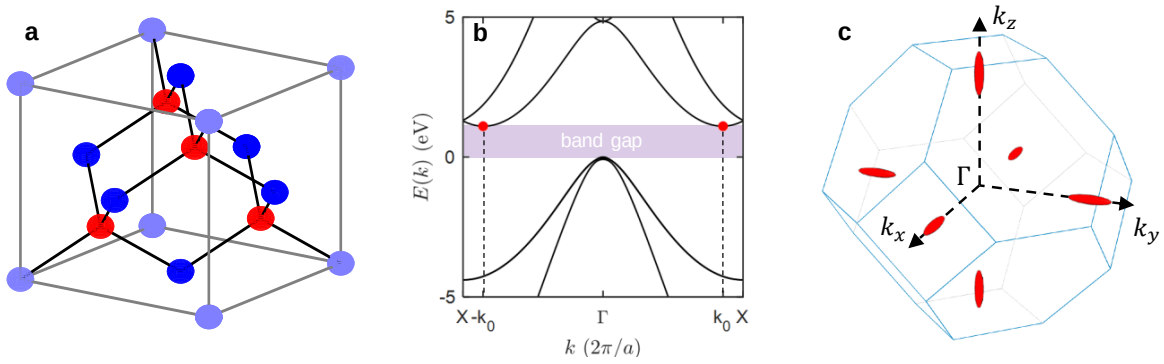

Figure 2.1: Silicon crystal and band structure. (A) The silicon primitive unit cell in real space adapted from [AM76]. Blue vertices are the traditional fcc lattice points, red points are the basis silicon atoms. (B) Silicon band structure near the band gap, calculated in Matlab using a pseudopotential script modified from [Zak10]. Valley states are indicated at $\pm k_0$ by red points. (C) Valley equipotentials shown as red ellipsoids within the first Brillouin zone.

Solving for $E(\mathbf{k})$ amounts to finding the eigenvalues of the matrix with elements

$$H_{i,j}(\mathbf{k}) = \frac{\hbar^2}{2m_0}|\mathbf{k} + \mathbf{G}_i|^2\delta_{i,j} + V_{\mathbf{G}_{i-j}}, \tag{2.4}$$

$$V_{\mathbf{G}_m} = V^S_{\mathbf{G}_m}\cos(\mathbf{G}_m \cdot \tau). \tag{2.5}$$

Here I've introduced the silicon symmetric form factor $V^S_{\mathbf{G}_m}$, found experimentally through x-ray attenuation [MMB85], and the reciprocal vector $\tau = \frac{1}{8}(1,1,1)$ representing the offset of the two basis silicon atoms from the lattice origin. Performing the diagonalization of (2.4) with 125 terms in the Fourier expansion [Zak10] took about 15 seconds on my laptop, a testament to the power of the pseudopotential method (Figure 2.1b).

In Figure 2.1b, the silicon bands are plotted along the k_z direction from one face of the fcc Brillouin zone to the opposite face through the zone center point Γ, in the vicinity of the band gap. There are several important quantities that can be extracted from the bands, notably the degeneracy, *effective masses*, and *crystal momenta* of electrons in the conduction band. As a relevant example for what is to follow, suppose an electron is in the lowest possible energy in the conduction band. From Figure 2.1b it is apparent that there

are at least two degenerate minima located at $\pm k_0 = \pm 0.82(2\pi/a)$, close to the Brillouin zone boundary. Considering there are six equivalent X points on the Brillouin zone, the conduction band minimum is actually six-fold degenerate. These six conduction states are known as the *valley states*.

2.2 Valley state electrons

2.2.1 Effective mass

Any local energy minimum can of course be expanded in a polynomial series and it is often a good approximation to keep terms up to degree 2, provided the region of interest doesn't deviate much from the minimum point. Using this approximation at a valley minimum in the conduction band and enforcing a dispersion relation of the form (2.2), it is possible to write the energy at, for instance, $\mathbf{k_0} = k_0\hat{z}$ as

$$E(\mathbf{k}) = E_0 + \frac{\hbar^2}{2}\left[\frac{k_x^2}{m_x} + \frac{k_y^2}{m_y} + \frac{(k_z - k_0)^2}{m_z}\right], \tag{2.6}$$

where m_x, m_y, and m_z are the electron's effective mass in the associated k space direction. This relation plots an ellipsoid, centered at $\mathbf{k_0}$, with axes determined by the effective mass components (Figure 2.1c). Appropriately, this is called the effective mass approximation [Kit05]. In silicon the two mass components perpendicular to the reciprocal vector given by $\overline{\Gamma X}$ are equal, so along the k_z axis the valley state energy terms are grouped together with a longitudinal mass m_l and a transverse mass m_t:

$$E(\mathbf{k}) = E_0 + \frac{\hbar^2(k_x^2 + k_y^2)}{2m_t} + \frac{\hbar^2(k_z - k_0)^2}{2m_l}. \tag{2.7}$$

Finally, the effective mass components can be calculated from the local band curvature:

$$\frac{1}{m_i} = \frac{1}{\hbar^2}\frac{\partial E(\mathbf{k})}{\partial k_i}. \tag{2.8}$$

Using the band calculations in the previous section, we get longitudinal and transverse effective masses of $m_l = 0.92m_0$ and $m_t = 0.19m_0$ [Gre90]. Considering the physical implications of the effective mass approximation, this result says that an electron in a valley state behaves like a free particle (subject to periodic boundary conditions) with a *fifth* of the electron rest mass. Despite the many bands of silicon and the details of the crystal structure that comprise band calculations, most of the relevant physics is simply encapsulated in the scalar effective mass terms.

2.2.2 Valley wavefunctions in bulk silicon

Using the effective mass approximation, it is now possible to obtain a simple form of the valley state wavefunctions in bulk silicon. Details of the potential landscape are wrapped into the mass, so the Hamiltonian of the system is just the kinetic energy given by (2.7). If the wave vector $\hbar\mathbf{k}$ is treated as a form of momentum (the crystal momentum), then the Schrödinger equation simply describes a free particle and the solutions are plane waves $e^{i\mathbf{k}\cdot\mathbf{r}}$. The solutions in just the k_z dimension, for instance, are a superposition of the two z valley Bloch waves [AFS82]

$$\psi_{\pm}(z) = \frac{1}{\sqrt{2}}[u_{+k_0}(z)e^{ik_0 z} \pm u_{-k_0}(z)e^{-ik_0 z}]. \tag{2.9}$$

This is an interesting result, because it shows that a conduction electron in the ground state in silicon has a wavefunction that rapidly oscillates in real space. In a material with $k_0 = 0$ (a direct gap semiconductor), the wavefunction is just the periodic term in the Bloch wavefunction (2.1). Since silicon has a nonzero k_0, and in fact a crystal momentum very close to the Brillouin zone boundary, the associated ground-state valley wavelength is on

the order of the atomic spacing. This in and of itself is a drastic departure from the classic "particle in a box" assumption that researchers would like to make when operating qubits, and leads to an acute sensitivity of electron physics to atomic-scale details of the quantum dot heterostructure.

2.3 Modifications to the valley states in quantum dot heterostructures

2.3.1 Heterostructure confinement

Thus far, the discussion has been limited to valley states in bulk silicon where the crystal symmetry guarantees that the valley states are sixfold degenerate. However, in quantum dot devices the valley state energies are modified. In Si/SiO_2 quantum dots, the out-of-plane (z) wavefunction is strongly confined from the sharp interface potential and the gate-generated electric field (see Figure 1.2). This breaks the symmetry in the z direction and lifts the valley degeneracy [AFS82]. In Si/SiGe quantum dots, the lattice mismatch between the silicon quantum well and the SiGe alloy buffer creates tensile strain in the quantum well, breaking the symmetry in the $x-y$ plane [Sch97]. In both cases, the result is a two-fold degenerate z-valley ground state, while the four-fold degenerate x and y valleys are lifted by around 20 meV in the case of Si/SiO_2 and 200 meV for Si/SiGe. Taking into account electrostatic confinement within a quantum dot, the degeneracy of the z valleys is lifted to form the ground state and first excited state of the quantum dot [SCH09][ZDM13]. The energy difference between z valleys, which will from now on will be referred to as the *valley splitting*, is around 1 meV in Si/SiO_2 and on the order of 0.1 meV in Si/SiGe in the ideal limit. Since the in-plane valley state energies are situated above the z valleys by tens or hundreds of meV, they are not particularly relevant on the energy scale of quantum dots, with charging energies of $1-10$ meV. However, the nearly degenerate out-of-plane valley states can wreak havoc on basic quantum dot measurement, for instance by allowing supposed violations of

the Pauli exclusion principle [CCL10]. Important for qubit operation, an uncontrolled state near the qubit ground state can become an avenue for quantum information leakage, being a state outside the qubit subspace.

2.3.2 Confined valley wavefunctions in the tight-binding model

To make any substantive theoretical predictions about the behavior of confined electrons in valley states, the issue again becomes correctly modeling the Bloch functions $u_{\mathbf{k}}(\mathbf{r})$. Effective mass theory is capable of producing analytic Bloch functions, and has been applied in detail to Si/SiGe heterostructures [FCT07], but the calculations can be strenuous. The tight-binding model is a simplified approach to lattice wavefunctions that accurately reproduces atomic-level behavior and avoids explicit calculation of the Bloch functions [SK54]. The basic assumption, rather than starting from the free electron case and applying weak effects from the lattice, is to start with non-interacting atoms at each lattice site and apply weak interaction between sites. This implies that the bound electron wavefunctions are more or less localized at individual lattice points rather than spread out over many atoms. Given some Hamiltonian H_{atom} for the dynamics of an electron bound to an isolated atom and a correction term $\Delta U(\mathbf{r})$ that contains all the interactions with neighboring sites, the tight-binding Hamiltonian can be written in second quantization formalism as [AS06]

$$H_{TB} = t_1 \sum_{i,j=nn} (c_i^\dagger c_j + c_i c_j^\dagger) + t_2 \sum_{k,l=nnn} (c_k^\dagger c_l + c_k c_l^\dagger) + \cdots , \tag{2.10}$$

where $c^\dagger$, c are creation and annihilation operators for atomic site occupation, indices i, j iterate over nearest atomic neighbors, and indices k, l iterate over next nearest neighbors. Coefficients t_n are overlap integrals that measure the amount of wavefunction overlap between bound electron wavefunctions, calculated in terms of the m^{th} orbital function $\phi_m(\mathbf{r})$ and

assumed to be small [AM76]:

$$t_n = -\int \phi_m^*(\mathbf{r})\Delta U(\mathbf{r})\phi_l(\mathbf{r}-\mathbf{R}_n)d^3\mathbf{r} \tag{2.11}$$

In (2.11), $\mathbf{R}_n$ is the real-space vector separation between n^{th} nearest neighbors. A further simplification, instead of directly calculating the overlap integrals, is to choose scalar values of t_n so that the eigenstates of (2.10) lead to known band structure characteristics. From the nearly free electron model we have established that ground state conduction electrons have a crystal momentum of $\hbar k_0$ and a longitudinal effective mass $m_l = 0.92m_0$, which leads to nearest-neighbor and next-nearest-neighbor overlap integrals of $t_1 = 0.683$ eV and $t_2 = 0.612$ eV [BKE04].

It may seem counter-intuitive to base some calculations in the tight-binding model to quantities obtained with the nearly-free electron model. The former assumes that electrons barely see the atomic lattice, and the latter assumes that electrons barely see beyond a single atomic potential. We can get away with this for two reasons: first, silicon as a semiconductor falls between the separate limits dealt with by the two models and so neither one is perfectly suited to deal with silicon bands. Second, the valley states as bounded by the constant-energy ellipses (2.7) are small enough compared to the full Brillouin zone that the parabolic dispersion approximation is quite accurate.

Finally, the valley wavefunctions in the out-of-plane direction confined to a silicon quantum well embedded in SiGe and in the presence of a gate-generated electric field F_z can be obtained by diagonalizing the full Hamiltonian

$$H = H_{TB} + V_{\text{well}}(z) + eF_z z. \tag{2.12}$$

The left panel of Figure 2.2 shows the valley state wavefunctions in a 10 nm wide quantum well (the details of this calculation are discussed in Chapter 8). As expected, the valley wavefunctions have fast oscillations with a periodicity of almost one atomic spacing. Confine-

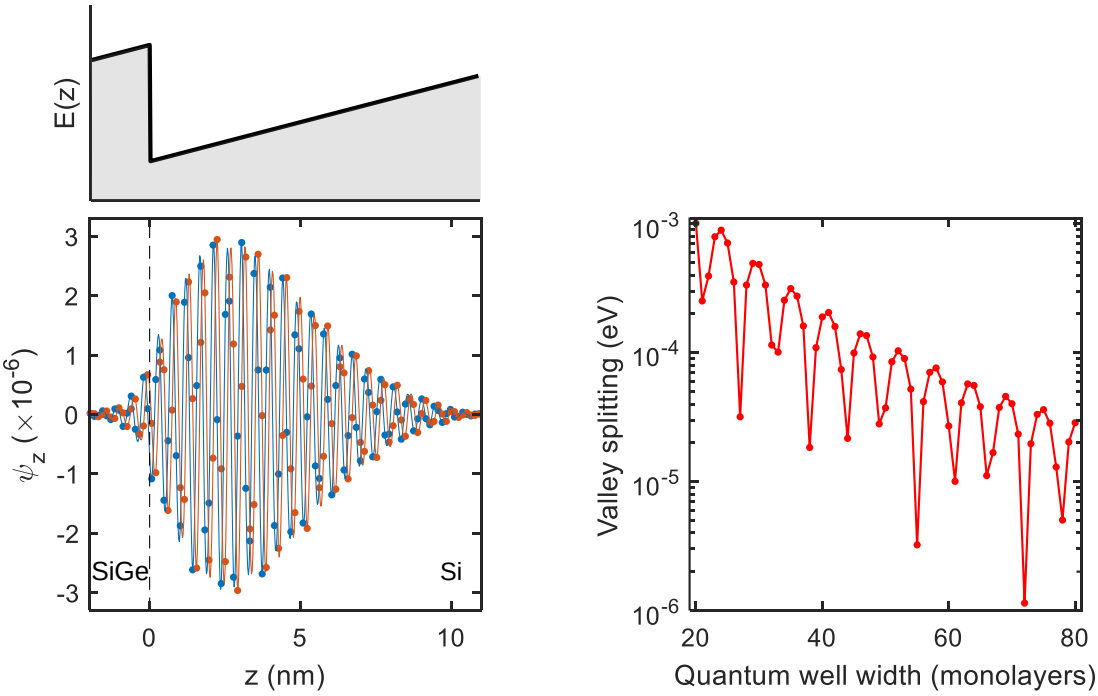

Figure 2.2: Valley state calculations with the tight-binding model (2.12). Left: ground state (blue) and excited state (orange) wavefunctions in a silicon quantum well with an applied electric field. The wavefunctions are described by a slowly varying orbital envelope function on top of a rapidly oscillating Bloch wave. Top: corresponding potential energy. Right: valley splitting as a function of the number of silicon atomic layers in the quantum well with no electric field. Oscillations become more dramatic as the quantum well is made thinner.

ment leads to a slowly varying envelope on top of the waves to satisfy boundary conditions, amounting to multiplying (2.9) by some normalized first orbital state of the well. In addition, there is a phase difference of almost $\pi/2$ between the ground state and excited state wavefunctions, called the *valley phase*, that relates to the valley splitting. Taken together, the oscillation wavelength and valley phase imply that the number of atomic layers in the quantum well have a substantial impact on the valley eigenstates, and therefore the valley splitting (Figure 2.2).

2.3.3 Effects of interface disorder

In physical heterostructures it isn't realistic to assume that the interface is atomically flat. Although the random placement of a few stray atoms at the interface may not have much affect on the orbital electron energies, it is clear that the valley wavefunctions can change if even a single atomic layer is added or removed from the quantum well. In Figure 2.2, the ground state wavefunction has a node at the upper Si/SiGe interface and, due to the valley phase, the excited state wavefunction is near a maximum at the same interface. If the quantum well width were now reduced by one atomic spacing, the excited state will change while the ground state is mostly unaffected. This leads to a measurable change in the valley splitting (Figure 2.2, right panel). Moreover, if the quantum well width has some in-plane spacial dependence then the valley splitting depends on the lateral quantum dot location. This is the origin of valley-orbit coupling, which can significantly reduce the valley splitting from the ideal device case. In Si/SiO_2, valley splitting is found experimentally to be around 100 µeV [VHY14][GHJ16]. In Si/SiGe, where the interface potential barrier isn't as sharp, the valley splitting can vary drastically from 10 to 100 µeV [MPB17][SFJ17][BRK11]. The variability seen in Si/SiGe devices presents yet another obstacle for reproducible qubit behavior, since it's impossible to know *a priori* what the valley splitting will be in a given quantum dot device. The various degeneracies of the valley states, including the reduction in valley splitting from disorder, are qualitatively displayed in Figure 2.3.

2.4 Forms of valley hybridization

The magnitude of the valley splitting, specifically compared with standard qubit bases, is a challenge in and of itself (for example, a spin qubit operated at a magnetic field of 1T and a charge qubit operated at the inter-dot anti-crossing will both have an energy splitting of $\sim$ 100 µeV). However, there is the opportunity for even bigger problems due to the hybridization of valley states with other measurable electron degrees of freedom. Mentioned

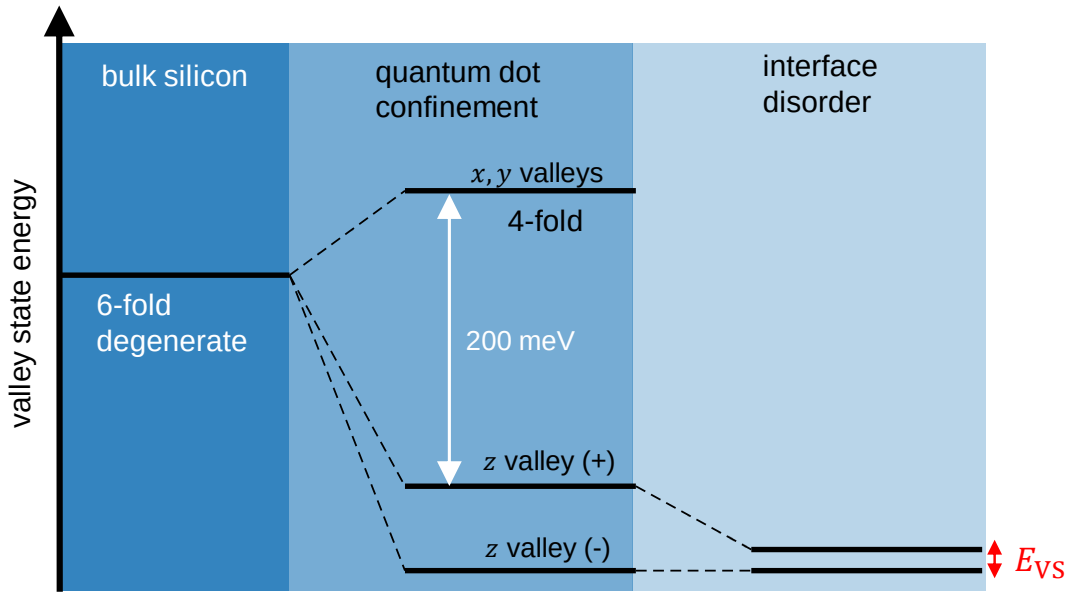

Figure 2.3: Lifting of the six-fold valley degeneracy. The z valleys are split off from the in-plane valleys due to lattice strain in Si/SiGe and are themselves split by quantum dot confinement. Interface roughness reduces the valley splitting depending on the amount of valley-orbit coupling.

in the previous section is valley-orbit coupling, responsible for a reduction in valley splitting. Coupling between valleys and spin states is also possible, leading to complex and often unwanted electron behavior.

2.4.1 Valley-orbit coupling

At this point I have established that valley-orbit coupling arises from spatial nonuniformity of the potential well at the atomic level. Valley-orbit coupling can be quantitatively calculated by considering the full electron wavefunction in the valley-orbit hybrid state $\psi^{(j)}_{\pm z}(\mathbf{r})$, which includes the z direction valley wavefunctions shown in Figure 2.2a and the in-plane function determined by the lateral, gate-defined quantum dot confinement. The valley-orbit coupling is then given by

$$\Delta^{(j)} = \langle \psi^{(j)}_{z} | V(\mathbf{r}) | \psi^{(j)}_{-z} \rangle \, . \tag{2.13}$$

If the interface potential $V(\mathbf{r}) = V(z)$, meaning total interface uniformity, then the coupling between valleys and in-plane orbital states will be zero as expected. It is useful to give a qualitative example of how such hybridization would affect the operation of a charge qubit. Consider an electron in a double quantum dot potential with some degree of inter-dot tunnel coupling Δ. Ignoring valleys and higher orbital states, the two-state subspace depends on the detuning ϵ, or the difference in energies between the two quantum dots. When $|\epsilon| >> 0$, the electron is almost certain to be found in the dot with the lowest energy and the eigenstates are just $|L\rangle$ and $|R\rangle$, corresponding to occupation in the left or right dot. When $\epsilon = 0$, the dot energies are equal and the electron can be measured in either dot with equal probability with eigenstates $|\pm\rangle = \frac{1}{\sqrt{2}}(|L\rangle \pm |R\rangle)$. The charge qubit Hamiltonian in the charge basis $\{|L\rangle, |R\rangle\}$ is

$$H = \begin{pmatrix} -\epsilon/2 & \Delta \\ \Delta & \epsilon/2 \end{pmatrix} \tag{2.14}$$

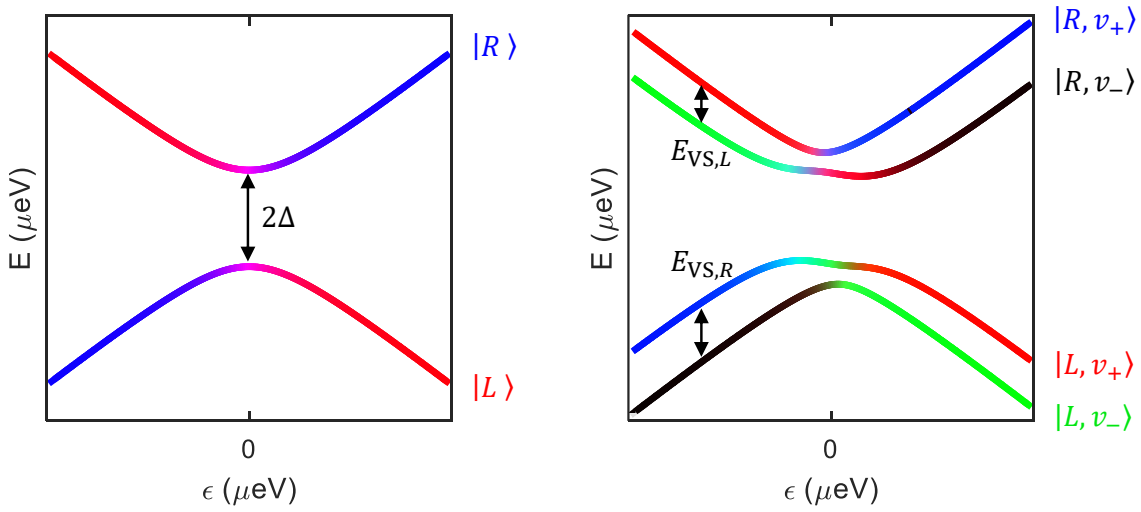

Figure 2.4: Left: a charge qubit spectrum. Lines are colored based on dot occupation (blue = more in the right dot, red = more in the left dot). Right: the same charge qubit in the presence of valley splitting. Note that the valley splitting in the two dots are different in principle.

and the energy gap at the zero detuning anti-crossing is 2Δ. The eigenenergies for this Hamiltonian are plotted against detuning in the left panel of Figure 2.4.

With the addition of non-degenerate valley states and valley-orbit coupling, the two-state spectrum turns into a four-state spectrum, two valleys per quantum dot, and each valley can couple to the two valleys in the opposite dot [GEC13][TH19]. In the pseudo-charge basis $\{|L, v_-\rangle, |L, v_+\rangle, |R, v_-\rangle, |R, v_+\rangle\}$, the general Hamiltonian can be written as

$$H = \begin{pmatrix} -\epsilon/2 & 0 & 0 & 0 \\ 0 & -\epsilon/2 + E_{\mathrm{VS}}(\mathbf{r}_L) & 0 & 0 \\ 0 & 0 & \epsilon/2 & 0 \\ 0 & 0 & 0 & \epsilon/2 + E_{\mathrm{VS}}(\mathbf{r}_R) \end{pmatrix} + \boldsymbol{\Delta}(\mathbf{r}_L, \mathbf{r}_R), \tag{2.15}$$

where $E_{\mathrm{VS}}(\mathbf{r}_i)$ is the local valley splitting in the vicinity of dot i and Hermitian matrix $\boldsymbol{\Delta}(\mathbf{r}_L, \mathbf{r}_R)$ contains off-diagonal terms that couple states of different charge occupation. Ex-

perimentally the coupling matrix and how it evolves with lateral dot positions isn't known, but it is possible to put (2.15) into a phenomenological form assuming the dot positions are independent of detuning:

$$H = \begin{pmatrix} -\epsilon/2 & 0 & \Delta_1 & -\Delta_2 \\ 0 & -\epsilon/2 + E_{\mathrm{VS},L} & -\Delta_3 & \Delta_4 \\ \Delta_1 & -\Delta_3 & \epsilon/2 & 0 \\ -\Delta_2 & \Delta_4 & 0 & \epsilon/2 + E_{\mathrm{VS},R} \end{pmatrix}. \tag{2.16}$$

The four-state spectrum is plotted in Figure 2.4 (right panel) in the case where the left and right dot valley splittings are less than the inter-dot coupling. Obviously, any researcher endeavoring to make a charge qubit that sees this spectrum would likely throw the device away and try a new one. However, certain aspects of the valley-orbit hybridization could lead to a unique qubit subspace, as demonstrated in Chapter 6.

2.4.2 spin-valley coupling

Pure spin states with their outstanding coherence times make an excellent qubit basis. An electron in a single quantum dot in the presence of an applied in-plane magnetic field B will have non-degenerate spin states with Zeeman splitting $E_Z = g\mu_B B$ (Figure 2.5, left panel). The ideal spin qubit Hamiltonian, again ignoring valleys and higher orbitals, is automatically diagonal, with eigenenergies $\pm E_Z/2$. However, spin states can in general couple to other electron degrees of freedom like orbital states and valley states. Intrinsic spin-orbit coupling in silicon is quite low which contributes to the appeal of silicon as a semiconductor qubit material [PKJ11], but spin-valley coupling is often non-negligible. Since spin energies of the same valley occupation diverge according to the Zeeman energy, spin-valley coupling occurs between states of different spin and valley numbers (Figure 2.5, right panel) leading to a

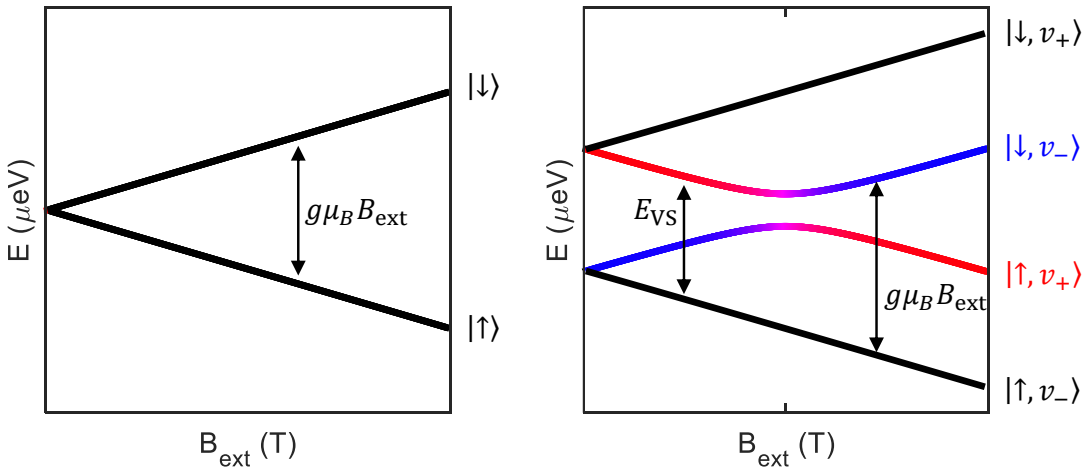

Figure 2.5: Left: a spin qubit spectrum. The spin states are split by the Zeeman energy. Right: the same spin qubit in the presence of valley splitting. The spin-valley anti-crossing occurs at $g\mu_B B_{\text{ext}} = E_{VS}$.

spin-valley Hamiltonian of the form

$$H = \begin{pmatrix} -\frac{1}{2}g\mu_B B & 0 & 0 & \Delta_a \\ 0 & -\frac{1}{2}g\mu_B B + E_{\text{VS}} & \Delta_a & 0 \\ 0 & \Delta_a & \frac{1}{2}g\mu_B B & 0 \\ \Delta_a & 0 & 0 & \frac{1}{2}g\mu_B B + E_{\text{VS}} \end{pmatrix} \tag{2.17}$$

in the spin-valley basis $\{|\uparrow, v_-\rangle, |\uparrow, v_+\rangle, |\downarrow, v_-\rangle, |\downarrow, v_+\rangle\}$. As I will discuss in Chapter 7, spin-valley coupling leads to spin decoherence, making careful characterization of the valley states critical for spin qubits.

CHAPTER 3

Device fabrication and testing capabilities

3.1 Fabrication

It is a long and sometimes painful process to go from a full silicon wafer to a grid of quantum dot devices. The gates used to define the dots are around 50 nm wide at their smallest and separated from other gates by less than that amount. These design constraints and others make careful fabrication crucial, since errors lead to un-reproducible device performance, shorted gates or unwanted conduction paths. Fortunately, we are able to carry out many of the semiconductor processing steps in-lab and accomplish what remains at the on-campus cleanroom facilities, the California NanoSystems Institute (CNSI) and the UCLA Nanofabrication Laboratory (Nanolab).

3.1.1 Quantum dot operating principle

Figure 3.1 shows the typical schematic of a double quantum dot device fabricated on a Si/SiGe wafer. Two layers of metallic gates, separated by an insulating oxide layer, are used to form quantum dot potential wells and conducting channels from the dots to source and drain charge reservoirs. The top layer is a global accumulation gate (or "top gate") below which a quasi-two-dimensional inversion layer of conduction electrons is formed in the silicon quantum well. The bottom metallic layer, deposited directly on the wafer, is composed of local depletion gates that selectively "turn off" the 2DEG, much like a hand in front of a movie projector selectively blocks light from reaching the screen. When the top gate is biased

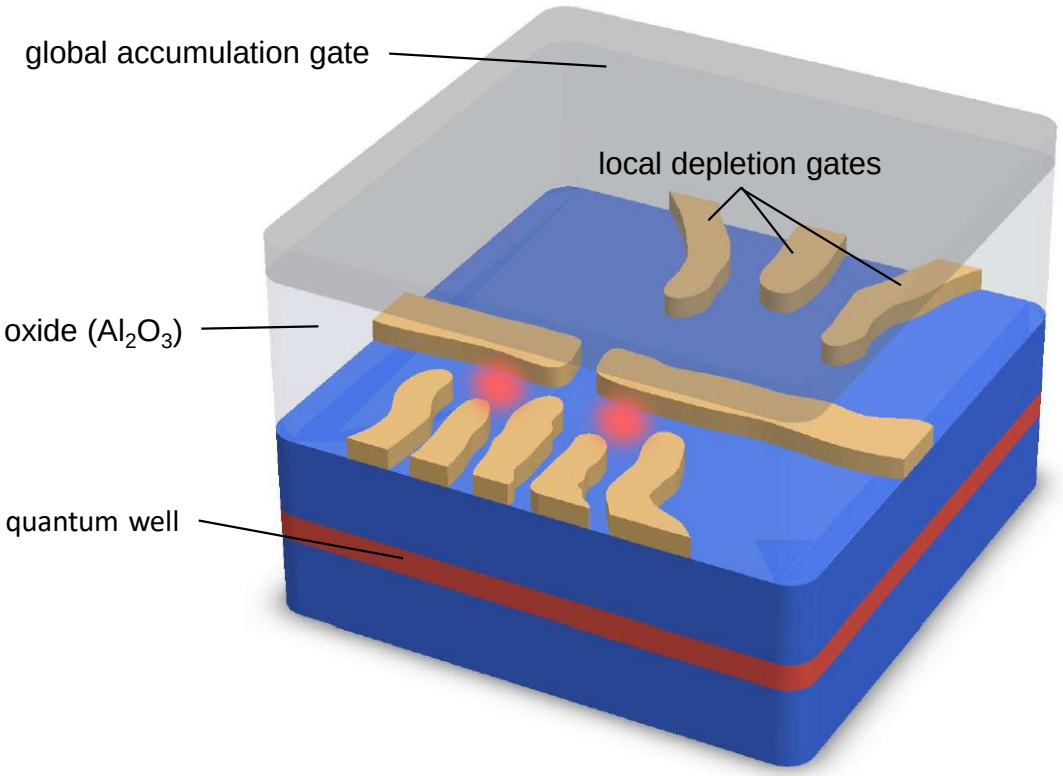

Figure 3.1: A typical schematic of the innermost portion of a double quantum dot device fabricated on Si/SiGe. The lateral positions of the two dots within the quantum well are shown as red areas surrounded by local depletion gates.

above the threshold voltage, the local gates control the dot sizes, positions, and coupling to each other and the nearby reservoirs. Due to the mode of operation, devices like these can be called accumulation-depletion devices.

It is important to point out that this type of quantum dot design is certainly not universal. In our accumulation-depletion designs, the quantum dots form next to or between local gates operating below the threshold voltage. There are other research groups using a pure accumulation-mode structures, where quantum dots form directly under local gates biased *above* the threshold voltage. This allows deeper potential wells and a higher degree of electrical control, at the cost of reduced robustness against insulator breakdown and more difficult fabrication.

3.1.2 Silicon wafer structure

All experiments detailed in Chapters 5 through 8 were carried out on a single device fabricated on a 6" Si/SiGe wafer, grown by Lisa Edge at HRL Laboratories and given to us by Jason Petta's lab at Princeton. Although some details of the wafer are confidential, some relevant cross-sectional details are presented in Figure 3.1. The lowest wafer layer is single-crystal silicon, followed by a $Si_{1-x}Ge_x$ alloy graded buffer. The alloy concentration x is spatially varied from 0 at the bottom to the final concentration of typically 0.3 at the top of the buffer [HLL12][LHR13]. Next is the 10 nm-wide strained silicon quantum well and a $Si_{1-x}Ge_x$ spacer of 30-50 nm, with a constant concentration x. Finally, the wafer is capped with a thin (2 nm) silicon layer.

3.1.3 Wafer characterization

Figures of merit for silicon wafer quality are electron mobility and electron density. The mobility μ is a scalar quantity that relates how fast conduction electrons drift on average in response to an electric field E [Kit05]:

$$v_d = \mu E, \tag{3.1}$$

where v_d is the average drift velocity. Mobility and electron density n are related to electrical conductivity σ by the relation $\sigma = ne\mu$. In general, high mobility is better for transistors (or quantum dot devices) since it implies low susceptibility to scattering sources.

Mobility and electron density can be measured with the Hall effect. To this end, a single aluminum gate in a Hall bar geometry was deposited with thermal evaporation on top of an aluminum oxide layer, grown with atomic layer deposition on the Si/SiGe wafer. The six contact points of the Hall bar were formed with ion-implanted Ohmic contacts that extend partially under the Hall bar top gate. Graduate student Blake Freeman carried

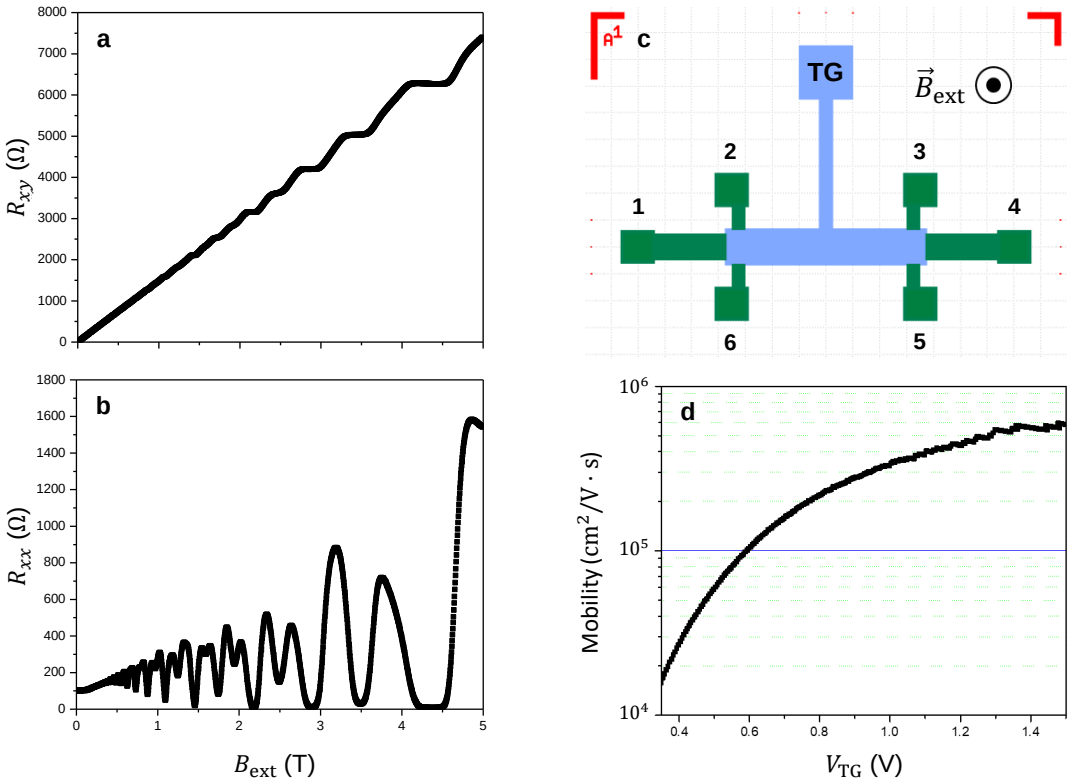

Figure 3.2: Si/SiGe mobility from Hall bar transport. (A) Transverse (Hall) resistance and (B) Longitudinal resistance as a function of applied out-of-plane magnetic field. (C) Hall bar design as seen by the photolithography mask (see Section 3.1.4). Green areas are ion-implanted Ohmic contacts and blue area is the top gate. (D) Mobility obtained from (3.4) showing saturation at 7×10^5 cm^2/V·s

.

out the fabrication and HongWen Jiang performed the Hall measurements at 300 mK. My contribution to this effort was the Hall bar design and corresponding photolithographic mask (Figure 3.2c).

In the presence of an out-of-plane magnetic field, electrons will be deflected according to the right-hand rule and generate a voltage perpendicular to the direction of applied current as charge accumulates along one edge of the conducting material. With the Hall bar geometry, this perpendicular voltage V_H is measured across terminals 2 and 6 or 3 and 5 with current I applied across the long axis to get a Hall resistivity (Figure 3.2a)

$$\rho_{xy} = \frac{V_H}{I}\frac{A}{b}. \tag{3.2}$$

In (3.2), A is the bar area and b is the distance between terminals. Similarly, a longitudinal resistance ρ_{xx} can be measured across adjacent terminals 2 and 3 or 5 and 6 (Figure 3.2b). Then electron density and mobility as a function of applied field B are given by [MHP15]

$$n = \frac{B}{e\rho_{xy}}, \tag{3.3}$$

$$\mu = \frac{1}{B}\frac{\rho_{xy}}{\rho_{xx}}. \tag{3.4}$$

At cryogenic temperatures, it is possible to see the quantum Hall effect wherein the Hall resistivity will be exactly quantized in steps of h/e^2 and longitudinal resistivity will exhibit Shubnikov-de Haas oscillations [KDP80]. Although the quantum Hall effect is itself a remarkable phenomenon, its presence in mobility and density measurements is not desirable and so the applied magnetic field is low enough that oscillations in longitudinal resistivity are not yet visible, below 0.5 T in our sample. Then the peak mobility can be determined by observing the saturation point as top gate voltage is increased (Figure 3.2d). We found

a peak mobility of 7×10^5 cm^2/V·s, which is comparable to the highest known published mobility value in Si/SiGe heterostructures [MDS17].

3.1.4 Fabrication procedure

The next sections will detail the steps for fabricating a quantum dot device on a Si/SiGe wafer. The procedure is the result of more than ten years' worth of refining over the course of four graduate students' PhD work. The foundational work in silicon metal-oxide-semiconductor (MOS) heterostructures was begun by Ming Xiao and is detailed in the dissertations of Matt House and Hong Pan [Hou12][Pan13], while the development of the design used in this work on Si/SiGe can be attributed to Blake Freeman and Joshua Schoenfield [Fre17][Sch17]. In addition to the standard fabrication recipe, I will also briefly discuss our development of a novel application of nano-imprint lithography to reduce charge impurities in silicon MOS in Section 3.2. Detailed procedures for standard fabrication and nano-imprint lithography can be found in Appendix B.

3.1.5 Alignment markers

In an ideal setting all fabrication would be done on a full wafer, with a subsequent cleaving into individual devices. However, some of the in-lab fabrication processes are area-limited (notably the electron-beam lithography) and require the wafer to be cleaved into four or more manageable pieces.

After the wafer is cleaved, a pattern of global alignment markers is photolithographically developed on each wafer piece and aligned to the square crystal lattice. Photolithography entails spinning a few-micron-thick layer of photoresist polymer onto the wafer, then exposing the polymer to a UV light source that is masked by a geometry of our design. After a bath in a developer solution, the only photoresist left on the wafer is the material that was not directly exposed to the UV source. Masks for photolithography were designed in KLayout

and made by UCLA Nanoelectronics Research Facility (NRF). The alignment marker mask is simply a set of brackets that define the corners of each device's working area. After photolithography, a 50 nm layer of chrome is thermally evaporated, only adhering to the wafer where the photoresist was removed. After a wash in acetone to dissolve the remaining photoresist, all that remains on the wafer are chrome brackets matching the bracket design on the photolithography mask (Figure 3.3a). All subsequent lithography steps will be aligned to these markers, or to features that were themselves aligned to the markers.

3.1.6 Ion implantation

The Ohmic contacts that allow direct electrical connection to the silicon quantum well are first defined with photolithography, this time with a double layer of photoresist, and aligned to the chrome markers. Then the wafer is sent out for implantation with 25-30 keV phosphorus ions at a dosage of 2×10^{15} cm^{-2} (Leonard Kroko, Inc.). Ion implantation has the effect of doping the silicon in select areas, increasing the electron concentration and effectively moving the Fermi level up to the conduction band, leading to fully conducting regions of silicon. These conducting regions extend out to the edges of the device area for later wire bonding and form channels that travel inward toward the center so that there are small portions of the ion implanted regions that are below where the global accumulation gate will be deposited (Figure 3.3b). The precise ion energy doesn't seem to have a significant impact on the Ohmic contact conductivity, although there are dangers in deviating too much from the 10-30 keV range. If the energy is too small, then the ions won't penetrate deep enough into the wafer and the conductivity will be reduced. If the energy is too large, then the ions will be able to penetrate the double photoresist layer and cause unwanted doping of the active quantum dot area. Following the ion implantation, the wafer undergoes a rigorous solvent clean to remove all burned-on photoresist.

3.1.7 Rapid thermal annealing

After experiencing high-energy ion bombardment, the silicon crystal lattice is physically damaged. Exposed to a high enough temperature, atoms in the lattice can migrate and repair most dislocations. The required temperatures, up to 1000 °C, can be reached within seconds using a rapid thermal annealer (RTA). In past years an Ulvac-Riko MIL-5000 in our lab was used, however the sample chamber is too small even for a quarter-wafer piece and using it required an additional cleaving step. We have since moved to the full-wafer MPTC RTP-600XP Rapid Thermal Annealing System at CNSI, which allows us to heat the wafer up to 700 °C for 30 seconds and reach room temperature within a minute. Since the implanted phosphorus ions can also migrate away from the Ohmic contact regions during RTA, it's important that the whole process is done as quickly as possible.

3.1.8 Outer depletion gates

The depletion gates start out very small near the center of the device where the quantum dots are formed, but they must end in large (20 mm) pads near the device perimeter so we can connect wires from the chip holder to the finished wafer piece. Masked photolithography is capable of defining the depletion gates on the larger scale, but is practically limited to about 1 mm minimum feature size. As a result, photolithography is performed to make a portion of the depletion gates that starts at the bonding pads and ends before reaching the device center, leaving a 16 mm × 16 mm empty square at the center of the device (Figure 3.3c). Following photolithography, 5 nm of chrome and 45 nm of gold are deposited with thermal evaporation (Cooke Vacuum Products). Gold is used for the gates due to its malleability and relatively good conductivity, but it doesn't adhere well to the bare silicon wafer. The initial chrome layer is needed because it has good surface adhesion to silicon and its oxides, and gold adheres well to the chrome intermediary layer. We also sometimes use electron beam evaporation at Nanolab or CNSI for this step to produce a higher quality metal film.

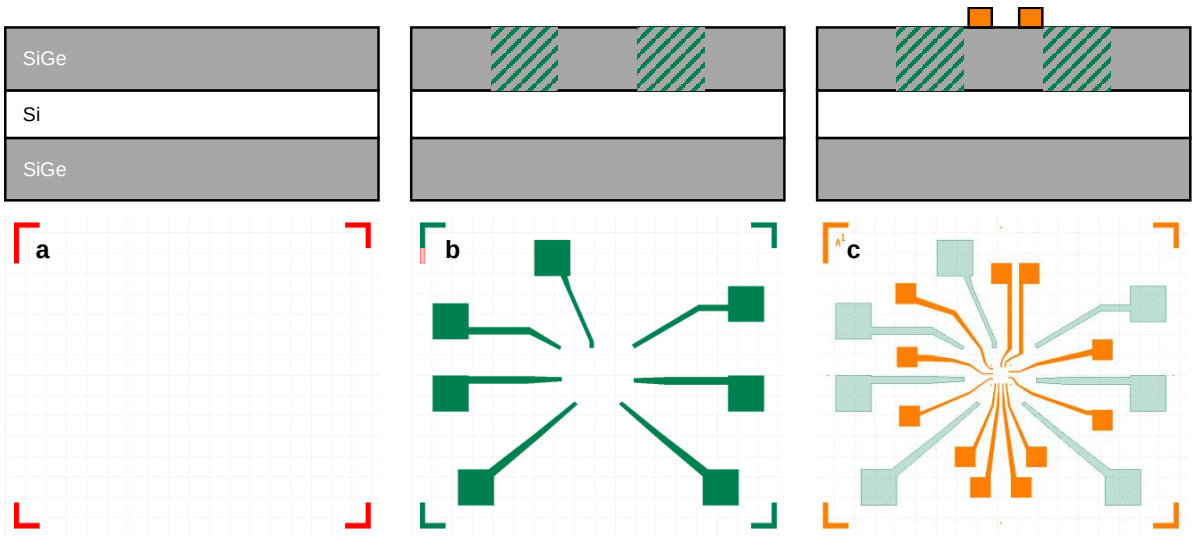

Figure 3.3: First three quantum dot fabrication steps. (A) Chrome alignment markers. (B) Ion-implanted regions. (C) chrome-gold or titanium-gold outer depletion gates. Top panels represent wafer cross-sections (not to scale) and lower panels are the mask patterns used for photolithography. Masks designed by Hong Pan.

In this case we start with 5 nm of titanium followed by 45 nm of gold.

3.1.9 Inner depletion gates

For the smallest features of the depletion gates, the resolution of photolithography is insufficient. Since electrons have a much smaller de Bloglie wavelength than UV photons, it is possible to perform electron-beam lithography to define features on the scale of tens of nanometers. Analogously to photolithography, we first apply a polymer resist that is developed by exposure to an electron beam. We use two resists for this step, first 950PMMA A4 and then 950PMMA A2. The A4 polymer is thicker and develops faster than its copolymer A2, so when the double layer is exposed and developed there will be an overhang of A2, making subsequent lift-off of metal films much easier. E-beam exposure takes place in our Hitachi S3000H scanning electron microscope (SEM), and the gate pattern is traced with a focused 30 keV beam controlled by Nano-Pattern Generation System (NPGS) software. Each device on the wafer piece is aligned in the SEM to markers defined as part of the outer

gate photolithography. Although there are some dedicated 1 mm square markers that can be used, in practice it is easier to simply align to four of the outer gates where they terminate at the edge of the e-beam writing area.

Compared to the photolithographic fabrication steps that take about 10 minutes of alignment time followed by 10 seconds of UV exposure for the entire wafer piece, e-beam lithography (EBL) is delicate and time-consuming. The writing area of our SEM is about 20 mm $\times$ 20 mm, meaning that each set of inner gates must be aligned and written individually. Furthermore, the electron beam moves in a raster pattern, so writing the diagonal lines that make up the gates is inefficient. We are beginning to use the Vistec EBPG 5000+ e-beam writer at CNSI that is capable of automatically writing a full wafer with better resolution than our SEM, and its writing area is large enough that the entire depletion gate pattern can be written without needing the previous photolithography step.

Following e-beam lithography, 5 nm of titanium and 45 nm of gold are deposited with e-beam evaporation (Figure 3.4a). For the inner gates, thermal evaporation isn't possible in our system due to gold spitting, a process where droplets of gold are ejected from the metal source and land on the wafer. Since the droplets are in a liquid phase and not the vapor phase, their viscosity prevents them from smoothly coating the wafer and the result is a very uneven metallic film. We can get away with a rough deposition for the outer gate pattern because the photoresist is much thicker than the gold film, but the size and intricacy of the inner gate pattern requires the higher-quality e-beam evaporation.

3.1.10 Top gate

The large accumulation gate used to turn on the device must be electrically isolated from the local depletion gates. To achieve this, we grow an insulating layer of aluminum oxide by atomic layer deposition (Savannah 100). The oxide thickness is 1000 atomic layers, roughly 100 nm. Then the top gate is defined with photolithography aligned to the initial alignment markers and 100 nm of aluminum is thermally evaporated on the oxide (Figure 3.4b).

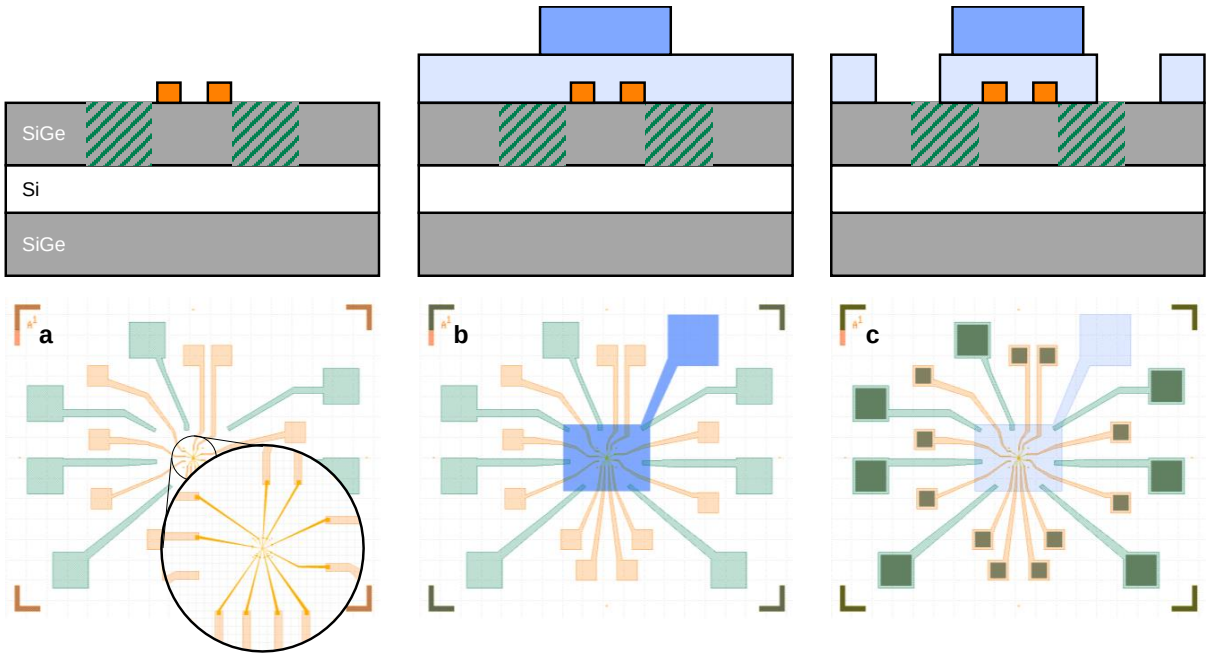

Figure 3.4: Last three quantum dot fabrication steps. (A) Titanium-gold inner depletion gates. (B) Aluminum oxide layer (not shown) and aluminum top gate. (C) Etch windows through the oxide to reach contact pads. Top panels represent wafer cross-sections (not to scale) and lower panels are the mask patterns used for photolithography / e-beam lithography.

3.1.11 Exposing the Ohmic contacts

With the deposition of a 100 nm-thick oxide layer, it is impossible to make good electrical connection to the ion-implanted Ohmic contacts or even the depletion gates from the wafer surface. To remove the oxide from the contact pads for the depletion gates and ion-implanted regions, square windows are first defined with photolithography over every pad. Then the wafer is briefly submerged in Transetch-N, a solvent that attacks aluminum oxide (and aluminum, to a lesser extent), heated to 150 °C. The oxide layer is eaten away in the windows while the photoresist protects the rest of the wafer (Figure 3.4c).

3.1.12 Mounting and electrical contacts

The finished wafer is first cleaved by hand with a diamond scribe to separate all of the fabricated devices. A dab of indium is placed with a low-power soldering iron on each of the Ohmic contact pads, visible by the etched window in the oxide. Each device to be tested is then mounted to a custom printed circuit board (PCB). Devices intended for high-throughput testing are mounted with super glue, while devices that may undergo extended experiments are mounted with silver epoxy. Unlike super glue, which can be easily removed with acetone, silver epoxy is permanent and gives better thermal contact between the device and the PCB. The final step is to bridge the device and PCB contacts, accomplished by wire bonding with a West Bond wedge bonder.

3.2 Nano-imprint lithography

Quantum dots in Si/SiGe heterostructures fabricated with the standard method described above are quite reliable, to the point where any quantum dot device that has passed initial screening can repeatably be tuned to the single-electron regime with no adverse effects from charge traps and defects in the aluminum oxide layer. Devices fabricated on silicon MOS

wafers, on the other hand, are often plagued by defects in the silicon oxide or at the Si/SiO_2 interface. If the charge impurity density were improved to the level of Si/SiGe, then silicon MOS would be the device material of choice with its lower charge noise [FSJ16], robust stability from stronger confinement [YLH20], and enhanced valley splitting. One way to reduce the impurity level is to cut out or replace fabrication steps that create defects. It has been known since the late 1980s that ionizing radiation leads to charge traps [TM92], and the radiation from high-energy electrons scattering in the oxide during e-beam lithography has more recently been shown to cause such traps [NES09][KTL17]. However, since it seems that e-beam lithography is an unavoidable processing step for nanoscale gates, there has been no way of isolating the effects of e-beam lithography on trap density in quantum dots. Nano-imprint lithography (NIL) is a process that uses a rigid mold to press a pattern into a polymer layer on the target wafer, just like an embosser imprints a design onto paper. Although the mold is ultimately fabricated using e-beam lithography, the target wafer never experiences ionizing radiation. Thus, devices made with NIL in place of EBL should in principle be completely free of charge traps arising during fabrication.

In a manner similar to [CGS03], the mold used in NIL can be fabricated from a silicon wafer with 350 nm of thermally grown oxide. After chrome alignment markers are deposited with photolithography and thermal evaporation, the outer gate pattern is photolithographically defined. Now, instead of evaporating metal, the wafer is submerged in a bath of hydrofluoric acid buffered oxide etchant for 4.5 minutes to remove all of the oxide in the gate pattern. After removal of the photoresist, the outer gate pattern is deeply etched into the oxide. Then the inner gate pattern is aligned to the outer gate shapes (which have high contrast since the etched regions go straight to the bare silicon) and written with EBL. Next, 50 nm of aluminum are evaporated on top of the double PMMA layer. After lift-off, the aluminum inner gates remain on the oxide surface. These gates serve as an etch mask for a reactive ion etch (RIE) with CHF_3 that uniformly removes about 120 nm of oxide from the wafer. Unlike a solvent etch, the RIE is highly anisotropic and only etches in the z

direction, into the wafer plane. When the aluminum mask is removed with Transetch-N, the inner gate pattern remains on the wafer as plateaus in the silicon oxide. To complete the mold, a self-assembled fluorocarbon monolayer was deposited on the wafer via a evaporation of an FDTS droplet at room temperature in an dry nitrogen environment. This layer is hydrophobic and prevents the mold from getting glued to the target wafer after imprinting.

The target MOS wafer is a 2" silicon wafer grown with the float zone process with 20 nm of thermal oxide, purchased from University Wafer. It is prepared with a single thick layer ($\approx$ 70 nm) of PMMA A2 as the imprinting polymer following the standard ion implantation. Then the target wafer and the mold are brought together in an Obducat EITRE 6 hot embosser at Nanolab (pressure of 44 bar at 130 °C). The imprinted pattern in the A2 polymer is a mirror image of the mold pattern. Despite the hydrophobic monolayer, the mold is difficult to remove from the target wafer without breaking one or both pieces. The rate of success was significantly increased by fixing double-sided tape on two halves of a small vice, securing the mold and wafer on one half, and then gently clamping down on the wafer pieces and slowly separating them.

With the gate pattern imprinted in the polymer coating, 35 nm of Ti/Au is evaporated followed by careful lift-off in acetone to complete the inner gates. Then the outer gate pattern is aligned to the inner gates with photolithography. The remaining fabrication steps follow the normal procedure, only an additional 30-second buffered oxide etch is required to remove the silicon oxide at the Ohmic contact pads. Then the wafer undergoes a 20-minute forming gas anneal (15% H_2, 85% N_2) at 400 °C as a final step before cleaving and mounting.

3.2.1 Reduction of charge impurities in the absence of electron-beam lithography

With the NIL procedure replacing EBL for forming the inner depletion gates, we fabricated single-quantum dot devices and analyzed their performance in comparison to nominally identical devices fabricated in the standard method. Although we discovered a clear qualitative

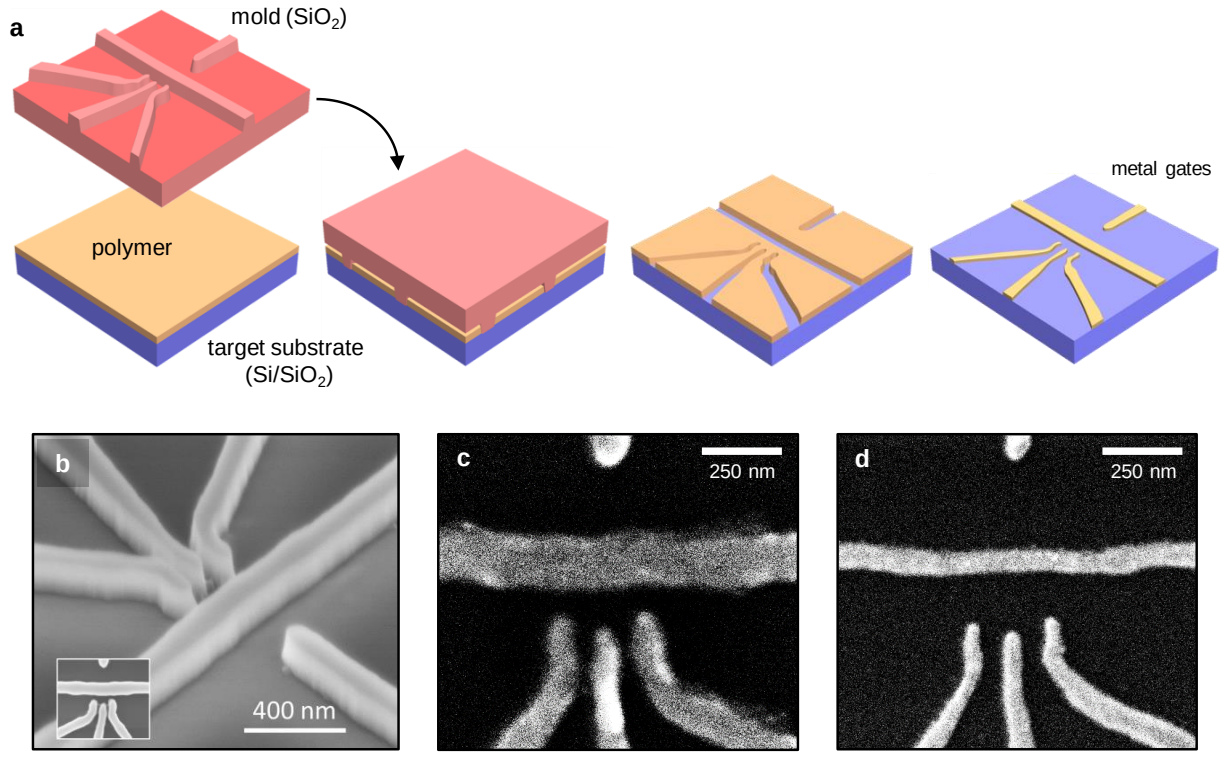

Figure 3.5: Nano-imprint lithography. (A) Schematic of the NIL process. A silicon oxide mold is fabricated with e-beam lithography and the target wafer is prepared with a polymer layer. The mold is pressed against the wafer at elevated temperature, leaving the mold pattern imprinted in the polymer. Then metal is evaporated and the polymer is dissolved to leave the metal gate pattern. (B) SEM image of the single-quantum-dot mold taken at an angle. Inset: top view. (C) SEM image of a device written with NIL. (D) A device written with e-beam lithography for comparison. The NIL device features are slightly distorted along one axis from lateral motion during imprinting.

improvement in the number of charge traps near and at the quantum dot locations, we were unable to completely remove defect effects. Further, the charge noise measured in NIL devices was unchanged from EBL devices. Since shallow traps near the Fermi level are the main contributors to charge noise, this implies that EBL primarily causes defects that create deep, localized charge traps. Further details and a thorough analysis can be found in our published work [PSR19b].

As to the feasibility of NIL as a tool for scalable quantum dot fabrication in silicon MOS, it is difficult to make a general conclusion. The hot embosser used to perform NIL had serious performance issues that almost certainly do not manifest in a high-end imprinting tool; for example, a dent in the base plate would cause the wafer and mold to shatter under the 44 bar pressure used for imprinting. The only way around this issue was to use small wafer pieces with at most 15 devices each and carefully place them to avoid the dent. In addition, the imprinter would regularly lose pressure and ruin the pattern transfer. A final problem was the completely inoperable mold alignment tool, without which precise placement of the mold on top of the target wafer was impossible. In lieu of a proper alignment, we were forced to place the molds on the wafer pieces by hand. These issues with the imprinting led to an atrocious device yield of less than 20%. However, state-of-the-art NIL technologies can certainly allow reliable, large-scale pattern transfer [BSH07]. We also encountered difficulties with the metal lift-off after imprinting. The double PMMA layer used for EBL allows for reliable lift-off, but using the same recipe for NIL is impossible since the two layers aren't well-defined after the mold is imprinted. Lift-off can be potentially improved by using a layer of Microposit Lift-Off Layer 2000 followed by a layer of PMMA A2. Provided the first polymer layer has a much higher viscosity than the upper polymer at imprinting temperatures, it should be possible to create the same PMMA A2 overhang that helps lift-off following EBL. Imprinting obstacles notwithstanding, this work provided a proof-of-principle study of the technique, which may one day be used to greater effect to provide full-wafer, EBL-free quantum dot fabrication.

3.3 Device testing environment

In order to operate a quantum dot qubit, two primary functions of the experimental apparatus must be satisfied. First, microwave (gigahertz frequency) signals must be able to reach the qubit. A spin qubit operated at $B_{\text{ext}} = 1$ T has spin states separated by $E_Z = 116$ μeV, meaning that a sinusoidal current or voltage with frequency $E_Z/h = 28$ GHz is needed to induce efficient Rabi oscillations. Similarly, operating a charge qubit with abrupt (diabatic) voltage pulses requires a pulse ramp time of around 0.1 ns. At microwave frequencies, current transmission through closely spaced wires is complicated by mutual interactions with electromagnetic fields, leading to unwanted signal attenuation and resonances without the proper microwave engineering. Second, the qubit must be operated at a sufficiently low temperature. This is again related to the spacing of relevant energy levels. When thermal fluctuations are comparable to or larger than the qubit energy splitting, the qubit no longer has well-defined states. At $T = 1$ K, thermal energy reaches $k_b T = 86$ μeV and random transitions are possible between qubit states. At $T = 12$ K, thermal energy exceeds 1 meV and overcomes the typical Coulomb repulsion of an electron in our quantum dots, meaning an additional electron can jump into the dot in a stochastic manner.

3.3.1 Microwave-compatible sample holders

After fabrication, devices are mounted onto PCBs that interface the various on-chip contacts with the instruments and circuitry needed to run experiments. They also provide protection against user error, such as the occasional tweezers-induced wafer scratch. For all experiments described here, we use the sample holder designed by Blake Freeman. The holder body is a four-layer PCB consisting of two layers of DC wires and one layer of high-frequency wires separated by a grounding plane (Figure 3.6). All wires are routed from standard connectors — SMA jacks for microwave lines and single in-line pin sockets for DC lines — to contact pads surrounding the sample space with minimal overlap between wires. The sample space

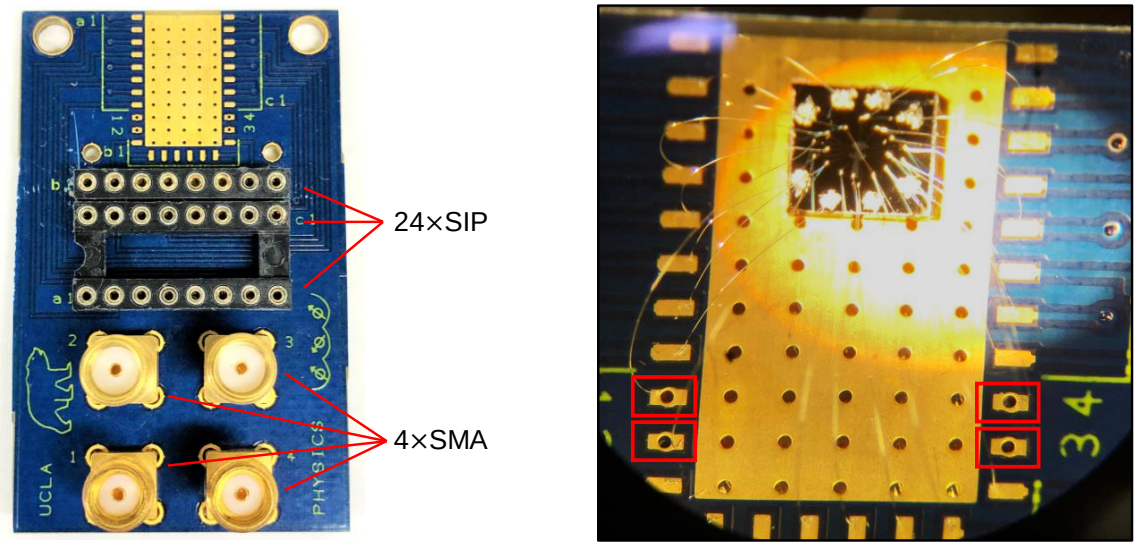

Figure 3.6: Left: the PCB sample holder. Right: a device super-glued to the sample area and connected with bonding wires. Bonding pads for the four high-frequency lines are indicated with red boxes.

itself is a rectangular area of exposed copper near the top of the PCB connected to the ground net. The back of the board will eventually be in thermal contact with the mixing chamber plate in a dilution refrigerator, so a grid of vias connects the sample space to the lower-most copper layer for increased thermal conductivity. In total, there are 24 DC lines and 4 microwave lines available on one sample holder and space in the sample area for two devices. For ease of wire bonding, all exposed copper is plated with gold. Once the devices are in place, a custom 3D-printed plastic shell is attached over the sample area to prevent us from accidentally breaking the wire bonds.

After attempting some high-frequency signals above 10 GHz, we began to suspect that microwave signals were heavily attenuated at some point between the signal generator and the device. This was proven to be the case with a transmission analysis. Although high-frequency lines on the PCB accounted for some attenuation, the wire bonds that link holder to sample were the dominant source. This is not so surprising, considering every bonding wire becomes an unshielded antenna at microwave frequencies. The four bonding pads for high-frequency signals are arranged in two pairs of adjacent contacts near the bottom of the

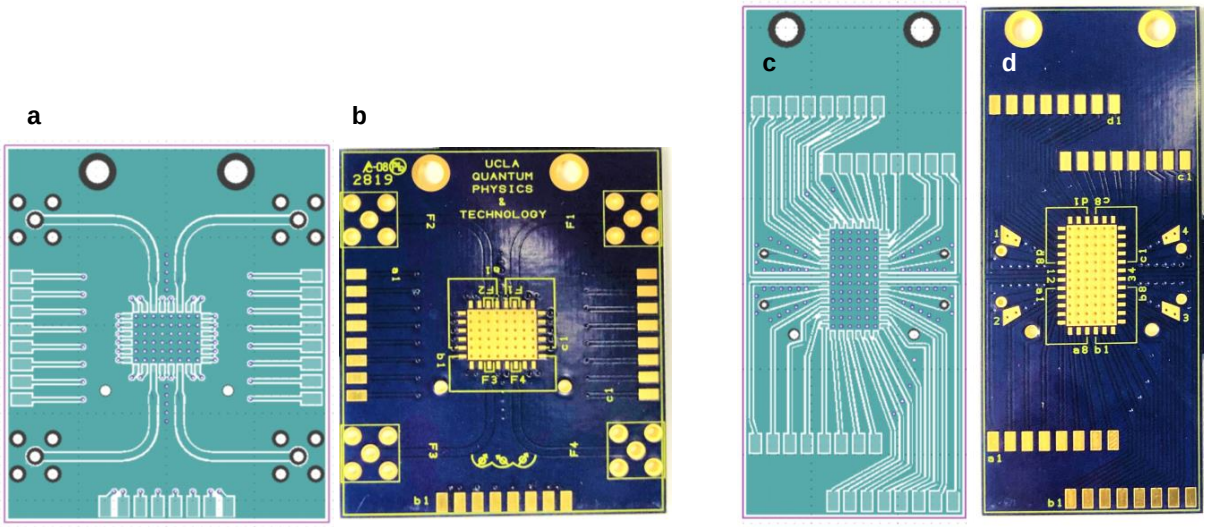

Figure 3.7: New PCB sample holders. (A) Top layer copper routes and (B) printed circuit board compatible with the Triton-200 refrigerator. (C),(D) sample holder compatible with Triton-200 and JDR-500 refrigerators.

sample area, meaning that the bonding wires run close to each other for the length of their trip to the device.

To improve attenuation, a new version of the sample holder was designed with several considerations in mind (Figure 3.7a,b). First, the bonding pads are around the entire perimeter of the sample area and the SMA/SIP connections are placed so that our wedge bonder can make the wire connections at most angles of approach. The high-frequency lines in the PCB are coplanar waveguides designed with an impedance of 50 Ohms and are well-separated from each other until they reach the sample area. Critically, the high-frequency line bonding pads are situated to be closest pads to the sample area center to minimize bonding wire length. The new sample holder was designed for the Triton-200 dry dilution refrigerator, but it is too big for our other dilution refrigerator. Therefore a version of the holder with different dimensions was made at the same time (Figure 3.7c,d). The PCBs were designed in PCBArtist and manufactured by Advanced Circuits.

3.3.2 Device screening at T = 77 K

When a new quantum dot design is made or a new batch of devices have been fabricated, we would like to be confident that all gates are working on each device before we commit to installing them in one of our cryogenic refrigerators. To this end, it is useful to screen samples at some temperature low enough that conduction is only possible by raising the top gate voltage. Low-temperature device testing is performed, one sample holder at a time, in a dewar of liquid nitrogen. At liquid nitrogen temperatures it is possible to measure current transport through the quantum dots with a positive top gate voltage, and the depletion gates can be tested by lowering each gate's voltage until the transport current is pinched off. Weeding out bad devices with 77 K screening ultimately saves time and valuable refrigerator real estate. Even though each device to be screened requires an hour or so of slow lowering into the liquid to prevent thermal shock, the danger of running a refrigerator for months with one or more bad devices stuck inside is incentive enough to carry out the screening process.

3.3.3 Principles of cryogenic refrigeration

To achieve single-Kelvin temperatures, it is necessary to thermally isolate the sample space from the 294 K lab environment. In liquid nitrogen dewars, heat conduction can be reduced considerably with a vacuum jacket that covers an interior volume, with only a small thermally insulating area connecting the inner volume to the dewar exterior. The entire dewar is made with stainless steel for its strength and poor thermal conductivity. This is sufficient for liquid nitrogen which is 77 K at atmospheric pressure, but does not provide enough thermal isolation for the liquid helium used in cryogenic refrigerators. Despite the vacuum jacket limiting direct heat conduction, black-body radiation can still transmit heat between the concentric surfaces that make up the vacuum jacket. However, since the energy of thermal radiation scales as T^4 according to the Stefan-Boltzmann law [Rei65], it is possible to reduce

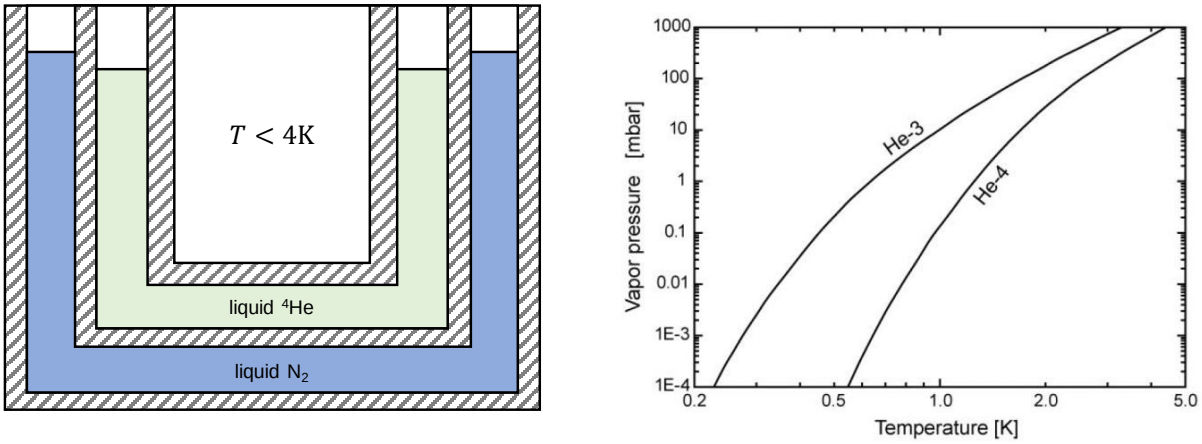

Figure 3.8: General cryogenic concepts. Left: radiation shielding with cryogen baths. Liquid nitrogen at 77 K is used to shield liquid helium at 4 K, which in turn shields the sample space at sub-Kelvin temperature. Each layer is separated by vacuum, indicated by cross-hatching. Right: vapor pressures of ^{3}He and ^{4}He as a function of temperature. Helium-3 can be brought to a lower temperature than helium-4 at the same vapor pressure through vacuum pumping. Figure from BlueFors Cryogenics BF-H400 operator's manual.

radiation heating by cooling the outer vacuum jacket area. With a volume of liquid nitrogen surrounding the vacuum jacket (with a second vacuum jacket surrounding the nitrogen to minimize boil-off), the radiation energy is reduced by a factor of $(294/77)^4 = 213$. This principle of radiation reduction can be carried out in series, so a sample space below 4 K is surrounded by vacuum, followed by a bath of liquid helium, followed by a vacuum jacket, followed by a liquid nitrogen bath, and finally a third vacuum jacket (Figure 3.8, left panel). The end result is a reduction of radiation heating by a factor of 3×10^7. Concentric radiation shields in vacuum are standard practice for cryogenic refrigerators.

Using the natural liquid phase temperature of ^{4}He at ambient pressure, it is possible to cool samples to 4 K. To go below that, one can simply decrease the working pressure of the helium bath with a vacuum pump. Practically speaking, pumping on liquid helium in the presence of a heat load brings down the temperature to $T \approx 1$ K. Operating silicon quantum dots requires milliKelvin temperatures, necessitating more advanced methods of cooling.

3.3.4 Oxford Helium-3 sorption refrigerator

With simple vacuum pumping, it is difficult to bring liquid ^{4}He below 1 Kelvin. However, the isotope ^{3}He in the liquid phase can be brought to a few hundred milliKelvin with the same vacuum pressure (Figure 3.8, right panel). This is the operation principle of the ^{3}He sorption-pumped refrigerator. Within an evacuated sample space that is radiation-shielded by concentric liquid helium-4 and nitrogen baths, gaseous ^{3}He can be introduced. At 4 Kelvin it is still in the gas phase, so a small reservoir of ^{4}He liquid in thermal contact with the sample space (called the "1 K pot") is vacuum pumped to $T = 1.2$ K. As the ^{3}He gas reaches thermal equilibrium with the 1 K pot, it condenses to the liquid phase and covers the sample. Now to reach lower temperatures the vapor pressure of liquid ^{3}He must be reduced by pumping; but rather than using an external vacuum pump, a charcoal sorb is used. When the sorb is cooled by the surrounding ^{4}He bath, incident helium-3 atoms will be adsorbed on the porous surface and the pressure drops. Our ^{3}He refrigerator can reach 300 mK and is equipped with a large superconducting electromagnet that allows single-axis fields of up to 7 T. Samples are loaded from the top and can be switched out without needing to warm up the refrigerator. The main benefits of this refrigerator are the fast sample loading and unloading time (6 hours, or less if liquid ^{4}He loss isn't a concern) and the magnetic field capabilities, but it is difficult to run extended experiments. The ^{3}He liquid is completely adsorbed within twenty-four hours, at which point the sample will heat up to 1 Kelvin. The sorb must then be heated with a resistive element so that it releases the ^{3}He as gas, to be re-condensed by the 1 K pot. In addition, this refrigerator has space and wiring for only a single quantum dot device. As such, the sorption refrigerator is best suited to characterization studies such as the Hall bar mobility measurements on a Si/SiGe wafer. Recently we have operated the refrigerator at 4 K for experiments on magnetic tunnel junctions.

3.3.5 JDR-500 dilution refrigerator

Extended experiments that require low temperatures and a magnetic field can be carried out in the Janis Dilution Refrigerator JDR-500. Dilution refrigerators are the most widely-used cryogenic systems for quantum computing due to their unparalleled base temperature of tens of milliKelvin. They employ a mixture of ^{3}He and ^{4}He that flows in a closed loop from a room-temperature pump through the radiation-shielded inner volume of the dilution unit. As the gaseous mixture enters the refrigerator, it is cooled to 1.2 K by a 1 K pot and condenses. The liquid flows down to the still, where returning mixture cools it below 1 Kelvin. At this temperature, the mixture separates into a concentrated phase of almost pure ^{3}He and a dilute phase of 6.6% ^{3}He. The separated phases enter the mixing chamber with the dilute phase resting on the concentrated phase like oil on water. In the mixing chamber, concentrated ^{3}He will cross through the phase boundary to the dilute phase in an endothermic process that drives the cooling power of the refrigerator. Then the dilute mixture leaves the mixing chamber and enters the still where it exchanges thermal energy with the incoming mixture, and back out to the pump to be recycled. This process can be used to achieve temperatures in the 10-20 mK range, however we usually run the JDR-500 without its still shield to give us extra sample space at the cost of a higher base temperature of 60-75 mK. As with the Oxford sorption-pumped refrigerator, the JDR-500 dilution unit is surrounded by baths of liquid helium and nitrogen that require weekly maintenance. It is the best choice for studying electron spins in quantum dots with a base temperature five times lower than what can be achieved in the Oxford refrigerator and a magnet capable of reaching 4 T. A major drawback is the sample loading process: the entire helium bath must be completely evaporated before samples can be taken out and replaced, which can take a few days to a few weeks. To load a new sample, a full 100-liter dewar of liquid helium is required to fill the helium bath and cool-down is a two-day procedure. Furthermore, the sample space is kept at ultra-high vacuum and a fresh indium seal is applied each time a sample is loaded. Although the seal is leak-checked at room temperature, a leak can appear

at cryogenic temperatures and make operation below 1 Kelvin impossible to attain. I learned of this particular issue from personal experience. Still, once a sample or two are successfully cooled to based temperature, the refrigerator can run for over a year with only minor routine maintenance required.

3.3.6 Triton-200 dry dilution refrigerator

This refrigerator can reasonably be considered the workhorse of the lab. Although it relies on the same endothermic phase transition in a mixture of ^{3}He and ^{4}He as JDR-500, the intermediate temperature stages are all cooled via pulse tube refrigeration by ultra-pure helium in a closed loop. This eliminates the need for a large helium bath or even a nitrogen radiation shield. The end result is a refrigerator that requires almost no maintenance while running and a fully automated cool-down procedure from room temperature over 24 hours. The sample space in thermal contact with the mixing chamber is the size of a dinner plate and there are 76 DC lines plus 14 high-frequency lines running to the sample space from outside the refrigerator. In total, it is possible to cool down and test 7 double-dot devices simultaneously at a base temperature of 36 mK. The Triton-200 gets the most daily use of all the refrigerators and is well-suited for a more careful screening of devices that pass the first round of 77 K screening. It is the only refrigerator that doesn't have a magnet installed, so spin physics must be studied in one of the other two refrigerators.

3.3.7 Electron temperature

When we measure the operating temperature of a device, we record the current through a silicon diode or a resistor with well-known thermal characteristics. This measurement gives the local temperature in the vicinity of the sample, and usually reflects the actual temperature of the silicon wafer. However, electrons in the inversion layer may have a much higher temperature than the silicon lattice. Electrical currents used to control the

device are generated from instruments at room temperature, and heat can travel via kinetic energy transfer between conduction electrons directly to electrons in the source and drain reservoirs. Even with no applied voltages, nonzero current is possible due to mismatched ground voltages between instruments or the refrigerator. Ground mismatch may only result in a picoamp-level current, but that is enough to severely limit device electron temperature to a few hundred milliKelvin.

There are several approaches to alleviating electron heating. Quantum dot researchers often run their signal lines through filter circuits in thermal contact with sequential temperature stages in the refrigerator. In a similar fashion, any DC-plus-microwave signals that are meant to be combined can be run through cryogenic bias tees at the mixing chamber, and signals intended to be reduced can be passed through cryogenic attenuators. In general, it is better to have passive circuitry moved into the refrigerator than to keep it at room temperature. If and when a full silicon quantum computer is demonstrated, I am confident that most of the signal generation and processing will happen at 4 Kelvin or lower. Perhaps more important than cryogenic circuitry, it is vital that instrument chassis all share a common ground and that the ground shields of every signal wire share another isolated ground point. We have seen the electron temperature improve by a factor of 3 with nothing more than thorough grounding.

3.4 Manipulation and measurement techniques

Next I will outline the standard equipment and techniques used to manipulate and read out the state of electrons in quantum dot devices. As mentioned in Chapter 1, the control knobs available to us are various gate voltages and the response is measured with a source-drain current. Within these simple constraints, many diverse electrical manipulations are possible. The techniques described here will be used to characterize devices (Chapter 4) and perform experiments on one or two isolated electrons (Chapters 5 – 7).

3.4.1 Source-drain current measurement

By applying a voltage to one Ohmic contact and measuring the transmitted current from another, the effective transconductance between contacts is measured. When the source-drain current passes through one or more dots, the conductance will depend of the number of electrons confined in each potential well, the dot energies, and the electron tunneling rates. The source-drain current can be measured by a Stanford Research Systems 570 current preamplifier or a DLPCA-200 low-noise current amplifier depending on the application. The DLPCA-200 has a higher bandwidth of 7 kHz compared to 200 Hz at a gain of 10 nA/V, making it better suited to real-time measurements. Since a current measurement gives a scalar quantity, it's impossible to know what the contributions of each device component to the conductance are with a single measurement. Instead, the effects of each dot or tunneling barrier can be surmised by seeing how the current changes while one or more gate voltages are modified.

Typical source-drain currents fall in the range of picoamps to nanoamps. In the presence of electrical noise, an electron signal that represents a fraction of the current may easily be lost. A simple background subtraction scheme often doesn't work because the background fluctuates on the same time scale as the measurement. The solution is a lock-in amplifier, a ubiquitous presence in all research labs performing high-sensitivity electronic measurements. The lock-in amplifier accomplishes what can be though of as a background subtraction on a timescale many times faster than the measurement time. Consider the simple example of a signal chopper. For some time δ the noisy signal is measured unimpeded, and then for another time interval δ the signal is cut off and the noise background is measured. In the case of a quantum dot measurement, the noisy signal could be thermally excited electron tunneling between locations when a gate voltage is V, and the background without the signal occurs at $V - \Delta V$. Then the DC output signal is given by

$$\tilde{I} = \frac{1}{2\delta}\left[\int_t^{t+\delta} I(V)dt' - \int_{t+\delta}^{t+2\delta} I(V-\Delta V)dt'\right] = \frac{1}{2}\left[I(V) - I(V-\Delta V)\right], \tag{3.5}$$

provided the noise doesn't fluctuate on the scale of δ. Making the further assumption that the current change in response to ΔV is very small, it can be said that the chopped signal is the numerical derivative of the noisy signal when divided by the gate voltage change ΔV:

$$\frac{\tilde{I}}{\Delta V} \approx \frac{1}{2}\frac{dI}{dV}. \tag{3.6}$$

A lock-in amplifier achieves a similar outcome by modulating gate voltages with a sinusoidal perturbation $\Delta V \sin \omega t$ and measuring only the Fourier component of the modulated signal that is equal to ω. When integrated over a time τ much longer than the modulation frequency, all frequency components of the signal except for ω average out:

$$I_{\text{out}}(t) = \frac{1}{\tau}\int_{t-\tau}^{t} \left[I(V + \Delta V \sin \omega t')\right] \sin \omega t' dt'. \tag{3.7}$$

Again, as long as the modulation amplitude is small enough, a lock-in measurement of the source-drain current over ΔV can be considered the *differential transconductance* of the current channel. We use Stanford Research Systems SR830 lock-in amplifiers with a typical modulation frequency on the order of 100 Hz and integration time 0.3 seconds. They have built-in current amplifiers with up to 10 nA/V gain and bandwidths of around 100 Hz. If a higher bandwidth is needed, the modulated current can be converted to a voltage with a current amplifier and sent to the lock-in's voltage input. Sometimes we want to modulate the signal with a separate source; this is possible by sending a square pulse trigger from the modulation source to the lock-in amplifier, as long as the frequency is less than 1 kHz.

3.4.2 Current in the time domain

Lock-in amplifiers are the best choice for signals averaged over 0.1 second or more, limiting their ability to capture faster signals in real time. Electron tunneling typically occurs at a rate on the order of 1-10 kHz for single-shot spin read-out and requires an oscilloscope to capture. For this, current is fed through the DLPCA-200 current amplifier and the voltage output is read out on the Agilent Infiniium 54855A oscilloscope, capable of 20×10^9 samples per second. This technique in particular requires a very good signal-to-noise ratio since there is no noise filtration.

3.4.3 Current in the frequency domain

A dominant source of decoherence in silicon quantum dot qubits is charge noise, manifesting as fluctuations in the quantum dot potential. The low-frequency noise spectrum can be studied to identify the nature of charge noise in these systems. The noisy signal is sent through a current amplifier to a spectrum analyzer, the SR 785 for frequencies below 100 Hz or the HP 8563E for frequencies up to 20 GHz. Since the amplifiers are bandwidth-limited to no more than 7 kHz at the required gain, the HP 8563E is not used for this particular application. An important consideration for spectrum measurements is the 60 Hz line noise of standard U. S. power lines. Despite electrical isolation of instrument power supplies from their voltage outputs, the line noise and its harmonics can bleed into the signal, upstream or downstream from the device. Ensuring that all output shields are isolated from instrumentation and are grounded to a common point can significantly reduce this effect.

3.4.4 DC gate biases

Every quantum dot gate needs its own low-noise DC voltage, requiring 8 to 16 simultaneously controlled voltage sources per device. These biases can be supplied from the floated auxiliary voltage outputs of our lock-in amplifiers, however there are only four outputs on each SR-

830. Lock-in auxiliary outputs can be supplemented with the BS-16 precision voltage source from Stahl Electronics. The BS-16 has 16 digital voltage outputs with a 16-bit resolution. Currently we have two BS-16s with grounded outputs, good for shielding high-frequency environmental noise, and an additional instrument with floated outputs to alleviate ground mismatch for low-frequency measurements. Source-drain biases are also supplied with these instruments, although an isolated battery supply is sometimes used to reduce noise.

DC biases are fed into the refrigerator through vacuum-sealed breakout boxes with BNC-type connectors. The wires that run down to the device are stainless steel mini coaxial cables from Cooner Wire to minimize heat load on the sample stage via thermal conductivity. Additionally, the wires are in good thermal contact with each temperature stage in the refrigerator to reduce heat exchange.

3.4.5 Arbitrary voltage waveforms

Many experiments make use of multi-stage pulses sequence consisting of several voltage levels. The Tektronics Arbitrary Waveform Generator (AWG) 520 and AWG 610 accept a string of voltages with some temporal spacing to create (aptly) an arbitrary periodic output. The maximum frequency that can be generated with an AWG is half its sampling rate — that is, alternating points of low and high voltage to create a triangular wave. The AWG 520 is equipped with two output channels that can send independently programmed waveforms with a sampling rate of 1 GHz. The AWG 610 has a faster sampling rate of 2.6 GHz with the trade-off being a single output channel. Both AWGs can operate in function generation mode, outputting standard functions with controllable frequency and amplitude like square, sinusoidal and sawtooth waves.

A powerful aspect of the AWG is the ability to construct a custom trigger that can be synchronized to any point of the waveform. The trigger or triggers can be sent to a lock-in amplifier for modulated signal measurement, or to a different function generator to chop the output. Both uses for the trigger are implemented in chapter 7.

3.4.6 Fast gate pulses and microwave signals

Qubit energy level spacing seen in our lab is usually 10–100 μeV. Addressing transitions between levels requires signals with frequency $\Delta E/h$ = 2.4–24 Ghz. Accordingly we use Anritsu 68369B signal generator or the Agilent N5183A microwave analog signal generator to output microwave voltages. The Anritsu generator is capable of 10 MHz to 40 GHz frequencies with 1 kHz resolution, while the Agilent generator can go from 100 KHz to 20 GHz with single Hz resolution. Normal use for qubit applications entails amplitude modulation with a pulsed trigger from an AWG, or faster chopping with a fast gate pulse via a Marki microwave mixer.

Qubit levels can also be addressed with sub-nanosecond square pulses on local gates. The Agilent 81134A pulse pattern generator can output pulses on two channels with independently set pulse heights, widths, and delays. Critically, pulses have a nominal rise time of 60 ps so diabatic level transitions are possible. Its minimum repetition rate is 3.35 GHz which is too fast for most electron relaxation processes, but the effective pulse rate can be lowered substantially. In data mode, each channel can accept a 12 megabit binary string, telling the pulse generator to turn on the pulse in period j when bit j is 1 and keep the pulse off when bit j is 0. Not only does data mode allow for slower pulse rates, but it also allows a kind of modulation where the pulse is on for x periods and off for the same number of periods. Then the bit string in voltage form can be fed to a lock-in amplifier as a trigger. Combinations of fast pulses from the 81134A are used extensively in Chapters 5 and 6.

Signals from these instruments experience too much attenuation from normal BNC cables, only rated for up to 1 GHz. We instead use semi-rigid SMA coaxial cables rated up to 20 GHz and connect them to hermetically sealed feedthroughs on the refrigerator. Inside the refrigerator, fast signals travel to the device by way of rigid stainless steel SMA coaxial cable, with heat sinking at every temperature stage. Fast signals are combined with the standard DC gate voltage using a bias tee at room temperature or, better, a cryogenic bias tee at the

refrigerator base temperature.

CHAPTER 4

Quantum dot characterization

Before any qubit experiments can be carried out, the quantum dot qubit device must be well-characterized. Characterization entails measuring the effects of each depletion gate, accurately counting the number of electrons in the quantum dot system, controlling various tunnel couplings, and tuning parameters to maximize measurement sensitivity. At this stage in quantum dot research, many characterization tools have become standardized and can be found with detailed discussion in review papers such as [KMM97], [vDE02], [HKP07] and [ZDM13]. These references have been ordered from more general to more specific.

4.1 Single quantum dot transport

The simplest possible measurement on a quantum dot is to pass a current from one Ohmic contact (designated as the source) to the other (drain). When a quantum dot is electrostatically formed, classical current transport is forbidden and electrons tunnel from source to drain via the dot. The quantized energy levels of the quantum dot are revealed in transport measurements by Coulomb blockade, discussed below.

4.1.1 The constant interaction model

To understand quantum dot transport from a theoretical perspective, and to provide insight into some common terminology used, the system can be modeled as a network of conductive nodes connected by capacitors (Figure 4.1a). The dot is assumed to be well-defined, meaning

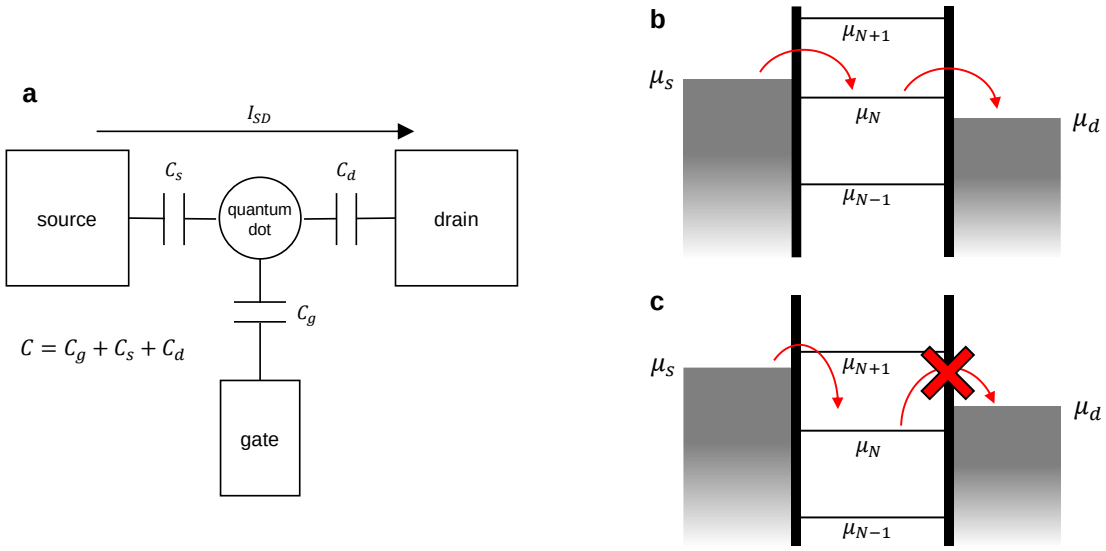

Figure 4.1: (A) Quantum dot equivalent circuit diagram. The dot is coupled to source and drain electron reservoirs by capacitances C_s and C_d, respectively. The plunger gate controlling the quantum dot energy is coupled to the dot by C_g. (B,C) Principle of current transport through a quantum dot. Current is allowed to flow from source to drain when there is at least one available quantum dot level between the source and drain electrochemical potentials. If there isn't a level in the bias window, current is blocked.

that the barrier equivalent resistances are large and tunneling into or out of the dot is restricted to first-order processes. The constant interaction model further assumes that interactions between dot electrons and source/drain electrons are encapsulated in a single constant capacitance C, and that the dot energy levels aren't affected by C [KMM97]. Then the electrochemical potential of a dot with N bound electrons is given by [HKP07]

$$\mu(N) = \left(N - \frac{1}{2}\right)\frac{e^2}{C} - \frac{|e|}{C}\left(\sum_j C_j V_j\right) + E_N, \tag{4.1}$$

where electrostatic potential term $C_j V_j$ represents the coupling of the dot to the source, drain, or any relevant gates biased at voltage V_j and E_N is the N^{th} single-particle energy level in the dot. According to (4.1), the dot electrochemical potential is controlled linearly with source, drain, and gate voltages. If an additional electron is added to the dot in the same energy level — in accordance with Hund's rules — then the change in electrochemical potential is just $\mu(N+1) - \mu(N) = e^2/C$. This can be thought of as the energy stored in capacitor C due to the charge of a single electron, and therefore $E_c \equiv e^2/C$ is called the *charging energy*.

The current through a quantum dot can be modeled in terms of tunneling rates through the left and right barriers Γ^l, Γ^r [Bee91]:

$$I_l = I_r = -|e|\sum_{j=1}^{\infty}\sum_{\{n\}}\Gamma_j^r(\mu)p(\{n\}). \tag{4.2}$$

In (4.2), j indexes dot states and the second sum is over all possible sets of energy level occupations $\{n\}$. The steady-state solution for the current requires that occupation probabilities are constant ($dp(\{n\})/dt = 0$) so the problem boils down to solving a system of coupled rate

equations [BDR02]:

$$\frac{d\mathbf{p}}{dt} = \mathbf{\Gamma} \cdot \mathbf{p} = 0, \tag{4.3}$$

$$\Gamma_{\alpha\beta} = \begin{cases} \Gamma_{\beta\to\alpha}, & \alpha \neq \beta \\ -\sum_{k\neq\alpha} \Gamma_{\alpha\to k}, & \text{otherwise.} \end{cases} \tag{4.4}$$

The tunneling rates from state α to state β have an implicit dependence on the electron temperature T and chemical potentials of both states:

$$\Gamma_{\alpha\to\beta}(\mu_\alpha, \mu_\beta, T) = \frac{\gamma_{\alpha\to\beta}}{1 + \exp\left[(\mu_\alpha - \mu_\beta)/k_b T\right]}, \tag{4.5}$$

where the denominator originates from the Fermi-Dirac distribution and $\gamma_{\alpha\to\beta}$ is determined by the tunneling barrier height in relation to the energies of states α and β. The null space of (4.3) can be fed back into (4.2) to produce a current.

4.1.2 Coulomb blockade

In the absence of quantum dot level quantization, transport as a function of gate voltage would appear very similar to the I-V characteristics of a field-effect transistor: As the depletion gate voltage is made more negative, current decreases monotonically and continuously until it is completely pinched off. The bound state energy levels have the effect of completely blocking electron tunneling into the dot unless there is an available level within the bias window $-|e|V_{\text{sd}} = \mu_{\text{source}} - \mu_{\text{drain}}$ (Figure 4.1b,c). As the gate voltage controlling the dot energy is varied, dot levels will pass in and out of the bias window to create sharp, periodic peaks in current where Coulomb blockade is lifted. If there are multiple dot levels below the source and drain Fermi levels, then electrons can tunnel from the reservoirs to fill them. Ultimately, in the steady state, each Coulomb peak represents the addition or subtraction of an electron from the dot. Coulomb blockade can therefore be used to count the total number

of dot electrons, starting with zero when the Coulomb peaks disappear at very negative gate voltages. Using the model in Section 4.1.1 in the limit of vanishing source-drain bias, we can replicate Coulomb blockade as a function of charging energy, temperature and dot Fermi level controlled by gate voltage V_g (Figure 4.2a).

4.1.3 Coulomb diamonds

When source-drain bias is increased, it becomes more likely that a quantum dot energy level will fall within the bias window and the Coulomb-blockaded region shrinks. When the bias window is further increased to surpass the charging energy, there will always be an available level between source and drain electrochemical potentials and Coulomb blockade is lifted. Since gate voltages control the dot potential with a linear dependence, the Coulomb-blockaded region is bounded by lines where the gate voltage or voltages match the source or drain potentials. Coulomb blockade will therefore form diamonds in $V_g - V_{\text{sd}}$ space (Figure 4.2b,c).

It is possible to extract all of the equivalent capacitive couplings of the circuit once Coulomb diamonds are observed. First, with the recognition that the tops and bottoms of the diamonds along the V_{sd} axis correspond to points where Coulomb blockade is lifted, we can extract the charging energy E_c as the diamond height. Then, knowing that the zero-bias separation between Coulomb blockade peaks is also equal to E_c, we obtain a conversion between gate voltage and dot energy: $\Delta V_g = \alpha_g E_c$, where ΔV_g is the separation of adjacent Coulomb peaks in gate voltage space. The coefficient α_g, with units eV/V, is known as the "lever arm" for gate g. This quantity is one of the key characteristic parameters for a quantum dot device since it allows us to know the dot energy, given some set of gate voltages. In terms of equivalent capacitances, the lever arm can be expressed as [HKP07]

$$\alpha_g = \frac{|e|C_g}{C}. \tag{4.6}$$

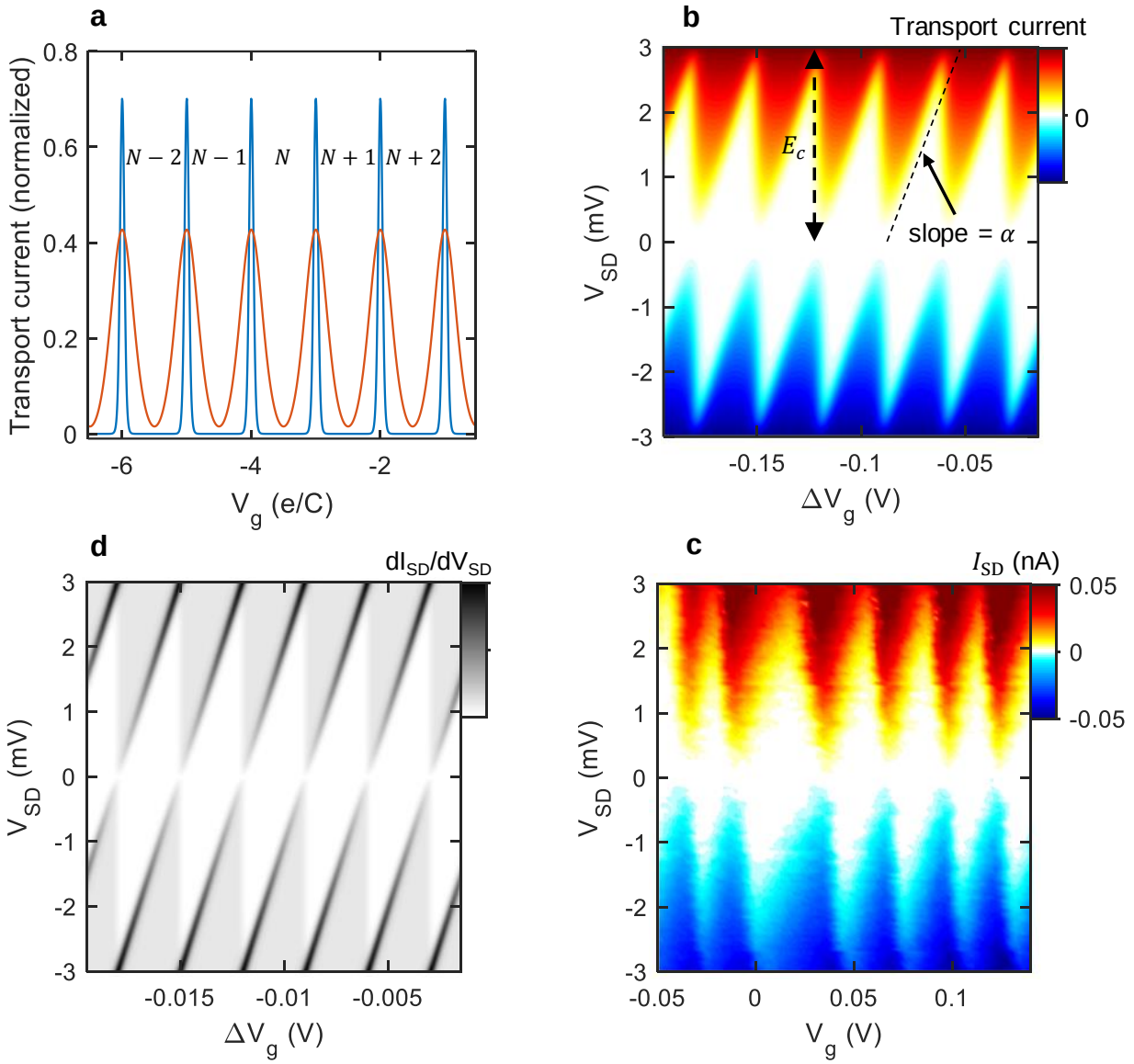

Figure 4.2: Coulomb blockade. (A) Simulated transport as a function of gate voltage at $T = 0.1$ K (blue) and $T = 0.7$ K (orange). (B) Simulated Coulomb blockade as the bias window V_{SD} is modified. Coulomb blockade is completely lifted when V_{SD} reaches the charging energy (3 meV). Gate lever arm α is obtained from the edge of a Coulomb diamond. (C) Experimental data taken on a Si/SiO_2 quantum dot. (D) Simulated differential transconductance using the parameters in (B).

4.1.4 Differential transconductance

To improve the signal-to-noise ratio, a small sinusoidal voltage can be added to the source-drain bias. The modulated transport current can then be read by a lock-in amplifier and divided by the modulation amplitude to obtain the differential transconductance through the quantum dot. This is a useful technique for bringing out the edges of the Coulomb peaks, especially in the low-bias regime (Figure 4.2d). Additionally, the differential transconductance can reveal the locations of excited states if relaxation and tunneling processes from the excited states are slow enough.

4.2 Charge sensing measurements

There are a few practical limitations to transport measurements. First, passing a current through the dot system strongly couples the dots to the measurement apparatus, reducing coherence times. Second, the gate or gates used to control the dot energies also have an effect on the tunneling barrier heights via stray capacitance. This means that as the dot energy is increased to remove electrons, the tunneling rates out of the dot are decreased. With the dot gate separated from the tunnel barrier gates by only tens of nanometers the stray capacitance can be considerable, making it impossible to tune to the single-electron regime and still have a healthy transport current. A less invasive method of probing quantum dots involves measuring transport through a nearby gate-defined conducting channel. As long as there is a high sensitivity of the tunneling current on local electric fields, such as the field from a single electron, then transport changes in a quantized manner every time an electron is added to or removed from the dot. In addition, charge sensing measurements do not require a source-drain current through the dot system to work.

4.2.1 Quantum point contact

A quantum point contact (QPC) can be formed with two depletion gates. The gap between gates forms a tunnel barrier through which a current can pass. When the QPC is narrow enough so that the opening width W is comparable to the wavelength of electrons at the Fermi level λ_F, then transverse wave-vectors are quantized: $k_y = n\pi/W, n = \pm 1, \pm 2, \cdots$ (here the current is taken to be in the x direction). Then the QPC conductance is given by [vvB88]

$$G = \sum_{n=1}^{\lfloor k_F W/\pi \rfloor} \frac{e^2}{\pi\hbar}. \tag{4.7}$$

At zero temperature, G is quantized in steps of $e^2/\pi\hbar$ and with nonzero temperature there is a finite-sloped transition between each step. The sloping transitions are the key to charge sensing with a QPC: when the QPC gate voltage — and therefore the QPC opening width — is adjusted to be between quantized conductance steps, then a small change in local electric field will cause a maximum change in transport current [FSP93]. The difference of one electron in the quantum dot can change QPC current by 1–100 pA depending on the proximity of the dot. More importantly, charge sensing is still effective at very low tunneling rates on the order of 10 Hz where dot transport is impossible.

4.2.2 Single-electron transistor

In recent years the common practice has been to use a single-electron transistor (SET) for sensing quantum dot charges. An SET is a tunnel junction that displays Coulomb blockade, so for all intents and purposes it is just another quantum dot. As shown in Section 4.1.2, transport through a quantum dot can produce incredibly sharp periodic peaks in conduction. Just as a QPC charge sensor is most sensitive where the conductance has the highest dependence on gate voltage, an SET charge sensor has the best sensitivity when the gate is set to the edge of a Coulomb peak. Unlike a QPC, the peaks aren't limited to an integer of $e^2/\pi\hbar$ and so an SET can yield a much higher sensitivity. The trade-off is a

smaller range of sensitivity, so an SET will quickly become maximally insensitive when local gates are changed too much. However, this problem is easily overcome either by introducing a feedback loop circuit to keep the SET at the sensitive configuration or by sweeping the charge sensor gates along with the dot gates to correct for stray capacitances. Using an SET charge sensor, we have been able to induce a change of 1 nA in SET transport with the addition of a single electron into a nearby quantum dot (Figure 4.3a).

4.2.3 Differential charge sensing

As with quantum dot transport measurements, a charge sensor's signal-to-noise ratio can be improved by use of modulation. Instead of modulating the sensor source-drain bias, a periodic perturbing voltage is added to one of the quantum dot gates. The resulting differential charge sensing current is essentially a derivative of the original transport current with respect to the gate voltage. Differential charge sensing on a single quantum dot as a function of gate voltage will then closely resemble normal Coulomb blockade despite the absence of current through the dot (Figure 4.3b,c).

4.2.4 Measuring electron temperature

With the quantities obtained in the previous sections, it is possible to get a measurement of the effective electron temperature with current transport. In the constant interaction model and at vanishing source-drain bias, the profile of a Coulomb peak at low temperatures is given by [KMM97]

$$I_{\mathrm{sd}}(E_{\mathrm{dot}}, T) \propto \frac{V_{\mathrm{sd}}}{T} \cosh^{-2}\left(\frac{E_{\mathrm{dot}} - E_0}{2k_bT}\right). \tag{4.8}$$

In (4.8), E_0 is the dot energy at which the Coulomb peak occurs. The width of the peak Δ at half the amplitude satisfies $\cosh^2(0.5\Delta/2k_bT) = 2$, or $\Delta = 3.5255\ k_bT$. Knowing that the linewidth in gate voltage space is just Δ/α, the electron temperature can be quoted directly from Coulomb blockade as a function of gate voltage. However, current transport isn't

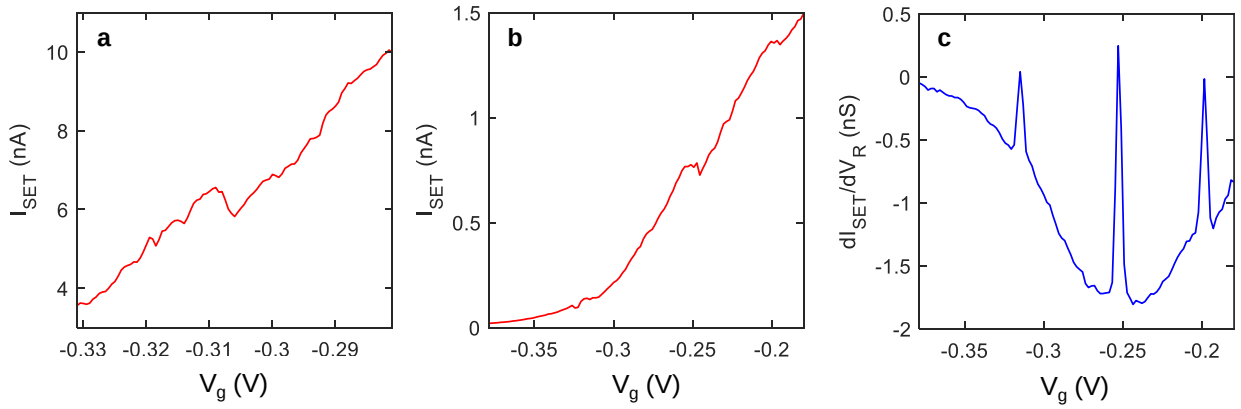

Figure 4.3: Charge sensing with an SET. (A) The discontinuity in SET transport current at $V_g = -0.308$V represents the addition of one electron to the quantum dot. This trace is taken at a maximally sensitive region where one electron causes a 1 nA change in charge sensing current. (B) SET transport over a wider range and (C) corresponding differential measurement recorded on a lock-in amplifier. Sensitivity quickly vanishes as V_g modifies the SET configuration.

the best method to measure electron temperature. Seeing a Coulomb peak experimentally involves getting sufficient current flow to increase the signal, but a source-drain bias increases the linewidth of Coulomb peaks and the profile is no longer described by (4.8). Additionally, a source-drain bias introduces Joule heating and charge noise that broaden the peak. It is much better to use differential charge sensing, either by taking a numerical derivative of transport current or by a lock-in measurement with sufficiently small modulation amplitude. Such a measurement will have the same form but without the back-action on the quantum dot.

4.3 Double quantum dot

The foundation for qubit entanglement and quantum simulation is a system containing multiple quantum dots with mutual interactions. The bulk of research we do is in double quantum dot systems, where the quantum dots share a tunneling barrier gate (Figure 4.4). The shared

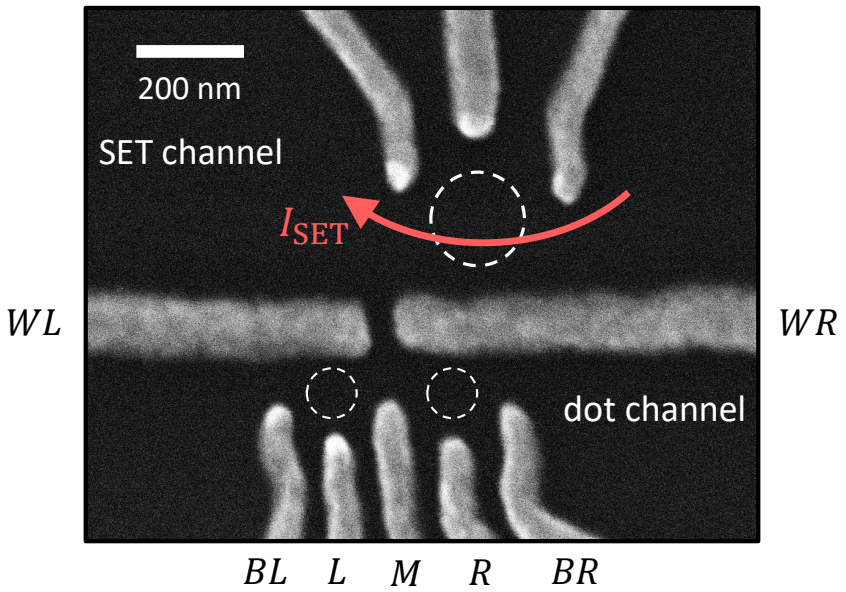

Figure 4.4: An SEM micrograph of the double quantum dot structure used in almost all experiments discussed here. The top three depletion gates form an SET charge sensor in the upper channel. Gates WL and WR are wall gates, usually grounded. Gate L (R) controls the energy of the left (right) dot, gate BL (BR) controls the tunnel rate from the left (right) dot to the adjacent charge reservoir, and gate M controls the inter-dot tunnel coupling. Global top gate is not shown.

gate M controls the tunnel coupling between the dots, plunger gates L and R control the dot energies, and gates B_L and B_R tune the tunneling rates from each dot to the adjacent electron reservoirs. There are two additional gates that separate the dot system from the charge sensor, W_L and W_R, that are almost always grounded during normal operation. The top half of the device contains a charge sensor, either a single-gate QPC or a triple-gate SET.

4.3.1 The stability diagram and inter-dot tunnel coupling

Mutual Coulomb repulsion modifies the electrochemical potentials of both dots, leading to complex behavior. If we have a double quantum dot with capacitance C_m between dot sites, then the charging energies of both dots are modified from the standard e^2/C_g as below

[vDE02]:

$$E_{c1} = \frac{e^2}{C_1}\left(\frac{1}{1 - C_m^2/C_1C_2}\right), \tag{4.9}$$

$$E_{c2} = \frac{e^2}{C_2}\left(\frac{1}{1 - C_m^2/C_1C_2}\right), \tag{4.10}$$

$$E_{cm} = \frac{e^2}{C_m}\left(\frac{1}{C_1C_2/C_m^2 - 1}\right). \tag{4.11}$$

In (4.11), the new quantity E_{cm} can be thought of as the energy change in one dot when an electron is added to the other dot. Then the electrochemical potentials of the two dots are given by

$$\mu_1(N_1, N_2) = \left(N_1 - \frac{1}{2}\right)E_{c1} + N_2E_{cm} - \frac{1}{|e|}(C_1V_1E_{c1} + C_2V_2E_{cm}), \tag{4.12}$$

$$\mu_2(N_1, N_2) = \left(N_2 - \frac{1}{2}\right)E_{c2} + N_1E_{cm} - \frac{1}{|e|}(C_1V_1E_{cm} + C_2V_2E_{c2}). \tag{4.13}$$

Equations (4.12 and 4.13) can be used to construct a *charge stability diagram* that depicts the number of electrons in each dot as a function of V_1 and V_2 at equilibrium for small to moderate inter-dot coupling C_m. This is accomplished by asserting that the electrochemical potential on dot 1 (dot 2) is lower than the source (drain) potential, assuming dot 1 is adjacent to the source. Imposing another physical constraint that electrons will continue to enter both dots until the chemical potentials are as close as possible — while still being lower — than the source and drain potentials, it is possible to find pairs (N_1, N_2) that meet these conditions for each set of gate voltages V_1, V_2 (Figure 4.5, left). The charge stability diagram is a series of hexagonal plateaus, each with a unique combination of left and right dot occupation number. The vertices are triple points where two stable charge regions with the same total number of electrons meet a third charge region with total charge differing by one. The spacing of triple points gives the charging energies of both dots. Charge stability diagrams can be measured directly with charge sensing, and the boundaries between occupations can be obtained from differential charge sensing.

At this point, the circuit model has given us all the information that it can give. It hasn't captured the important effect of inter-dot tunnel coupling, however. When inter-dot coupling is added, the eigenstates of a constant-N configuration become hybridized and the quantities N_1, N_2 are no longer good quantum numbers. At extreme coupling strengths, the system merges into a single dot. To go further, we need to employ an explicitly quantum mechanical model. In a manner suggestive of the potential applications to quantum simulation, we can use a two-site Hubbard model to give a more accurate depiction of the stability diagram [YWD11]. Neglecting exchange terms, the two-site Hubbard Hamiltonian is given by $H = H_\mu + H_U + H_t$ where

$$H_\mu = -\sum_{i,\sigma} \mu_i n_{i\sigma}, \tag{4.14}$$

$$H_U = \sum_i U_i n_{i\uparrow} n_{i\downarrow} + U_{12} \sum_{\sigma,\sigma'} n_{1\sigma} n_{2\sigma'}, \tag{4.15}$$

$$H_t = -t \sum_\sigma (c^\dagger_{1\sigma} c_{2\sigma} + c_{1\sigma} c^\dagger_{2\sigma}). \tag{4.16}$$

In (4.14)–(4.16), $i = \{1, 2\}$ iterates over dot sites, $\sigma = \{\uparrow, \downarrow\}$ iterates over electron spin states and $c^\dagger_{i\sigma}, c_{i\sigma}$ are creation and annihilation operators. H_μ simply describes the electrochemical potential of the double-dot electron configuration and H_U describes Coulomb repulsion between two electrons on the same site (with repulsion strength $U1, U2$) and inter-site Coulomb repulsion parameterized by U_{12}. Using only these two terms, the Hubbard Hamiltonian is equivalent to the classical capacitance model. Hubbard model parameters can then be mapped to capacitive terms [YWD11]: $U_i = E_{c_i}$, $U_{12} = E_{c_m}$, $\mu_1 = |e|(\alpha_L V_L + \alpha_{LR} V_R) - E_{c1}/2$, $\mu_2 = |e|(\alpha_R V_R + \alpha LRV_L) - E_{c2}/2$. The terms in H_t parameterized by hopping amplitude t contain the inter-dot tunnel coupling and are not present in the classical capacitance model. These Hamiltonian terms are accompanied by certain boundary conditions. Each quantum dot "valence" shell can only contain zero, one or two electrons. Additionally, Pauli exclusion prevents two electrons of the same spin and valley-orbital states to exist in the same

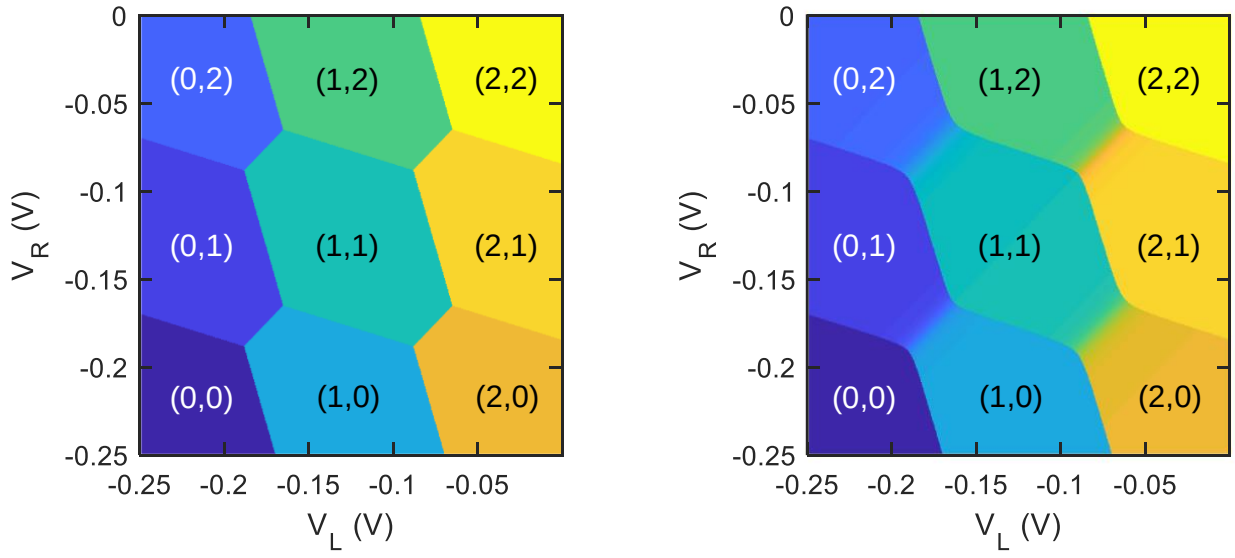

Figure 4.5: Simulated charge stability diagrams for a double quantum dot. Left: regions of stable charge calculated with the circuit model (Equations 4.12 and 4.13). Right: Equivalent calculations using a two-site Hubbard model (Equations 4.14–4.16). The Hubbard model reproduces the quantum dot hybridization effects arising from nearest-neighbor hopping.

quantum dot. If we consider only the lowest valley-orbital level in each dot, then two spins in the same dot must be anti-parallel.

When the full Hamiltonian is diagonalized, the lowest-energy eigenstate represents the true electron occupation in the double quantum dot, in general a superposition of N_1 and N_2 (Figure 4.5, right). Framing the stability diagram as the outcome of a Hubbard model hints at the important application of quantum dot arrays as quantum simulators [HFJ17]. As seen in Figure 4.6, the Hubbard model closely resembles actual data taken with differential charge sensing.

4.3.2 Transport

Current transport through two quantum dots can be addressed with the same constant-interaction circuit model and transition-balancing strategies used for the single-dot case

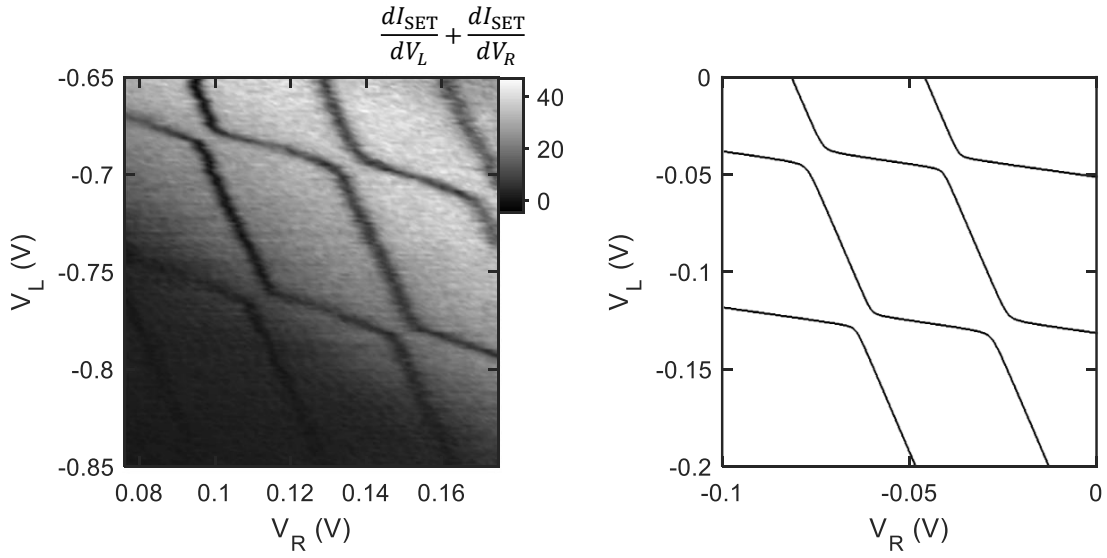

Figure 4.6: Left: experimental charge stability diagram from differential charge sensing with the same modulation applied to V_L and V_R. Right: simulated Hubbard model stability diagram. Parameters are $U_1 = 3.2$ meV, $U_2 = 6$ meV, $U_{12} = 0.5$ meV, and $t = 0.1$ meV. Lever arms are $\alpha_1 = 0.09$, $\alpha_2 = 0.075$, $\alpha_{12} = \alpha_{21} = 0.02$.

in Section 4.1.1, where now a source-drain bias is applied across the dots. In the circuit picture, current will flow only when both dots have levels that are in the bias window, *and* the available level in the dot closest to the source is at a higher energy than the dot near the drain. Resonant tunneling, which should give the strongest transport signal, occurs when both dot levels are equal (and in the bias window, of course). The triple points at zero bias now become bias triangles, representing the only region where Coulomb blockade is lifted [vDE02]. Just as the slope along one edge of a Coulomb diamond gives the plunger gate's lever arm, two side lengths of a bias triangle give the lever arms of the double dot plunger gates. However, when inter-dot capacitance C_m is small enough so that $C_m \sim C_1 C_2 V/|e|$, then the bias triangles from nearby triple points begin to merge together Figure (4.7, left).

The circuit model falls short when it comes to considering spin states, even when they are degenerate at zero magnetic field. If there is one valence electron in the left dot, for instance, and zero in the right dot, then an interesting current rectification effect can transpire. When

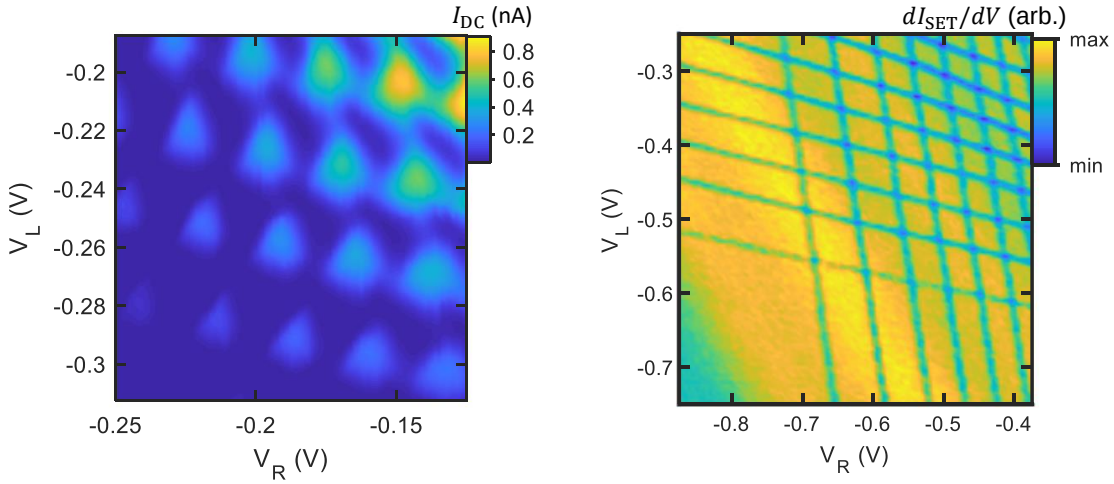

Figure 4.7: Left: current transport through a double quantum dot in the multi-electron regime. Bias triangles appear where Coulomb blockade is lifted, with positions corresponding to vertices of the charge stability diagram (triple points). Visibility decreases with decreasing V_L, V_R due to stray capacitance effects on the tunnel barriers. Right: differential charge sensing in the single-electron regime. All tunnel couplings are much smaller, making transport in this regime virtually impossible.

an electron flows tunnels from the source to the left dot, it must occupy the empty spin state to form a singlet with the existing electron. Then it can tunnel to the right dot and leave the system through the drain. However, when the bias is reversed then an electron entering the right dot can occupy either spin state since spin coupling with the bound left dot electron is very weak. At this point the electron is not allowed to tunnel from the right dot to the left if its spin is parallel with the left electron's spin. In other words, there is classical transport when current flows from the singly occupied dot to the unoccupied dot and there is Pauli spin blockade when current tries to flow in the opposite direction [OAT02][JPM05].

4.3.3 Charge sensing

Charge sensing is, for most applications, a far better choice than transport for probing a double quantum dot due to the ability to measure charge transitions at very low tunneling rates and the reduced electrical noise (there are also dispersive read-out techniques that have less back-action than charge sensing and a much higher bandwidth [HCC17], but they remain un-implemented in our lab for the time being). As long as electrons have a tunneling path from one of the dots to one of the charge reservoirs, even if the inter-dot coupling is vanishingly small, charge transitions can be observed (Figure 4.7, right).

Transport through a charge sensor as a function of dot plunger gate voltages V_L and V_R will yield a stability diagram almost identical in structure to Figure 4.5, with incremental plateaus of conductance representing different charge configurations in the double dot after a linear background conductance has been subtracted [PJM04]. The source and drain reservoirs adjacent to the dots are typically grounded for these measurements. To increase contrast, differential charge sensing measurements can be used to show only the boundaries of each stable charge region (Figure 4.6). Again, differential charge sensing can be replicated with simple transport by taking a numerical derivative of the current with respect to a gate voltage, provided the signal-to-noise ratio is good enough.

With two dot plunger gates, there are four choices for modulating the charge sensor

signal. The modulation can be applied to either the left or right plunger, causing only the left or right charging lines to appear in the lock-in signal. One can also apply the same modulation in phase to both gates, yielding sets of charging lines with the same polarity (as in Figure 4.6). An third option is to apply modulation to both gates with a 180° phase difference, so that the charging lines from one dot will appear as dips in current and the other set of lines will appear as peaks. This method can be used to effectively discriminate sets of lines, and it also brings out the inter-dot charge transition for smaller values of inter-dot coupling. The 180° phase is accomplished with an inverting amplifier. A final modulation strategy is to modulate both gates with a relative phase of 90°. This will shunt charge transition signals of one dot to the Y channel of the lock-in amplifier and leave the other dot's charging lines in the X channel, allowing each dot to be addressed separately in measurements. Practically, this last option is not too useful since it requires two lock-in amplifiers to produce the modulation, or one lock-in and a phase shifter.

4.4 Determining tunnel rates

At zero temperature, charge transitions are abrupt: Coulomb peaks become delta functions and charge sensing transport in this limit would show steps in conductance with infinitesimal transition times. Thermal energy adds the possibility of an electron jumping into or out of the quantum dot to make some excited state configuration, which can then decay back to the ground state naturally or through thermal processes. The probability of thermal excitations occurring increases as the dot electrochemical potential nears the source or drain potential, creating broadened Coulomb peaks and conductance transitions. Broadening is merely the result of averaging over many instances of abrupt thermally excited charge transitions, an averaging that every experimental measurement tool does to some extent; a voltmeter that measures post-amplification source-drain current is actually performing many averages over some integration time determined by the circuitry, for example. When we probe a charging

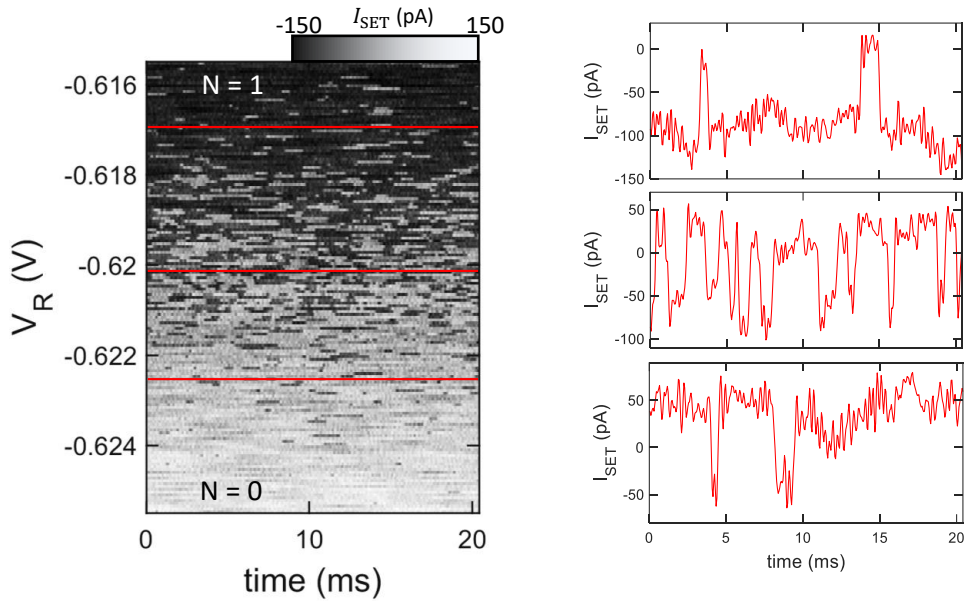

Figure 4.8: Real-time thermally excited tunneling events in the vicinity of the $N = 0 \rightarrow 1$ charge transition with electron temperature $T \approx 0.2$ K. Left: SET transport as a function of measurement time and V_R. Right: individual traces taken from the right plot at three values of V_R showing random telegraph noise. Individual tunneling events turn into a thermally broadened signal when averaged many times.

line, we are actually recording the ensemble effect of an electron hopping in and out of the dot with characteristic frequency Γ (Figure 4.8). When we refer to the tunnel rate, we are discussing Γ. Tunnel rates depend on many factors, including the barrier height and the available dot levels involved in the transition.

4.4.1 Tunnel rate through pulsed modulation

Typically we modulate our charge sensing measurements with a sine wave from the lock-in amplifier. We can also modulate the gate voltage with a square pulse with pulse width τ and repetition rate $1/2\tau$. Pulse modulation provides nearly the same measurement, except not all Fourier components of the square pulse have the same phase, leading to some of the signal appearing in the lock-in Y channel. The benefit with pulse modulation is it becomes very easy to describe the average electron tunneling behavior. When the rising edge of the

pulse modulation voltage crosses a charge transition line at time t_0, a single electron will tunnel into the dot with probability $1-e^{-\Gamma(t-t_0)}$. Then, as the falling edge of the pulse passes back over the transition, the electron will tunnel back out of the dot giving an occupation probability of $e^{-\Gamma(t-t_0-\tau)}$. As long as the pulse width $\tau >> 1/\Gamma$, the electron will always tunnel in or out of the dot before the pulse voltage changes and the differential charge sensing will show the maximum possible transition peak height. However, when τ gets shorter it becomes less and less likely that the electron will be able to hop between do and reservoir. It has been found that the charging line peak height as a function of pulse height, as measured with a lock-in amplifier, is given by [EHW04a]

$$\frac{I}{I_0} = 1 - \frac{\pi^2}{\Gamma^2\tau^2 + \pi^2}. \tag{4.17}$$

From (4.17), the peak height will drop to half its maximum value I_0 when $\tau = \pi/\Gamma$. Therefore, the tunnel rate can be found be scanning over a charging line and stepping up the pulse rate until peak current drops by a factor of 2 (Figure 4.9, left). This strategy is very useful for measuring tunnel rates that are too fast to capture with real-time charge sensing measurements. In our case, the bandwidth is limited by the lock-in amplifier maximum lock frequency of 100 kHz, meaning we should be able to measure tunnel rates up to $2\pi f = 630$ kHz.

4.4.2 Direct time-domain measurement

Alternatively, if there is an oscilloscope nearby it is possible to see the exponential tunneling probability directly. As before, a pulse train is applied when the gate voltage is just below a charging line. In this instance the pulse height doesn't matter provided it's large enough to fully cross the thermally broadened transition. When the oscilloscope is measuring charge sensor current triggered on the pulse, then it will see single-electron tunneling in real-time. Oscilloscope traces can be averaged many times to obtain the exponential behavior repre-

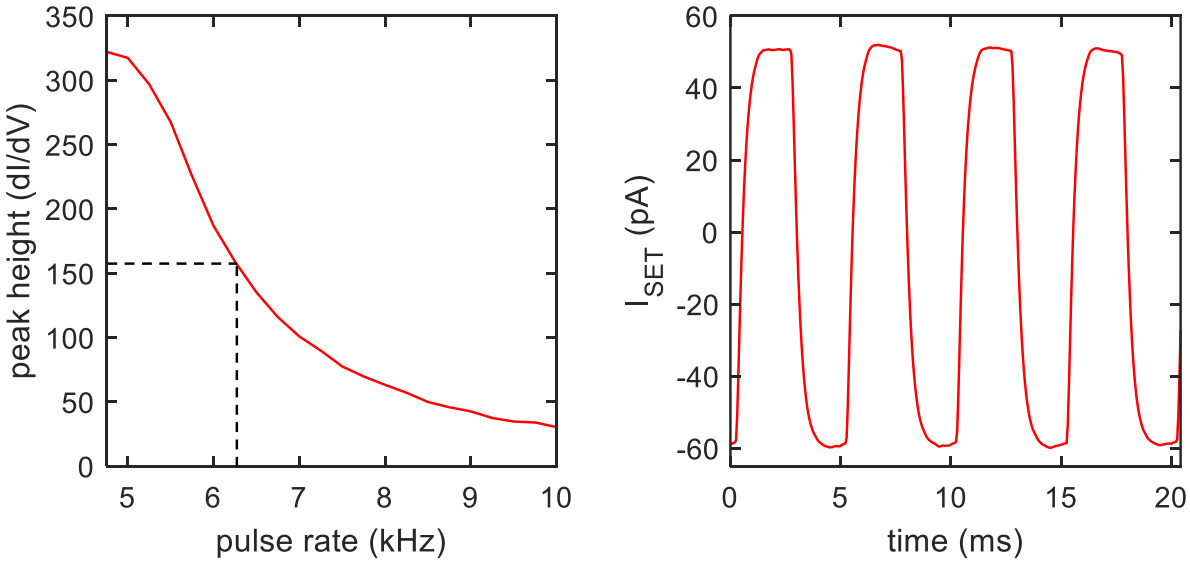

Figure 4.9: Determining tunnel rates using the pulsed modulation technique (left) and real-time exponential fitting technique (right). The left curve follows Equation (4.17) and the average tunnel rate Γ is given by $\Gamma = 2\pi f_0$, where f_0 is the pulse rate at the point where the charge sensing peak height is half its maximum value. In this case, $\Gamma = 40$ kHz. In the right plot, tunnel-in and tunnel-out rates can be determined separately by fitting the rising and falling exponentials with probablity at the start of a pulse period given by Equation (4.19). Here, a periodic background containing the capacitive effects of the voltage pulses has been subtracted to leave the pure electron tunneling response and the data has been averaged 2000 times. Fitting results in $\Gamma_{\text{in}} = \Gamma_{\text{out}} = 3$ kHz.

senting the quantum dot occupation probability distribution over time.

The averaged oscilloscope data can be recorded over a single period to obtain tunnel-in and tunnel-out rates Γ_{in} and Γ_{out} by fitting to exponential functions $1-e^{-\Gamma_{\text{in}}t}$ and $e^{-\Gamma_{\text{out}}(t-\tau)}$. I found that a more precise method involves fitting several periods to an exact probability function, obtained in the following way. Given a pulse with width τ and period T, then the n^{th} period begins with an initial occupation probability of p_n. Over the course of the pulse, the probability of occupation increases as $p(t,n) = 1-(1-p_n)e^{-\Gamma_{\text{in}}t}$. At the end of the pulse, the probability is $p_n' = 1-(1-p_n)e^{-\Gamma_{\text{in}}\tau}$. Then, when the pulse voltage returns zero,

occupation is given by $p'(t,n) = p'_n e^{-\Gamma_{\text{out}}(t-\tau)}$. The start of the next period begins with initial probability $p_{n+1} = p'(T, n+1)$. This can be collapsed recursively to the starting point with initial probability $p_0 = 0$. Ultimately, initial occupation in the n^{th} period is given by the sum

$$p_n = (1 - e^{\Gamma_{\text{in}}\tau})e^{-\Gamma_{\text{out}}(T-\tau)} \sum_{j=0}^{n-1} e^{-j[\Gamma_{\text{in}}\tau + \Gamma_{\text{out}}(T-\tau)]}. \tag{4.18}$$

After many repetitions, p_n trends toward p_{n+1}. The steady-state solution is given for $n \to \infty$, which converges as a geometric sum:

$$p_{n\to\infty} = \frac{e^{\Gamma_{\text{in}}\tau} - 1}{e^{\Gamma_{\text{in}}\tau + \Gamma_{\text{out}}(T-\tau)} - 1}. \tag{4.19}$$

We can verify that when $\Gamma \gg \tau$, $p_{n\to\infty} = 0$ and when $\Gamma \ll \tau$, $p_{n\to\infty} = 0.5$ as expected.

With an algebraic expression for the initial occupation probability after many pulses, we can fit the average time-domain data to extract tunnel-in and tunnel-out rates (Figure 4.9). The nice thing about this technique is it gives us separate values for Γ_{in} and Γ_{out}, but it is limited by the bandwidth of the charge sensor (tens of kHz).

4.4.3 Inter-dot tunneling

As discussed in Section 4.3.1, inter-dot tunnel coupling causes mixing of charge configurations with the same total number of electrons. Until now we have relied on equivalent capacitive elements to relate experimental observables with electrostatic quantities. Since inter-dot coupling does not factor into the circuit model, we need a new method for characterization. A quick and simple solution is to simply fit the charge transitions to the Hubbard model and find the value of t that gives the best fit. A more precise metric is the width of the $(N, M) \to (N-1, M+1)$ transition. If we perform charge sensing on the left dot, for instance, while scanning plunger voltages to cross the inter-dot line, we should see a jump in conductance. In the limit of zero tunnel coupling, the jump should be perfectly abrupt

(subject to thermal broadening, of course). As the tunnel coupling increases, the transition will look like [WPD13]

$$P_{(N,M)} = \frac{1}{2}\left[1 - \frac{\epsilon}{\Omega}\tanh\left(\frac{\Omega}{2k_BT}\right)\right], \tag{4.20}$$

where $\epsilon = \alpha_R V_R - \alpha_L V_L$ is the energy difference between dots and $\Omega = \sqrt{\epsilon^2 + t^2}$. As long as the tunnel coupling is larger than k_BT, the linewidth should be determined by t. However, in practice it is difficult to have a large enough tunnel coupling for this measurement while also keeping the inter-dot transition abrupt. In Chapter 5 we find the tunnel coupling directly with Ramsey spectroscopy, giving us values of $2t$ = 108-132 μeV depending on the valley state occupation for large values of V_M.

4.5 Counting electrons

Ideally, it should be possible to determine the number of electrons in each quantum dot by decreasing the relevant plunger gates further and further until there are no more charge transitions. As I alluded earlier, this is usually not a robust method of electron counting because of the contributions of plunger gates to the tunneling barriers via stray capacitance. As the dot energy increases, it becomes more isolated from electron reservoirs and other dots nearby. As such, observing the complete absence of charging lines in a charge sensing measurement does not always constitute the complete absence of confined electrons.

4.5.1 Magnetospectroscopy

The least ambiguous method of precisely determining the number of electrons is with magnetospectroscopy by exploiting the interactions of electron spin with available valley states and orbital levels [LYZ11]. In the presence of an out-of-plane (z) magnetic field, the spin degeneracy is lifted and Zeeman levels diverge. However, valley and orbital states (which will here be referred to collectively as valley-orbit levels due to disorder-induced hybridization)

are either weakly dependent or independent of the same magnetic field, meaning that the spin states will have an avoided crossing with each valley-orbit level it encounters as the magnetic field is increased. The $N = 1$ ground state experiences a linear decrease in energy with magnetic field as $\frac{1}{2}g\mu_B B_{\text{ext}}$ and remains the ground state for all $|B_{\text{ext}}| > 0$. However, when a second electron is added to the dot at zero field it must occupy the excited spin state to form a singlet due to Pauli exclusion. Accordingly, when the field is increased, the energy of the two-electron state gets larger. Then, when the magnetic field is increased to exceed the valley-orbit splitting, it becomes energetically favorable for the second electron to occupy the first excited valley-orbital level and form a spin triplet with the first electron. At this point, the second electron ground state begins to *decrease* with increasing field (Figure 4.10). It turns out that any electron occupation $N > 1$ will experience at least one crossing with a valley-orbit state and its energy dependence versus field will change sign each time a crossing occurs. Thus, the $N = 0 \rightarrow 1$ charge transition can always be positively identified as the only transition that does not experience a sign change in slope as the magnetic field is increased from zero.

Experimentally, performing this measurement entails scanning a plunger gate voltage across a charge transition and repeating the scan while incrementing the magnetic field. As long as the transition linewidth — determined by the electron temperature and modulation amplitude, if any — is less than the splitting between the ground state and the first valley-orbital level and the scan is slow enough that the N^{th} electron is always in its ground state, then it should be possible to identify any level crossings that occur. Electron counting with magnetospectroscopy fails when the valley splitting approaches $E_{VS} \sim k_b T$, or when the spin relaxation time is slow compared to the scanning rate. However, magnetospectroscopy is a useful tool in characterizing quantum dots beyond electron counting. For instance, knowing that the slope of a charging line (neglecting any sign changes) in E_{dot}—B space is $\left|\frac{dE}{dB}\right| = \frac{1}{2}g\mu_B$, then the slope of the charging line in V_g—B space is $\frac{dV_g}{dB} = \alpha_g \frac{dE}{dB}$. This leads

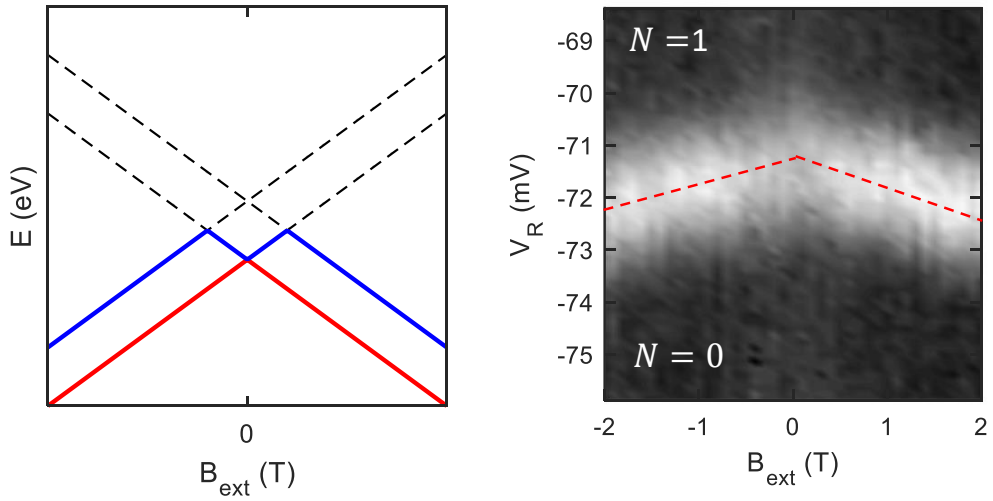

Figure 4.10: Ground-state magnetospectroscopy on the right dot in a double quantum dot devices. Left: first two valley-orbital levels. Red trace: ground state for a single electron. Blue trace: ground state for the two-electron configuration. The second electron is forced into the excited valley-orbit state by Pauli exclusion. Right: differential charge sensing measurement of the $N = 0 \rightarrow 1$ transition as a function of magnetic field. As expected, the position of the peak follows the red path in the left plot.

to a nice way of determining the gate lever arm:

$$\alpha_g = \frac{2}{g\mu_B}\left|\frac{dV_g}{dB}\right|. \tag{4.21}$$

4.5.2 Tunneling cut-off

Given that magnetospectroscopy requires a sizable external magnetic field and long scan times, we often use an alternate technique for counting electrons that utilizes the idea of relative lever arms. As a plunger gate voltage is decreased to deplete its quantum dot, the stray capacitance effect on the tunneling barrier can be compensated for as long as we know the ratio of plunger gate lever arm to barrier gate lever arm. This information can be acquired simply from a scan of charge sensing current as a function of plunger gate and barrier gate in some region that contains charge transition lines. The apparent line slope $dV_{\text{barrier}}/dV_{\text{plunger}}$ is equal to $\alpha_{\text{barrier}}/\alpha_{\text{plunger}}$. This ratio then tells us how much to compensate the barrier gate voltage as we squeeze down on the plunger gate to empty electrons from the quantum dot. The assumption here is that the lever arms are constant with respect to the number of electrons and gate voltages, which isn't generally the case. However, that assumption isn't even needed if we just scan the barrier gate and plunger gate voltages over a large enough range. With a wide scanning window, it should be possible to see where the charging lines cut off due to slow tunneling rates, as in Section 4.4. That cut-off point should be more or less the same for each charge transition, accounting for stray capacitance effects. We can say with confidence that we have emptied the dot of all electrons when we see no more charge transitions while (1) the barrier gate voltage is positive enough to allow for fast tunneling out of the dot if there remain confined electrons and (2) the gate voltage has been decreased to at least twice the nearest observed charging energy (Figure 4.11).

If the tunneling cut-off method is used in conjunction with pulsed modulation, then the barrier-plunger plots also give us a rough estimate of the tunnel rates. When the a given transition's tunnel rate is fast compared to the pulse width, then the electron occupation

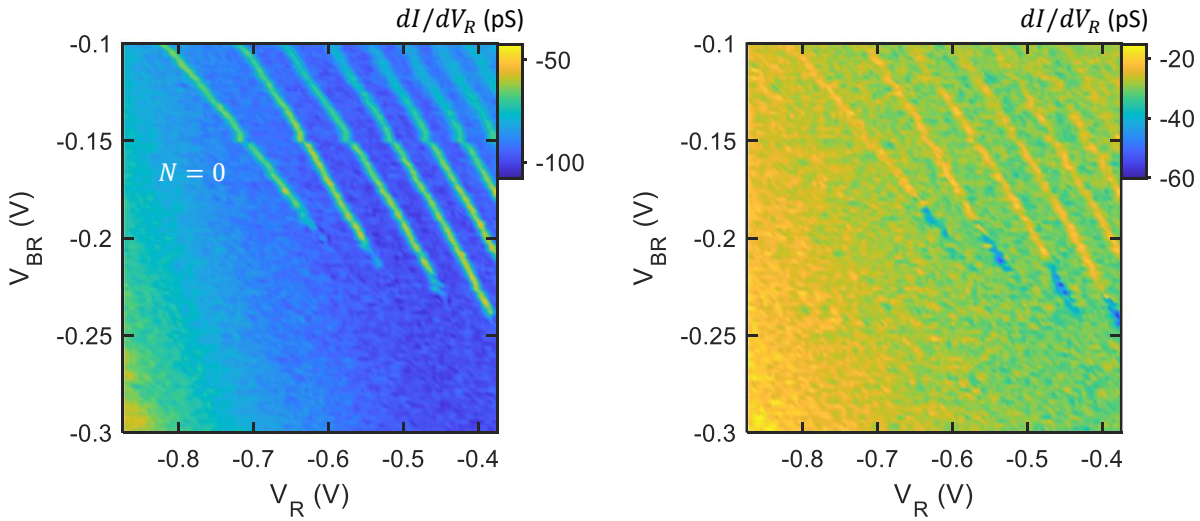

Figure 4.11: Counting electrons from zero. Scanning a quantum dot's plunger gate and barrier gate together allows us to see how the plunger gate affects the tunneling rate via stray capacitance. In the X channel of the lock-in measurement (left), V_R seems to affect the tunnel barrier linearly as seen by the points where charge sensing is cut off, making it easy to see where the final charge transition is located. Right: the same data measured in the lock-in amplifier Y channel. The transitions reverse sign and become dips when the average tunnel rate is close to the pulse rate. Here the pulse rate is 200 Hz.

probability follows the pulse shape closely and the transition line will appear mostly in-phase with the modulation (i. e. in the lock-in amplifier X channel). When the tunnel rate falls below approximately $8/\tau$, or four times the pulse repetition rate, then the average occupation probability is close to 90° out of phase with the pulse and the charging line will appear mostly in the lock-in amplifier Y channel.

CHAPTER 5

Valley-orbit spectroscopy

From the discussion in Chapter 2, a good understanding of the valley states and their effects on quantum dot electrons is crucial. Small valley splitting leads to quantum information leakage and can interfere with standard quantum state read-out techniques like Pauli spin blockade and double-dot occupation. In Si/SiGe heterostructures, we have almost no control over the magnitude of the valley splitting due to its dependence on atomic-level interface details. It is therefore important for the silicon qubit research community to have a toolkit for valley characterization. Like the spin quantum number, valley occupation does not easily couple to electric fields and so manipulation and charge-based read-out of valley states is challenging. However, three years ago our group demonstrated electrical manipulation and charge-sensor measurement of valleys using fast square voltage pulses [SFJ17]. This strategy leverages inter-dot valley-orbit coupling to transform a double quantum dot charge state into a single-dot valley state and back again. This chapter and its successor are based on our group's published work [PSR19a].

5.1 Pulse-excited coherent oscillations

We begin by utilizing the same square-pulse technique to probe valley states in a double quantum dot as in [SFJ17]. This scheme presupposes a energy spectrum of the form (2.16), where a given valley state in each quantum dot can couple to both valleys in the other dot. We use the device shown in Figure 5.1a, where gates in the lower channel form the double quantum dot and we pass a current through a large dot in the upper channel to sense the

charge occupation of the double dot system. The sensor is closer to the right quantum dot, so we generally see a weaker signal from the left dot. Gate M is given a large positive bias of around 0.4 V to strongly couple the dots.

5.1.1 Procedure

The device is kept at a based temperature of 36 mK, as measured on the mixing chamber plate, in our Triton 200 dry dilution refrigerator. The quantum dot channel began to accumulate charges at a top gate voltage of around 3 V. We first tune into the two-electron region by squeezing down on gates L and R. We focus on the $(2,0) \leftrightarrow (1,1)$ transition, where one electron is always in the left dot and a second electron is free to tunnel between the two dots (Figure 5.1b). Then a fast voltage pulse with a roughly 200 ps rise time is applied simultaneously to both plunger gates with opposite polarity to create a pulse that moves diagonally through V_L–V_R space. If we start in $(1,1)$ and pulse diagonally to $(2,0)$ through the inter-dot transition, we are effectively pulsing from negative to positive detuning $\epsilon = E_R - E_L$. Similarly if we start in $(2,0)$ and pulse into $(1,1)$, the transition is from positive to negative detuning. The inter-dot transition line represents zero detuning where the dot energies are equal. The outcome of the pulse is measured by a lock-in amplifier with modulation applied to L and R.

In both pulse directions, subject to some constraints, oscillations in charge sensing current are visible as a function of pulse width (5.1c,d). At large pulse heights (highly positive or negative detuning), the oscillation frequency and phase are constant with detuning. These oscillations can be understood as arising from Larmor precession between valley states in whichever dot the pulse travels to and are discussed in the following sections.

To avoid singlet-triplet complications we would like to be in a region with one electron shared between dots. However, in this device the $(1,0) \leftrightarrow (0,1)$ hybridization isn't strong enough to achieve the desired transition so we instead stay in the $(1,1) \leftrightarrow (2,0)$ region. Since we find the same oscillatory behavior when pulsing in the $(1,1) \rightarrow (2,0)$ direction as

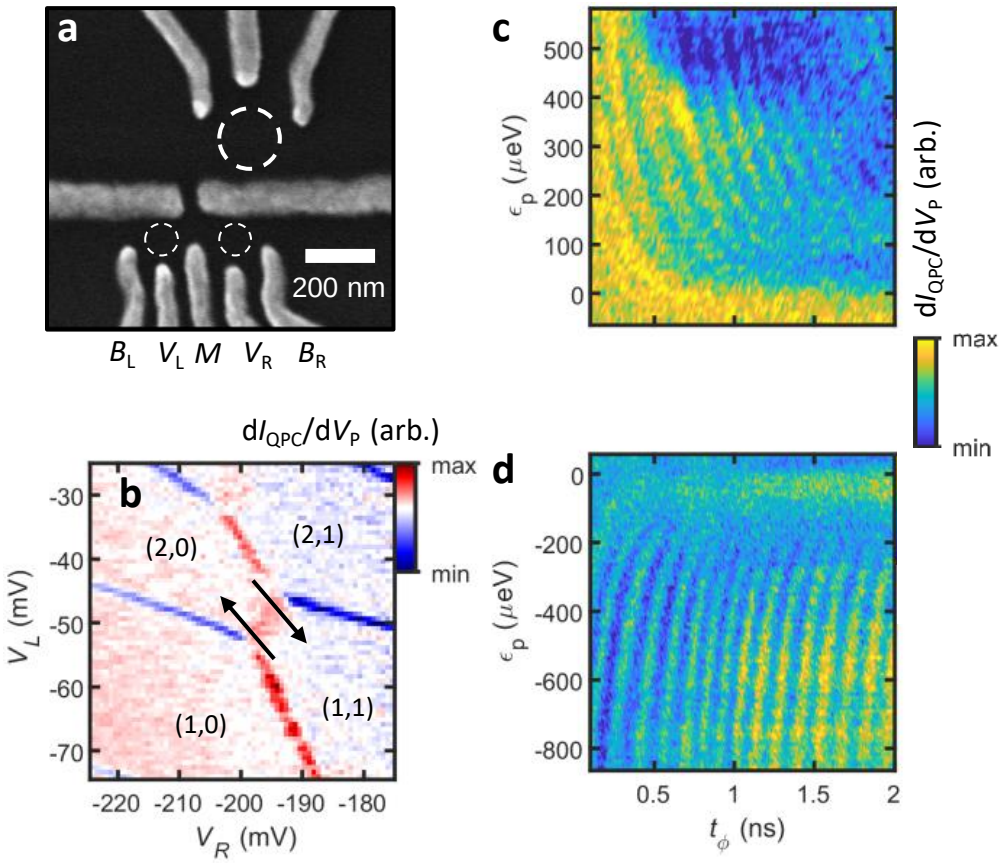

Figure 5.1: Coherent valley oscillations excited with a square detuning pulse. (A) SEM micrograph of the double-dot device used. Pulses are applied to gates L and R with opposite polarity. (B) Charge stability diagram in the vicinity of the $(2,0) \leftrightarrow (1,1)$ configuration. Arrows indicate the approximate start positions and directions of the detuning pulse. (C) Precession between left dot valleys when pulsing to $(2,0)$ and (D) precession between right dot valleys when pulsing to $(1,1)$.

when we pulse in the $(2,0) \rightarrow (1,1)$ direction, we can conclude that the spin states do not dramatically affect the operation.

5.1.2 Operation mechanism

As the detuning pulse rises to its maximum value determined by the pulse height, it can pass through an anti-crossing between the lowest two energy levels in the four-state system. Pulse operation relies on a Landau-Zener transition between the lowest two energy levels of the double dot system in the vicinity of this anti-crossing [Wit05][PLG10]. Essentially, the Landau-Zener formula is a generalization of transitions in two-state systems subject to a time-dependent Hamiltonian:

$$P_D = e^{-2\pi\Gamma}, \qquad \Gamma = \frac{\Delta^2/\hbar}{\frac{d}{dt}\frac{\partial}{\partial\epsilon}|E_2 - E_1|}, \tag{5.1}$$

where P_D is the probability of a diabatic transition Δ is the effective coupling between the two states with energies E_1 and E_2. Two known limits can be extracted from (5.1). If the pulse is abrupt with respect to the coupling, then the probability of a transition from one state to the other approaches 1. In the opposite limit, the pulse is slow enough to maintain adiabatic evolution and the transition probability is close to zero. To maximize Larmor precession between valley states, the pulse must produce a Landau-Zener transition with probability 0.5. If the pulse rise time is too slow or the inter-dot coupling is too large, then the system will evolve smoothly from $|R, v_-\rangle$ to $|L, v_-\rangle$ or the other way around. On the other hand, if the pulse is too fast then the initial state $|L, v_-\rangle$ or $|R, v_-\rangle$ with initial Hamiltonian $H_i = \epsilon/2\sigma_z$ will encounter a final Hamiltonian of the form $H_f = E_{\mathrm{VS}} |\mathrm{ES}\rangle \langle \mathrm{ES}|$ where ES is the excited valley in whichever dot is being pulsed into. Since the initial wavefunction is also an eigenstate of the final Hamiltonian, there is no time evolution of the state. The pulse shape must fall between these limits in order to see oscillations.

5.1.3 Read-out mechanism

At the height of the pulse, provided the Landau-Zener transition generated a good valley superposition of the form $|\psi\rangle = \frac{1}{\sqrt{2}}(|v_-\rangle + e^{i\phi_0}|v_+\rangle)$, the state will undergo Larmor precession between valley states. Phase is accumulated as the state precesses leading to an overall phase difference of $\phi_0 + \frac{E_{\mathrm{VS}}}{\hbar}t$. We know that any projective measurement in the $|v_-\rangle, |v_+\rangle$ basis at this point would always yield a probability of 0.5 to be in either valley, and a charge sensing measurement is incapable of distinguishing valley occupation even if the projective measurement was able to probe the phase. Both problems are solved with a second Landau-Zener transition as the pulse again passes through the anti-crossing to return to the initialization point. The pulse is fast enough compared to the anti-crossing energy gap that the valley superposition is mapped to double-dot charge occupation, and it is slow compared to the two highest energy states that most quantum information stays in the lowest two states. Ultimately, the falling edge of the pulse performs the mapping $|L, v_-\rangle \mapsto |R, v_-\rangle, |L, v_+\rangle \mapsto |L, v_-\rangle$ in the case of a $(1,1) \to (2,0)$ pulse direction. The final state is a superposition of both dot ground states, and a projective measurement can therefore be accomplished with charge sensing.

5.1.4 Valley phase coherence

We can fit the oscillations to a decaying sinusoidal function to obtain the precession frequency and the decay constant. Assuming the initial state is pure, the damped oscillations will have the form

$$P(t) = \frac{1}{2}\left[1 + e^{-(t/T_2)^{\alpha}} \cos\left(\frac{E_{\mathrm{VS}}}{\hbar}t - \phi_0\right)\right]. \tag{5.2}$$

In (5.2), T_2 is the dephasing time and α is a coefficient that depends on the noise source. For $1/f$ charge noise, $\alpha = 2$. Dephasing manifests as decay in the average precession amplitude, leading to a maximally mixed state (Bloch vector has length 0) and a constant projective probability of 0.5 in the limit where $t \gg T_2$. In silicon quantum dot systems, any quantum

states that are in some way dependent on the detuning parameter are coherence-limited by low-frequency charge noise, which manifests as perturbations in detuning. When systemic fluctuations play a large enough role in coherence, T_2 is replaced with the inhomogeneous dephasing time T_2^*. The value of T_2^* obtained from fitting the data to (5.2) reflects the worst possible dephasing time that can give the experimentally observed decay in precession. For a charge qubit, dephasing away from the anti-crossing at $\epsilon = 0$ will be determined by T_2^*. However, the charge qubit level splitting in the vicinity of the anti-crossing can be expanded to second order as $2\Delta + \frac{1}{2}(\epsilon/2\Delta)^2$, meaning that charge noise doesn't effect coherence at $\epsilon = 0$ to first order. This has been experimentally verified in semiconductor charge qubits, where dephasing at the inter-dot transition is an order of magnitude longer than dephasing elsewhere [PPL10].

The four-state spectrum required to give us coherent valley oscillations at positive and negative detuning gives us a unique opportunity to explore the idea of states protected against dephasing. Since the valley states are parallel sufficiently far away from zero detuning, the valley splitting should be independent of detuning. This is verified by examining the frequency of precession at large pulse heights, which is constant to within error bars. In this scenario, perturbations in detuning due to charge noise should have no effect on the valley states to N^{th} order, giving electron spin-like coherence times. This provides the ultimate motivation for valley qubit proposals, where the valleys themselves are the qubit basis states [CSK12][RRB14][BSC16].

We find a maximum valley dephasing time of $T_2^* \approx 7$ ns with the square pulse procedure. Observed valley coherence is substantially shorter than what is typically seen in spin systems, which we attribute to charge noise fluctuations in coupling parameters (off-diagonal terms in the Hamiltonian) and a small but non-negligible first-order dependence of the valley splitting on detuning. To make comparisons to charge qubit dephasing, we can make use of an independent measurement of the low-frequency $1/f$ charge noise spectrum in a similarly patterned Si/SiGe device [FSJ16]. Charge noise at 1 Hz was found consistently to be $\sigma_\epsilon \approx 2$

μeV, which can be used to estimate the inhomogeneous dephasing time for a charge qubit at the same operation point as the valley oscillations. Using the expression

$$T_2^* = \frac{\sqrt{2}\hbar}{\sigma_\epsilon}, \tag{5.3}$$

the equivalent charge qubit dephasing time is 0.5 ns, consistent with reported values [PJM04] [PPL10]. The valley dephasing time, on the other hand, is 14 times longer than an average charge qubit T_2^*. This confirms that there does exist some form of charge noise protection in the far-detuned valley basis.

In principle we should also be able to see valley relaxation (parameterized by relaxation time T_1) during precession. However, indirect measurements have put valley relaxation in the microsecond range, much longer than the valley dephasing time [KSW14]. As detailed in Chapter 7, we later directly measure valley relaxation as $T_1 = 12$ ms in this device.

5.2 Constraints on coherent valley oscillations

With enough parameter tweaking, we have been able to see pulse-induced valley oscillations in every sufficiently tunable double-dot device tested, with frequencies no larger than 15 GHz and no smaller than 2 GHz. This isn't to say that the pulse operation is trivial; there are several limitations during initialization, pulse operation, and read-out that first needed to be understood.

5.2.1 Initialization constraints

Referring back to the DiVincenzo criteria from Chapter 1, the ability to initialize the system into a simple, well-known state is crucial for qubit implementations. To maximize the oscillation amplitude and also to better model quantum dynamics, the initial state in the $(1,1)$ or $(2,0)$ configuration is made to be the ground state, i. e. $|R, v_-\rangle$ or $|L, v_-\rangle$. Once a pulse

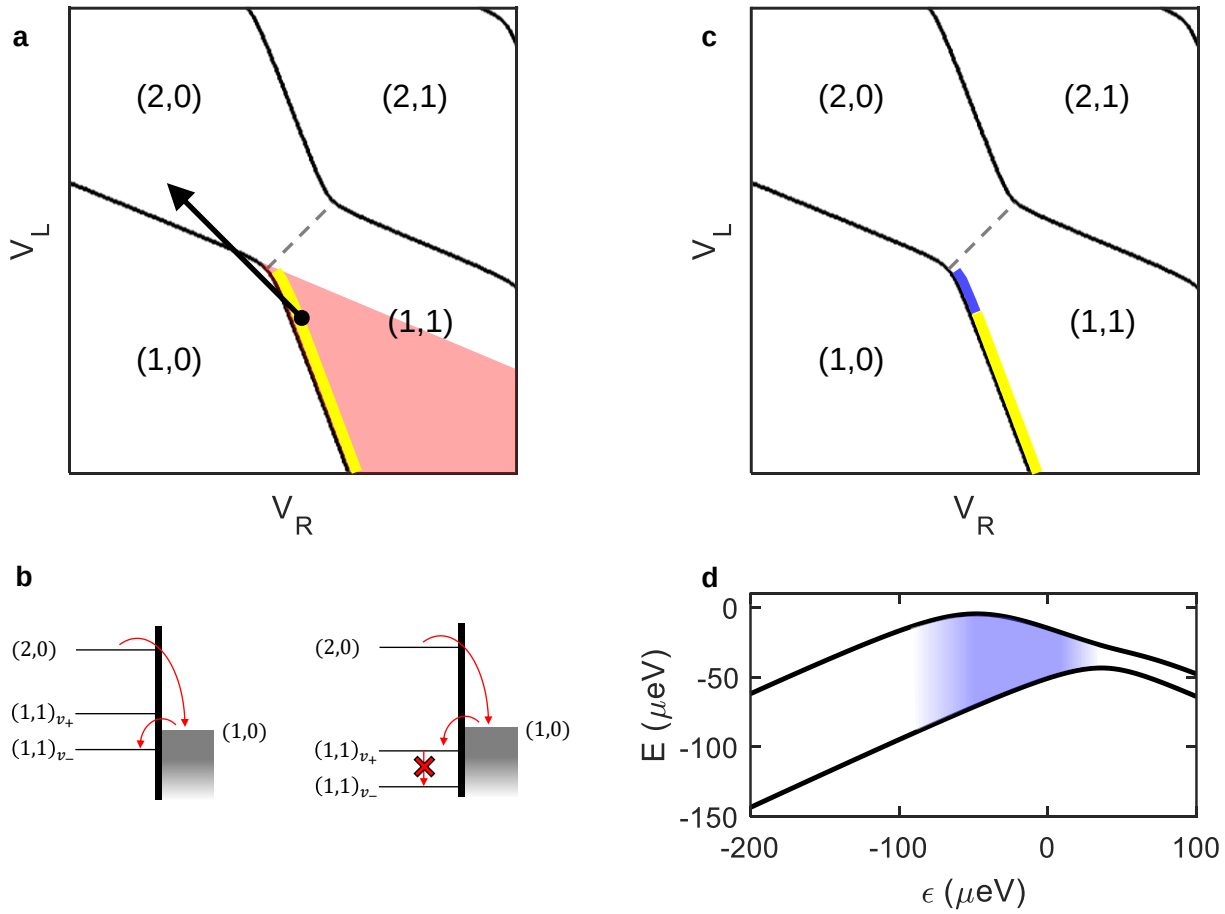

Figure 5.2: Constraints on pulse-excited valley oscillations. (A) The charge qubit enhanced co-tunneling initialization is shown as a red triangle in the $(1,1)$ configuration. The true enhanced initialization window is given by the yellow region. (B) In a dot with valley splitting, co-tunneling to the ground state via $(1,0)$ can only occur if the $(1,1)$ valleys straddle the $(1,0)$ electrochemical potential (left). If both valleys are lower than $(1,0)$, then the electron can get stuck in the excited valley (right). (C) Blue area within the initialization window represents the read-out region. If read-out occurs too far into $(1,1)$, then the lowest states are the right dot valleys with equal charge content. (D) good read-out occurs at a range of detuning where the lowest states have different charge content.

is applied and subsequently ends at the initialization point, the final quantum state could be any superposition of $|R, v_-\rangle$ and $|L, v_-\rangle$. If the excited state is occupied, there must be enough time between pulses for the electron to relax to the ground state. For our fast pulse generator, the maximum time between pulses was around 30 ns. Unfortunately, natural charge relaxation is comparable to or slightly less than our pulse period, meaning that the electron does not always fully return to the initial state. This is not a unique problem by any means, and we can gain some insight from the charge qubit literature. If, for instance, initialization occurs in the $(1, 1)$ configuration, then the $(1, 0) \leftrightarrow (2, 0)$ transition line can be extended into $(1, 1)$ region to form a triangular area of enhanced relaxation (red area in Figure 5.2a). In this area, it is energetically favorable for an electron in the excited state $(2, 0)$ to tunnel out of the dot to $(1, 0)$ and back into the $(1, 1)$ ground state rather than decay directly to $(1, 1)$. This tunnel process occurs faster than natural charge relaxation, leading to quick initialization.

The charge qubit enhanced relaxation region does not impose a strict enough constraint on initialization in our system, because we must still contend with valley splitting in the dot we initialize into. If the excited valley in $(1, 1)$ is lower in energy than $(1, 0)$, then enhanced tunneling may lead to that excited valley being occupied instead of the ground state. The only subsequent pathway to the ground state is through pure valley relaxation, which occurs on a much slower timescale (Figure 5.2b). Accordingly, the true enhanced relaxation region is a line along the $(1, 0) \leftrightarrow (1, 1)$ boundary, with a width equal to the right dot valley splitting [JPC19] (Figure 5.2a, yellow region).

5.2.2 Operation constraints

Due to the nature of the Landau-Zener transition needed to observe coherent valley oscillations, operation fidelity is determined by the pulse ramp slope $d\epsilon/dt$ in relation to inter-dot coupling. We are limited in shaping the pulse itself due to severe attenuation through wire bonds by the time the signal gets to the device, but we have excellent control of the tunnel

coupling through gate M. We can tune the voltage on M until we maximize visibility of oscillations, which in this device occurs at a tunnel coupling of around 100 μeV as measured in section 5.3. In relation to the charging energy, the required tunnel coupling is substantial and the double quantum dot begins to resemble a single, peanut-shaped dot. The oscillations can completely disappear if V_M is reduced by as little as 2 mV, placing stringent limits on the optimal coupling strength. This is also the reason that we did not see oscillations in the single-electron region, because stray capacitance from the plunger gates increased the effective inter-dot tunneling barrier to the point where we couldn't compensate with gate M.

5.2.3 Read-out constraints

For good valley-to-charge conversion, read-out must take place at a detuning where the lowest two levels have very different double-dot charge content. In the absence of valley splitting in the initialization and read-out charge configuration, every value of detuning such that $|\epsilon| - 2\Delta \gg 0$ is sufficient for charge sensor measurement, where Δ is the inter-dot coupling. When valley splitting is considered, this is no longer the case. At very large detuning, the lowest levels are the valley states that contain equal charge content. If read-out takes place too far from $\epsilon = 0$, then the valley precession will map to (as an example) $|R, v_-\rangle$ and $|R, v_+\rangle$ instead of $|L, v_-\rangle$ and $|R, v_-\rangle$ (Figure 5.2). This places a final, tight constraint on the pulse starting location to a subset of the initialization window, represented as the blue region in Figure 5.2c.

5.3 Ramsey spectroscopy

The technique described above is relatively simple to implement and allows us to quickly identify the parameter space that gives us high-visibility valley oscillations. One major downside with the square pulse is that the visibility of oscillations reduces to zero as the

pulse height approaches the anti-crossing. This is because evolution becomes more adiabatic as the pulse height is reduced as governed by (5.1). To get around this issue, we implement a Ramsey fringe experiment. The construction starts with the same square pulse as before beginning in $(1,1)$, with initialization and tunnel coupling tuned to produce maximum-amplitude oscillations. The square pulse will generate a state composed of equal parts $|L,v_-\rangle$ and $|L,v_+\rangle$. A dip is inserted in the middle of the pulse of variable height and width, and the dip position ϵ_p is swept through the detuning region we wish to probe (Figure 5.3c, inset). As long as the dip isn't too abrupt, the valley superposition will never be an eigenstate of the Hamiltonian at ϵ_p and Larmor precession will continue for the duration of the dip. Then the pulse voltage is brought back to its maximum detuning and returned to the initialization point for read-out.

To construct the Ramsey pulse, two channels of the Agilent 81134A pulse generator were added with a high-frequency combiner. Channel 1 was used as the standard square pulse, and channel 2 with negative polarity was added to channel 1 as the central dip. Consequentially, we could no longer pulse along a V_L/V_R diagonal and were forced to add the pulse to V_R only. Ultimately this provided the same oscillations as the diagonal pulse, but at a cost of coherence. Beyond a pulse width of 2 ns, the oscillation amplitude rapidly decreases with a decay envelope that isn't well described by exponential or gaussian processes. Since the pulse now passes over the $(1,1) \leftrightarrow (1,0)$ transition line, we speculate that the loss in coherence is caused by fast relaxation to $(1,0)$ with a rate that is exponentially dependent on how deep into $(1,0)$ the pulse travels. If relaxation out of the qubit subspace is treated as an effective dephasing process (which is a little dubious), then the effective T_2^* with a horizontal or vertical pulse in place of a diagonal pulse is around 1.5 ns, a five-fold decrease from the original 7 ns dephasing time.

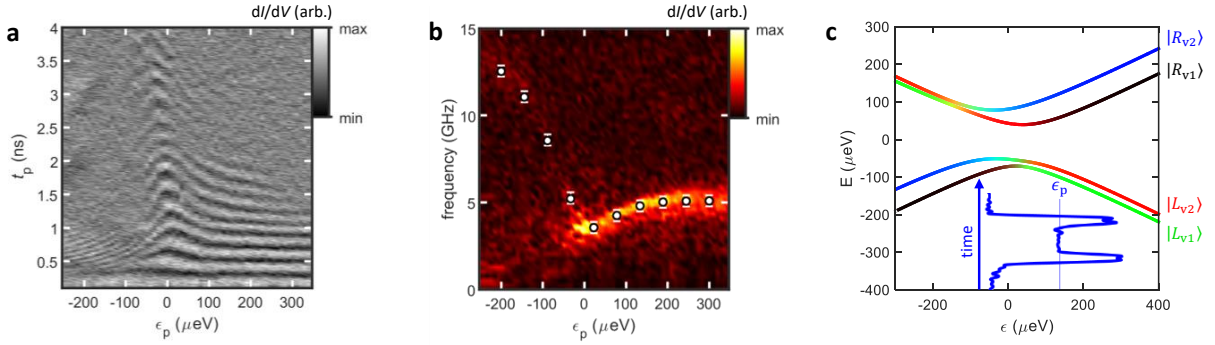

Figure 5.3: Ramsey spectroscopy of valley-orbit states. (A) Larmor precession between the lowest two valley-orbit levels is visible at all values of detuning. (B) The Fourier transform of (A). White points represent the frequency of oscillations we would expect to see given precession between the lowest two states according to the model fit. (C) The four-state spectrum modeled by (5.4), fit to the data in (B). Line colors represent state occupation in the charge-valley basis. Inset: pulse profile.

5.3.1 The valley-orbit spectrum

When the Ramsey pulse is carried out for different ϵ_p, oscillations are visible as a function of dip width t_p (Figure 5.3a). As expected, the oscillations remain in the vicinity of the anti-crossing at $\epsilon \approx 0$. The minimum oscillation frequency is not exactly at zero detuning because inter-dot coupling modifies the position. We can fit the frequency of oscillations as a function of detuning to extract a full four-state energy spectrum using the model obtained from diagonalizing (5.4), repeated here for readability:

$$H = \begin{pmatrix} -\epsilon/2 & 0 & \Delta_1 & -\Delta_2 \\ 0 & -\epsilon/2 + E_{\mathrm{VS},L} & -\Delta_3 & \Delta_4 \\ \Delta_1 & -\Delta_3 & \epsilon/2 & 0 \\ -\Delta_2 & \Delta_4 & 0 & \epsilon/2 + E_{\mathrm{VS},R} \end{pmatrix}. \tag{5.4}$$

In Figure 5.3b, the Fourier transform of the original Ramsey pulse-induced oscillations is shown with white points indicating the oscillation frequencies expected from the fit results.

The good agreement suggests that while coupling terms Δ_i and valley splittings E_{VS} may have some detuning dependence expected from the dots moving through an interface disorder landscape, the effect is small enough in our detuning range that the Hamiltonian parameters can safely be treated as constant.

Figure 5.3c shows the calculated four-state spectrum, with colors corresponding to the charge-valley basis state coefficients. The only parameter that does not have a unique solution from the fit of Figure 5.3a is Δ_4, which couples the left and right dot excited valleys. This is because the $|L, v_+\rangle/|R, v_+\rangle$ mixing occurs between the highest two energy levels, inaccessible to the applied pulse from rise time considerations. We find precise values of the valley splitting in the limit $|\epsilon| \to \infty$ as $E_{\mathrm{VS},L} = 4.55$ GHz and $E_{\mathrm{VS},R} = 15.74$ GHz. Additionally, we find a valley-dependent inter-dot coupling of $\Delta_2 = 12.7$ GHz and $\Delta_3 = 15.6$ GHz. The coupling responsible for the Landau-Zener transition is described by $\Delta_1 = 1.8$ GHz and we set $\Delta_4 = 2$ GHz, motivated by symmetry considerations.

Surprisingly, the quantum states at the anti-crossing ($\epsilon = 45$ μeV) are not simple bonding and anti-bonding states $\frac{1}{\sqrt{2}}(|L, v_-\rangle \pm |R, v_-\rangle)$ as is the case with charge qubits. Instead, they are given by a superposition of all four charge-valley basis states:

$$|-\rangle = -0.47\,|R, v_-\rangle + 0.36\,|R, v_+\rangle + 0.66\,|L, v_-\rangle - 0.46\,|L, v_+\rangle\,, \tag{5.5}$$

$$|+\rangle = 0.52\,|R, v_-\rangle + 0.30\,|R, v_+\rangle + 0.59\,|L, v_-\rangle + 0.55\,|L, v_+\rangle\,. \tag{5.6}$$

This is a consequence of the inter-dot couplings Δ_2, Δ_3 being larger than inter-dot, intra-valley couplings Δ_1, Δ_4. It also may explain the impressive coherence at the anti-crossing seen in Figure 5.3a. Due to pulse imperfections, the oscillations appear to drift with increasing t_p making it hard to analyze the oscillations at that location.

5.4 Simulating dynamics

We can gain insight into valley-orbit dynamics and predict how certain pulse shapes drive state transitions through numerical simulation. The simplest case with no decoherence effects can be calculated with the von Neumann equation (1.16). Here the Hamiltonian acquires time dependence through the pulse effect on detuning: $\epsilon \rightarrow \epsilon(t)$. For a pure initial state and fully coherent operations, the density matrix formalism is overkill and evolution can be calculated much faster with other state vector methods. However, any time we consider decoherence we must use the Lindblad equation to solve the quantum dynamics:

$$\frac{\partial \rho}{\partial t} = -\frac{i}{\hbar}[H, \rho] + \sum_{j=1}^{N^2-1} \gamma_j \left(L_j \rho L_j^\dagger - \frac{1}{2}\{L_j^\dagger L_j, \rho\} \right). \tag{5.7}$$

The first term on the right hand side is just the von Neumann equation, and the coefficients γ_j are rates associated with jump operators L_j. Pure dephasing is associated with operators of the form $\gamma_j L_j = \frac{1}{T_2} |j\rangle \langle j|$ and leads to off-diagonal damping terms. For relaxation processes, the coefficient will just be $\gamma_j = 1/T_1$ with associated operator $L_j = |R\rangle \langle L|$ in the case of relaxation from the left dot to the right dot. This operator applied to a two-state system will make the second and third terms on the right hand side of (5.7) look like

$$\frac{1}{T_1}\left(|R\rangle \langle L| \rho |L\rangle \langle R| - \frac{1}{2}\{|L\rangle \langle L|, \rho\} \right) = \frac{1}{T_1} \begin{pmatrix} \rho_{RR} & -\frac{1}{2}\rho_{RL} \\ -\frac{1}{2}\rho_{LR} & -\rho_{LL} \end{pmatrix}. \tag{5.8}$$

Note that terms with this relaxation operator contribute diagonal *and* off-diagonal terms to the equations of motion, meaning relaxation leads to an additional dephasing effect separate from T_2 or T_2^*. As an additional complication, the decoherence operators only hold in the diagonalized basis instead of the charge-valley basis. This can be seen by considering charge relaxation in a double quantum dot. At negative detuning, relaxation occurs from the excited left dot state to the right dot. However, at positive detuning the same relaxation process

occurs in the opposite direction, from the excited right dot state to the left dot. The only basis in which the process is unchanged for all detuning is the diagonalized basis. Since we put in an initial state measured in the charge-valley basis and get out a final state in that same basis, I found the most natural version of the Lindblad equation comes from diagonalizing the Hamiltonian H so that $\tilde{H} = V^{-1}HV$ for some matrix of column eigenstates V, and then applying the same transformation to the density matrix and performing the inverse transformation after adding the Lindblad operators:

$$\frac{\partial \rho}{\partial t} = V\left[-\frac{i}{\hbar}[\tilde{H}, \tilde{\rho}] + \sum_{j=1}^{N^2-1} \cdots\right] V^{-1}, \tag{5.9}$$

where $\tilde{\rho} = V^{-1}\rho V$ is the density matrix in the diagonalized basis. Since V is composed of normalized, orthogonal column vectors by construction (i. e. unitary), $V^{-1} = V^{\dagger}$ and the transformations are computationally inexpensive. See Appendix A for details on implementing numerical simulations in MATLAB.

Using the four-state spectrum obtained in Section 5.3.1, we simulated the effects of square pulses and the Ramsey pulse. We get good agreement between calculations and experimental results, indicating that the process applied to the quantum state are well understood.

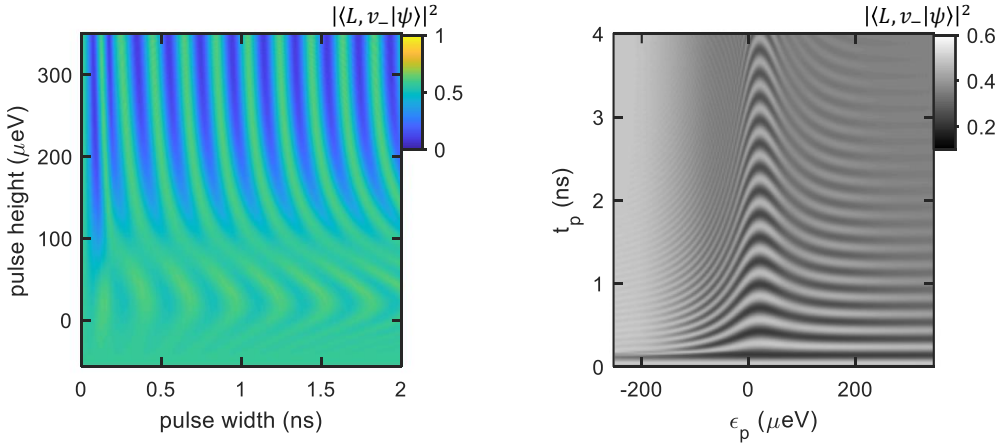

Figure 5.4: Numerical simulation of detuning pulses. Left: simulation of a square pulse from $(1, 1)$ to $(2, 0)$. Right: simulation of the Ramsey spectroscopy experiment in Figure 5.3. Simulations use the Lindblad equation (5.7) with dephasing and no relaxation. Parameters are $E_{\mathrm{VS},L} = 4.55$ GHz, $E_{\mathrm{VS},R} = 15.74$ GHz, $\Delta_1 = 1.8$ GHz, $\Delta_2 = 12.7$ GHz, $\Delta_3 = 15.6$ GHz, and $\Delta_4 = 2.0$ GHz.

CHAPTER 6

Two-axis valley qubit control

Now that we have a good idea of the valley-orbit spectrum accessible by Ramsey spectroscopy, we can perform valley qubit operations. Whatever set of operations we choose to perform must be able to transform any point on the Bloch sphere to any other point before the qubit loses coherence. Since complete qubit control in this manner requires at least two independent rotation axes to implement, we consider two-axis control requisite in demonstrating a valley qubit.

One way to achieve two-axis control is with resonant rf gating. A microwave burst is applied in detuning space via one or more gates that drives Rabi oscillations for some controlled amount of time. As long as the qubit states couple to electric fields, Rabi oscillations will lead to X rotations in the interaction frame. The second axis is simply Larmor precession about z. This form of control has been achieved to great effect with the hybrid qubit, a very similar qubit system [KWS15]. In that work, researchers found that they could stay in the far-detuned regime for operation and read-out, relying on the qubit energy levels straddling the ground state in a different double-dot charge configuration to give state-dependent tunneling rates out of the qubit subspace. In operating this way, the qubit remains protected against charge noise at all times. We found resonant gating to be challenging to implement for several reasons. First, valley states can only couple to electric fields if there is sufficiently strong valley-orbit coupling [VRY15][SKJ17][CBM18], so electrically driven valley resonance has yet to be observed. From a more practical standpoint, we've established that the attenuation from wire bonds between the device and PCB sample holder is substantial beyond

about 3 GHz, meaning that addressing a valley splitting of 5 GHz or larger requires a large input power.

6.1 Pulse operation

Having already demonstrated baseband control of valley oscillations in Chapter 5, we are able to borrow from another publication on the hybrid qubit to implement a DC-gated pulse scheme [KSS14]. The pulse consists of three stages, each separated by a mostly diabatic transition, that allows us to excite precession in the left dot valleys and read out when the right dot is the ground state (Figure 6.1). As with the pulse used in Ramsey spectroscopy, the qubit control sequence is constructed from the summation of two pulse channels from the Agilent 81134A pulse generator. We initialize the qubit into state $|R, v_-\rangle$ at detuning point $\epsilon_0 < 0$. The effective two-state Hamiltonian at this point is $H_{\text{eff}}(\epsilon_0) = \frac{\epsilon}{2}(|R, v_-\rangle\langle R, v_-| - |L, v_-\rangle\langle L, v_-|)$. In the first stage of the pulse, the detuning is abruptly brought to the anti-crossing at ϵ_x and held there for time t_θ. At ϵ_x, the new effective Hamiltonian is approximately given by $H_{\text{eff}}(\epsilon_x) \approx \Delta_1(|R, v_-\rangle\langle R, v_-| + |L, v_-\rangle\langle L, v_-|)$. This new Hamiltonian is orthogonal to $H_{\text{eff}}(\epsilon_0)$, meaning that the state will precess with total accumulated angle $\theta(t) = 2\Delta_1 t_\theta/\hbar$. Note that the Bloch sphere at this point is actually in the $\{|-\rangle, |+\rangle\}$ basis with states defined by equations (5.5) and (5.6). In the valley basis these rotations will show up mostly in the center of the Bloch sphere as mixed states.

In the second stage of the pulse, the detuning is abruptly brought to the left dot valley basis at $\epsilon_z \gg 0$ and held there for time t_ϕ. Now we have an effective Hamiltonian $H_{\text{eff}}(\epsilon_z) = E_{\text{VS},L}|L, v_+\rangle\langle L, v_+|$ which is again orthogonal to the previous stage's Hamiltonian. The qubit will precess about the z axis in the valley-basis Bloch sphere to reach an azimuthal angle $\phi = E_{\text{VS},L} t_\phi/\hbar$.

The third pulse stage consists of a return to ϵ_x for a second set of x rotations, with duration t_θ as in the first pulse stage. In principle the time spent in this stage could be set

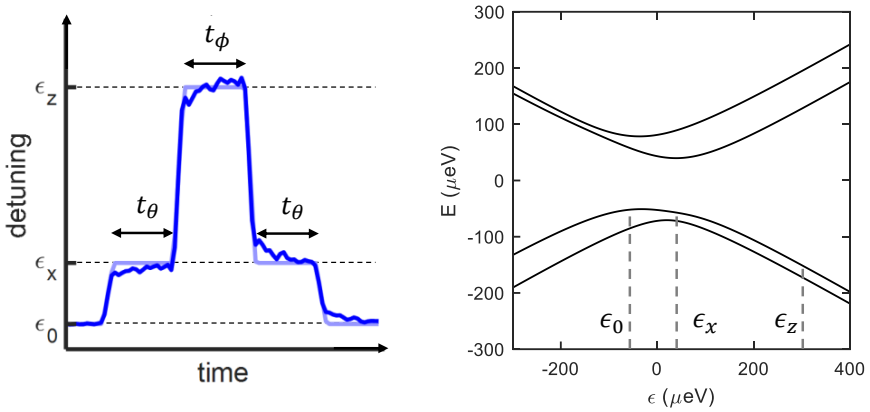

Figure 6.1: The valley qubit control pulse sequence. Left: pulse profile. Right: the locations of operation points ϵ_x and ϵ_z and initialization/read-out ϵ_0 in the valley-orbit spectrum.

so that the qubit rotates by exactly $\theta = \pi/2$, allowing us to measure the y projection of the qubit state during Z rotations. However, we don't know before applying the pulse what time or detuning point is required for a perfect X rotation. We can identify a theoretical operation point and duration from spectroscopy, but in reality pulse imperfections and charge drift make that difficult. After the third and final pulse stage, the detuning is brought back to the initialization point at ϵ_0 for charge sensing read-out.

The danger when carrying out detuning-dependent qubit operations is that decoherence from charge noise can severely limit Bloch rotation fidelity. Although the valley basis in the limit of inter-dot valley couplings $\Delta_1, \Delta_4 << \epsilon$ is insensitive to detuning and has strong protection against charge noise, this is not generally true for other areas of detuning. However, a key feature of the three-step pulse sequence is the majority of operation time is spent at two detuning points ϵ_x and ϵ_z that are both at least first-order insensitive to charge noise. In addition to the valley state protection and analogous to the charge qubit, operation point ϵ_x is located at an anti-crossing and the energy gap there is a constant to first order in Δ_1. Consequently, the bulk of the operation time during the pulse is spent in protected regions. The qubit is subject to the most dephasing during transitions from one operation point to the next (determined by the pulse ramp time after transmission loss of around 250 ps) and

at the read-out point where charge noise susceptibility is maximal.

6.2 Tracing the Bloch sphere

Using the pulse described above and initializing in the right dot ground state (which through adiabatic passage maps to $|L, v_-\rangle$), it is possible to sweep the qubit vector through every direction in the Bloch sphere. Ignoring the effects of dephasing, this set of operations would return all possible pure states. Bloch sphere tracing is accomplished by changing the times t_θ and t_ϕ spent during X and Z rotations. The probability of being in the left dot excited state, designated as the logical $|1\rangle$, as a function of rotation times at fixed ϵ_x, ϵ_z is shown in Figure 6.2a. Two-axis qubit control is evident in this plot by independent oscillations along both operation axes. Furthermore, the frequency of oscillations along the t_ϕ axis is equal to the left dot valley splitting and the frequency of oscillations along the t_θ axis is equal to the energy gap at the inter-dot, intra-valley coupling point. A careful reader will notice that the applied pulse results in two sets of X rotations, which should lead to an X rotation frequency of *twice* the energy gap. This missing factor of two, as well as the t_θ-dependent phase shift in valley oscillations, is accounted for in Section 6.3.

Figure 6.2a can be interpreted in the following way. Valley oscillations have maximum amplitude along the Bloch sphere equator, so θ at these points will be an odd multiple of $\pi/2$. By contrast, valley oscillations should completely vanish when the state vector points along the z axis so the horizontal low-contrast lines represent points where θ is a multiple of π (Figure 6.2c). Turning to rotations along z now at $\theta = \pi/2$, the probability of measuring the qubit in state $|1\rangle = |L, v_+\rangle$ is highest when the qubit state is $\frac{1}{\sqrt{2}}(|0\rangle - i\,|1\rangle) = |-y\rangle$ before the final X rotation. Since we have some freedom in defining what encapsulates the qubit operation and what can be considered state measurement, we can choose to wrap the final X rotation into the projective measurement and make the claim that the first two pulse stages perform the qubit operation. Framed in this way, we perform an arbitrary X rotation

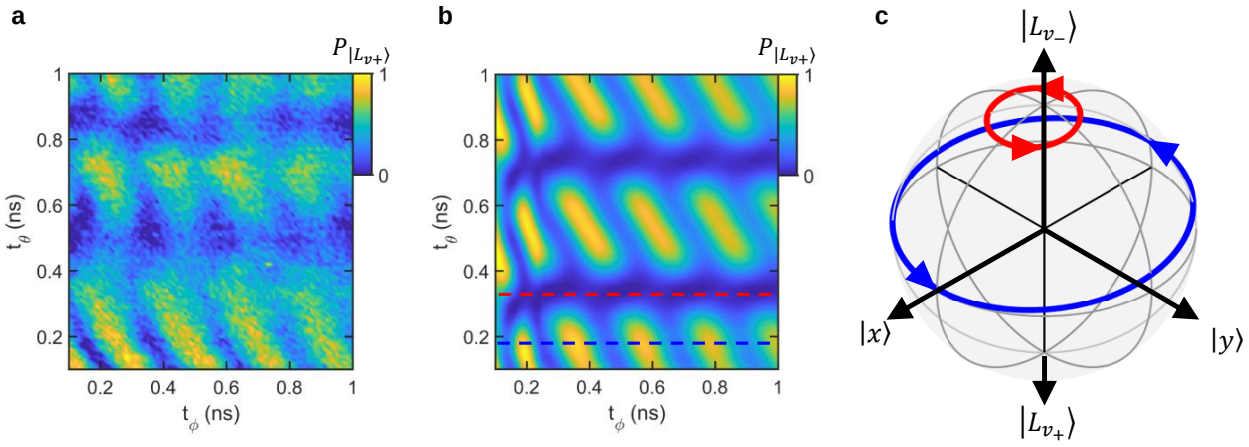

Figure 6.2: Two-axis control of the valley qubit. (A) Measurement of qubit state $|1\rangle$ as a function of X and Z operation times t_θ and t_ϕ. (B) Numerical simulation of (A), including dephasing, calculated by plugging the four-state system Hamiltonian into the Lindblad equation. (C) Qubit trajectories on the Bloch sphere for two fixed values of t_θ. Red trace: oscillations near the Bloch sphere pole are very small (dotted red line in (B)). Blue trace: oscillations near the equator have maximum amplitude (dotted blue line in (B)).

followed by an arbitrary Z rotation and then measure the resulting state with a dynamical projection axis determined by t_θ. I will establish in Section 6.3 that the final rotation is not truly about the x axis at all, which complicates the state projection considerably but doesn't effect two-axis control.

6.2.1 Numerical simulation

The simulated results of our control pulse capture the key aspects of the experiment, including the initially baffling X rotation frequency of roughly 2.5 GHz (Figure 6.2b). When simulated without dephasing effects, high-frequency oscillations corresponding to precession between the first and second excited states near the X rotation point were faintly visible on top of the qubit oscillations. There is no sign of such oscillations in the experimental data, leading me to speculate that they are artifacts of the simulated pulse profile. The control pulse was modeled as three flat operation points separated by abrupt, linear slopes with

a fixed ramp time. In reality, transmission loss would act as a low-pass filter and smooth out the sharp pulse edges. The high-frequency oscillations were removed by adding charge qubit-like dephasing during precession involving states outside the qubit subspace. This procedure keeps the effects of leakage into the highest-energy states which must be acknowledged in fidelity calculations, while maintaining oscillation frequencies corresponding to pure state transformations. Additionally, dephasing within the qubit subspace was added using experimentally determined values of T_2^* at the two operation points. Since the operation detuning doesn't change during the experiment, it was enough to treat dephasing as a step function in detuning, with an abrupt transition from $T_2^* \approx 10$ ns at the anti-crossing to $T_2^* = 1.5$ ns in the valley basis. As was the case with Ramsey spectroscopy, the effective T_2^* during Z rotations is reduced from 7 ns because we are forced to pulse purely along V_R and expose the qubit to enhanced relaxation processes. Dephasing at smaller ϵ_p, such as near the anti-crossing, is reduced for the same reason.

It is generally possible to plot the qubit state trajectory on the Bloch sphere from the results of numerical simulation in order to quantify rotation errors, leakage and decoherence. This is easily accomplished when the X rotation brings the qubit to the Bloch sphere equator, since the basis states are simply the qubit states. Simulations reveal that valley precession does result in rotations very nearly about the z axis, with deviations of about 6°. However, plotting the qubit trajectory during X rotations for a fixed ϕ is not as instructive since rotations are occurring in a different 2-state subspace. They appear in the qubit basis as small rotations, roughly about x, but far from the Bloch sphere surface indicating a mixed state.

6.3 A unitary operation model

As previously discussed, the experimental result of our three-stage control pulse didn't quite match what we expected to see. Rotations about z in the valley basis behaved as predicted

up to a phase shift that was in some way dependent on t_θ, but the X rotation frequency was off by a factor of two. To gain understanding about state evolution during the pulse, we turn to a simple model of SU(2) rotation operations. This model does not assume anything about the system Hamiltonian or pulse details. Individual rotations are expressed in the form

$$U(\hat{n}, \varphi) = \exp(-i\boldsymbol{\sigma} \cdot \hat{n}), \tag{6.1}$$

where $\hat{n}$ is a unit vector defining the rotation axis, φ is the total rotation angle about $\hat{n}$, and Cartesian components of $\boldsymbol{\sigma}$ are Pauli matrices.

6.3.1 Perfect rotations

To start, we assume that the control pulse results in rotations purely about x and z. The three pulse stages will then have associated operators

$$U_1(\theta) = \cos\left(\frac{\theta}{2}\right) - i\sin\left(\frac{\theta}{2}\right)\sigma_x, \tag{6.2}$$

$$U_2(\phi) = \cos\left(\frac{\phi}{2}\right) - i\sin\left(\frac{\phi}{2}\right)\sigma_z, \tag{6.3}$$

$$U_3(\theta') = \cos\left(\frac{\theta'}{2}\right) - i\sin\left(\frac{\theta'}{2}\right)\sigma_x. \tag{6.4}$$

The resulting probability of measuring the qubit in $|1\rangle$ is then
$|\langle L, v_+|U_3(\phi)U_2(\theta)U_1(\phi)|L, v_-\rangle|^2 = 1/4[1-\cos(2\theta)][1+\cos(\phi)]$. Here we set $\theta' = \theta$ because the X rotation operation times are equal. This solution is periodic in ϕ and independently periodic in 2θ, as expected from pulse construction (Figure 6.3a). However, this solution doesn't capture key aspects of the experimental results, especially the θ-dependent phase shift in Z rotations and the true θ periodicity.

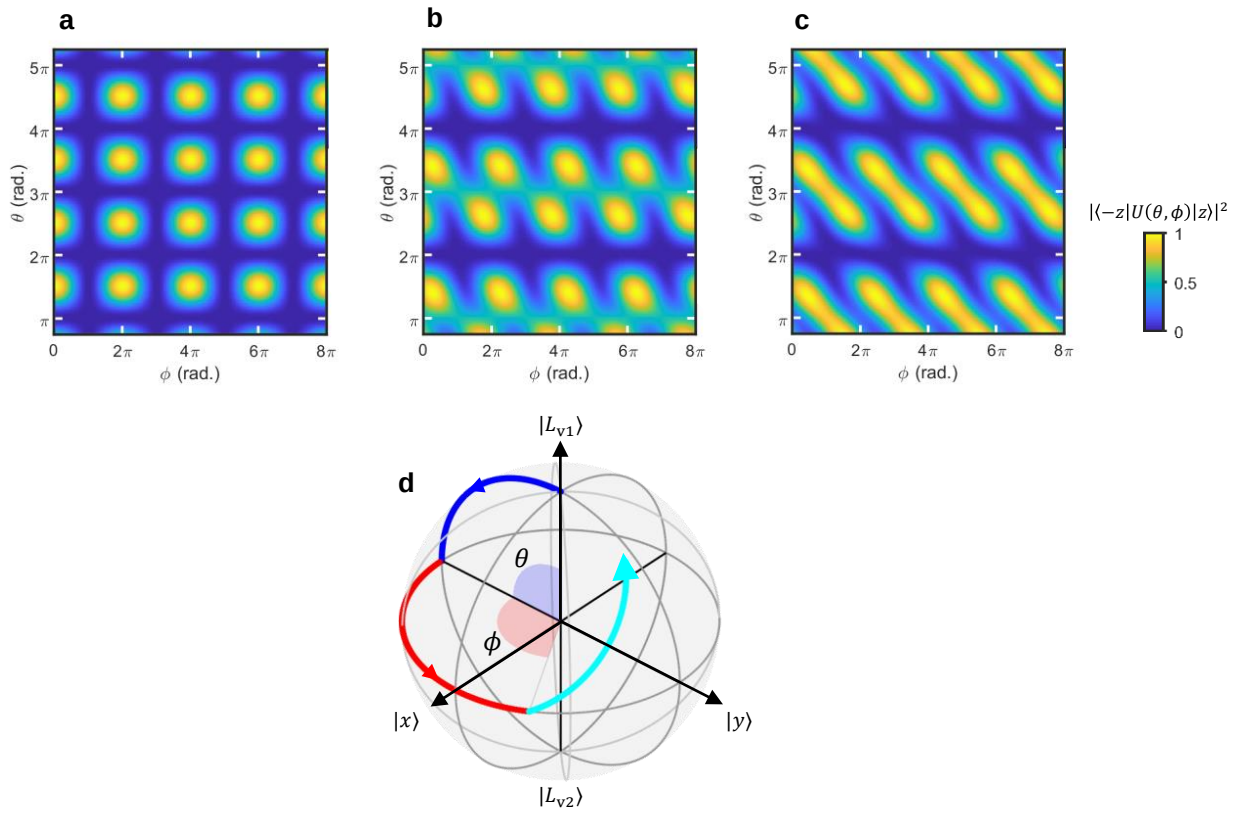

Figure 6.3: Effects of off-axis tilt during rotations. (A) Pure X and Z rotations with no errors lead to oscillations periodic in ϕ and 2θ. (B) The outcome when the third rotation is about an axis in the x–z plane making an angle of $\alpha = \pi/4$ with the x axis. (C) Adding rotation tilts to the first two operation stages of 18° and 6° lead to a result that qualitatively matches the experiment. (D) Qubit trajectory on the Bloch sphere during the control pulse with the parameters in (B).

6.3.2 Rotation errors

The perfect rotation model assumes that the pulse is sufficiently abrupt and that the operation detuning points are perfectly tuned. If either one of these assumptions isn't true then errors in rotation can occur. We can first consider errors in the final X rotation, motivated by the small change in qubit frequency between ϵ_z and ϵ_x that can lead to an adiabatic component in evolution. The true error-prone rotation axis is fixed to lie in the x–z plane and the deviation angle α from the x axis is increased from zero. Now the final unitary transformation has the form

$$U_3(\theta') = \cos\left(\frac{\theta'}{2}\right) - i\sin\left(\frac{\theta'}{2}\right)(\sigma_x\cos\alpha + \sigma_z\sin\alpha). \tag{6.5}$$

With this modification, the probability of measuring the qubit to be in $|L, v_+\rangle$ as a function of θ with $\alpha = \pi/4$ looks like

$$|\langle L, v_+|U(\theta, \phi = 0)|L, v_-\rangle|^2 = (1 - \cos\theta)\left(1 + \frac{1}{\sqrt{2}}\cos\theta\right), \tag{6.6}$$

where $U(\theta, \phi)$ is the product of the three pulse stage operators. This solution goes to zero when θ is an even multiple of π, giving the function an overall periodicity in θ of 2π instead of π (Figure 6.3b and d). This is the origin of the missing factor of two from earlier.

The solution with a sizable tilt in the final rotation still does not give qualitative agreement with experiment. However, it is certainly conceivable that rotation errors occur in the other two pulse stages. We know from numerical simulation that the Z rotation has a tilt of about 6°. By also allowing the first X rotation to have a tilt of 18° from x in the x–z plane, we arrive at a result that closely resembles the data (Figure 6.3c). Critically, the solution maintains periodicity of 2π in θ and ϕ, and now it includes the phase shift that appears to slant the oscillations.

6.4 Benchmarking valley qubit performance

Now that we understand the operations that are truly being applied to the qubit with the control pulse, we can see how well qubit operations fulfill their intended purpose. A figure of merit for qubit operations is the *fidelity*, which has many definitions but generally involves comparing a measured quantum state before and after some string of operations to the expected "ideal" case. For state-of-the-art qubits, the accepted methodology is randomized benchmarking, where N randomly selected operations from some universal set are applied to the qubit(s) initialized at $|0\rangle$, and then a final operation is performed to bring the quantum state back to $|0\rangle$. The fidelity with randomized benchmarking describes how well the final state matches the initial state as a function of N. However, this technique relies on an incredibly stable device and a great deal of flexibility in control pulse shaping. With our valley qubit, we decided to perform *quantum process tomography* (QPT) to measure operation fidelities. With our control pulse and the data in Figure 6.2a, we can first extract the state vector at every point along θ and ϕ. Then we can define the prepared qubit state at the point just before the Z rotation occurs.

6.4.1 State tomography

The first step in QPT is to find the state vector for a given θ and ϕ. We are most interested in the fidelities of processes occurring in the valley basis, so the goal is to prepare various input states along Cartesian axes and see how they each evolve under Z rotations. With the variable t_θ spanning a few periods, we automatically have initial states prepared as $|0\rangle$, $|\pm y\rangle$, and $|1\rangle$. We don't explicitly prepare $|\pm x\rangle$ and they will be needed for QPT later, but they can be extracted from traces at fixed $\theta = 3\pi/2, 7\pi/2, \cdots$ where the phase shift from the tilted third rotation is equal to $\pi/2$. Strictly speaking, traces satisfying this condition are still Z rotations with prepared state $|\pm y\rangle$, but they allow us to fill in the remaining state preparations without double-counting other Z rotation data. For each prepared state,

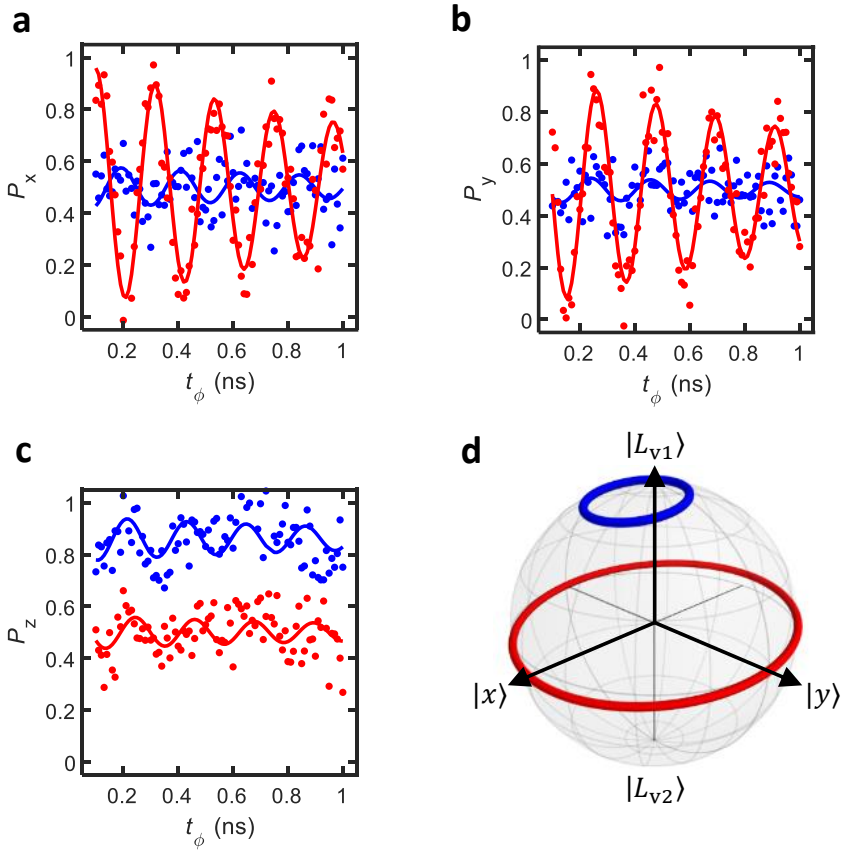

Figure 6.4: Quantum state tomography. Red traces indicate an input state of $|0\rangle$, while blue traces indicate an input state of $|-y\rangle$. Projection (A) is along $|x\rangle$, (B) is along $|y\rangle$, and (C) is along $|z\rangle$. (D) Equivalent trajectories on the Bloch sphere.

projections along x, y, and z must be captured during Z rotations. Given the dynamic projection axes determined by t_θ in the third pulse stage, it becomes possible to find traces with θ such that the tilted third rotation projects the qubit state along the desired axis (Figure 6.4). It is important to stress that this is certainly not the best way to obtain a full set of state tomography. Ideally, with better pulse control, we can construct individual pulse sequences to prepare arbitrary states and then measure them along an arbitrary projections axis. In lieu of proper pulse engineering, the partial data set from our control pulse is sufficient to find reasonable process fidelities from QPT.

6.4.2 Quantum process tomography

The goal of QPT is to find an expression for a process—consisting of a chain of Bloch rotations—in terms of some set of basis operators. Since QPT handles processes that may include decoherence, the involved states are density matrices instead of state vectors. The basis set of operators must form all possible transformations on the Bloch sphere; in other words, they must form a basis for the vector space of 2×2 Hermitian matrices. Any basis set will work, although a natural choice is the Pauli matrices together with the identity operator. Armed with this basis set $\mathbf{B}$, the map function $\mathcal{E}$ for a given input state ρ is given by [CGT09]

$$\mathcal{E}(\rho) = \sum_{m,n=1}^{d^2} \chi_{mn} B_m \rho B_n^\dagger, \tag{6.7}$$

where $d = 2$ is the Hilbert space dimension and χ is the *process matrix*. The matrix described by χ is unique for each quantum operation but independent of the choice of input state. Due to this state preparation invariance, χ is a good metric for process quality. By comparing an experimentally determined χ to the ideal target process matrix χ_{ideal}, we can determine the process fidelity:

$$\mathcal{F} = \text{Tr}[\chi_{\text{ideal}} \chi]. \tag{6.8}$$

In practice, output states $\mathcal{E}(\rho)$ are determined by state tomography and χ is found by inverting (6.7). In what follows, at least d^2 linearly independent input states are needed for each quantum process. With density matrices and the basis set $\{I, \sigma_x, \sigma_y, \sigma_z\}$, it is straightforward to show that states $|0\rangle$, $|1\rangle$, $|x\rangle$ and $|y\rangle$ are linearly independent (note that this is not true in the space of pure state vectors).

6.4.3 Calculating the process matrix

The first step is to combine the state projections obtained from state tomography into density matrices. Given probabilities P_x, P_y, and P_z, the density matrix can be obtained from Stokes

parameters s_i relating the probabilities to points on or in the Bloch sphere:

$$s_i = 2\left(P_i - \frac{1}{2}\right). \tag{6.9}$$

The Stokes parameters have origins in the area of polarized radiation, but they can easily be generalized to any two-dimensional mixed state. Starting with these quantities, a density matrix can be written as

$$\rho = \begin{pmatrix} 1+s_z & s_x - is_y \\ s_x + is_y & 1-s_z \end{pmatrix}. \tag{6.10}$$

In calculating the input and output density matrices, complications can arise from noise in the system. Fluctuations may lead to non-physical density matrices where $\mathrm{Tr}[\rho] \neq 1$, for instance. To enforce that ρ is positive semi-definite and Hermitian with a trace of 1, it can be written in the following way [Bha14]:

$$\rho = \frac{T^\dagger T}{\mathrm{Tr}[T^\dagger T]}, \qquad T = \begin{pmatrix} t_1 & 0 \\ t_3 + it_4 & t2 \end{pmatrix} \tag{6.11}$$

Real-valued coefficients t_i can then be calculated by maximum likelihood estimation (MLE). This involves finding the values of t_i that minimize the sum of squares $\sum_{m,n}(\rho_{mn} - \rho'_{mn})^2$, where ρ' is the density matrix calculated from T.

The next step in calculating χ is to solve (6.7) by linear inversion. Note this will not always result in a physical (positive, Hermitian) process matrix. First, (6.7) must be expressed as some matrix λ times the density matrix basis $\boldsymbol{\rho}$ such that $\mathcal{E}(\rho_j) = \lambda_{jk}\rho_k$ [CCL01]. This can be related to the process matrix as

$$\lambda_{jk} = \beta_{jk}^{mn}\chi_{mn}, \qquad \beta_{jk}^{mn}\rho_k = B_m\rho_j B_n^\dagger. \tag{6.12}$$

If we then use composite indices jk and mn to make β_{jk}^{mn} a two-dimensional matrix and

λ_{jk}, χ_{mn} vectors, then the result is a vector equation that can be inverted to solve for χ:

$$\beta\boldsymbol{\chi} = \boldsymbol{\lambda} \Longrightarrow \boldsymbol{\chi} = \kappa\boldsymbol{\lambda}, \tag{6.13}$$

where κ is the pseudoinverse of β.

The result (6.13) is a starting point for another round of maximum likelihood estimation to enforce that χ is positive semi-definite and Hermitian with a trace of 1. As in (6.11), the process matrix can be written in terms of a T matrix [JKM01]:

$$\chi = \frac{T^\dagger T}{\mathrm{Tr}[T^\dagger T]}, \qquad T = \begin{pmatrix} t_1 & 0 & 0 & 0 \\ t_5 + it_6 & t_2 & 0 & 0 \\ t_{11} + it_{12} & t_7 + it_8 & t_3 & 0 \\ t_{15} + it_{16} & t_{13} + it_{14} & t_9 + it_{10} & t4 \end{pmatrix}. \tag{6.14}$$

With MLE, the set of real-valued t_i is found by minimizing the sum of squares

$$f(\mathbf{t}) = \sum_{j,k=1}^{2} \left(\rho_{\mathrm{out},jk} - \mathcal{E}(\rho_{\mathrm{in},jk}, \mathbf{t})\right)^2, \tag{6.15}$$

where $\mathcal{E}(\rho)$ is obtained from (6.7) with χ in the form (6.14). The initial guess of χ is the solution to linear inversion, i. e. (6.13).

6.4.4 Valley operation fidelities

Input and output states for a given process are taken directly from the three state tomography projections. For the $Z_{\pi/2}$ process, for instance, we choose an arbitrary starting point $t_{\phi,0}$ as the input and identify the point at $t_{\phi,0} + t_{\pi/2}$ as the output state. Given the qubit frequency $E_{\mathrm{VS},L}/h$, we have $t_{\pi/2} = h/4E_{\mathrm{VS},L}$. Similarly, $t_\pi = h/2E_{\mathrm{VS},L}$ and $t_{2\pi} = h/E_{\mathrm{VS},L}$.

We are prevented from directly plugging in our noisy data into (6.15) for two reasons. First, there are some physically impossible points where the sum of projections is greater

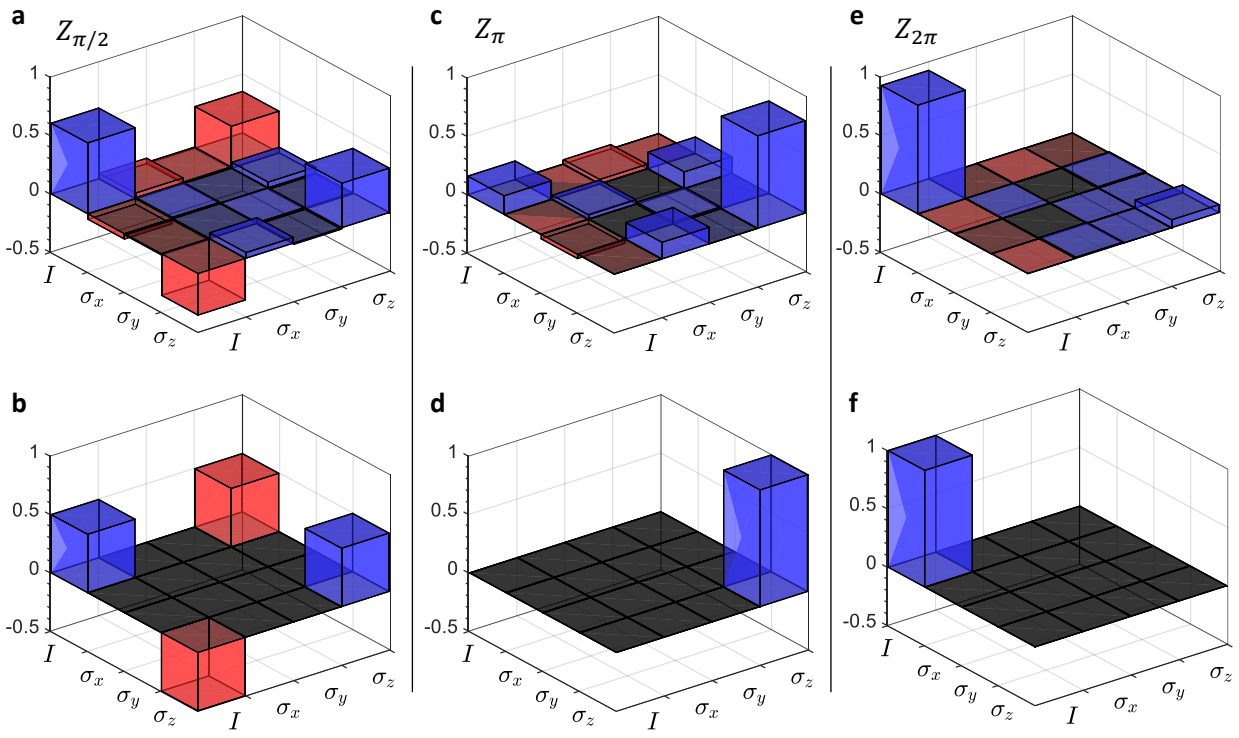

Figure 6.5: Calculated process matrices in quantum process tomography. (A,B) Measured and ideal matrix elements of $\chi_{\pi/2}$. (C,D) Measured and ideal matrix elements of χ_{π}. (E,F) Measured and ideal matrix elements of $\chi_{2\pi}$. Colors indicate complex phase: blue is real, red is imaginary.

than 1 due to read-out noise. Second, the maximum likelihood calculation is incredibly sensitive to the initial guess of χ, since there are many local minima giving wildly different process matrices. For these reasons, we use a fit to the data in the form of a decaying sinusoid for each t_ϕ-dependent set of state tomography. In doing this, we lose information related to uncertainty in state preparation and measurement. However, the fidelity calculation precision in this case is dominated by uncertainty in MLE and can be obtained by performing separate fidelity calculations for every input state at $t_{\phi,0}$. The variance of fidelities then produces a reasonable standard error. After obtaining χ for a given process at all $t_{\phi,0}$, the process matrix corresponding to the median fidelity in the data set is used as the starting point for a second iteration of MLE. This can continue for as many iterations as needed to approach the true process matrix, but in practice it usually only takes two iterations.

The process matrices for $Z_{\pi/2}$, Z_π, and $Z_{2\pi}$ and the corresponding ideal cases are shown in Figure 6.5. There is good qualitative agreement between χ and χ_{ideal}, confirming that we are performing the intended quantum operations. Process fidelities are found to be $\mathcal{F}_{\pi/2} = 0.85 \pm 0.02$, $\mathcal{F}_\pi = 0.79 \pm 0.02$, and $\mathcal{F}_{2\pi} = 0.93 \pm 0.01$. Compared to recent reports of spin qubits with 99.9% NOT fidelity [YTO18], our valley qubit is certainly inferior. However, the valley qubit benefits from fast (GHz) operation speeds and operation at zero magnetic field with no need for microwave signals. As a proof of principle experiment with minimal effort on our part towards parameter optimization, our results indicate a promising future in this area of research.

6.4.5 Principle sources of error

We know from the dephasing time scale that charge noise dominates decoherence. Additionally, from our analysis of the rotation tilts in Section 6.3 we are aware of systemic operation errors that can also limit process fidelity. For future improvements of the valley qubit, it is important to understand the contributions of each error source. Process fidelities can be calculated for a simulated scenario in which there is dephasing but no rotation errors, and

separately in the case where there are rotation errors but no dephasing. In both cases, a simplified version of the fidelity estimate is used [NC00]:

$$\mathcal{F} = \mathrm{Tr}[\sqrt{\rho_t}\rho\sqrt{\rho_t}]. \tag{6.16}$$

Here, ρ_t is the target density matrix resulting from an error-free operation and ρ is the "measured" density matrix after the imperfect operation. This expression does contain an implicit dependence on the input state and is therefore less rigorous than the fidelity calculation involving process matrices, but it is useful as a comparison tool between situations with identical inputs.

In the pure dephasing case, the fidelity decreases monotonically with decreasing T_2^* as expected (Figure 6.6a). Fidelities for Z rotations of $\pi/2$, π, and 2π are estimated to be 0.98, 0.97 and 0.94 when the experimentally determined $T_2^* = 1.54$ ns is used. Since the $Z_{2\pi}$ operation takes the longest amount of time to perform, it has the worst fidelity of the three processes. However, our experimental $\mathcal{F}_{2\pi}$ is actually the best of the three processes despite the operation time.

The case with rotation errors and no dephasing can be simulated by returning to the unitary operation model and applying tilts to the first two rotations in the control pulse sequence. When θ is fixed at $\pi/2$, we can see how tilt errors affect the fidelity (Figure 6.6b,c,d). In this situation, $\mathcal{F}_{2\pi}$ is always the highest possible fidelity because the identity operation is minimally sensitive to the choice in rotation axis. Similarly, $\mathcal{F}_{\pi}$ will always be the lowest fidelity because the NOT operation is maximally sensitive to the rotation axis. These predictions are consistent with our observed fidelities. In fact, when dephasing is ignored altogether and tilts in the X and Z rotation axes are set at 18° and 6° respectively, then we arrive at $\mathcal{F}_{\pi/2} = 0.87$, $\mathcal{F}_{\pi} = 0.84$, and $\mathcal{F}_{2\pi} = 0.9$. These values are fairly close to the measured fidelities.

This analysis suggests that the fidelities are not yet limited by coherence, and are instead

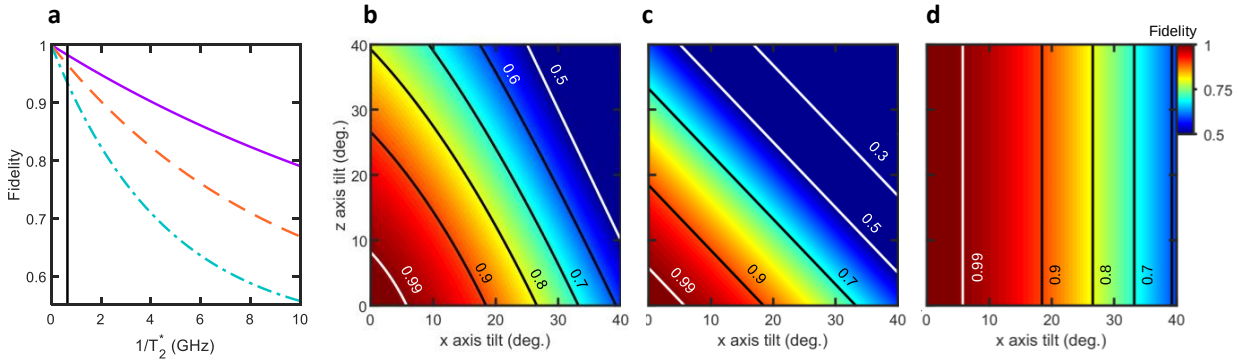

Figure 6.6: Theoretical effects of error sources on qubit fidelity. (A) Effect of dephasing in the absence of rotation errors for operations $Z_{\pi/2}$ (solid purple), Z_{π} (dashed orange), and $Z_{2\pi}$ (dot-dashed teal). (B,C,D) Effect of rotation errors in the absence of dephasing for $Z_{\pi/2}$ (B), Z_{π} (C), and $Z_{2\pi}$ (D).

largely determined by rotation errors. This is good news for the valley qubit, because experimental errors are much easier to address than fundamental limitations like charge noise. Proper pulse engineering can mitigate these errors, for example by correcting for voltage drift during operations or reducing transmission loss effects to increase pulse ramp time.

6.5 Conclusions, Chapters 5 and 6

Using simple square voltage pulses with a sufficiently slow rise time applied to plunger gates in a double quantum dot, we induced Landau-Zener transitions that first lead to Larmor precession between valleys and then map the precession phase back to double-dot charge occupation for read-out. This process provides a good experimental technique to quickly identify the proper regions for cotunneling initialization and charge-like read-out in the presence of valley splitting.

We then demonstrated pulse spectroscopy that enabled us to map out the four-level valley-orbit spectrum in the double quantum dot. With this process we determined the

valley-dependent inter-dot tunnel coupling as well as the valley splitting in both dots. Coherent spectroscopy performed in this way may prove useful to the semiconductor quantum computing research community, since valley splitting and valley-orbit coupling are important factors in electron dynamics regardless of qubit implementation. Additionally, our Ramsey spectroscopy can be done with no applied magnetic fields and at any electron configuration (constrained by the Landau-Zener transition probability).

From the results of spectroscopy, we identified the exact location of the anti-crossing between the lowest two levels and implemented valley qubit operations in a charge noise-insensitive regime. Despite a reduced dephasing time due to relaxation processes, we demonstrated full quantum control with sub-nanosecond operations along two independent rotation axes. Importantly, we showed that the valley qubit was limited by errors in rotation axis rather than decoherence, so improvements to the pulse design could significantly improve qubit performance.

CHAPTER 7

Intervalley relaxation

One main reason silicon is an appealing candidate for semiconductor quantum computing is the small intrinsic spin-orbit coupling and weak hyperfine interaction from nuclear spins. These two qualities imply that electron spins aren't greatly affected by charge or magnetic noise, both of which have a $1/f$ spectral density. When operated well away from any spin-orbital crossings and with recent advancements in isotopically purified ^{28}Si with no net magnetic moment, silicon spin qubits can have dephasing times on the order of tens of microseconds and relaxation times on the order of seconds [YTO18][YCH19].

Interestingly, there is no allowed decay process between pure spin states. There does exist a nonzero amount of spin-orbit coupling, but orbital spacing is typically around 1 meV, an order of magnitude larger than the spin splitting at a typical spin qubit operation point of $B_{\text{ext}} = 1$ T. However, spin relaxation is possible even in the total absence of spin-orbit coupling due, of course, to the valley states. As long as there is some degree of spin-valley coupling, spin relaxation mediated by pure valley relaxation will occur. In other words, at a fundamental level, spin coherence is determined by valley coherence when orbital coupling is negligible. It is therefore important to understand valley relaxation in order to fully characterize spin systems in silicon. Despite this, there has never been a direct measurement of intervalley relaxation in silicon quantum dots (to our knowledge).

In the context of valley qubits, and with our valley qubit in particular, knowing how long quantum information can be stored in the excited state before spontaneously decaying to the ground state is of great interest as well. For purely practical reasons related to the

valley qubit control pulse construction, we were unable to get a measurement of the valley relaxation time T_1 using coherent excitation in the double quantum dot. This chapter and the next will closely follow our recent work [PSE20], which as of writing has been submitted for publication, in which we directly measure valley relaxation and relate it to spin coherence.

7.1 Electron coherence in spin and valley states

As briefly discussed in Chapter 2, states of different spin and valley quantum numbers can hybridize at the point where the Zeeman splitting $g\mu_B B$ matches the valley splitting. This spin-valley coupling exposes electron spins to environmental noise that would otherwise only affect valley coherence. Considering the presence of valley-orbit coupling in realistic quantum dot systems with disorder, spin and valley hybridization can be treated identically to spin-orbit coupling.

7.1.1 Traditional spin-orbit coupling

Traditional spin-orbit interactions arise from the magnetic field proportional to $\mathbf{E} \times \mathbf{k}$ generated by an electron with crystal momentum $\mathbf{k}$ moving through an electric field $\mathbf{E}$ [HKP07]. It comes in two varieties related to asymmetries in electron confinement and the crystal lattice, referred to as the Rashba [Ras60] and Dresselhaus [Dre55] contributions. In semiconductor heterostructures, Rashba spin-orbit coupling arises from the asymmetric (roughly triangular) confinement potential generated by the heterostructure interface and an applied out-of-plane electric field. The Rashba Hamiltonian at the interface has the form

$$H_R = \alpha(\sigma_x k_y - \sigma_y k_x), \tag{7.1}$$

where α is a material-specific, experimentally determined constant. The Dresselhaus contribution is the result of inversion asymmetry in bulk crystals and can also arise from an

abrupt change in crystal structure at heterostructure interfaces. It has a form similar to the Rashba contribution:

$$H_D = \beta(\sigma_x k_x - \sigma_y k_y), \tag{7.2}$$

where as before the coefficient β depends on the heterostructure materials.

Due to the Pauli matrices σ_x and σ_y, both spin-orbit contributions appear as off-diagonal elements in the total Hamiltonian and lead to inter-spin coupling (allowing for relaxation) proportional to electric dipole matrix elements $r_{\uparrow\downarrow}$:

$$\langle\uparrow|H_R + H_D|\downarrow\rangle \propto (\beta - \alpha) r_{\uparrow\downarrow}, \qquad r_{\uparrow\downarrow} = \langle\uparrow|\mathbf{r}|\downarrow\rangle . \tag{7.3}$$

In bulk silicon, inversion symmetry requires zero Dresselhaus spin-orbit coupling and Rashba terms are generally small, $\alpha \approx 5 \times 10^{-14}$ eV $\cdot$ cm [HVZ17].

7.1.2 Valley-mediated spin-orbit coupling

In the space of spin-valley states spanned by $\{|v_+,\uparrow\rangle, |v_+,\downarrow\rangle, |v_-,\uparrow\rangle, |v_-,\downarrow\rangle\}$, the 4×4 valley spin-orbit Hamiltonian at the heterostructure interface becomes [VRY15]

$$H_{\text{SOC}} = \begin{pmatrix} s_R h_R + s_D h_D & V + \chi_R h_R + \chi_D h_D \\ V^* + \chi_R^* h_R^\dagger + \chi_D^* h_D^\dagger & s_R h_R + s_D h_D \end{pmatrix}. \tag{7.4}$$

In (7.4), h_R and h_D are the standard Rashba and Dresselhaus Hamiltonians without the coefficients α and β, and $V = |V|e^{i\phi_V} \approx E_{\text{VS}}$ is the valley-orbit coupling parameter with associated valley phase ϕ_V. The block-diagonal elements of this Hamiltonian correspond to intravalley transitions—that is, transitions involving a change in spin within the same valley—with new Rashba and Dresselhaus coefficients s_R, s_D roughly corresponding to α and β. The off-diagonal 2×2 blocks describe intervalley transitions, either within the same spin state with amplitude V or involving a spin flip according to the spin-orbit coefficients χ_R

and χ_D. With the approximation that the valley splitting is large compared to spin-flipping amplitudes, (7.4) can be transformed to be approximately diagonal with respect to the valley basis. Then, in the valley subspace $\{|v_-\rangle, |v_+\rangle\}$, the effective 2×2 spin-orbit Hamiltonian can be written in the familiar form [VRY15]

$$H_{\text{eff}} = \alpha_{v_\pm} h_R + \beta_{v_\pm} h_D. \tag{7.5}$$

Now, the coefficients depend on the intervalley and intravalley transition amplitudes as well as the valley phase ϕ_V and the valley splitting E_{VS}:

$$\alpha_{v_\pm} = s_R \mp |\chi_R| \cos(\phi_R - \phi_V), \tag{7.6}$$

$$\beta_{v_\pm} = s_D \mp |\chi_D| \cos(\phi_D - \phi_V). \tag{7.7}$$

The spin-valley coupling amplitude with $|\downarrow\rangle$ being the lower energy spin state is then given by

$$\Delta_a = 2|\langle \downarrow, v_+ | H_{\text{eff}} | \uparrow, v_- \rangle| = \frac{m_t E_{\text{VS}}}{\sqrt{2}\hbar} r(\langle\beta\rangle - \langle\alpha\rangle), \tag{7.8}$$

where $\langle\alpha\rangle = \sqrt{\alpha_{v_-}\alpha_{v_+}}$ and similarly for $\langle\beta\rangle$. This is an important result, as it shows that spin-valley coupling in silicon increases with the magnitude of the valley splitting.

7.1.3 Spin relaxation

In the presence of spin-valley coupling (Figure 7.1), spin relaxation can be found in terms of the bare valley relaxation rate Γ_v simply by analyzing the spin-valley Hamiltonian found in Chapter 2 (Equation 2.17). The following calculations were presented in the seminal work by Yang, *et al* [YRR13].

We start with the unperturbed spin-valley eigenstates $|\sigma, v\rangle$. With the admixture of

$|\downarrow, v_+\rangle$ and $|\uparrow, v_-\rangle$ near $E_Z = E_{\mathrm{VS}}$, the first and second excited states need to be renormalized:

$$|\tilde{2}\rangle = \sin\left(\frac{\gamma}{2}\right)|\uparrow, v_-\rangle - \cos\left(\frac{\gamma}{2}\right)|\downarrow, v_+\rangle\,, \tag{7.9}$$

$$|\tilde{3}\rangle = \cos\left(\frac{\gamma}{2}\right)|\uparrow, v_-\rangle + \sin\left(\frac{\gamma}{2}\right)|\downarrow, v_+\rangle\,, \tag{7.10}$$

where $\gamma = \arctan(\Delta_a/\delta)$ with $\delta = g\mu_B B_{\mathrm{ext}} - E_{\mathrm{VS}}$ being the distance from the spin-valley anti-crossing. Then the spin relaxation rate determined by Γ_v is screened by the degree of spin-valley coupling at a given δ:

$$\Gamma_{\uparrow\to\downarrow} = \frac{\sqrt{\delta^2 + \Delta_a^2} + |\delta|}{2\sqrt{\delta^2 + \Delta_a^2}}\Gamma_v. \tag{7.11}$$

Equation 7.11 has a maximum at $\Gamma_v/2$ when $\delta = 0$, or when the applied field matches the valley splitting. This is the infamous "hot spot" where the spin relaxation time T_1 sharply drops by several orders of magnitude [BZH19].

In the two-electron case and at fields $B_{\mathrm{ext}} < E_{\mathrm{VS}}/g\mu_B$, the ground state is the spin singlet S and the first excited state formed with the second electron in the upper valley is the spin triplet T_-. As the Zeeman energy is increased to E_{VS}, there is an anti-crossing between S and T_- since the singlet is unaffected by magnetic fields. The renormalized states that are composed of hybridized singlet and triplet states $|S, v_-, v_-\rangle$ and $|T_-, v_-, v_+\rangle$ are given by

$$|\tilde{1}\rangle_{2e} = \sin\left(\frac{\gamma}{2}\right)|S, v_-, v_-\rangle - \cos\left(\frac{\gamma}{2}\right)|T_-, v_-, v_+\rangle\,, \tag{7.12}$$

$$|\tilde{2}\rangle_{2e} = \cos\left(\frac{\gamma}{2}\right)|S, v_-, v_-\rangle + \sin\left(\frac{\gamma}{2}\right)|T_-, v_-, v_+\rangle\,, \tag{7.13}$$

with γ defined as before. The singlet-triplet relaxation is given by an expression that explicitly includes E_{VS} as well as dipole matrix elements $\mathbf{r}_{--} = \langle v_-|\mathbf{r}|v_-\rangle$ and $\mathbf{r}_{++} = \langle v_+|\mathbf{r}|v_+\rangle$:

$$\Gamma_{\tilde{2}\to\tilde{1}} = \sin^2\left(\frac{\gamma}{2}\right)\cos^2\left(\frac{\gamma}{2}\right)\Gamma_v[E_{\mathrm{VS}}, \mathbf{r}_{--} - \mathbf{r}_{++}]. \tag{7.14}$$

Despite $|\mathbf{r}|$ generally being small (1–3 nm), experimentally measured singlet-triplet relaxation is fast compared to single-electron spin relaxation far below the spin-valley anti-crossing. This is due in part to singlet-triplet splitting $\Delta E_{ST} \geq E_{\mathrm{VS}}$, and a larger splitting samples a higher frequency of environmental noise. Interestingly, singlet-triplet relaxation experiences a "cold spot" in the vicinity of the spin-valley anti-crossing, with origins that can be traced to the fact that the hybridization involves the ground state (as opposed to the single-spin case where hybridization involves the first two excited states).

7.1.4 Valley relaxation

The expression for intervalley relaxation (with no spin-flip transition) can be obtained for a given noise energy spectrum $S^E(\omega)$ with Fermi's golden rule. For single-electron inter-valley relaxation, the rate is given by [HH14]

$$\Gamma_v = \frac{4\pi e^2}{\hbar^2} \sum_{i=x,y,z} |\langle v_-|r_i|v_+\rangle|^2 S^E_{ii}(E_{\mathrm{VS}}/\hbar). \tag{7.15}$$

Sources of electronic noise that can contribute to valley relaxation are charge noise, Johnson noise, and phonons in the form of lattice deformation. Since charge noise has a $1/f$ spectrum, its effect at valley splittings in the several GHz range is quite small. Johnson noise arises from thermal effects in resistive circuit elements, with a spectrum of the form

$$S^E_J(\omega) = \frac{1}{(el_0)^2} \frac{2\xi\omega\hbar^2}{1+(\omega RC)^2} \coth\left(\frac{\hbar\omega}{2k_BT}\right), \tag{7.16}$$

where $\xi = e^2R/h$ is the circuit resistance R divided by the quantum resistance, C is any equivalent capacitance in series with R, and l_0 is the length scale of the resistive circuit element. Under the reasonable assumption that GHz-level Johnson noise from room-temperature elements is cut off due to the 1.9 MHz low-pass filters applied to all DC voltages, we can treat l_0 on the scale of tens of nanometers representing the distance from source to

drain of the charge sensor, or from source to dot. At low temperatures, $\coth(\hbar\omega/2k_BT) \to 1$. Additionally, the cutoff frequency $1/RC$ for the noise is fast compared to the valley splitting due to a small capacitive coupling C of the dot(s) to the source or drain, meaning that the ωRC term in (7.16) is very small. With these approximations, the Johnson noise spectrum becomes white noise proportional to ω.

Acoustic-mode phonon noise expectedly depends on lattice properties, specifically deformation potentials, and the direction of propagation. With silicon-specific dilation and uniaxial shear deformation potential constants Ξ_d and Ξ_u, the longitudinal deformation potential strength is $\Xi_l = \Xi_d + \Xi_u \cos^2\theta$ and the two transverse strengths are $\Xi_t = \Xi_u \cos\theta \sin\theta$, $\Xi_t' = 0$. Here θ is a polar angle in momentum space describing the phonon propagation vector [HH14]. Without derivation, the phonon spectrum along three crystal directions in the dipole approximation are given by

$$S_{xx}^E(\omega) = S_{yy}^E(\omega) = \sum_{j=x,y,z} \frac{\hbar\omega^5(2N_\omega+1)}{16\pi^2 e^2 \rho_c v_j^7} \int_0^{\pi/2} d\theta \Xi_{j\theta}^2 \sin^3\theta, \tag{7.17}$$

$$S_{zz}^E(\omega) = \sum_{j=x,y,z} \frac{\hbar\omega^5(2N_\omega+1)}{8\pi^2 e^2 \rho_c v_j^7} \int_0^{\pi/2} d\theta \Xi_{j\theta}^2 \sin\theta \cos^2\theta, \tag{7.18}$$

where phonon excitation number N_ω obeys the Bose-Einstein distribution. Again with low temperature, $N_\omega \to 0$ and the phonon spectra take on a ω^5 dependence.

Combining the effects of Johnson noise and phonon noise, intervalley relaxation will have a general form:

$$\Gamma_v = c_{\mathrm{J}} E_{\mathrm{VS}} + c_{\mathrm{ph}} E_{\mathrm{VS}}^5, \tag{7.19}$$

with coefficients c_{J} and c_{ph} implicitly depending on the intervalley dipole moment according to (7.15). The phonon contribution, which experimentally kicks in at around $E_{VS} \approx 100$ μeV, gives intervalley relaxation a strong dependence on valley splitting (Figure 7.1). This imposes a significant limitation on what valley dynamics can be experimentally probed. In [YRR13], the theoretically predicted relaxation rate for a valley splitting of $E_{\mathrm{VS}} = 0.33$ meV

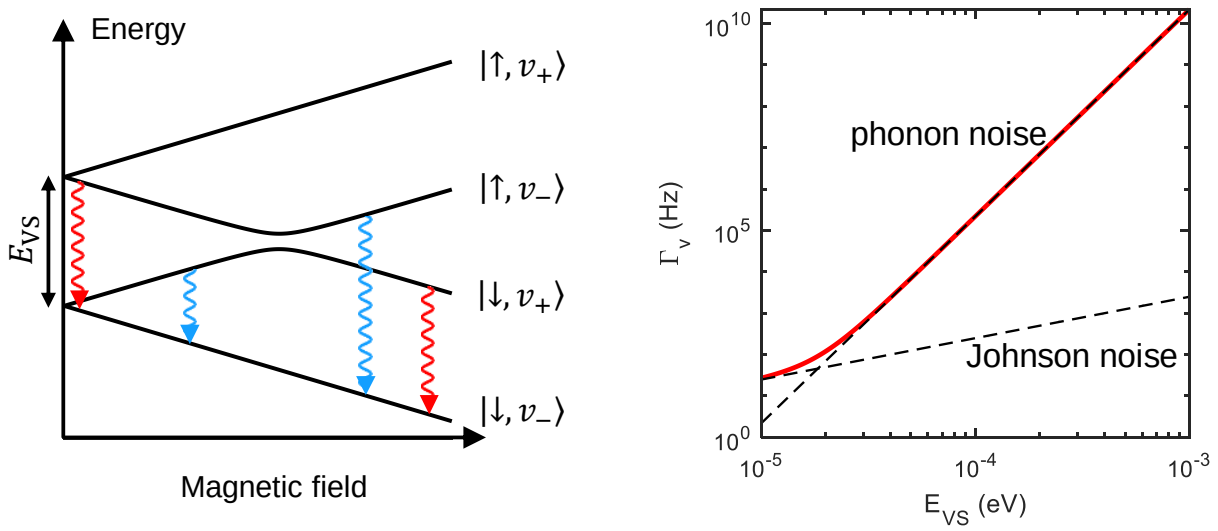

Figure 7.1: Left: spin-valley relaxation processes. Blue transitions: intravalley spin relaxation. Red transitions: intervalley relaxation. Right: theoretical intervalley relaxation rate as a function of valley splitting according to (7.19). Parameters are chosen to match ref. [YRR13] at large valley splitting.

was 10-100 MHz, too fast for state-of-the-art rf reflectometry [HCC17] and far beyond the capabilities of standard charge sensing.

7.1.5 Magnetic field dependence of relaxation

For an in-plane magnetic field B_{ext}, the valley splitting (and therefore Γ_v) should be invariant. This seems to suggest that spin relaxation as per (7.11) only contains dependence on B_{ext} within the spin-valley coupling terms involving δ and Δ_a. This is not quite the case, because an analysis of single-electron spin relaxation rates on either side of the anti-crossing $\Gamma_{\tilde{2}1}$ and $\Gamma_{\tilde{3}1}$ using the conventions of (7.15) are:

$$\Gamma_{\tilde{2}1} = \frac{4\pi e^2}{\hbar^2} \sum_{i=x,y,z} |\langle 1|r_i|\tilde{2}\rangle|^2 S_{ii}^E(\Delta E_{\tilde{2}1}/\hbar), \tag{7.20}$$

$$\Gamma_{\tilde{3}1} = \frac{4\pi e^2}{\hbar^2} \sum_{i=x,y,z} |\langle 1|r_i|\tilde{3}\rangle|^2 S_{ii}^E(\Delta E_{\tilde{3}1}/\hbar). \tag{7.21}$$

Due to spin-valley coupling, the dipole matrix elements contain inter-valley terms $\langle v_-|\mathbf{r}|v_+\rangle$ (they should be zero in the absence of coupling). However, the noise spectra are being sampled at the field-dependent renormalized spin state splitting $\Delta E_{\tilde{2}1}, \Delta E_{\tilde{3}1}$. Therefore, despite the field invariance of pure valley relaxation, spin-valley mixing leads to a field dependence arising from Zeeman splitting [PBE18]:

$$\Gamma_{\uparrow\to\downarrow} = F_{SV}(E_Z)(c_{\mathrm{J}}E_Z + c_{\mathrm{ph}}E_Z^5), \qquad F_{SV}(E_Z) = 1 - \left[1 + \frac{\Delta_a^2}{(E_{\mathrm{VS}} - E_Z)^2}\right]^{-\frac{1}{2}}. \tag{7.22}$$

The spin-valley screening function $F_{SV}(E_Z)$ is composed of the leading terms in 7.11. Measuring spin relaxation as a function of field can therefore reveal the electrical noise spectrum beyond the noise at the valley splitting.

7.2 Single-dot valley-to-charge conversion

From (7.19), the hope for real-time observation of intervalley relaxation depends upon a small enough valley splitting. Assuming that such a condition is met in our device, which may be the case based on our Ramsey spectroscopy in Chapter 5, we first need a method for single-dot valley read-out in a regime with negligible inter-dot valley coupling. Our coherent spectroscopy relied on strong inter-dot coupling, so it can't be used in this case.

7.2.1 Energy-selective tunneling pulse sequence

Fortunately, there already exists a well-established method for distinguishing any two arbitrary adjacent levels in a single quantum dot based on energy-selective tunneling [EHW04b]. The technique is widely used to measure spin state occupation and provides the most common method of spin relaxation measurement [XHJ10]. It utilizes a slow pulse sequence on the plunger gate of the quantum dot of interest, beginning with an initialization where the quantum dot is empty (Figure 7.2). The first stage involves loading a single electron into

the dot by pulsing the gate voltage across the $N = 0 \rightarrow 1$ charge transition line. The probabilities of the electron occupying the excited state and the ground state are roughly even. Next, the gate voltage is moved to the transition line where the two dot levels of interest straddle the reservoir Fermi level. At this point it is energetically favorable for the electron to tunnel out of the dot only if it's occupying the excited state. Then another electron from the reservoir can tunnel into the ground state. The charge sensor transport current, which only differentiates between the dot being occupied and unoccupied, will experience an abrupt increase when the electron leaves the dot and an equally abrupt return to the baseline value when an electron tunnels back in. If the loaded electron is already in the ground state during this stage, then it will never tunnel out of the dot and the current is unchanged. Essentially, during the second ("measurement") phase of the pulse, there will be a brief change in charge sensor current only if the electron was in the excited state prior to measurement. In the final stage, the gate voltage is moved back to the $N = 0$ region to empty the dot. When the level splitting is sufficiently larger than $k_B T$ (that is, no random thermal population of the excited state during measurement is possible), then this measurement can be accomplished with single-shot read-out [MPZ10]. When thermally excited population is possible, then the measurement signal must be averaged over many instances of the pulse. The ensemble average over many (noisy) single-shot measurements will then yield a smooth curve with a "tunneling peak" near the beginning of the measurement pulse phase, with an amplitude proportional to the fraction of instances in which the electron was in the excited state.

7.2.2 Experimental details

We use the same double quantum device as in Chapters 5 and 6. From our valley qubit study, we know that the valley splitting in both dots is on the order of tens of µeV and so we would expect a slow intervalley relaxation time. Since we would also like to examine spin dynamics, we transferred the device to the JDR-500 refrigerator from the Triton-200. The base temperature during measurements was about 60 mK.

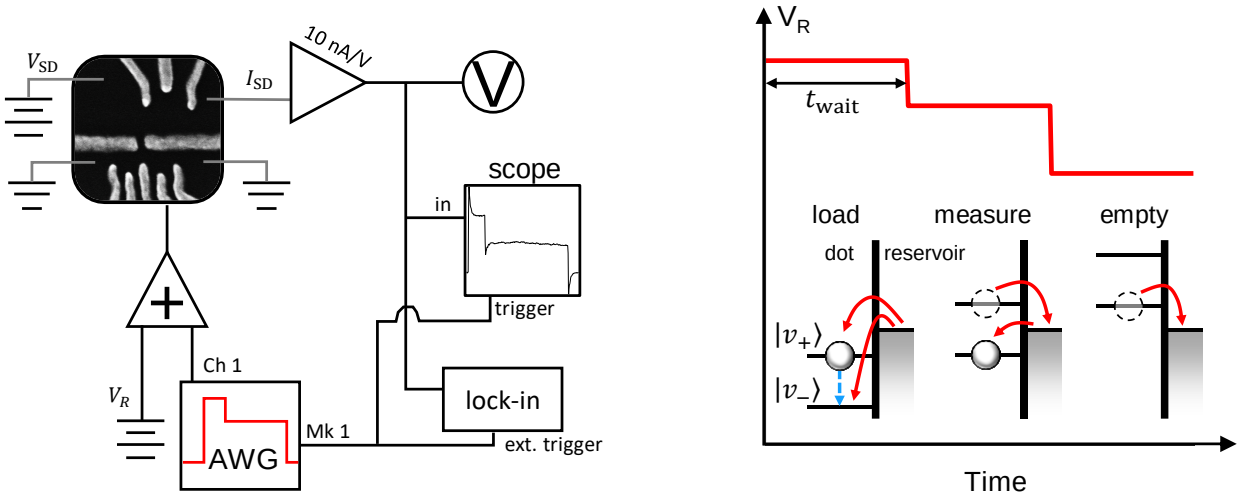

Figure 7.2: Pulse sequence and circuit diagram for relaxation measurements. Left: the pulse is added to V_R and applied to gate R. The charge sensing current is read with a current amplifier and sent to a DMM, an oscilloscope and a lock-in amplifier for various average and real-time measurements. Right: the energy-selective tunneling read-out sequence.

The device was tuned to the single-electron regime and inter-dot tunneling was heavily suppressed by a negative bias on gate M. Tunneling is then restricted to occur only between a single quantum dot and its adjacent electron reservoir, kept grounded.

The pulse sequence was generated with the Tektronics AWG 520 with a 30 dB attenuator on the channel 1 output. It starts with a high-level voltage of around 0.1 V before attenuation to load the electron for time t_{wait}, then a period of 10-20 ms at 0 V for measurement, and then a period of 4-7 ms at -0.15 V for emptying the dot. The sequence is combined with the standard DC plunger gate voltage using a summing amplifier. The charge sensor response was fed through a high-bandwidth current amplifier (DLPCA-200 set at 10 nA/V gain) and then to a variable low-pass filter with a cutoff frequency of 7 GHz and post-filtering gain of 10 dB. The filtered signal was sent to an oscilloscope (Agilent 54855A) and triggered on the AWG 520 channel 1 marker, which was constructed to pulse at the start of the measurement phase. The current amplifier output was also sent to a standard DMM so we could monitor the DC charge sensing transport current, and to a lock-in amplifier in voltage mode so we

could perform differential measurements with the AWG in function generation mode (Figure 7.2). The tunnel barriers were tuned with V_{BL} and V_{BR} so that the tunnel rate from each dot to the reservoir was around 2 kHz.

Proper grounding of all instruments was essential to reduce the electron temperature and improve the signal-to-noise ratio. Initially this involved triggering the oscilloscope on the line frequency of 60 Hz and monitoring the average background noise amplitude far from the charge transition. Instrument chassis were grounded to the instrument rack, and thick stainless steel wire mesh ribbons were used to directly connect the BNC shields of signal outputs to a common ground point. Instrument signals were added to the ground network one at a time to check that the total noise didn't increase. Eventually we were able to reduce the electron temperature to about 150 mK from linewidth measurements, which allowed us to observe random telegraph signal in realtime with a signal-to-noise ratio of about 3:1, and potentially would have allowed us to perform single-shot spin readout at fields above 1 T. However, this still wasn't enough of an improvement to do single-shot measurements on valley states with small splitting. We therefore average the signal over 2000 oscilloscope traces for right dot measurements and 4000 traces for the left dot since the charge sensor is farther away. We also tried switching from a Stahl BS-16 power supply with BNC output shields grounded to the chassis with an identical model but with the shields floated on the supply side. This led to a noticeable improvement in the low-frequency background, but caused a substantial increase in higher frequency (> 7 kHz) noise that artificially broadened the charging lines.

7.3 Valley T_1

By performing the energy-selective tunneling read-out pulse sequence and extending the time t_{wait} spent in the "load" stage, an excited state electron has a higher probability of relaxing to the ground state. This in turn reduces the probability of co-tunneling during

the measurement stage, which causes the tunneling peak amplitude to decrease. As long as the tunneling rates in the measurement stage are faster than the relaxation rate, then the tunneling peak amplitude should follow an exponential decay as e^{-t_{wait}/T_1} with $T_1 = 1/\Gamma_v$ in the case of valley relaxation [XHJ10].

7.3.1 Converting charge sensing current to occupation probability

The raw transport current seen on the oscilloscope contains the capacitive effect of a single dot electron modifying the charge sensor conductance as well as stray capacitance from the plunger gate that is being pulsed on (Figure 7.3a). These contributions are roughly equal with proper tuning of the charge sensor. To extract the probability of the dot being occupied by the electron during the entire pulse sequence, we need to subtract the stray capacitance contribution. At the start of all measurements, we first take an ensemble-averaged trace with the same pulse scheme sufficiently far away from the charge transition so that electron tunneling is energetically unlikely. This trace only contains the stray capacitance contribution (Figure 7.3b). Then we perform the measurement in the vicinity of the charge transition and subtract the baseline current from it (Figure 7.3c). We know that the probability of the dot being *un*occupied will be exactly 0 by the end of the "load" stage provided the load time is long enough compared to the 2 kHz tunneling rate, and we also know that it will be 1 by the end of the "empty" stage. These provide the calibration, as we take the background-subtracted data and re-scale it to match the expected occupation probabilities.

7.3.2 Observation of the valley tunneling peak

Figure 7.4a shows the results of a valley occupation measurement in the right dot with $t_{\text{wait}} = 4$ ms. At zero field, the spin states are degenerate so the visible tunneling peak in the measurement stage can't be spin-related. It is conceivable that the peak is related to orbital levels, but we establish later that the probed level splitting is far too small for

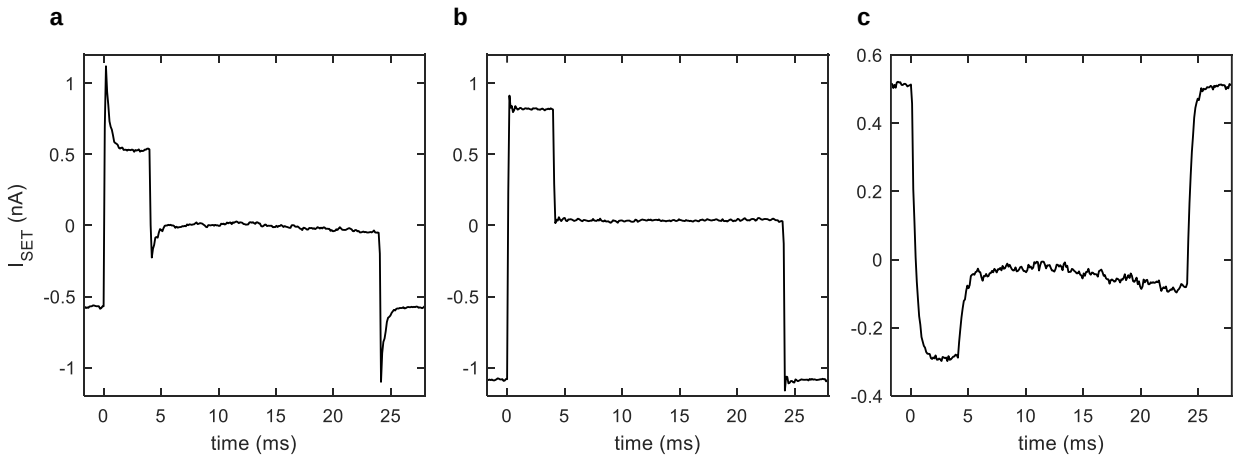

Figure 7.3: Calibrating the right dot occupation probability. (A) Raw SET transport current. The "load" stage occurs from 0 to 4 ms, the "measure" stage ends at 24 ms, and the "empty" stage ends at 28 ms. (B) Results of the same pulse with no electron tunneling events. This represents the pure stray capacitance effects from the pulsed gate. (C) The result of subtracting (B) from (A), representing the charge sensor response to a single electron tunneling in and out of the dot.

orbital spacing. We can therefore conclude, and later confirm, that the tunneling peak arises from the valley states in the right dot. The unoccupation probability tends toward a constant, nonzero value at large measurement times, which is caused by the thermally excited random telegraph signal of an electron hopping from the dot ground state into the reservoir. Accordingly we define the tunneling peak amplitude as the maximum probability in the measurement stage minus the probability at the end of the measurement stage.

7.3.3 Tunneling peak vs. load time

We measure the tunneling peak amplitude as a function of t_{wait} and observe that the trend is remarkably consistent with the expected exponential e^{-t_{wait}/T_1}. This leads to a valley T_1 of 12.0 ± 0.3 ms, found by fitting the data in semi-log with standard linear regression (Figure 7.4b). To our knowledge, this is the first direct measurement of pure valley relaxation. This value is somewhat surprising, since the only indirect experimental estimate in Si/SiGe

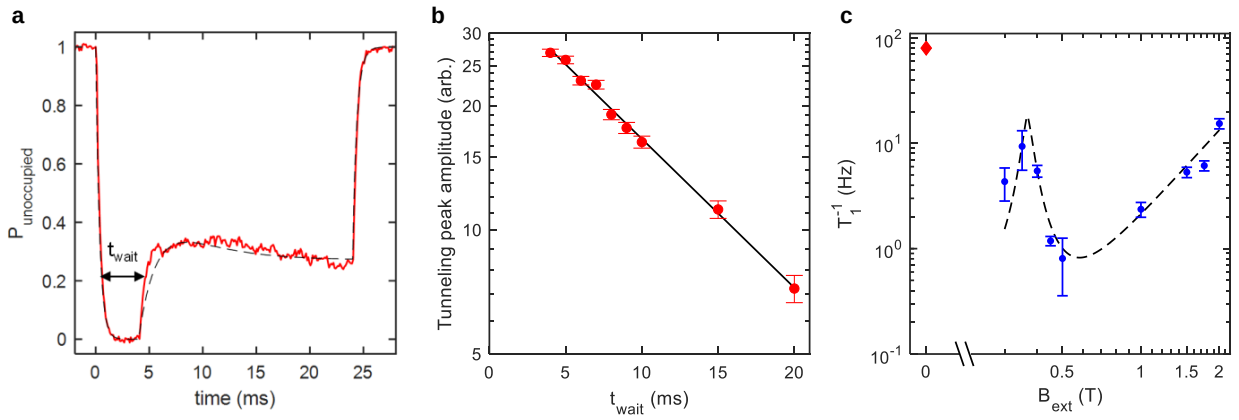

Figure 7.4: Measurement of intervalley relaxation. (A) Valley tunneling peak at zero field with $t_{\text{wait}} = 4$ ms. Dotted line is the solution to a rate equation model (Chapter 8). (B) valley tunneling peak amplitude as a function of t_{wait}, displaying a decaying exponential trend. The decay time constant is $T_1 = 12 \pm 0.3$ ms. (C) Field dependence of spin relaxation. The spin-valley hot spot occurs at 0.37 T. Red diamond at 80 Hz is the valley relaxation rate at zero field for comparison.

quantum dots placed the valley T_1 with comparable valley splitting to ours in the microsecond range [KSW14]. Our measurement is three orders of magnitude longer. However, it should be noted that the valley T_1 estimate in [KSW14] comes from the Rabi oscillation T_2, under the speculation that T_2 is limited by valley relaxation. Further, the valley splitting in that work is only inferred from Rabi frequency shifts and not directly measured. It is also important to remember that relaxation depends on the valley dipole term, which can be quite different between systems and even within the same device.

7.4 Spin relaxation

Before claiming that our direct intervalley relaxation measurement is valid, it is important to establish a second independent measurement and check for consistency. This can be achieved through spin measurements by noting that single-electron spin relaxation reduces to $\Gamma_{\text{spin}} = \Gamma_v/2$ according to (7.11) when $\delta = 0$. Measuring spin relaxation as a function

of field near the hot spot should therefore give us a reasonable estimate of the valley T_1. Even better, the position of the hot spot will give us an estimate of the valley splitting (which may well have changed due to thermal cycling from spectroscopy measurements in a different refrigerator) and the overall trend of spin relaxation versus field will allow us to make conclusions about the dominant noise sources as per Section 7.1.5.

7.4.1 Spin read-out

Reading out the spin state works in exactly the same way as the energy-selective valley-to-charge conversion. The same pulse sequence is applied in the presence of $B_{\text{ext}} > 0$ to load, measure, and empty an electron. Strictly speaking, there are now four available spin-valley states that can be probed with the read-out process. However, as long as the voltage level during the "measure" stage is between states of opposite spin and the "load" stage level is above both spin states, the presence of valleys will not affect the measurement. This will not be true at small fields where the valley splitting is larger than the Zeeman splitting, but at that point read-out becomes difficult in any case.

In contrast to the valley tunneling peak, the spin tunneling peak is much easier to identify due to a sharper profile. Since the tunneling peak is determined by the tunnel rate out of the excited state and the tunnel rate into the ground state from the reservoir, we can conclude that tunneling associated with these spin states is faster than valley state tunneling. This is not generally the case, and in fact has nothing to do with the nature of the involved states. As we will show in the next chapter, the factor determining tunneling peak sharpness is the level separation. As the magnetic field is decreased, the spin tunneling peak becomes broader.

7.4.2 Spin relaxation hot spot

Spin relaxation is obtained by varying t_{wait} as before to allow an excited spin to decay. Since the spin tunneling peak signal-to-noise ratio is much better than that of the valley tunneling peak, the precision of amplitude measurements was improved. Signal quality notwithstanding, an unexpected complication with read-out fidelity caused spin T_1 measurements to have worse precision than the valley T_1 measurement. Our SET charge sensor experienced stochastic drift on the timescale of an hour; for probing valley relaxation on the order of 10 ms, and considering 2000 trace averages, the valley relaxation measurement would take about 3 hours total. With some luck, the SET wouldn't drift during that time and the valley T_1 precision would be limited by the tunneling peak precision. However, we found that the maximum spin relaxation time was around one second, requiring much longer measurement times to capture. In the worst case, we were only able to take four amplitude-versus-t_{wait} data points to extract a spin T_1 before the SET drifted.

Despite the problems with long spin relaxation times, we were able to plot the relaxation rate $1/T_1$ as a function of external field (Figure 7.4c). We can easily identify the hot spot where the spin and valley states mix, occurring at $B_{\text{ext}} = 0.37 \pm 0.03$ T. This corresponds to a right dot valley splitting of 43 ± 3 μeV, a 30% change from our Ramsey spectroscopy measurement in the Triton-200 refrigerator. The change likely has less to do with thermal cycling and more to do with the quantum dot position, which has significantly shifted to the right from a decrease in V_M of about 0.8 V. Lateral motion of the quantum dot causes the electron wavefunction to sample a different portion of the interface disorder landscape, leading to a different valley splitting.

Fitting the spin relaxation data to the form (7.22), we can get an estimate for the peak hot spot relaxation rate, $1/T_1(\delta = 0) = 20$ Hz. From (7.11) this leads to an indirect result for the valley T_1 of 25 ms, about a factor of two slower than the direct measurement. While the two values disagree, they both suggest a surprisingly long intervalley relaxation time. It is

worth pointing out that the inferred spin relaxation rate at the hot spot is fairly imprecise, given the error bars on the valley splitting and on individual data points. Additionally, we rely on a fit to the data with noise amplitude coefficients c_{J} and c_{ph} treated as free parameters, leading to further errors in hot spot relaxation. With this in mind, a factor of two discrepancy between the direct and indirect valley T_1 measurements is not unexpected. This result also leads to a relatively simple way of estimating the valley T_1, provided the noise model gives a sufficiently good fit to the data. The hot spot estimate technique could be especially useful in situations where the valley splitting is too small to probe, or where the valley T_1 is too short.

7.5 Spin and valley read-out at nonzero field

It is possible to probe spin and valley dynamics within the same measurement at $B_{\mathrm{ext}} > E_{\mathrm{VS}}$. This is achieved by applying the same waveform to the plunger gate while modifying the dot energy with a DC voltage. We already do this to obtain the background trace in calibrating occupation probability, but this process also allows us to move between a spin-discriminating tunneling peak measurement and a valley-discriminating measurement (Figure 7.5a,b). Provided the "load" stage pulse height $\Delta\mu_{\mathrm{load}}$ satisfies $E_{\mathrm{VS}} < \Delta\mu_{\mathrm{load}} < \mu_{\uparrow,v_-} - \mu_{\downarrow,v_+}$, then the experiment will measure spin occupation when the DC plunger gate level moves states $|\uparrow, v_-\rangle$ and $|\downarrow, v_+\rangle$ to straddle the reservoir Fermi level. Similarly, it will measure valley occupation when the reservoir level is between $|\downarrow, v_-\rangle$ and $|\downarrow, v_+\rangle$. In principle the valley states can be probed at a measurement level between $|\uparrow, v_-\rangle$ and $|\uparrow, v_+\rangle$ as well, but this proves difficult because the tunneling rate from the reservoir to the true ground state grows exponentially with the distance from the tunnel barrier and the valley tunneling peak becomes incredibly weak.

Keeping the read-out constraints in mind, it is possible to measure valley relaxation as a function of field (Figure 7.5c). We find that the valley T_1 is independent of B_{ext} to within

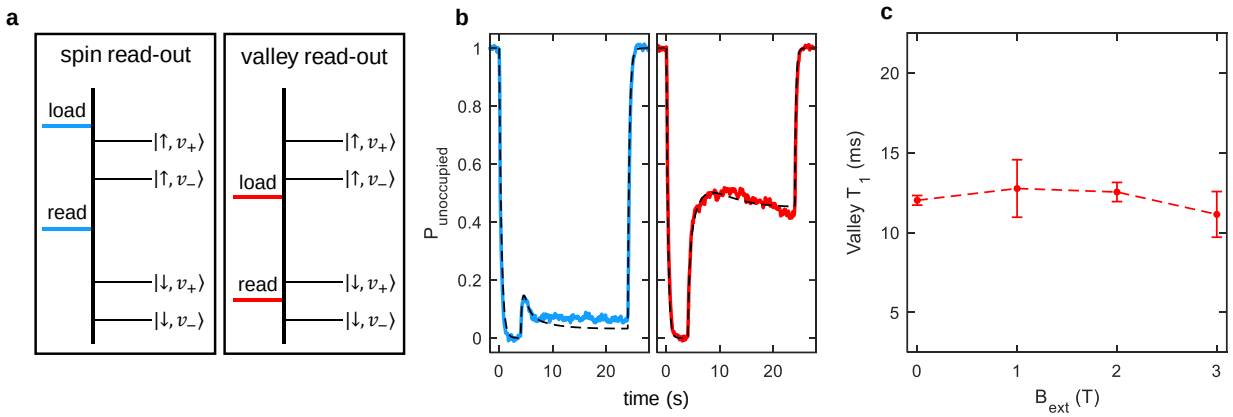

Figure 7.5: Reading out spin and valley occupation at nonzero field. (A) schematic of the load and read levels (with fixed separation) in relation to the spin-valley quantum dot states. Spin-discriminating read-out occurs when the read level is between states of opposite spin, and valley-discriminating read-out occurs when the read level is between the lowest two valley states and the load level is below the excited spin states. (B) A spin tunneling peak (left) and a valley tunneling peak (right) measured at $B_{\text{ext}} = 2$ T. Dotted lines are fits to rate equation model (see Chapter 8). (C) Valley relaxation as a function of field. There is no field dependence, confirming the behavior of valley splitting and allowing us to conclude that second-order tunneling is not occurring.

error bars up to $B_{\text{ext}} = 3$ T. This result may seem trivial, but it does allow us to confirm several things. First, we can now rule out orbital splitting as the origin of the zero-field tunneling peak and subsequent relaxation measurement. Second, this indicates that the valley splitting is field-invariant as expected. Third, we can conclude that valley relaxation at an electron temperature of 150 mK is determined by first-order processes (if second-order processes with additional states were involved, then valley relaxation should have a field dependence and we couldn't claim direct intervalley decay).

7.5.1 Valley decoherence mechanisms

From the fit to the data in Figure 7.4c, we can get an idea of the regimes in which the two primary noise sources (Johnson noise and lattice deformation phonons) play the biggest role

in decoherence. We find that below about $B_{\text{ext}} = 0.5$ T, spin relaxation is dominated by Johnson noise contributions and phonon noise doesn't really kick in until $B_{\text{ext}} \geq 1$ T. This information can be used to draw conclusions about valley relaxation as well. With a splitting of $E_{\text{VS}}/g\mu_B = 0.37$ T, the valley states fall squarely in the frequency range where Johnson noise plays the biggest role. We can therefore say with some confidence that intervalley relaxation is caused mostly by Johnson noise in this device. Of course, this is not generally the case; for a quantum dot with larger valley splitting, phonon noise will be the biggest contribution.

CHAPTER 8

Modeling spin and valley tunneling peaks

In performing the spin and valley tunneling peak measurements in the previous chapter, there were some features of the data that didn't match our understanding of the relevant electron dynamics. First, the valley tunneling peak was much broader than the spin tunneling peak, meaning that the tunneling processes involved in the valley measurement were slower. By carefully modeling the single-dot system and incorporating effects related to thermal excitations and details of the tunnel barrier, we were able to address these features. Second, we found that the window in quantum dot electrochemical potential for resolving the valley tunneling peak was wider than we would have expected purely from energy considerations. Finally, the tunneling rates associated with the ground valley state were found to be slower than the tunneling rates associated with the excited valley. These last two observations were explained with valley-orbit coupling that can lead to valley-dependent electron tunneling. The observations and theoretical framework discussed in this chapter provide new insights into valley physics in disordered quantum dot systems.

8.1 Classical rate equations

Time evolution of electron state occupation in the presence of relaxation can be described by the Lindblad equation (5.7) as we've already seen. However, the tunneling events that occur during the energy-selective tunneling read-out pulse are purely incoherent processes and so expressing the time dependence with quantum formalism is overkill. Instead, we can use a system of intuitive classical rate equations to replicate our measurements without resorting

to calculating full density matrices [BDR02]. The probabilities of finding the electron in all accessible discrete states can be contained in a vector $\mathbf{p}$ of length $N+1$, where N is the number of confined dot levels (The additional state is the probability of the dot being unoccupied, relevant when the electron tunnels out of the dot). Then the equations of motion are given by the same expression used to describe current transport:

$$\frac{d\mathbf{p}}{dt} = \mathbf{\Gamma} \cdot \mathbf{p}, \qquad \Gamma_{\alpha\beta} = \begin{cases} \Gamma_{\beta\to\alpha}, & \alpha \neq \beta \\ -\sum_{k\neq\alpha} \Gamma_{\alpha\to k}, & \text{otherwise.} \end{cases} \tag{8.1}$$

The goal now is to find the tunneling rates to and from each available state from every other state, during each stage of the waveform.

8.1.1 Two dot states, zero temperature

In the simplest case, the transition matrix $\mathbf{\Gamma}$ in the basis $\{p_{\text{dot},2}, p_{\text{dot},1}, p_{\text{empty}}\}$ is written as

$$\mathbf{\Gamma} = \begin{pmatrix} -\Gamma_{2\to0}\Theta(\mu_0-\mu_2) - \Gamma_{2\to1} & 0 & \Gamma_{0\to2}\Theta(\mu_2-\mu_0) \\ \Gamma_{2\to1} & -\Gamma_{1\to0}\Theta(\mu_0-\mu_1) & \Gamma_{0\to1}\Theta(\mu_1-\mu_0) \\ \Gamma_{2\to0}\Theta(\mu_0-\mu_2) & \Gamma_{1\to0}\Theta(\mu_0-\mu_1) & -\Gamma_{0\to2}\Theta(\mu_2-\mu_0) - \Gamma_{0\to1}\Theta(\mu_1-\mu_0) \end{pmatrix}, \tag{8.2}$$

where μ_i is the chemical potential in state i ($i=0$ is the reservoir Fermi level) and $\Theta(\mu)$ is the Heaviside step function. It is simple to confirm that this transition matrix is probability-conserving, as the sum of rates in a given column always equals zero. The transition matrix for each stage of the measurement waveform can be obtained by setting $\mu_0 > \mu_2$ for the "load" stage, $\mu_2 > \mu_0 > \mu_1$ for the "measure" stage, and $\mu_0 < \mu_1$ for the "empty" stage. In doing so, we recover the three separate transition matrices shown in [XHJ10]. In the zero-temperature limit, a tunneling peak is only visible when the reservoir Fermi level is between dot levels and the starting probability $p_{\text{dot},2}$ is nonzero. The amplitude of the tunneling peak also depends on the relative tunneling rates out of the excited state and into the ground state.

In a situation where the excited state tunneling rates are much slower than the ground state tunneling rates, the peak will disappear.

8.1.2 Thermal effects

A nonzero electron temperature drives stochastic jumps between states that would otherwise be energetically forbidden. On average, thermal effects lead to a distribution of tunneling probabilities, with a transition from state A to state B becoming more likely as μ_A is increased to approach μ_B. At temperature T, the step functions in (8.2) become Fermi-Dirac distributions:

$$\Gamma_{\alpha\to\beta}(\mu_\alpha, \mu_\beta, T) = \frac{\Gamma^0_{\alpha\to\beta}}{1 + \exp[(\mu_\beta - \mu_\alpha)/k_B T]}. \tag{8.3}$$

The tunneling peak amplitude decreases quickly as temperature is increased or the dot energy splitting is decreased, which from a practical standpoint makes the measurement difficult when the electron temperature is above 200 mK. Additionally, at long measurement times the occupation probability will saturate at some value less than one. This is in contrast to the zero-temperature case, where the dot ground state will always end up occupied by the end of the measurement phase.

8.1.3 Energy-dependent tunneling

Under normal circumstances, incorporating the temperature dependence of tunneling rates is sufficient to reproduce tunneling peaks during the measurement phase of the waveform. However, the model fails when attempting to incorporate the dynamics during the "load" and "empty" phases in a self-consistent way. For instance, a solution that accurately fits the tunneling peak will underestimate the empty phase tunneling rates and overestimate the load phase tunneling rates. More subtly, a model that only includes temperature dependence does not reproduce the effects of dot level splitting on tunneling rates.

Under the assumption of purely elastic tunneling, we can treat the dot-reservoir system

in one dimension as two discrete bound states with an infinite barrier on one side and some arbitrary finite barrier on the other side. Any undergraduate-level quantum mechanics textbook [Gri05] will include an expression for the wavefunction corresponding to bound state j within the barrier given by some potential $V(x)$ in the WKB approximation (not necessarily normalized):

$$\psi_j(x) = \frac{1}{[2m(V-E_j)]^{\frac{1}{4}}} e^{\pm\frac{1}{\hbar}\int dx\sqrt{2m[V(x)-E_j]}}. \tag{8.4}$$

This wavefunction can be linearized in E_j and $V(x)$ to give an expression for the tunneling rate [MAR07]:

$$\Gamma(E_j) = \Gamma_{0,j} e^{-\beta(\delta V - \delta E_j)}. \tag{8.5}$$

According to (8.5), the tunneling rate increases as the dot energy is increased relative to the barrier. This gels with intuition when considering the case where the dot energy is above the reservoir Fermi energy: the electron will certainly tunnel out of the dot faster if $\mu_{\text{dot}} \gg \mu_F$. However, energy-dependent tunneling has the same tendency in *both* tunneling directions. This means that the tunneling rate into the dot will actually decrease as the reservoir level increases. This is again due to the fact that (8.5) only depends on the relation of the occupied state to the barrier, not to the final state.

The exponential coefficient β and the constant $\Gamma_{0,j}$ contain the details of the tunneling barrier and must be experimentally determined. Although we treat $\Gamma_{0,j}$ as a free parameter for each discrete state, it is best to directly measure β from real-time tunneling. By applying the read-out waveform to the right dot while varying the DC plunger gate voltage, we find very consistent exponential dependence of the electron tunneling rate into the dot during the "load" stage and out of the dot during the "empty" stage (Figure 8.1). The data is fit to the form $\Gamma \sim e^{-\lambda V_{\text{R}}}$, giving a coefficient $\lambda = 395\ \text{V}^{-1}$. The right dot plunger gate lever arm was previously found to be $\alpha \approx 0.15$ eV/V from magnetospectroscopy, which led to the determination of $\beta = \lambda/\alpha = 6 \times 10^3\ \text{eV}^{-1}$. With the effects of elastic tunneling included,

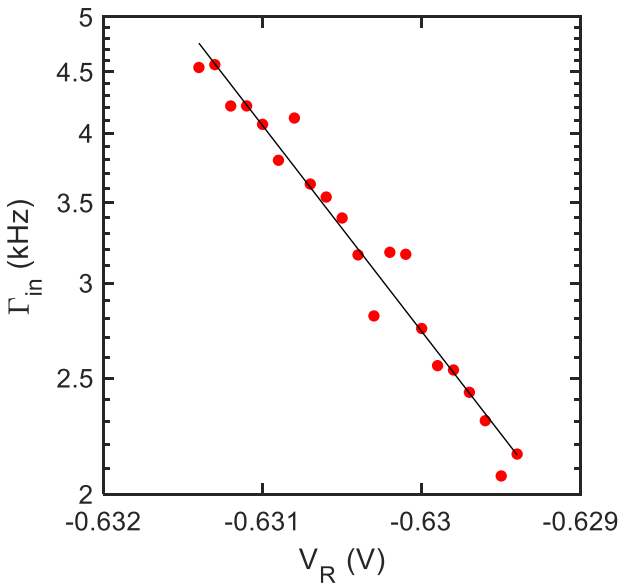

Figure 8.1: Energy-dependent tunneling in the right quantum dot. Each data point is obtained from an ensemble-averaged real-time current trace, which is fit to an exponential function to extract tunneling rates. The trend with dot plunger gate voltage is fit to $e^{-\lambda V_R}$.

the final expressions for tunneling rates into and out of dot state j are given by

$$\Gamma_j^{\text{in}}(\mu_0, T) = \Gamma_{j,0}^{\text{in}} n(\mu_j - \mu_0, T) e^{-\beta(\mu_0 - \mu_j)}, \tag{8.6}$$

$$\Gamma_j^{\text{out}}(\mu_0, T) = \Gamma_{j,0}^{\text{out}} n(\mu_0 - \mu_j, T) e^{-\beta(\mu_0 - \mu_j)}. \tag{8.7}$$

In (8.6) and (8.7), $n(E, T)$ is the Fermi-Dirac distribution. The first argument in the rate function is the reservoir Fermi level instead of the individual dot level because the measurement waveform only changes the dot levels uniformly with respect to the Fermi level. In other words, increasing the Fermi level is equivalent to decreasing all dot levels by the same amount.

8.2 Valley states at zero field

With no applied field, the available quantum dot levels are just the valley states and we can use a 3×3 transition matrix to describe possible tunneling paths. Incorporating thermal effects and energy-dependent tunneling, the transition matrix in the basis $\{p_{v_+}, p_{v_-}, p_0\}$ becomes

$$\mathbf{\Gamma} = \begin{pmatrix} -\Gamma^{\text{out}}_{v_+}(\mu_0, T) - \Gamma_v & 0 & \Gamma^{\text{in}}_{v_+}(\mu_0, T) \\ \Gamma_v & -\Gamma^{\text{out}}_{v_-}(\mu_0, T) & \Gamma^{\text{in}}_{v_-}(\mu_0, T) \\ \Gamma^{\text{out}}_{v_+}(\mu_0, T) & \Gamma^{\text{out}}_{v_-}(\mu_0, T) & -\Gamma^{\text{in}}_{v_+}(\mu_0, T) - \Gamma^{\text{in}}_{v_-}(\mu_0, T) \end{pmatrix}. \tag{8.8}$$

Given our measurements of intervalley relaxation $\Gamma_v = 83$ Hz and valley splitting $E_{\text{VS}} = 43$ μeV, we set up the model so that the two dot levels are fixed at $\mu_{v_\pm} = \pm E_{\text{VS}}/2$ (Figure 8.2). Then we find from a best fit to the data the nominal tunneling rates $\Gamma^{\text{in}}_{v_+,0} = 11.4$ kHz, $\Gamma^{\text{in}}_{v_-,0} = 2.3$ kHz, $\Gamma^{\text{out}}_{v_+,0} = 209$ Hz, and $\Gamma^{\text{out}}_{v_-,0} = 67$ Hz (Figure 8.2). These values don't mean much on their own, and it is more useful to quote the actual tunneling rates in the measurement phase: $\Gamma^{\text{in}}_{v_+} = 97$ Hz, $\Gamma^{\text{in}}_{v_-} = 177$ Hz, $\Gamma^{\text{out}}_{v_+} = 361$ Hz, and $\Gamma^{\text{out}}_{v_-} = 85$ Hz. Assuming an electron is fully loaded into the dot prior to measurement, the occupation probability during the measurement phase is therefore initially dominated by $\Gamma^{\text{out}}_{v_+}$ and then later determined by the slower $\Gamma^{\text{in}}_{v_-}$. The dotted fit line in Figure 7.4a is taken with a Fermi level of $\mu_0 = -70$ μeV, which is actually below both valley states. Tunneling into the dot is made possible through thermal excitations, and the electron is likely to be found in the ground valley state as $t \to \infty$ because $\Gamma^{\text{in}}_{v_-} + \Gamma_v > \Gamma^{\text{out}}_{v_-}$. This leads to an interesting extended read-out window that allows us to resolve the valley tunneling peak even when μ_0 does not fall between the valley states. A possible physical origin for the tunnel rate discrepancy that allows this will be discussed in Section 8.4. Lending to our confidence that the model reflects experimental observations, electron dynamics in the "load" and "empty" phases are self-consistently reproduced with the same tunneling parameters.

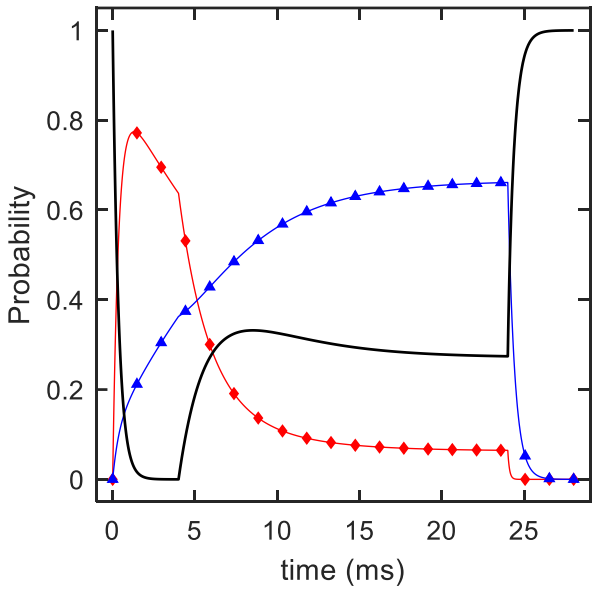

Figure 8.2: Calculated state occupation probabilities during the valley read-out sequence at zero field. Red diamonds: probability of the excited valley being occupied p_{v_+}. Blue triangles: probability of the ground state being occupied p_{v_-}. Solid black line: probability of the dot being unoccupied, proportional to the charge sensor current. The valley tunneling peak is visible between 4 ms and 24 ms.

8.3 Spin-valley states at nonzero field

The five-state spin-valley transition matrix obtained for fields $g\mu_B B_{\text{ext}} > E_{\text{VS}}$ can be written for the probability vector $\mathbf{p} = (p_{\uparrow,v_+}, p_{\uparrow,v_-}, p_{\downarrow,v_+}, p_{\downarrow,v_-}, p_0)$ as

$$\mathbf{\Gamma} = \begin{pmatrix} -\Gamma^{\text{out}}_{\uparrow,v_+} - \Gamma_w - \Gamma_v & 0 & 0 & 0 & \Gamma^{\text{in}}_{\uparrow,v_+} \\ \Gamma_v & -\Gamma^{\text{out}}_{\uparrow,v_-} - \Gamma_u - \Gamma_w & 0 & 0 & \Gamma^{\text{in}}_{\uparrow,v_-} \\ \Gamma_w & \Gamma_u & -\Gamma^{\text{out}}_{\downarrow,v_+} - \Gamma_v & 0 & \Gamma^{\text{in}}_{\downarrow,v_+} \\ 0 & \Gamma_w & \Gamma_v & -\Gamma^{\text{out}}_{\downarrow,v_-} & \Gamma^{\text{in}}_{\downarrow,v_-} \\ \Gamma^{\text{out}}_{\uparrow,v_+} & \Gamma^{\text{out}}_{\uparrow,v_-} & \Gamma^{\text{out}}_{\downarrow,v_+} & \Gamma^{\text{out}}_{\downarrow,v_-} & -\sum_{\sigma,v}\Gamma^{\text{in}}_{\sigma,v} \end{pmatrix}, \quad (8.9)$$

where the functional dependence of tunnel rates on the Fermi level and temperature are suppressed for compactness. Here I've introduced rates associated with intervalley and intravalley spin-flip transitions: from $|\uparrow, v_+\rangle$ to $|\downarrow, v_+\rangle$ with rate Γ_w, and from $|\uparrow, v_-\rangle$ to $|\downarrow, v_+\rangle$ with rate Γ_u. Γ_w describes simple spin relaxation, which for low fields is on the order of 1 Hz. Intervalley spin decay given by Γ_u is proportional to the difference in on-diagonal dipole elements $\langle v_-|\mathbf{r}|v_-\rangle - \langle v_+|\mathbf{r}|v_+\rangle$ according to [HH14], but under the assumption that electrical noise affects both valleys equally, Γ_u vanishes. We subsequently set $\Gamma_w = 1$ Hz and $\Gamma_u = 0$. With nondegenerate spin states, intervalley relaxation can now occur as $|\uparrow, v_+\rangle \rightarrow |\uparrow, v_-\rangle$ and $|\downarrow, v_+\rangle \rightarrow |\downarrow, v_-\rangle$; we assume Γ_v is independent of spin quantum number. Additionally, there is also the possibility of an electron in $|\uparrow, v_+\rangle$ to decay directly to the ground state $|\downarrow, v_-\rangle$ as another form of intervalley spin-flip transition. However, given the energy splitting between the two states the probability is likely quite small.

Similar to the zero-field case, the available dot levels are fixed and the reservoir Fermi level is moved in relation to the dot levels for different operating voltages (Figure 8.3). The levels are $\mu_{\uparrow,v_\pm} = \frac{1}{2}(g\mu_B B_{\text{ext}} \pm E_{\text{VS}})$ and $\mu_{\downarrow,v_\pm} = \frac{1}{2}(-g\mu_B B_{\text{ext}} \pm E_{\text{VS}})$. These are constructed so that a spin measurement can be achieved at $\mu_0 = 0$ and a valley measurement can be performed at $\mu_0 = \pm\frac{1}{2}g\mu_B B_{\text{ext}}$. The nominal tunneling rates and actual rates at the desired

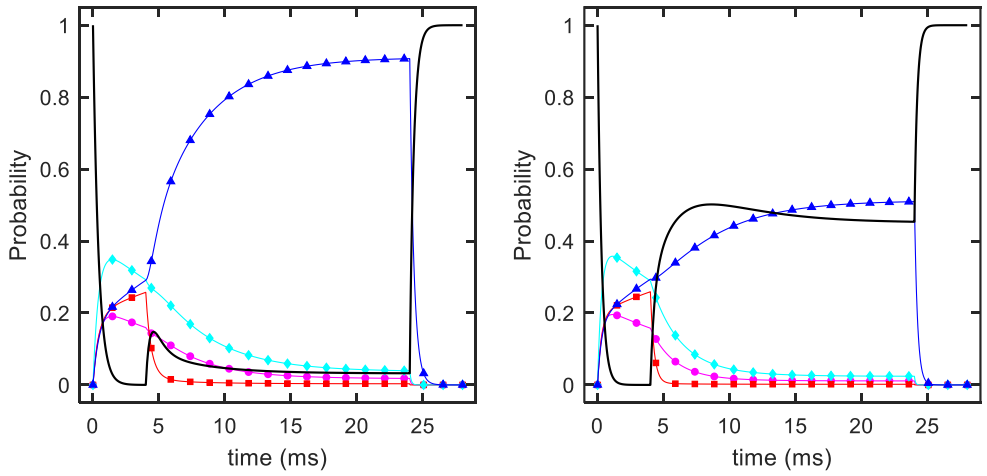

Figure 8.3: Calculated state occupation probabilities during spin read-out (left) and valley read-out (right) at $B_{\text{ext}} = 2$ T. Magenta circles indicate $p_{\uparrow,v_+}$, red squares indicate $p_{\uparrow,v_-}$, cyan diamonds indicate $p_{\downarrow,v_+}$ and blue triangles indicate the ground state $p_{\downarrow,v_-}$. Solid black line: probability of the dot being unoccupied, with a tunneling peak visible in both read-out regimes.

measurement level are enumerated in Table 8.1.

When the Fermi level falls within the valley read-out window, an electron initially in the excited spin state $|\uparrow, v_\pm\rangle$ quickly tunnels out of the dot at a rate $\Gamma \approx 2$ kHz at the start of the measurement phase. Similarly, an electron in the first excited state $|\downarrow, v_+\rangle$ will tunnel out of the dot at a rate of 370 Hz. The electron will then slowly tunnel in to the ground state, the only level with a sizable tunnel-in rate at this configuration. This could potentially lead to simultaneous spin and valley tunneling peaks, but a loaded electron only has a 20% initial chance of being in the excited spin state so spin-related contribution is small.

In the spin read-out window, the tunneling peak is largely determined by the three fastest rates $\Gamma^{\text{out}}_{\uparrow,v_+}$, $\Gamma^{\text{out}}_{\uparrow,v_-}$, and $\Gamma^{\text{in}}_{\downarrow,v_-}$. An important point to highlight is the difference in rates between the two read-out windows. The spin tunneling peak has an average rise rate of roughly 1.5 kHz and a fall rate of 1.4 kHz, whereas the valley tunneling peak rises with a rate of 373 Hz and falls at 95 Hz. This leads to the observed sharp spin tunneling peak and broad valley tunneling peak, with origins in the energy-dependent tunneling terms in (8.6) and (8.7).

Table 8.1: Tunneling rates used to fit spin and valley tunneling peaks at $B_{\text{ext}} = 2$ T.

$\boldsymbol{\Gamma}$	Nominal	$E = -159$ μeV (spin read-out)	$E = -215$ μeV (valley read-out)
$\Gamma^{\text{in}}_{\uparrow,v_+}$ (Hz)	1800	0	0
$\Gamma^{\text{out}}_{\uparrow,v_+}$ (Hz)	287	1697	2373
$\Gamma^{\text{in}}_{\uparrow,v_-}$ (Hz)	660	0	0
$\Gamma^{\text{out}}_{\uparrow,v_-}$ (Hz)	306	1402	1960
$\Gamma^{\text{in}}_{\downarrow,v_+}$ (Hz)	16930	564	32
$\Gamma^{\text{out}}_{\downarrow,v_+}$ (Hz)	180	261	373
$\Gamma^{\text{in}}_{\downarrow,v_-}$ (Hz)	5530	1371	95
$\Gamma^{\text{out}}_{\downarrow,v_-}$ (Hz)	55	49	87

8.4 Evidence of valley-dependent tunneling

In Table 8.1, there is clearly a discrepancy between the tunnel-out rates of the lower valley and excited valley. This would generally be true of the tunnel-in rates as well, if it weren't for the Fermi-Dirac statistics that come into play when the read level is below the relevant dot levels. The difference is most evident in both read-out configurations between $\Gamma_{\downarrow,v_+}$ and $\Gamma_{\downarrow,v_-}$: there's a factor of 5 difference in the spin read-out region and a factor of 4 difference in the valley read-out region. The nominal tunneling rates, independent of read-out, also reflect this discrepancy (at least in the lower energy spin state).

Perhaps the most concrete evidence of valley-dependent tunneling is the observed valley read-out window of 80 μeV, twice the valley splitting. This sort of extended read-out window is only possible if the excited state tunneling rates are greater than the ground state tunneling rates. These observations together point to a state-dependent tunneling effect, which we investigate to give compelling evidence for a mechanism of valley-dependent tunneling.

8.4.1 Ruling out general barrier effects

Tunneling rate differences do in fact arise from generic effects originating from bound state wavefunctions and realistic tunnel barriers. In a one-dimensional harmonic potential, for instance, the first excited state wavefunction penetrates deeper into the classically forbidden

region outside of the potential well, leading to a higher probability of an excited state tunneling out. This is the origin of spin-dependent tunneling in GaAs quantum dots [HvV05], where the second electron in a spin triplet must occupy the orbital excited state due to Pauli exclusion, leading to an order of magnitude difference in tunneling rates depending on the spin state. This effect can be neglected in silicon, since the second electron in a triplet state occupies the excited valley and not the excited orbital. Material notwithstanding, our experiment occurs with a single electron and has been done at zero field.

Despite the absence of excited orbital occupation, there is a state-dependent tunneling effect from elastic scattering that does come into play in our system. As a given occupied level is moved closer to the tunnel barrier, the tunneling rate out of the state should increase. This is, in fact, the same energy-dependent tunneling mechanism that was taken into account with the rate expressions (8.6) and (8.7). That the nominal rates in the two valleys are different is sufficient evidence that energy-dependent tunneling does not fully explain the observed rate discrepancy; however, we can also measure the impact of state energy on tunneling by recognizing that in the absence of temperature effects, the ratio of tunneling rate out of state j to tunneling rate out of state k is given by

$$\frac{\Gamma_j}{\Gamma_k} = \frac{\Gamma_{j,0}}{\Gamma_{k,0}} e^{\beta(\mu_j - \mu_k)}. \tag{8.10}$$

With all other barrier-related effects held equal, $\Gamma_{j,0} = \Gamma_{k,0}$ and the ratio reduces to the exponential term. Having already measured β, we can calculate the expected rate ratio due purely to energy-dependent tunneling as $e^{\beta(\mu_{v_+} - \mu_{v_-})} = e^{\beta E_{\mathrm{VS}}} = 1.3$. This is not at all close to the factor of 4 or 5 observed, so we can safely conclude that there is another factor at work leading to valley-dependent tunneling.

8.4.2 Calculating valley wavefunctions: ideal interface

For a theoretically grounded discussion on valley state tunneling effects, we must calculate the full wavefunction of an electron in the ground or excited valley state. There are many ways to approach this problem using tight-binding models [BKF04][BKE04] or the effective mass approximation [FCT07][FC10][CHD10]. Lately the effective mass approaches have been favored due to the analytic solutions that allow theorists to gain deeper insights about valley states. However, we are only interested in numerical wavefunction solutions for fixed parameters and so the tight-binding model is better suited for the problem.

Elements of the tight-binding Hamiltonian matrix with nearest and next-nearest neighbor hopping amplitudes $t_1 = 683$ meV and $t_2 = 612$ meV are given by [BSC16]

$$H_{jk} = t_1(\delta_{j,k+1} + \delta_{j,k-1}) + t_2(\delta_{j,k+2} + \delta_{j,k-2}) + V_{\text{SiGe}}(j)\delta_{j,k} + eF_z z_j \delta_{j,k}, \tag{8.11}$$

where F_z is the applied out-of-plane electric field at the Si/SiGe interface and $z_j = (j - 1/2)a_0/4$ is the real-space coordinate of atomic site j. The quantum well potential $V_{\text{SiGe}}(j)$ is treated as a finite square well with energy V_0 outside the well:

$$V_{\text{SiGe}}(j) = \begin{cases} 0, & 0 < j \leq 74 \\ V_0, & \text{otherwise.} \end{cases} \tag{8.12}$$

As our Si/SiGe wafer has a quantum well width of 10 nm, the well potential is zero for 73 atomic layers ($a_0 = 0.543$ nm), or 9.91 nm.

With $V_0 = 150$ meV representing the conduction band offset of SiGe and applied interfacial field $F_z = 3$ MV/m, the valley wavefunctions in the z direction are given by the lowest-energy eigenstates of (8.11). To accommodate wavefunction penetration into the SiGe barrier on both sides of the well, 50 atomic layers were included in the calculation added to the $-z$ side of the well ($-50 < j \leq 0$) and 60 layers were added to the $+z$ side ($74 < j \leq 134$).

This resulted in a 184×184 Hamiltonian that was numerically diagonalized.

The tight-binding model accurately describes the valley wavefunctions in the out-of-plane (z) direction, but we are most interested in the in-plane behavior leading to tunneling in and out of the quantum dot. The gate-defined electrostatic potential that molds the quantum dot is often modeled as a circular harmonic potential [TJ14], and it can be applied here as well since the two quantum dots are only weakly coupled in these experiments. At first glance it may seem that we must use the tight-binding model for the full three-dimensional wavefunction, but fortunately the cardinal solutions are fully separable for a perfectly flat interface. At this point it may become obvious that the valley wavefunctions calculated in this way cannot possibly give rise to valley-dependent tunneling, but the form of the solution and the obtained eigenstates will be useful in later discussions.

Claiming full separability of solutions, we can safely use the effective mass approximation for the two in-plane components. The harmonic potential is given by

$$H_{xy} = \frac{p_x^2 + p_y^2}{2m_t} + \frac{1}{2} m_t \omega_0^2 (x^2 + y^2), \tag{8.13}$$

where $m_t = 0.19 m_0$ is the transverse electron effective mass in silicon and we take $\hbar\omega_0 = 0.5$ meV as the orbital spacing, corresponding to a quantum dot diameter of about 50 nm. Solutions are the well-known quantum harmonic oscillator eigenstates in two dimensions taking the form of Hermite functions, with energies $E_{n_x,n_y} = (n_x + n_y + 1)\hbar\omega_0$. From Figure 8.4b,c with $n_x = n_y = 0$, both three-dimensional valley wavefunctions have identical envelopes with the fast valley oscillations differing by some phase factor. Since the probability distribution is the same for both wavefunctions as a function of x and y, the valley states will have the same tunneling rate.

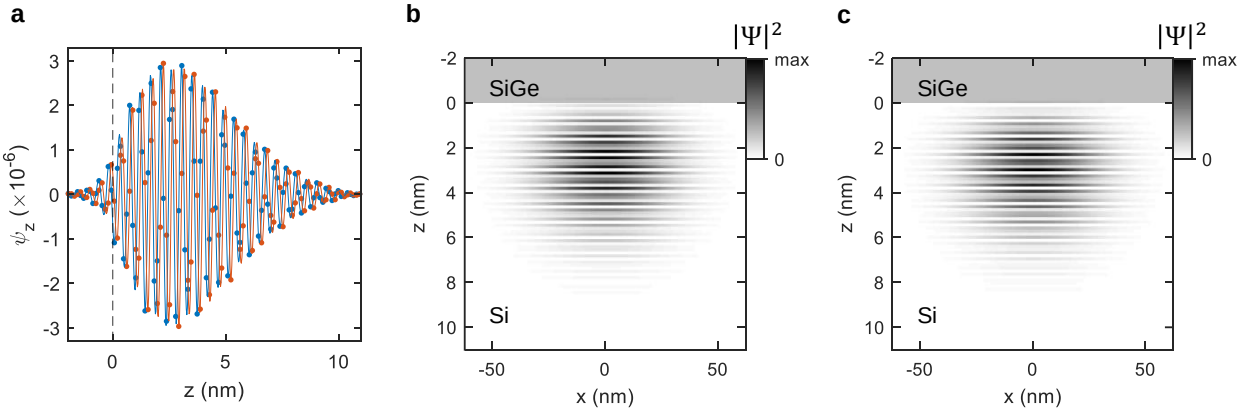

Figure 8.4: Valley state wavefunctions in the case of a flat interface. (A) The z component of the wavefunctions obtained from diagonalizing (8.11). Blue line: ground valley state. Orange line: excited valley state. The two eigenstates differ by a valley phase close to 90°. (B) Total ground state wavefunction in the x–z plane. (C) Total excited valley wavefunction. The envelope functions are the same for both states, which results in identical tunneling rates.

8.4.3 Calculating valley wavefunctions: valley-orbit coupling

In the discussion of Section 8.4.1, it was slightly misleading to claim that the excited orbital occupation is not affected by valley occupation. The concept of valley-orbit coupling has already come up several times in this dissertation, and it is a likely suspect for the origin of valley-dependent tunneling. Our motivation in investigating valley-orbit coupling comes from two observations: first, the valley splitting in both dots in this device was found to be small from coherent spectroscopy measurements and the position of the spin-valley hot spot. As referenced in Chapter 2, the valley splitting is reduced from a few hundred μeV in Si/SiGe quantum dots due to valley-orbit coupling. Second, we've already seen strong inter-dot valley hybridization that allowed use to implement the valley qubit.

To introduce valley-orbit coupling, some perturbation must be added to the ideal model described in the previous section that contains a dependence on z and on x or y. The perturbation must also represent a physically realizable situation related to the quantum dot formation or device fabrication. Valley-orbit coupling is often introduced as a single

atomic step at the Si/SiGe interface, terminating at some location r_0 in the x–y plane [BSC16][HVZ17]. Such a step could arise stochastically during wafer growth. Given the circular symmetry of the quantum dot confinement, the step can be set to be purely along x without loss of generality. Of course, we can't know that this is truly the origin of valley-orbit coupling in our double quantum dot since we have no way of imaging the interface in the vicinity of the dots without destroying the device. However, the results obtained from a commonly-used model of the confinement potential with a commonly-used approach to valley-orbit coupling will produce a qualitative picture of the effect that can be readily compared to theoretical studies.

The single-step perturbation occurs at the $-z$ interface, corresponding to the interface closest to the surface of the wafer. With $j = 1$ being the first atomic layer in the silicon quantum well, the perturbation has the form $H_1(x, j) = V_0\Theta(x - x_0)\delta_{j,1}$. Adding this to the full Hamiltonian presents a problem, since we treated the out-of-plane solution with a discrete-space tight-binding model and the in-plane solutions with a continuous-space effective mass model. However, we can always express H_1 as an infinite sum of unperturbed basis states, and then add it to the (diagonalized) unperturbed Hamiltonian to find eigenstates of the complete Hamiltonian $H_{xy} + H_z + H_1$. The sum can be terminated to a computationally reasonable number of basis states as long as the perturbation is small [GEC13].

In MATLAB, the numerical diagonalization of the unperturbed Hamiltonian takes less than a second, but calculating the matrix elements of H_1 in the unperturbed state space takes much longer. This is exacerbated by the absence of unperturbed z eigenstates that are solutions when the quantum well is one atomic layer thinner, which is the situation when $x_0 \to \infty$. Many z eigenstates are needed to get a good approximation for the narrower quantum well, which severely increases the computation time. A solution with less than 10% error required an expansion truncated to $n_x = 6$, $n_y = 1$, and $n_z = 20$, taking about a half an hour to calculate. Despite the computation time, the disorder-expansion technique is a useful tool that can in principle address any perturbation potential, not just the single

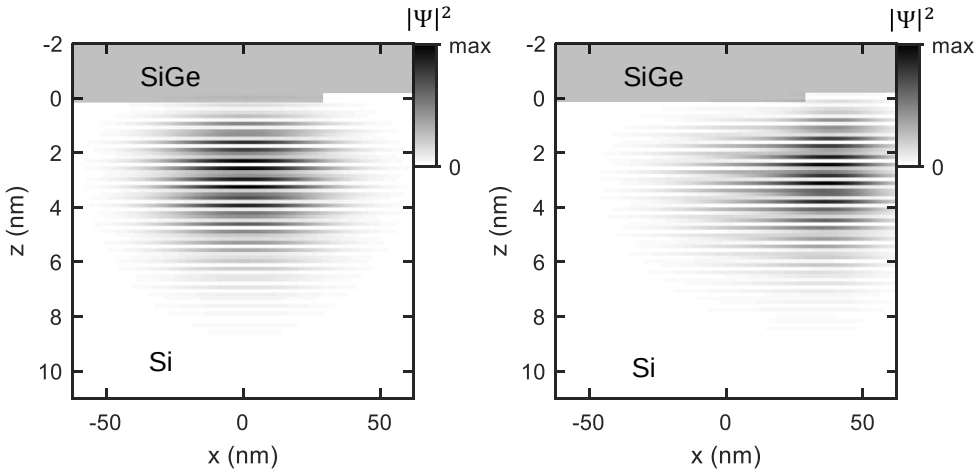

Figure 8.5: Valley state wavefunctions in the presence of a single interface step. Left: the ground state wavefunction is not noticeably affected by the perturbation. Right: the excited valley wavefunction is shifted to the right due to valley-orbit coupling. This leads to valley-dependent tunneling.

interface step.

The results of the calculation with valley-orbit coupling are shown in Figure 8.5. When the interface step terminates at $x_0 = \sqrt{\hbar/m_t\omega_0}$, the excited valley state wavefunction is shifted noticeably to the right with respect to the ground state wavefunction. The ratio of tunneling rates is then given by the relative integrated probability distributions in the classically forbidden region:

$$\frac{\Gamma_{v_+}}{\Gamma_{v_-}} = \frac{\int_{-\infty}^{\infty} dz \int_{x_c}^{\infty} dx |\psi_{v_+}(x,z)|^2}{\int_{-\infty}^{\infty} dz \int_{x_c}^{\infty} dx |\psi_{v_-}(x,z)|^2}. \tag{8.14}$$

In (8.14), the y component of the full solution is still separable and normalized, so it is unnecessary to include y dependence in the calculation. With $x_c > 0$ set to the classical turning point of the harmonic potential, we get a ratio of $\Gamma_{v_+}/\Gamma_{v_-} = 6.4$, close to the inferred value from the rate equation fit. It is important to note that valley-dependent tunneling under these conditions will be largely dependent on the position of the quantum dot relative to the interface step. In fact, the valley tunneling peak would likely vanish when the dot

potential is shifted to the right of the step termination, where the ratio is less than one and the read-out window is reduced. This may help to explain why we were unable to reliably see a valley tunneling peak in the left dot, as some luck involving the exact quantum dot position is required.

8.5 Conclusions, Chapters 7 and 8

We demonstrated a real-time valley-to-charge conversion technique based on energy-selective tunneling in a single quantum dot. As this method is adapted directly from the widely-used single-electron spin read-out pulse sequence, it is easily implemented in any lab setting familiar with spin qubits. Additionally, it allows for measurements of both spin and valley occupation within the same measurement by adjusting the dot energy. With this read-out scheme, we obtained the first direct measurement of the intervalley relaxation $T_1 = 12$ ms in the right dot, a surprisingly large value that can be attributed to the small valley splitting. Although different devices may have vastly different valley relaxation, our result does serve as a cautionary note for silicon spin qubit implementations: valley dynamics can't always be treated as negligibly fast compared to spin dynamics. Beyond that, our measurement provides a much-needed benchmark for the silicon quantum dot community. In the context of valley qubits such as the one we demonstrated in Chapter 6, this type of measurement could prove valuable for understanding qubit coherence and, separately, as a read-out mechanism that doesn't have the same strict constraints that charge-based read-out has.

We were also able to verify an indirect measurement of the valley T_1 using spin dynamics by recognizing that spin-valley coupling leads to spin relaxation on the order of pure valley relaxation in the vicinity of the spin-valley anti-crossing. The indirect method through spin relaxation is robust against small valley splittings and prohibitively fast valley relaxation as long as the fit to the data is sufficiently precise, which makes it a powerful tool. Additionally, the magnetic field dependence of spin relaxation provides valuable insight into the noise

sources experienced by the valley states. We found from fitting that intervalley relaxation was dominated by Johnson noise, as opposed to phonon noise.

Finally, we found compelling evidence of valley-dependent tunneling that leads to an enhanced window for observing the valley tunneling peak. This is likely due to valley-orbit coupling, which we address with a hybrid tight-binding and effective mass formalism to calculate the valley wavefunctions. From the good agreement between our calculated valley-dependent tunneling and our experimental observations, orbital coupling is a likely candidate for the tunneling behavior. This result implies that the fidelity of the single-dot valley read-out will depend on the exact position of the quantum dot within the interface disorder landscape, leading to random variations in the tunneling peak amplitude from dot to dot.

CHAPTER 9

Discussion

9.1 Conclusions

If only one thing may be concluded from the work detailed here, it is that the silicon band structure asserts itself in almost every aspect of electron dynamics and interactions in the quantum regime. A quantum dot in silicon cannot be treated truthfully as a simple potential well, nor is there a perfect analogy between quantum dots and two-dimensional atoms, all because of the lattice-specific valley states that provide an extra degree of freedom. It is a testament to the great potential of silicon quantum computing that researchers haven't simply abandoned the platform when faced with these complications. A great deal of work has been devoted to understanding the valley states in the past ten years since quantum computing in silicon began attracting interest, and I hope that our research in this area will help progress understanding. We developed new ways of probing the valley states with charge sensing measurements, either coherently through inter-dot valley-orbit coupling or incoherently in a single quantum dot with real-time tunneling read-out. These techniques may be of general interest for investigating valley physics beyond what we demonstrated here, especially in exploring ways to avoid the valleys or mitigate their effects. On the other hand, the valleys can themselves be leveraged as a viable qubit basis, perhaps with the help of interface engineering to manufacture valley-orbit coupling or to create a dephasing-free subspace. In that sense, our demonstration of a valley qubit may provide a starting point for future improvements.

As a way of unifying the key findings of this dissertation, we can make some conclusions about the coherence of valley states using insights gained from Chapters 5 through 8. From our valley qubit work, we established an inhomogeneous dephasing time of $T_2^* \approx 7$ ns. This value is limited by low-frequency charge noise, which seeps into the system through a small detuning dependence of the valley splitting. Additionally, according to our investigation of spin-valley dynamics, the intervalley relaxation time was found to be $T_1 = 12$ ms. From spin relaxation measurements we established that relaxation in our particular device was determined by Johnson noise rather than phonon noise. Both decoherence effects are a direct result of valley-orbit coupling, which creates an electric dipole moment and makes electric field-dependent modifications to the valley states.

9.2 Future directions

There are a number of fascinating possibilities for further research with the tools and findings enumerated in this work. With a reliable and sensitive method of valley-orbit spectroscopy, it becomes possible to measure small changes in valley splitting in response to quantum dot position, applied magnetic field, and number of electrons. All of these effects can provide valuable insight into the nature of the heterostructure interface that gives rise to the slight lifting of valley degeneracy. In realistic applications, our coherent spectroscopy can be used to characterize qubits independent of the charge configuration. In an extreme ideal case, it could even be possible to map out the interface topology using valley splitting experienced by a quantum dot as it moves laterally, almost like the cantilever element in an atomic force microscope.

Much is still not understood about valley relaxation processes. Since 2013 [YRR13], the only experimental work involving valley decay has focused on its effects on spin relaxation. With a way of directly addressing valley state occupation in real time, it now becomes feasible to measure intervalley relaxation as it depends on key parameters like valley splitting. In

that sense, we have provided only a single T_1 data point that may be one of many with future experiments. Electron temperature will play a critical role in how well the valley read-out can be accomplished, and there are some well-studied measures that we can take to improve the temperature such as cryogenic amplification and DC signal filtering.

Our valley qubit and the control methods associated with it have a more defined future. Now that we have demonstrated that full quantum control is possible, it is important to improve single-qubit operation and read-out fidelities. A large component of this will be in solving the high-frequency transmission loss issues that prevent abrupt pulses from reaching the sample. Since we have good evidence that wire-bonds are the main source of loss, a re-design of the circuit board sample holder that minimizes wire length is critical. An additional step that can be taken is to modify the on-chip lithography to include grounding planes in a properly impedance-matched coplanar waveguide design. With these adjustments, the rotation errors observed in the qubit operations can be substantially reduced. Qubit measurement fidelity is also an issue, which is greatly affected by the valley splitting near the initialization and read-out location. In lieu of robust control of valley splitting, it may help to experiment with different numbers of electrons in the read-out configuration. With three electrons in one dot, for instance, the "valence" electron occupies the excited valley [VRY15] which may lift the strict constraints on initialization and read-out.

Demonstrating single-qubit operations is not sufficient evidence for a well-defined qubit, however. Referring back to the first DiVincenzo criterion, we must have a scalable system with well-characterized qubits. This requires the capability of coupling two or more qubits with multi-qubit gates. Coupling two valley qubits together is an open problem, one that is actively being pursued in our lab. With the charge qubit-like qualities of the valley qubit read-out, it is possible to use simple capacitive coupling, equivalent to the operating principle of a charge sensor. However, this requires coupling operations to occur in detuning regions that are susceptible to charge noise. The best method of valley qubit coupling would be some form of exchange interaction when both qubits are in the valley basis, reminiscent of

electron spin exchange. This effect has in fact been predicted to occur when mediated by spin exchange of a singlet-triplet system [RRB14], which would require two double quantum dots and a static magnetic field. Regardless of the ultimate implementation, valley qubit superposition is an exciting prospect that could reveal new valley physics.

Compared to other qubit encoding schemes, the silicon spin qubit is a relatively mature technology. Although we and other groups have shown that spin coherence is harmed by nondegenerate valleys, there is also a unique opportunity to exploit spin-valley coupling as a novel form of electric control. In silicon MOS, where the abrupt surface potential allows for precise tuning of the valley splitting through gate voltages [GHJ16], it becomes possible to induce electron spin resonance mediated by electrical control of the valleys [CBM18]. In Si/SiGe quantum dots, where the valley splitting is largely determined by spatial non-uniformity of the interface, a similar effect may be obtained by perturbing the position of the quantum dot to create electron dipole spin resonance [HVZ17]. This method could have several advantages over existing forms of spin control: the dot can be moved to a location with high valley-orbit coupling to allow for fast control and measurement, and then the dot can be moved to a slightly different location that doesn't contain interface disorder for high-coherence precession. This is in contrast to traditional electron dipole spin resonance in the presence of a micromagnet, where extrinsic spin-orbit coupling uniformly increases susceptibility to charge noise. Valley-controlled spin qubits may achieve the middle ground between coherence and electrical control.

9.3 Something completely different: magnetic skyrmions

It may come as a surprise to members of my dissertation committee that this work focuses exclusively on silicon quantum dots. In fact, my initial research (and the original subject of my thesis proposal) was on a topic with virtually no conceptual overlap with the topics presented here. Within magnetic tunnel junctions provided to us through a collaboration with

Avalanche Technology, we were able to electrically create and detect a non-uniform magnetic configuration that we identify as a skyrmion through magnetic resonance measurements and micromagnetic simulations [PHW19]. Possible applications of our findings include low-energy non-volatile magnetic RAM and neuromorphic computing. Eventually, this project may be taken further by introducing an anti-symmetric exchange through interface engineering to stabilize skyrmions at room temperature. This research involved interesting and novel physics; despite that, I felt that it shouldn't be included in the main text for the sake of narrative cohesion and coherence — no pun intended.

9.4 Final thoughts

Despite the challenges we as a research community still face, quantum computing in silicon has the unique potential to grow beyond other leading architectures. In Si/SiGe systems, small valley splitting is a leading issue; however, recent work utilizing improvements in wafer growth technology has shown a valley splitting in excess of 200 µeV [HSL20], a larger value than some reports in Si/SiO_2. Together with unparalleled quantum dot tunability and the reduction of magnetic noise with the use of isotopically enriched ^{28}Si, quantum dots in Si/SiGe afford greater flexibility in qubit implementation than other host materials. Silicon MOS systems, on the other hand, allow the formation of incredibly small quantum dots with deep potentials. This is important primarily because the potential well depth becomes larger than the spurious potentials formed by interfacial charge traps in Si/SiO_2, reducing a major problem with that material system. In addition, a deep potential well allows for higher-temperature operation. Very recently, multiple groups have reported coupled spin qubit operations above 1 Kelvin [YLH20] [PER20], which goes a long way in solving one main scalability concern related to the heat load of many qubits and their control circuitry.

It is still unclear what the greatest demand will be for a universal quantum computer if or when it is demonstrated. Cryptography is often cited as an application in order to

secure government funding, but many more possibilities lie with quantum simulation. Once the physics of many-body quantum systems can be solved exactly, new emergent behavior is likely to be discovered and new frontiers in the fields of condensed matter and quantum chemistry can be reached. While many more years of research are needed until this technology can compete with modern supercomputers, it is my fervent hope that our work here can contribute in some way toward that ultimate goal.

APPENDIX A

GPU-accelerated numerical simulations

Simulating a single time step in a qubit experiment with 200×200-point resolution requires 40,000 back-to-back calculations with a CPU. To accurately calculate the dynamics of coherent precession at frequencies of order 10 GHz, we need a time resolution of around 10 ps. All told, for a 5 ns process it takes roughly $40000 \times 500 = 20$ million computations, a number that scales quadratically with the resolution. For this reason, numerical simulations can often take hours to complete with standard CPUs. Fortunately, we can exploit the natural parallelism of the problem. Each data point represents a separate realization of the same experiment, except with slightly different parameters. The qubit is initialized in the same way, an operation is performed, and then identical projective measurements are made. For the data in Figure 6.2, everything is held equal at each point with the exception of the operation times t_θ and t_ϕ. Critically, each grid point is uncorrelated with all others. This means we can assign individual time evolution problems to smaller, dedicated cores in a GPU. As long as the simulation grid contains a smaller number of points than the number of GPU cores, simulations can be performed in constant time (with respect to grid size). In the rough calculation given above, using a GPU will reduce the number of computations from 20 million to 500, now limited by the time step.

GPU-accelerated simulations were implemented in MATLAB with the parallel computing toolbox. The number of mathematical operations and data structures that can be constructed with GPU compatibility is limited to a very small subset of all MATLAB operations, which makes an otherwise simple set of differential equations challenging to construct.

GPUArray objects can only interact through simple addition, subtraction and multiplication, so the goal is to convert discrete-time differentiation into a functional algebraic form. Consider the arbitrary example:

$$\frac{\partial Y}{\partial x} = Ax^2Y^\dagger - BY, \tag{A.1}$$

where y is some matrix. This can be well-approximated by the expression

$$\delta Y = (Ax^2Y^\dagger - BY)\delta x, \tag{A.2}$$

provided the discrete step δx is small enough. We must now generate a function that takes the constants A and B as well as the elements in Y as inputs and produces the elements of matrix $Y + \delta Y$. This function $f(A, B, Y_{ij})$ is guaranteed to include only simple arithmetic expressions allowing it to be computed on GPU cores. This method is also used to handle matrix operations, such as the trace function in projection measurements. In Algorithm 1, there are multiple variable assignments with "functional(inputs,outputs)" that describe this mapping.

Again using the example of Figure 6.2, each GPU core (or cores, depending on how MATLAB distributes computations) is given a set of identical parameters describing the initialization detuning, valley splitting, and inter-dot couplings. Each core is also given a unique combination t_θ, t_ϕ that is used to generate a unique pulse. Then the cores will simultaneously solve the Lindblad equation (in an algebraic form) for their assigned pulse shape. At the end of the simulation, the individual solutions are "gathered" into the CPU for plotting and saving to data files. Former graduate students Blake Freeman and Joshua Schoenfield both developed GPU scripts for simulations with varying degrees of specificity, but it was important for my spectroscopy data to have exact detuning-dependent decoherence processes included in the calculations. Algorithm 1 below, written in pseudocode, describes this process in a language-invariant manner. All simulations shown in this work

were performed on an EVGA GeForce GTX 1060 GPU with 1152 CUDA cores and a base clock of 1607 MHz.

Algorithm 1 accepts an initial pure state $\mathbf{p}_0$ and two variables $xvar$ and $yvar$ to scan over. These variables can be elements of the Hamiltonian or pulse parameters. Vectors $\mathbf{x}$ and $\mathbf{y}$ describe the ranges over which the variables are scanned. H_0 describes the time-independent Hamiltonian of the system (obtained from spectroscopy). The time dependence comes from some function $pulse(t)$, which may be a matrix of parameters. Decoherence is encapsulated in vector $\boldsymbol{\gamma}$, elements of which take the form $1/T_x$ and are associated with individual jump operators. The number of time steps is given by n_{steps}, and must be large compared to $f_0 t_{max}$ where f_0 is the natural qubit frequency.

Algorithm 1 Simulating quantum evolution with GPU acceleration

function SIMULATE($\mathbf{p}_0$, $xvar$, $yvar$, $\mathbf{x}$, $\mathbf{y}$, H_0, $pulse(t)$, γ, n_{steps}, directory)
  $dim \leftarrow \text{size}(H_0)$
  $n_{comps} \leftarrow \text{length}(\mathbf{x}) \cdot \text{length}(\mathbf{y})$ ▷ number of GPU cores needed
  t_{max} defined by maximum time required in $pulse(t)$
  $\mathbf{t} \leftarrow \text{linspace}(0, t_{max}, n_{steps})$
  $X \leftarrow \text{map}[\mathbf{x} \mapsto \text{array}(\text{length}(\mathbf{y}), 1)]$ ▷ $\mathbf{x}$ is repeated length(y) times in a matrix
  $Y \leftarrow \text{map}[\mathbf{y} \mapsto \text{array}(\text{length}(\mathbf{x}), 1)^T]$ ▷ X and Y have same dimensions

  for $j \leftarrow$ unique variables in $\{H_0, pulse(t), \Gamma\}$, $j \neq xvar, yvar$ **do**
    $\{j\}_{GPU} \leftarrow \text{map}[j \mapsto \text{GPUarray}(1, n_{comps})]$
    ▷ each constant parameter is repeated in a $1 \times n_{comps}$ GPU array
  end for
  $X_{GPU} \leftarrow \text{map}[X \mapsto \text{GPUarray}(1, n_{comps})]$
  $Y_{GPU} \leftarrow \text{map}[Y \mapsto \text{GPUarray}(1, n_{comps})]$

  $\rho_0 \leftarrow \text{diag}(\mathbf{p}_0)$ ▷ square diagonal matrix
  for j in upper_triangle(ρ_0) **do** ▷ upper triangular elements of ρ_0
    $\rho_{j,GPU} \leftarrow \text{map}[j \mapsto \text{GPUarray}(1, n_{comps})]$
    ▷ Initial unique ρ elements stored in each GPU cell
  end for
  $dt_{GPU} \leftarrow \text{map}[t_{max}/n_{steps} \mapsto \text{GPUarray}(1, n_{comps})]$

  define $\tilde{H}_0$, symbolic matrix with dimensions of H_0
  $H_{in} \leftarrow \{h\}$, set of unique variables in H_0 ▷ function inputs
  $H_{out} \leftarrow \text{upper\_triangle}(\tilde{H}_0)$ ▷ function outputs
  $H_{fnc} \leftarrow \text{functional}(H_{in}, H_{out})$
  ▷ functional form of symbolic expression $H_0 = f(var1, var2, \cdots)$

  define $\tilde{\rho}$, symbolic matrix with dimensions of H_0.
  $\rho_{in} \leftarrow \text{upper\_triangle}(\tilde{\rho})$
  for $m \leftarrow 1, dim$ **do**
    $p_{fnc,m} \leftarrow \text{functional}(\rho_{in}, \text{Tr}[B_m^\dagger B_m \rho_{in}])$
    ▷ functional forms of all projections with basis states B
  end for

Simulating quantum evolution, continued

for $j \leftarrow 1, \text{length}(\mathbf{t})$ **do**
▷ Compute each cell in $\{\mathbf{x}, \mathbf{y}\}$ simultaneously at a given time step t_j
$t_j \leftarrow \text{map}[\mathbf{t}_j \mapsto \text{GPUarray}(1, n_{comps})]$
elements of $H_j \leftarrow H_{fnc}(\{h\}_{GPU}) + pulse(t = t_j)$
$\rho_{fnc} \leftarrow$ time_evolver(dim,L_k) ▷ See Algorithm 2 for details
elements of $\rho_{GPU} \leftarrow \rho_{fnc}(H_j, \gamma, \rho_{GPU}, dt_{GPU})$
end for

for $m \leftarrow 1, dim$ **do** ▷ calculate final probabilities
$p_{m,GPU} \leftarrow pfnc, m(\rho_{GPU})$
$p_m \leftarrow \text{gather}(p_{m,GPU})$ ▷ transfer data from GPU to CPU
end for

return p
end function

Algorithm 2 Converting Lindblad expression into a scalar functional form for use with GPU programming

function TIME_EVOLVER(N, L_j)
ensure length(L) $= N^2 - 2$ ▷ jump operators, each with dimensions $N \times N$
define $\tilde{H}, \tilde{\rho}$, $N \times N$ symbolic matrices
define $\tilde{\boldsymbol{\gamma}}$, symbolic vector of length $N^2 - 1$
$\tilde{H} \leftarrow \text{upper\_triangle}(\tilde{H}) + \text{lower\_triangle}(\tilde{H}^\dagger)$ ▷ enforce Hermicity
$\tilde{\rho} \leftarrow \text{upper\_triangle}(\tilde{\rho}) + \text{lower\_triangle}(\tilde{\rho}^\dagger)$

$\tilde{\mathbf{E}} \leftarrow \text{eigenvalues}(\tilde{H})$
$\tilde{V} \leftarrow \text{eigenstates}(\tilde{H})$ ▷ each column of V is an eigenstate
$\tilde{\rho}' \leftarrow \tilde{V}^\dagger \tilde{\rho} \tilde{V}$ ▷ density matrix in state space
$\tilde{H}' \leftarrow \text{diag}(\tilde{\mathbf{E}})$ ▷ square diagonal matrix with eigenenergies on main diagonal
$R \leftarrow \text{zeros}(N, N)$
for $j \leftarrow 0, N^2 - 2$ **do**
$R \leftarrow R + \tilde{\boldsymbol{\gamma}}_j \left(L_j \tilde{\rho}' L_j^\dagger - \frac{1}{2} \{ L_j^\dagger L_j, \tilde{\rho}' \} \right)$ ▷ populate decoherence matrix
end for
$\tilde{\delta\rho} \leftarrow \tilde{\delta t} \tilde{V} \left(-\frac{i}{\hbar} [\tilde{H}', \tilde{\rho}'] + R \right) \tilde{V}^\dagger$
$\tilde{\rho}_{t+\delta t} \leftarrow \tilde{\rho} + \tilde{\delta\rho}$ ▷ valid for small $\tilde{\delta t}$ relative to dynamics

return functional($\{\tilde{H}$,$\tilde{\rho}$,$\tilde{\gamma}\}$,$\tilde{\rho}_{t+\delta t}$)
▷ functional form of symbolic expression $f(H_{ij}, \rho_{ij}, \boldsymbol{\gamma}_i, \delta t)$
end function

APPENDIX B

Fabrication recipes

B.1 Standard fabrication steps for Si/SiGe

1. Active solvent clean
   (a) 1 minute each of acetone, isopropyl alcohol (IPA) and de-ionized (DI) water baths
   (b) Sonication during each solvent bath
   (c) Blow dry with nitrogen
   (d) 4 minute de-scum in an oxygen plasma
2. Global alignment markers
   (a) Single layer of AZ5214-EIR photoresist
      i. Spin HMDS: 5 seconds at 600 RPM, 50 seconds at 4500 RPM
      ii. Spin AZ5214: 5 seconds at 600 RPM, 50 seconds at 4500 RPM
      iii. Bake: 2 minutes at 95 °C
   (b) Expose: $\sim$ 10 seconds in UV mask aligner
   (c) Develop: 30-50 seconds in dilute solution (1 part AZ-400K developer to 3 parts DI water)
      i. Immediately transfer to DI water stop bath for 1 minute, then blow dry with nitrogen
      ii. 30 second de-scum in oxygen plasma

(d) Evaporate: 50 nm chrome (thermal evaporation is acceptable)

(e) Lift-off: 5 minutes in acetone bath, last minute with sonication

(f) Rinse in IPA, then submerge in IPA in Petri dish and check lift-off results under a microscope

(g) Clean: 5 minutes in IPA, 5 minutes in DI water, blow dry with nitrogen

3. Ion-implanted regions

(a) Active solvent clean (1), if needed

(b) Double layer of AZ5214-EIR photoresist

i. Spin HMDS: 5 seconds at 600 RPM, 50 seconds at 4500 RPM

ii. Spin AZ5214: 5 seconds at 600 RPM, 50 seconds at 4500 RPM

iii. Bake: 1 minute at 95 °C

iv. Spin AZ5214: 5 seconds at 600 RPM, 50 seconds at 4500 RPM

v. Bake: 2 minutes at 95 °C

(c) Expose: $\sim$ 12 seconds in UV mask aligner

(d) Develop: 1 minute in dilute AZ-400K (see step 2c)

(e) Send out for ion implantation: 2×10^{15} cm^{-2} dosage at 25-30 keV

(f) Remove photoresist: heat bath of AZ-400T to 80 °C, submerge for 10-20 minutes, then rinse with IPA

(g) Active solvent clean (see step 1)

(h) Rapid thermal anneal: 30 seconds at 750 °C

4. Outer depletion gates

(a) Single layer of AZ5214-EIR photoresist (see step 2a)

(b) Expose:$\sim$ 10 seconds in UV mask aligner

(c) Develop: 30-50 seconds in dilute AZ-400K (see step 2c)

(d) Evaporate: 5 nm titanium + 45 nm gold without breaking vacuum

i. E-beam evaporation recommended: 1 Å/s for Ti, 2 Å/s for Au

(e) Lift-off: 5 minutes in acetone bath, last minute with sonication

(f) Transfer to a Petri dish with IPA and examine under a microscope

(g) Clean: 5 minutes in IPA, 5 minutes in DI water, blow dry with nitrogen

5. Inner depletion gates

(a) Active solvent clean, if needed (see step 1)

(b) Double layer of E-beam resist

i. Spin PMMA 950 A4: 5 seconds at 600 RPM, 50 seconds at 5000 rpm

ii. Bake: 90 seconds at 180 °C

iii. Spin PMMA 950 A2: 5 seconds at 600 RPM, 50 seconds at 5000 rpm

iv. Bake: 90 seconds at 180 °C

(c) Dab gold colloid solution with toothpick near the e-beam write area on each device pattern for beam focusing (only necessary for our Hitachi + NPGS setup)

(d) Expose: 30 keV beam energy, 10 pA current

i. Calibrate beam dosage at Faraday cup

ii. Focus on a gold particle from the colloid solution at maximum magnification

iii. Move to the writing area, use outer gate features as alignment markers

iv. Dosage for innermost features: ~ 750 µC/cm^2

v. Dosage for intermediate features: 600 µC/cm^2

vi. Dosage for largest features: 500 µC/cm^2

(e) Develop: 45 seconds in pre-mixed 1:3 MIBK:IPA

i. Immediately transfer to IPA stop bath for 1 minute, then rinse with DI water and blow dry with nitrogen

(f) Evaporate: 5 nm titanium + 45 nm gold with E-beam evaporation

i. 0.5 Å/s for Ti, 1 Å/s for Au

(g) Lift-off: 10-20 minutes in acetone bath with gentle agitation

(h) Transfer to a Petri dish with IPA to examine under microscope, replace in acetone as needed

(i) Rinse in IPA, then DI water, then blow dry with nitrogen

6. Aluminum oxide

(a) Passive solvent clean

i. 5 minutes each of acetone, IPA and DI water baths

ii. Blow dry with nitrogen

iii. 4 minute de-scum in an oxygen plasma

(b) Deposit 910 cycles (100 nm) of AL_2O_3 via atomic layer deposition

i. Set chamber temperature to 200 °C

ii. 5 seconds between TMA and H_2O pulses

iii. 20 sccm nitrogen flow

7. Global top gate

(a) Passive solvent clean (see step 6a)

(b) Single layer of AZ5214-EIR photoresist (see step 2a)

(c) Expose: ∼10 seconds in UV mask aligner

(d) Develop: 30-50 seconds in dilute EZ-400K (see step 2c)

(e) Evaporate: 100 nm aluminum (thermal evaporation acceptable)

(f) Lift-off: 5 minutes in acetone bath

(g) Transfer to Petri dish with IPA to verify lift-off

(h) Clean: 5 minutes in IPA, 5 minutes in DI water, blow dry with nitrogen

8. Etch windows

(a) Passive solvent clean, if necessary (see step 6a)

(b) Single layer of AZ5214-EIR photoresist (see step 2a)

(c) Expose: $\sim$ 10 seconds in UV mask aligner

(d) Develop: 30-50 seconds in dilute EZ-400K (see step 2c)

(e) Etch: 5 seconds in Transene Transetch-N at 150 °C

(f) Immediately move to a DI water stop bath with agitation for $\sim$ 30 seconds

(g) Move to a second DI water bath for 5 minutes

B.2 Nano-imprint lithography for Si/SiO_2

1. Prepare target wafer

(a) Modified solvent clean

i. 1 minute each of acetone, IPA and DI water baths with sonication

ii. Blow dry with nitrogen

iii. 4 minute de-scum in matrix asher

(b) Global alignment markers

i. Bake wafer at 120 °C

ii. Single layer of AZ5214-EIR photoresist

iii. Expose: $\sim$ 10 seconds in UV mask aligner

iv. Develop: 30-50 seconds in dilute AZ-400K:H_2O 1:3, then 1 minute in DI water stop bath

v. 30 second de-scum in matrix asher

vi. Evaporate: 30 nm chrome

vii. Lift-off: 5 minutes in acetone bath, last minute with sonication

viii. Check lift-off in Petri dish with IPA

(c) Ion-implanted regions

i. Modified solvent clean (see step 1a)

ii. Double layer of AZ5214-EIR photoresist

iii. Expose: $\sim$ 12 seconds in UV mask aligner

iv. Develop: 1 minute in dilute AZ-400K:H_2O 1:3, then 1 minute in DI water stop bath

v. Send out for ion implantation: 2×10^{15} cm^{-2} dosage at 25 keV

vi. Remove photoresist: heat bath of AZ-400T to 80 °C, submerge for 10-20 minutes, then rinse with IPA

vii. Modified solvent clean (see step 1a)

viii. Rapid thermal anneal: 1 minute at 920 °C

2. Prepare mold for inner depletion gates

(a) Solvent clean: 1 minute each of acetone, IPA, and DI water with sonication followed by a 4 minute de-scum in oxygen plasma

(b) Inner gate alignment markers

i. Single layer of AZ5214-EIR photoresist

ii. Expose: $\sim$ 10 seconds in UV mask aligner

iii. Develop: 30-50 seconds in dilute AZ-400K:H_2O 1:3, then 1 minute DI water stop bath

iv. 4 minute de-scum in oxygen plasma

v. Oxide etch: submerge in buffered oxide etch (BOE) solution for 4.5 minutes, then two subsequent DI water stop baths for 30 seconds each

vi. Solvent clean: 5 minutes each of acetone, IPA, and DI water

(c) Inner gate pattern

i. Spin PMMA 950 A4: 5 seconds at 600 RPM, 50 seconds at 5000 RPM

ii. Bake: 90 seconds at 180 °C

iii. Spin PMMA 950 A2: 5 seconds at 600 RPM, 50 seconds at 5000 RPM

iv. Bake: 90 seconds at 180 °C

v. Expose: 30 keV E-beam energy, 10 pA current

A. Design should be mirror image of final pattern

B. Align to etched markers

C. Dosage for smallest features: 480 $\mu C/cm^2$

vi. Develop: 45 seconds in pre-mixed 1:3 MIBK:IPA, then 1 minute DI water stop bath

vii. Evaporate: 50 nm aluminum with E-beam evaporation at 1 Å/s

viii. Lift-off: 10 minutes in acetone bath with gentle agitation

ix. 5 minutes each in IPA, then DI water, then blow dry with nitrogen

x. Reactive ion etch (RIE): slow etch rate with CHF_3

xi. Remove aluminum with 5 seconds in Transene Transetch-N heated to 150 °C followed by two DI water stop baths with agitation

(d) FDTS deposition

i. Clean with 5 minutes each of acetone, then IPA, then DI water baths

ii. Place mold in Petri dish with one drop of FDTS within a dry nitrogen environment

iii. Allow FDTS to evaporate at room temperature (overnight)

iv. Bake for 20 minutes at 150 °C

3. Imprint

   (a) Clean target wafer as in step 1a

   (b) Spin single layer of PMMA 950 A2 on target wafer: 5 seconds at 500 RPM, 50 seconds at 2300 RPM

   (c) Bake target wafer for 2 minutes at 180 °C

   (d) Pre-imprint wafer clean: 5 minutes each in IPA and DI water with sonication

   (e) Bring mold and target wafer together

   (f) Imprint: 44 bar at 130 °C for 20 minutes

   (g) Carefully de-laminate the mold and wafer, set mold aside

   (h) Reactive ion etch: 3 seconds with oxygen at low power

   (i) Evaporate: 5 nm titanium and 30 nm gold at 0.5 Å/s / 0.7 Å/s

   (j) Lift-off: 30 minutes in acetone bath with agitation

   (k) Check lift-off with wafer in IPA in a Petri dish

   (l) Clean: 5 minutes in IPA, 5 minutes in DI water, blow dry with nitrogen

4. Outer depletion gates

   (a) Spin single layer of AZ5214-EIR photoresist

   (b) Align to inner gate pattern, NOT the chrome alignment markers

   (c) Expose: $\sim$ 10 seconds in UV mask aligner

   (d) Develop: 30-50 seconds in dilute AZ-400K:H_2O 1:3, then 1 minute in DI water stop bath

   (e) 30 second de-scum in matrix asher

(f) Evaporate: 5 nm titanium and 45 nm gold at 1 Å/s / 2 Å/s

(g) Lift-off: 20 minutes in acetone bath with agitation

(h) Rinse in IPA and DI water, blow dry with nitrogen

5. Aluminum oxide

(a) Solvent clean: 5 minutes each in acetone, IPA, and DI water baths

(b) 4 minute de-scum in matrix asher

(c) Deposit 910 cycles (100 nm) of Al_2O_3 via atomic layer deposition at 200 °C, 20 sccm nitrogen flow

6. Global top gate

(a) Solvent clean: 5 minutes each in aceton, IPA, and DI water baths

(b) Single layer of AZ5214-EIR photoresist

(c) Expose: $\sim$ 10 seconds in UV mask aligner

(d) Develop: 30-50 seconds in dilute AZ-400K:H_2O 1:3, then 1 minute in DI water stop bath

(e) Evaporate: 100 nm aluminum with thermal evaporation

(f) Lift-off: 5 minutes in acetone bath

(g) Clean: 5 minutes in IPA, 5 minutes in DI water, blow dry with nitrogen

7. Etch windows

(a) Pre-bake wafer for 2 minutes at 120 °C

(b) Spin single layer of AZ5214-EIR photoresist

(c) Expose: $\sim$ 10 seconds in UV mask aligner

(d) Develop: 30-50 seconds in dilute AZ-400K:H_2O 1:3, then 1 minute in DI water stop bath

(e) 30 second de-scum in oxygen plasma

(f) Aluminum oxide etch: 5 seconds in Transene Transetch-N heated to 150 °C followed by two DI water stop baths with agitation

(g) Silicon oxide etch: 30 seconds in BOE solution followed by two DI water stop baths

(h) Solvent clean: 5 minutes each of acetone, IPA and DI water

8. Forming gas anneal

(a) Evacuate sample space

(b) Introduce 15 mT vacuum pressure of 15% H_2, 85% N_2 mixture

(c) Heat sample space to 400 °C, hold there for 20 minutes

(d) Cool back to room temperature and vent sample space

[202] Nobel Media AB 2020. "The Nobel Prize in Physics 1956." https://www.nobelprize.org/prizes/physics/1956/summary/.

[AFD07] Susan J. Angus, Andrew J. Ferguson, Andrew S. Dzurak, and Robert G. Clark. "Gate-Defined Quantum Dots in Intrinsic Silicon." *Nano Lett.*, **7**(7):2051–2055, July 2007.

[AFS82] Tsuneya Ando, Alan B. Fowler, and Frank Stern. "Electronic Properties of Two-Dimensional Systems." *Rev. Mod. Phys.*, **54**(2):437–672, April 1982.

[AM76] Niel W. Ashcroft and N. David Mermin. *Solid State Physics*. Brooks/Cole, first edition, 1976.

[AMM14] Matthew Amy, Dmitri Maslov, and Michele Mosca. "Polynomial-Time T-Depth Optimization of Clifford+T Circuits Via Matroid Partitioning." *IEEE Transactions on Computer-Aided Design of Integrated Circuits and Systems*, **33**(10):1476–1489, October 2014.

[AS06] Alexander Altland and Ben Simmons. *Condensed Matter Field Theory*. Cambridge University Press, 2006.

[BDR02] Edgar Bonet, Mandar M. Deshmukh, and D. C. Ralph. "Solving Rate Equations for Electron Tunneling via Discrete Quantum States." *Phys. Rev. B*, **65**(4):045317, January 2002.

[Bee91] C. W. J. Beenakker. "Theory of Coulomb-Blockade Oscillations in the Conductance of a Quantum Dot." *Phys. Rev. B*, **44**(4):1646–1656, July 1991.

[Ben80] Paul Benioff. "The Computer as a Physical System: A Microscopic Quantum Mechanical Hamiltonian Model of Computers as Represented by Turing Machines." *J Stat Phys*, **22**(5):563–591, May 1980.

[Bha14] Ramesh Bhandari. "On Single Qubit Quantum State Tomography." *arXiv:1407.6668 [quant-ph]*, July 2014.

[BKE04] Timothy B. Boykin, Gerhard Klimeck, M. A. Eriksson, Mark Friesen, S. N. Coppersmith, Paul von Allmen, Fabiano Oyafuso, and Seungwon Lee. "Valley Splitting in Strained Silicon Quantum Wells." *Appl. Phys. Lett.*, **84**(1):115–117, January 2004.

[BKF04] Timothy B. Boykin, Gerhard Klimeck, Mark Friesen, S. N. Coppersmith, Paul von Allmen, Fabiano Oyafuso, and Seungwon Lee. "Valley Splitting in Low-Density Quantum-Confined Heterostructures Studied Using Tight-Binding Models." *Phys. Rev. B*, **70**(16):165325, October 2004.

[BRK11] M. G. Borselli, R. S. Ross, A. A. Kiselev, E. T. Croke, K. S. Holabird, P. W. Deelman, L. D. Warren, I. Alvarado-Rodriguez, I. Milosavljevic, F. C. Ku, W. S. Wong, A. E. Schmitz, M. Sokolich, M. F. Gyure, and A. T. Hunter. "Measurement of Valley Splitting in High-Symmetry Si/SiGe Quantum Dots." *Appl. Phys. Lett.*, **98**(12):123118, March 2011.

[BSC16] Péter Boross, Gábor Széchenyi, Dimitrie Culcer, and András Pályi. "Control of Valley Dynamics in Silicon Quantum Dots in the Presence of an Interface Step." *Phys. Rev. B*, **94**(3):035438, July 2016.

[BSH07] D. R. Barbero, M. S. M. Saifullah, P. Hoffmann, H. J. Mathieu, D. Anderson, G. A. C. Jones, M. E. Welland, and U. Steiner. "High-Resolution Nanoimprinting with a Robust and Reusable Polymer Mold." *Adv. Funct. Mater.*, **17**(14):2419–2425, September 2007.

[BSK12] Joseph W. Britton, Brian C. Sawyer, Adam C. Keith, C.-C. Joseph Wang, James K. Freericks, Hermann Uys, Michael J. Biercuk, and John J. Bollinger. "Engineered Two-Dimensional Ising Interactions in a Trapped-Ion Quantum Simulator with Hundreds of Spins." *Nature*, **484**(7395):489–492, April 2012.

[BZH19] F. Borjans, D.M. Zajac, T.M. Hazard, and J.R. Petta. "Single-Spin Relaxation in a Synthetic Spin-Orbit Field." *Phys. Rev. Applied*, **11**(4):044063, April 2019.

[Cas17] Davide Castelvecchi. "Quantum Computers Ready to Leap out of the Lab in 2017." *Nature News*, **541**(7635):9, January 2017.

[CBM18] Andrea Corna, Léo Bourdet, Romain Maurand, Alessandro Crippa, Dharmraj Kotekar-Patil, Heorhii Bohuslavskyi, Romain Laviéville, Louis Hutin, Sylvain Barraud, Xavier Jehl, Maud Vinet, Silvano De Franceschi, Yann-Michel Niquet, and Marc Sanquer. "Electrically Driven Electron Spin Resonance Mediated by Spin–Valley–Orbit Coupling in a Silicon Quantum Dot." *npj Quantum Inf*, **4**(1):6, December 2018.

[CCL01] Andrew M. Childs, Isaac L. Chuang, and Debbie W. Leung. "Realization of Quantum Process Tomography in NMR." *Phys. Rev. A*, **64**(1):012314, June 2001.

[CCL10] Dimitrie Culcer, Łukasz Cywiński, Qiuzi Li, Xuedong Hu, and S. Das Sarma. "Quantum Dot Spin Qubits in Silicon: Multivalley Physics." *Phys. Rev. B*, **82**(15):155312, October 2010.

[CGS03] P. Carlberg, M Graczyk, E.-L. Sarwe, I. Maximov, M. Beck, and L. Montelius. "Lift-off Process for Nanoimprint Lithography." *Microelectronic Engineering*, **67-68**:203–207, June 2003.

[CGT09] J. M. Chow, J. M. Gambetta, L. Tornberg, Jens Koch, Lev S. Bishop, A. A. Houck, B. R. Johnson, L. Frunzio, S. M. Girvin, and R. J. Schoelkopf. "Randomized Benchmarking and Process Tomography for Gate Errors in a Solid-State Qubit." *Phys. Rev. Lett.*, **102**(9):090502, March 2009.

[CHD10] Dimitrie Culcer, Xuedong Hu, and S. Das Sarma. "Interface Roughness, Valley-Orbit Coupling, and Valley Manipulation in Quantum Dots." *Phys. Rev. B*, **82**(20):205315, November 2010.

[CSD20] Anasua Chatterjee, Paul Stevenson, Silvano De Franceschi, Andrea Morello, Nathalie de Leon, and Ferdinand Kuemmeth. "Semiconductor Qubits In Practice." *arXiv:2005.06564 [cond-mat, physics:quant-ph]*, May 2020.

[CSK12] Dimitrie Culcer, A. L. Saraiva, Belita Koiller, Xuedong Hu, and S. Das Sarma. "Valley-Based Noise-Resistant Quantum Computation Using Si Quantum Dots." *Phys. Rev. Lett.*, **108**(12):126804, March 2012.

[DiV00] David P DiVincenzo. "The Physical Implementation of Quantum Computation." *Fortschr. Phys.*, p. 13, 2000.

[Dre55] G. Dresselhaus. "Spin-Orbit Coupling Effects in Zinc Blende Structures." *Phys. Rev.*, **100**(2):580–586, October 1955.

[DSH13] O. E. Dial, M. D. Shulman, S. P. Harvey, H. Bluhm, V. Umansky, and A. Yacoby. "Charge Noise Spectroscopy Using Coherent Exchange Oscillations in a Singlet-Triplet Qubit." *Phys. Rev. Lett.*, **110**(14):146804, April 2013.

[EHW04a] J. M. Elzerman, R. Hanson, L. H. Willems van Beveren, L. M. K. Vandersypen, and L. P. Kouwenhoven. "Excited-State Spectroscopy on a Nearly Closed Quantum Dot via Charge Detection." *Appl. Phys. Lett.*, **84**(23):4617–4619, June 2004.

[EHW04b] J. M. Elzerman, R. Hanson, L. H. Willems van Beveren, B. Witkamp, L. M. K. Vandersypen, and L. P. Kouwenhoven. "Single-Shot Read-out of an Individual Electron Spin in a Quantum Dot." *Nature*, **430**(6998):431–435, July 2004.

[FC10] Mark Friesen and S. N. Coppersmith. "Theory of Valley-Orbit Coupling in a Si/SiGe Quantum Dot." *Phys. Rev. B*, **81**(11):115324, March 2010.

[FCT07] Mark Friesen, Sucismita Chutia, Charles Tahan, and S. N. Coppersmith. "Valley Splitting Theory of Si Ge / Si / Si Ge Quantum Wells." *Phys. Rev. B*, **75**(11):115318, March 2007.

[Fey82] Richard P Feynman. "Simulating Physics with Computers." *International Journal of Theoretical Physics*, **21**:22, 1982.

[Fre17] Blake Freeman. *Charge Noise and Dephasing in Silicon-Based Lateral Quantum Dots*. PhD Thesis, University of California Los Angeles, 2017.

[FSJ16] Blake M. Freeman, Joshua S. Schoenfield, and HongWen Jiang. "Comparison of Low Frequency Charge Noise in Identically Patterned Si/SiO $_2$ and Si/SiGe Quantum Dots." *Appl. Phys. Lett.*, **108**(25):253108, June 2016.

[FSP93] M. Field, C. G. Smith, M. Pepper, D. A. Ritchie, J. E. F. Frost, G. A. C. Jones, and D. G. Hasko. "Measurements of Coulomb Blockade with a Noninvasive Voltage Probe." *Phys. Rev. Lett.*, **70**(9):1311–1314, March 1993.

[GEC13] John King Gamble, M. A. Eriksson, S. N. Coppersmith, and Mark Friesen. "Disorder-Induced Valley-Orbit Hybrid States in Si Quantum Dots." *Phys. Rev. B*, **88**(3):035310, July 2013.

[GHJ16] John King Gamble, Patrick Harvey-Collard, N. Tobias Jacobson, Andrew D. Baczewski, Erik Nielsen, Leon Maurer, Inès Montaño, Martin Rudolph, M. S. Carroll, C. H. Yang, A. Rossi, A. S. Dzurak, and Richard P. Muller. "Valley Splitting of Single-Electron Si MOS Quantum Dots." *Appl. Phys. Lett.*, **109**(25):253101, December 2016.

[Gre90] Martin A. Green. "Intrinsic Concentration, Effective Densities of States, and Effective Mass in Silicon." *Journal of Applied Physics*, **67**(6):2944–2954, March 1990.

[Gri05] David J. Griffiths. *Introduction to Quantum Mechanics*. Pearson Education, Inc., second edition, 2005.

[HCC17] TianYi Han, MingBo Chen, Gang Cao, HaiOu Li, Ming Xiao, and GuoPing Guo. "Radio-Frequency Measurement in Semiconductor Quantum Computation." *Sci. China Phys. Mech. Astron.*, **60**(5):057301, May 2017.

[HFJ17] T. Hensgens, T. Fujita, L. Janssen, Xiao Li, C. J. Van Diepen, C. Reichl, W. Wegscheider, S. Das Sarma, and L. M. K. Vandersypen. "Quantum Simulation of a Fermi–Hubbard Model Using a Semiconductor Quantum Dot Array." *Nature*, **548**(7665):70–73, August 2017.

[HH14] Peihao Huang and Xuedong Hu. "Spin Relaxation in a Si Quantum Dot Due to Spin-Valley Mixing." *Phys. Rev. B*, **90**(23):235315, December 2014.

[HKP07] R. Hanson, L. P. Kouwenhoven, J. R. Petta, S. Tarucha, and L. M. K. Vandersypen. "Spins in Few-Electron Quantum Dots." *Rev. Mod. Phys.*, **79**(4):1217–1265, October 2007.

[HLL12] S.-H. Huang, T.-M. Lu, S.-C. Lu, C.-H. Lee, C. W. Liu, and D. C. Tsui. "Mobility Enhancement of Strained Si by Optimized SiGe/Si/SiGe Structures." *Appl. Phys. Lett.*, **101**(4):042111, July 2012.

[Hou12] Matthew House. *Lateral Quantum Dots for Quantum Information Processing.* PhD Thesis, University of California Los Angeles, 2012.

[HRX14] Xiaojie Hao, Rusko Ruskov, Ming Xiao, Charles Tahan, and HongWen Jiang. "Electron Spin Resonance and Spin–Valley Physics in a Silicon Double Quantum Dot." *Nat Commun*, **5**(1):3860, September 2014.

[HSL20] Arne Hollmann, Tom Struck, Veit Langrock, Andreas Schmidbauer, Floyd Schauer, Tim Leonhardt, Kentarou Sawano, Helge Riemann, Nikolay V. Abrosimov, Dominique Bougeard, and Lars R. Schreiber. "Large, Tunable Valley Splitting and Single-Spin Relaxation Mechanisms in a Si / Si x Ge 1 - x Quantum Dot." *Phys. Rev. Applied*, **13**(3):034068, March 2020.

[HVv04] R. Hanson, L. M. K. Vandersypen, L. H. Willems van Beveren, J. M. Elzerman, I. T. Vink, and L. P. Kouwenhoven. "Semiconductor Few-Electron Quantum Dot Operated as a Bipolar Spin Filter." *Phys. Rev. B*, **70**(24):241304, December 2004.

[HvV05] R. Hanson, L. H. Willems van Beveren, I. T. Vink, J. M. Elzerman, W. J. M. Naber, F. H. L. Koppens, L. P. Kouwenhoven, and L. M. K. Vandersypen. "Single-Shot Readout of Electron Spin States in a Quantum Dot Using Spin-Dependent Tunnel Rates." *Phys. Rev. Lett.*, **94**(19):196802, May 2005.

[HVZ17] Wister Huang, Menno Veldhorst, Neil M. Zimmerman, Andrew S. Dzurak, and Dimitrie Culcer. "Electrically Driven Spin Qubit Based on Valley Mixing." *Phys. Rev. B*, **95**(7):075403, February 2017.

[JAG11] M. W. Johnson, M. H. S. Amin, S. Gildert, T. Lanting, F. Hamze, N. Dickson, R. Harris, A. J. Berkley, J. Johansson, P. Bunyk, E. M. Chapple, C. Enderud, J. P. Hilton, K. Karimi, E. Ladizinsky, N. Ladizinsky, T. Oh, I. Perminov, C. Rich, M. C. Thom, E. Tolkacheva, C. J. S. Truncik, S. Uchaikin, J. Wang, B. Wilson, and G. Rose. "Quantum Annealing with Manufactured Spins." *Nature*, **473**(7346):194–198, May 2011.

[JJH18] Ryan M. Jock, N. Tobias Jacobson, Patrick Harvey-Collard, Andrew M. Mounce, Vanita Srinivasa, Dan R. Ward, John Anderson, Ron Manginell, Joel R. Wendt, Martin Rudolph, Tammy Pluym, John King Gamble, Andrew D. Baczewski, Wayne M. Witzel, and Malcolm S. Carroll. "A Silicon Metal-Oxide-Semiconductor Electron Spin-Orbit Qubit." *Nat Commun*, **9**(1):1768, December 2018.

[JKM01] Daniel F. V. James, Paul G. Kwiat, William J. Munro, and Andrew G. White. "Measurement of Qubits." *Phys. Rev. A*, **64**(5):052312, October 2001.

[JPC19] A.M. Jones, E.J. Pritchett, E.H. Chen, T.E. Keating, R.W. Andrews, J.Z. Blumoff, L.A. De Lorenzo, K. Eng, S.D. Ha, A.A. Kiselev, S.M. Meenehan, S.T. Merkel, J.A. Wright, L.F. Edge, R.S. Ross, M.T. Rakher, M.G. Borselli, and A. Hunter. "Spin-Blockade Spectroscopy of Si / Si - Ge Quantum Dots." *Phys. Rev. Applied*, **12**(1):014026, July 2019.

[JPM05] A. C. Johnson, J. R. Petta, C. M. Marcus, M. P. Hanson, and A. C. Gossard. "Singlet-Triplet Spin Blockade and Charge Sensing in a Few-Electron Double Quantum Dot." *Phys. Rev. B*, **72**(16):165308, October 2005.

[KDP80] K. v. Klitzing, G. Dorda, and M. Pepper. "New Method for High-Accuracy Determination of the Fine-Structure Constant Based on Quantized Hall Resistance." *Phys. Rev. Lett.*, **45**(6):494–497, August 1980.

[Kit05] Charles Kittel. *Introduction to Solid State Physics*. John Wiley & Sons, Inc., eighth edition, 2005.

[KMM97] Leo P Kouwenhoven, Charles M Marcus, Paul L Mceuen, Seigo Tarucha, and Ned S Wingreen. "ELECTRON TRANSPORT IN QUANTUM DOTS." *QUANTUM DOTS*, p. 110, 1997.

[KMM13] Vadym Kliuchnikov, Dmitri Maslov, and Michele Mosca. "Asymptotically Optimal Approximation of Single Qubit Unitaries by Clifford and T Circuits Using a Constant Number of Ancillary Qubits." *Phys. Rev. Lett.*, **110**(19):190502, May 2013.

[KSS14] Dohun Kim, Zhan Shi, C. B. Simmons, D. R. Ward, J. R. Prance, Teck Seng Koh, John King Gamble, D. E. Savage, M. G. Lagally, Mark Friesen, S. N. Coppersmith, and Mark A. Eriksson. "Quantum Control and Process Tomography of a Semiconductor Quantum Dot Hybrid Qubit." *Nature*, **511**(7507):70–74, July 2014.

[KSW14] E. Kawakami, P. Scarlino, D. R. Ward, F. R. Braakman, D. E. Savage, M. G. Lagally, Mark Friesen, S. N. Coppersmith, M. A. Eriksson, and L. M. K. Vandersypen. "Electrical Control of a Long-Lived Spin Qubit in a Si/SiGe Quantum Dot." *Nature Nanotech*, **9**(9):666–670, September 2014.

[KTL17] J.-S. Kim, A. M. Tyryshkin, and S. A. Lyon. "Annealing Shallow Si/SiO_2 Interface Traps in Electron-Beam Irradiated High-Mobility Metal-Oxide-Silicon Transistors." *Appl. Phys. Lett.*, **110**(12):123505, March 2017.

[KWS15] Dohun Kim, Daniel R Ward, Christie B Simmons, Don E Savage, Max G Lagally, Mark Friesen, Susan N Coppersmith, and Mark A Eriksson. "High-Fidelity Resonant Gating of a Silicon-Based Quantum Dot Hybrid Qubit." *npj Quantum Inf*, **1**(1):15004, December 2015.

[LD98] Daniel Loss and David P. DiVincenzo. "Quantum Computation with Quantum Dots." *Phys. Rev. A*, **57**(1):120–126, January 1998.

[LHR13] Jiun-Yun Li, Chiao-Ti Huang, Leonid P. Rokhinson, and James C. Sturm. "Extremely High Electron Mobility in Isotopically-Enriched ^{28} Si Two-Dimensional Electron Gases Grown by Chemical Vapor Deposition." *Appl. Phys. Lett.*, **103**(16):162105, October 2013.

[LPF18] Ruoyu Li, Luca Petit, David P. Franke, Juan Pablo Dehollain, Jonas Helsen, Mark Steudtner, Nicole K. Thomas, Zachary R. Yoscovits, Kanwal J. Singh, Stephanie Wehner, Lieven M. K. Vandersypen, James S. Clarke, and Menno Veldhorst. "A Crossbar Network for Silicon Quantum Dot Qubits." *Science Advances*, **4**(7):eaar3960, July 2018.

[LYZ11] W H Lim, C H Yang, F A Zwanenburg, and A S Dzurak. "Spin Filling of Valley–Orbit States in a Silicon Quantum Dot." *Nanotechnology*, **22**(33):335704, August 2011.

[MAR07] K. MacLean, S. Amasha, Iuliana P. Radu, D. M. Zumbühl, M. A. Kastner, M. P. Hanson, and A. C. Gossard. "Energy-Dependent Tunneling in a Quantum Dot." *Phys. Rev. Lett.*, **98**(3):036802, January 2007.

[MDS17] M. Yu. Melnikov, V. T. Dolgopolov, A. A. Shashkin, S.-H. Huang, C. W. Liu, and S. V. Kravchenko. "Unusual Anisotropy of Inplane Field Magnetoresistance in Ultra-High Mobility SiGe/Si/SiGe Quantum Wells." *Journal of Applied Physics*, **122**(22):224301, December 2017.

[MHP15] X. Mi, T. M. Hazard, C. Payette, K. Wang, D. M. Zajac, J. V. Cady, and J. R. Petta. "Magnetotransport Studies of Mobility Limiting Mechanisms in Undoped Si/SiGe Heterostructures." *Phys. Rev. B*, **92**(3):035304, July 2015.

[MMB85] J F Mika, L J Martin, and Z Barnea. "X-Ray Attenuation of Silicon in the Energy Range 25-50 keV." *J. Phys. C: Solid State Phys.*, **18**(26):5215–5223, September 1985.

[MPB17] X. Mi, Csaba G. Péterfalvi, Guido Burkard, and J. R. Petta. "High-Resolution Valley Spectroscopy of Si Quantum Dots." *Phys. Rev. Lett.*, **119**(17):176803, October 2017.

[MPZ10] Andrea Morello, Jarryd J. Pla, Floris A. Zwanenburg, Kok W. Chan, Kuan Y. Tan, Hans Huebl, Mikko Möttönen, Christopher D. Nugroho, Changyi Yang, Jessica A. van Donkelaar, Andrew D. C. Alves, David N. Jamieson, Christopher C. Escott, Lloyd C. L. Hollenberg, Robert G. Clark, and Andrew S. Dzurak. "Single-Shot Readout of an Electron Spin in Silicon." *Nature*, **467**(7316):687–691, October 2010.

[MRT19] Christopher Monroe, Michael G. Raymer, and Jacob Taylor. "The U.S. National Quantum Initiative: From Act to Action." *Science*, **364**(6439):440–442, May 2019.

[MSS01] Yuriy Makhlin, Gerd Schön, and Alexander Shnirman. "Quantum-State Engineering with Josephson-Junction Devices." *Rev. Mod. Phys.*, **73**(2):357–400, May 2001.

[NC00] M. A. Nielsen and I. L. Chuang. *Quantum Computation and Quantum Information*. Cambridge University Press, 2000.

[NES09] E. P. Nordberg, G. A. Ten Eyck, H. L. Stalford, R. P. Muller, R. W. Young, K. Eng, L. A. Tracy, K. D. Childs, J. R. Wendt, R. K. Grubbs, J. Stevens, M. P. Lilly, M. A. Eriksson, and M. S. Carroll. "Enhancement-Mode Double-Top-Gated Metal-Oxide-Semiconductor Nanostructures with Tunable Lateral Geometry." *Phys. Rev. B*, **80**(11):115331, September 2009.

[OAT02] K. Ono, D. G. Austing, Y. Tokura, and S. Tarucha. "Current Rectification by Pauli Exclusion in a Weakly Coupled Double Quantum Dot System." *Science*, **297**(5585):1313–1317, August 2002.

[Pan13] Hong Pan. *Experimental Investigation of Silicon Metal-Oxide-Semiconductor Based Triple Quantum Dot*. PhD Thesis, University of California Los Angeles, 2013.

[PBE18] L. Petit, J. M. Boter, H. G. J. Eenink, G. Droulers, M. L. V. Tagliaferri, R. Li, D. P. Franke, K. J. Singh, J. S. Clarke, R. N. Schouten, V. V. Dobrovitski, L. M. K. Vandersypen, and M. Veldhorst. "Spin Lifetime and Charge Noise in Hot Silicon Quantum Dot Qubits." *Phys. Rev. Lett.*, **121**(7):076801, August 2018.

[PER20] L. Petit, H. G. J. Eenink, M. Russ, W. I. L. Lawrie, N. W. Hendrickx, S. G. J. Philips, J. S. Clarke, L. M. K. Vandersypen, and M. Veldhorst. "Universal Quantum Logic in Hot Silicon Qubits." *Nature*, **580**(7803):355–359, April 2020.

[Phi58] James C. Phillips. "Energy-Band Interpolation Scheme Based on a Pseudopotential." *Phys. Rev.*, **112**(3):685–695, November 1958.

[PHW19] N. E. Penthorn, X. Hao, Z. Wang, Y. Huai, and H. W. Jiang. "Experimental Observation of Single Skyrmion Signatures in a Magnetic Tunnel Junction." *Phys. Rev. Lett.*, **122**(25):257201, June 2019.

[PJM04] J. R. Petta, A. C. Johnson, C. M. Marcus, M. P. Hanson, and A. C. Gossard. "Manipulation of a Single Charge in a Double Quantum Dot." *Phys. Rev. Lett.*, **93**(18):186802, October 2004.

[PKJ11] M Prada, G Klimeck, and R Joynt. "Spin–Orbit Splittings in Si/SiGe Quantum Wells: From Ideal Si Membranes to Realistic Heterostructures." *New J. Phys.*, **13**(1):013009, January 2011.

[PLG10] J. R. Petta, H. Lu, and A. C. Gossard. "A Coherent Beam Splitter for Electronic Spin States." *Science*, **327**(5966):669–672, February 2010.

[PPL10] K. D. Petersson, J. R. Petta, H. Lu, and A. C. Gossard. "Quantum Coherence in a One-Electron Semiconductor Charge Qubit." *Phys. Rev. Lett.*, **105**(24):246804, December 2010.

[PSE20] Nicholas E. Penthorn, Joshua S. Schoenfield, Lisa F. Edge, and HongWen Jiang. "Direct Measurement of Electron Intervalley Relaxation in a Si/SiGe Quantum Dot." *arXiv:2007.08680 [cond-mat.mes-hall]*, July 2020.

[PSR19a] Nicholas E. Penthorn, Joshua S. Schoenfield, John D. Rooney, Lisa F. Edge, and HongWen Jiang. "Two-Axis Quantum Control of a Fast Valley Qubit in Silicon." *npj Quantum Inf*, **5**(1):94, December 2019.

[PSR19b] Nicholas E Penthorn, Joshua S Schoenfield, John D Rooney, and HongWen Jiang. "Reduction of Charge Impurities in a Silicon Metal-Oxide-Semiconductor Quantum Dot Qubit Device Patterned with Nano-Imprint Lithography." *Nanotechnology*, **30**(46):465302, November 2019.

[PYA03] Yu A Pashkin, T Yamamoto, O Astafiev, Y Nakamura, D V Averin, and J S Tsai. "Quantum Oscillations in Two Coupled Charge Qubits." *Nature*, **421**:4, 2003.

[Ras60] E. I. Rashba. "Properties of Semiconductors with a Loop of Extrema, I. Cyclotron and Combined Resonances in a Perpendicular Field." *Sov. Phys. Solid State*, **2**:1109, 1960.

[Rei65] F. Reif. *Fundamentals of Statistical and Thermal Physics*. Waveland Press, Inc., first edition, 1965.

[RRB14] Niklas Rohling, Maximilian Russ, and Guido Burkard. "Hybrid Spin and Valley Quantum Computing with Singlet-Triplet Qubits." *Phys. Rev. Lett.*, **113**(17):176801, October 2014.

[Sch97] Friedrich Schäffler. "High-Mobility Si and Ge Structures." *Semicond. Sci. Technol.*, **12**(12):1515–1549, December 1997.

[SCH09] A. L. Saraiva, M. J. Calderón, Xuedong Hu, S. Das Sarma, and Belita Koiller. "Physical Mechanisms of Interface-Mediated Intervalley Coupling in Si." *Phys. Rev. B*, **80**(8):081305, August 2009.

[Sch17] Joshua Schoenfield. *Coherent Control and Spectroscopy of Valley States of Individual Electrons in Silicon Quantum Dots*. PhD Thesis, University of California Los Angeles, 2017.

[SFJ17] Joshua S. Schoenfield, Blake M. Freeman, and HongWen Jiang. "Coherent Manipulation of Valley States at Multiple Charge Configurations of a Silicon Quantum Dot Device." *Nat Commun*, **8**(1):64, December 2017.

[Sho94] P.W. Shor. "Algorithms for Quantum Computation: Discrete Logarithms and Factoring." In *Proceedings 35th Annual Symposium on Foundations of Computer Science*, pp. 124–134, November 1994.

[SK54] J. C. Slater and G. F. Koster. "Simplified LCAO Method for the Periodic Potential Problem." *Phys. Rev.*, **94**(6):1498–1524, June 1954.

[SKJ17] P. Scarlino, E. Kawakami, T. Jullien, D. R. Ward, D. E. Savage, M. G. Lagally, Mark Friesen, S. N. Coppersmith, M. A. Eriksson, and L. M. K. Vandersypen. "Dressed Photon-Orbital States in a Quantum Dot: Intervalley Spin Resonance." *Phys. Rev. B*, **95**(16):165429, April 2017.

[Str] Moor Insights and Strategy. "Quantum USA Vs. Quantum China: The World's Most Important Technology Race." https://www.forbes.com/sites/moorinsights/2019/10/10/quantum-usa-vs-quantum-china-the-worlds-most-important-technology-race/.

[TH19] Bilal Tariq and Xuedong Hu. "Effects of Interface Steps on the Valley-Orbit Coupling in a Si/SiGe Quantum Dot." *Phys. Rev. B*, **100**(12):125309, September 2019.

[TJ14] Charles Tahan and Robert Joynt. "Relaxation of Excited Spin, Orbital, and Valley Qubit States in Ideal Silicon Quantum Dots." *Phys. Rev. B*, **89**(7):075302, February 2014.

[TM92] M.-H. Tsai and T.P. Ma. "Effect of Radiation-Induced Interface Traps on 1/f Noise in MOSFET's." *IEEE Transactions on Nuclear Science*, **39**(6):2178–2185, December 1992.

[vDE02] W. G. van der Wiel, S. De Franceschi, J. M. Elzerman, T. Fujisawa, S. Tarucha, and L. P. Kouwenhoven. "Electron Transport through Double Quantum Dots." *Rev. Mod. Phys.*, **75**(1):1–22, December 2002.

[VHY14] M. Veldhorst, J. C. C. Hwang, C. H. Yang, A. W. Leenstra, B. de Ronde, J. P. Dehollain, J. T. Muhonen, F. E. Hudson, K. M. Itoh, A. Morello, and A. S. Dzurak. "An Addressable Quantum Dot Qubit with Fault-Tolerant Control-Fidelity." *Nature Nanotech*, **9**(12):981–985, December 2014.

[VRY15] M. Veldhorst, R. Ruskov, C. H. Yang, J. C. C. Hwang, F. E. Hudson, M. E. Flatté, C. Tahan, K. M. Itoh, A. Morello, and A. S. Dzurak. "Spin-Orbit Coupling and Operation of Multivalley Spin Qubits." *Phys. Rev. B*, **92**(20):201401, November 2015.

[vvB88] B. J. van Wees, H. van Houten, C. W. J. Beenakker, J. G. Williamson, L. P. Kouwenhoven, D. van der Marel, and C. T. Foxon. "Quantized Conductance of Point Contacts in a Two-Dimensional Electron Gas." *Phys. Rev. Lett.*, **60**(9):848–850, February 1988.

[Wit05] Curt Wittig. "The Landau-Zener Formula." *J. Phys. Chem. B*, **109**(17):8428–8430, May 2005.

[WPD13] K. Wang, C. Payette, Y. Dovzhenko, P. W. Deelman, and J. R. Petta. "Charge Relaxation in a Single-Electron Si / SiGe Double Quantum Dot." *Phys. Rev. Lett.*, **111**(4):046801, July 2013.

[XHJ10] M. Xiao, M. G. House, and H. W. Jiang. "Measurement of the Spin Relaxation Time of Single Electrons in a Silicon Metal-Oxide-Semiconductor-Based Quantum Dot." *Phys. Rev. Lett.*, **104**(9):096801, March 2010.

[YCH19] C. H. Yang, K. W. Chan, R. Harper, W. Huang, T. Evans, J. C. C. Hwang, B. Hensen, A. Laucht, T. Tanttu, F. E. Hudson, S. T. Flammia, K. M. Itoh, A. Morello, S. D. Bartlett, and A. S. Dzurak. "Silicon Qubit Fidelities Approaching Incoherent Noise Limits via Pulse Engineering." *Nat Electron*, **2**(4):151–158, April 2019.

[YLH20] C. H. Yang, R. C. C. Leon, J. C. C. Hwang, A. Saraiva, T. Tanttu, W. Huang, J. Camirand Lemyre, K. W. Chan, K. Y. Tan, F. E. Hudson, K. M. Itoh, A. Morello, M. Pioro-Ladrière, A. Laucht, and A. S. Dzurak. "Operation of a Silicon Quantum Processor Unit Cell above One Kelvin." *Nature*, **580**(7803):350–354, April 2020.

[YLL20] Juan Yin, Yu-Huai Li, Sheng-Kai Liao, Meng Yang, Yuan Cao, Liang Zhang, Ji-Gang Ren, Wen-Qi Cai, Wei-Yue Liu, Shuang-Lin Li, Rong Shu, Yong-Mei Huang, Lei Deng, Li Li, Qiang Zhang, Nai-Le Liu, Yu-Ao Chen, Chao-Yang Lu,

Xiang-Bin Wang, Feihu Xu, Jian-Yu Wang, Cheng-Zhi Peng, Artur K. Ekert, and Jian-Wei Pan. "Entanglement-Based Secure Quantum Cryptography over 1,120 Kilometres." *Nature*, June 2020.

[YRR13] C. H. Yang, A. Rossi, R. Ruskov, N. S. Lai, F. A. Mohiyaddin, S. Lee, C. Tahan, G. Klimeck, A. Morello, and A. S. Dzurak. "Spin-Valley Lifetimes in a Silicon Quantum Dot with Tunable Valley Splitting." *Nat Commun*, **4**(1):2069, October 2013.

[YTO18] Jun Yoneda, Kenta Takeda, Tomohiro Otsuka, Takashi Nakajima, Matthieu R. Delbecq, Giles Allison, Takumu Honda, Tetsuo Kodera, Shunri Oda, Yusuke Hoshi, Noritaka Usami, Kohei M. Itoh, and Seigo Tarucha. "A Quantum-Dot Spin Qubit with Coherence Limited by Charge Noise and Fidelity Higher than 99.9%." *Nature Nanotech*, **13**(2):102–106, February 2018.

[YWD11] Shuo Yang, Xin Wang, and S. Das Sarma. "Generic Hubbard Model Description of Semiconductor Quantum-Dot Spin Qubits." *Phys. Rev. B*, **83**(16):161301, April 2011.

[Zak10] Muhanad Zaki. "Bulk Bandstructure in MATLAB: Pseudopotential Method.", 2010.

[ZDM13] Floris A. Zwanenburg, Andrew S. Dzurak, Andrea Morello, Michelle Y. Simmons, Lloyd C. L. Hollenberg, Gerhard Klimeck, Sven Rogge, Susan N. Coppersmith, and Mark A. Eriksson. "Silicon Quantum Electronics." *Rev. Mod. Phys.*, **85**(3):961–1019, July 2013.

[ZTT19] R. Zhao, T. Tanttu, K. Y. Tan, B. Hensen, K. W. Chan, J. C. C. Hwang, R. C. C. Leon, C. H. Yang, W. Gilbert, F. E. Hudson, K. M. Itoh, A. A. Kiselev, T. D. Ladd, A. Morello, A. Laucht, and A. S. Dzurak. "Single-Spin Qubits in Isotopically Enriched Silicon at Low Magnetic Field." *Nat Commun*, **10**(1):5500, December 2019.